Doctoral Thesis

Synthesis and Architecture-Controlled Assembly of Functional Nanomaterials for Energy Conversion and Storage

Minsu Gu

Department of Energy Engineering

(Energy Engineering)

Graduate School of UNIST

2018

Synthesis and Architecture-Controlled Assembly of Functional Nanomaterials for Energy Conversion and Storage

Minsu Gu

Department of Energy Engineering

(Energy Engineering)

Graduate School of UNIST

Synthesis and Architecture-Controlled Assembly of Functional Nanomaterials for Energy Conversion and Storage

A thesis/dissertation
submitted to the Graduate School of UNIST
in partial fulfillment of the
requirements for the degree of
Doctor of Philosophy

Minsu Gu

July/06/2018

Approved by

Advisor
Byeong-Su Kim

Synthesis and Architecture-Controlled Assembly of Functional Nanomaterials for Energy Conversion and Storage

Minsu Gu

This certifies that the thesis/dissertation of Minsu Gu is approved.

July/06/2018

signature

Advisor: Byeong-Su Kim

signature

Soojin Park: Thesis Committee Member #1

signature

Hyun-Kon Song: Thesis Committee Member #2

signature

Jungki Ryu: Thesis Committee Member #3

signature

Ik-Soo Shin: Thesis Committee Member #4;

Abstract

In this thesis, I will present the research achievement and progress in synthesis and architecture-controlled assembly of functional nanomaterials, especially graphene-based nanocomposites hybridized with various nanomaterials such as carbon nanomaterials, polymers, and inorganic nanoparticles for energy conversion and storage applications.

Two-dimensional (2D) graphene sheets have become a versatile platform for the fabrication of innovative hybrid materials with various functions due to their unique electrical, optical, thermal, and mechanical properties. The preparation of graphene-based composites with nanoscale precision is highly important for reproducible and controllable performance through the analysis of interplay between each component. In particular, the layer-by-layer (LbL) assembly technique is known as a simple, inexpensive, and versatile process for the fabrication of highly ordered multilayer film structures from various types of materials. The LbL structures capable of controlling nanoscale composition and architectures are achieved through the sequential adsorption of oppositely charged components by attractive forces such as electrostatic interactions. Multilayered graphene nanocomposites exhibit improved physical/chemical properties and superior performance compared with the individual components due to the synergistic effects in various applications including electric devices, energy storage and conversion.

Contents

List of Figures

Figure. 3.1.4. Films growth characteristics of LbL assembled multilayer electrodes. (a) UV/vis absorbance spectra of $(GO/Au/GO/Pd)_n$ multilayer thin films. Inset image represents the samples prepared. (b) The corresponding absorbance maxima of multilayer films at 215 nm with $(GO/Au)_n$ and $(GO/Pd)_n$. Inset represents the corresponding absorbance maxima of multilayer films at 600 nm. (c) The thickness of each film measured by a surface profiler. (d) Mass change by QCM analysis as a function of the number of tetralayer of $(GO/Au/GO/Pd)_n$ multilayer thin films.

Figure 3.1.5. UV/vis absorbance spectra of (a) $(GO/Au)_n$ and (b) $(GO/Pd)_n$ multilayer thin films. (c) Comparison of absorbance of GO layer at 215 nm in (red triangle) bimetallic $(GO/Au/GO/Pd)_n$ multilayer and (black square) the sum of two individual monometallic $(GO/Au)_n$ and $(GO/Pd)_n$ multilayers.

Figure 3.1.6. Catalytic effect for methanol oxidation reaction. Cyclic voltammograms (CVs) of (a) $(GO/Pd)_n$ multilayer thin films with an inset of the current density plot as a function of number of bilayer (BL) in $(GO/Pd)_n$ multilayer films. (b) Comparison of electrocatalytic activity of $(GO/Au)_3$, $(GO/Pd)_3$ and $(GO/Au/GO/Pd)_3$ films. Inset in Figure b shows a magnified CV of $(GO/Au)_3$. All measurements were performed in 0.10 M KOH with 1.0 M CH_3OH in a saturated N_2 at a scan rate of 20 mV s^{-1}.

Figure 3.1.7. CV of $(GO/Pd)_n$ multilayer thin films (n = 2, 4, 6, 8 and 10) in 0.10 M KOH in a saturated N_2 at a scan rate of 20 mV s^{-1}.

Figure 3.1.8. CV of $(GO/Au)_n$ multilayer thin films of (a) 2 BL, (b) 4 BL and (c) 6 BL in 0.10 M KOH and 1.0 M CH_3OH solution under a saturated N_2 at various scan rates. (d) Plots of log i_p vs log v to determine the reaction kinetics. The slope is reduced from 0.71 to 0.60 as the film thickness increases.

Figure 3.1.9. High-resolution XPS spectra of (a) Au 4f and (b) Au 4d and Pd 3d for $(GO/Au)_3$, $(GO/Pd)_3$ and $(GO/Au/GO/Pd)_3$ multilayer thin films.

Figure 3.1.10. CV of bimetallic multilayer electrodes prepared under different sequence of layering. (red) $(GO/Au/GO/Pd)_3$ and (black) $(GO/Pd/GO/Au)_3$ in 0.10 M KOH and 1.0 M CH_3OH solution under a saturated N_2 at a scan rate of 20 mV s^{-1}.

Figure 3.1.11. Stability test of bimetallic $(GO/Au/GO/Pd)_3$ thin film electrode through (a) CV and (b) corresponding cycle retention, comparing with monometallic $(GO/Pd)_6$ thin film for 100 cycles measured in 0.10 M KOH with 1.0 M CH_3OH in a saturated N_2 at a scan rate of 20 mV s^{-1}.

Figure 3.1.12. Architecture controlled multilayer thin films. Representative cross-sectional high-resolution TEM and HAADF-STEM images with composed elemental mapping images of Au and Pd of (a) $(GO/Au/GO/Pd)_3$, (b) $(GO/Au)_3/(GO/Pd)_3$ and (c) $(GO/Pd)_3/(GO/Au)_3$ multilayer thin films.

Figure 3.1.13. Representative cross-sectional high-resolution TEM of $(GO/Pd)_3/(GO/Au)_3$ multilayer thin film with a schematic illustration.

Figure 3.1.14. AFM images of (a) $(GO/Au/GO/Pd)_3$, (b) $(GO/Au)_3/(GO/Pd)_3$ and (c) $(GO/Pd)_3/(GO/Au)_3$ multilayer thin films with schematic illustrations. The scale bar of each image is 1.0 μm.

Figure 3.1.15. SEM images of (a) $(GO/Au/GO/Pd)_3$, (b) $(GO/Au)_3/(GO/Pd)_3$ and (c) $(GO/Pd)_3/(GO/Au)_3$ multilayer thin films with schematic illustrations. The scale bar of each image is 400 nm.

Figure 3.1.16. Architectural effect in 3D multilayer electrode for methanol oxidation. (a) Cyclic voltammograms, (b) corresponding Tafel plots and (c) calculated αn, product of transfer coefficient (α) and number of electrons (n) of $(GO/Au)_3$, $(GO/Pd)_3$, $(GO/Au)_3/(GO/Pd)_3$, $(GO/Pd)_3/(GO/Au)_3$ and $(GO/Au/GO/Pd)_3$ multilayer films. (d) Cyclic voltammograms of $(GO/Au)_n/(GO/Pd)_{6-n}$ (dotted line), $(GO/Pd)_n/(GO/Au)_{6-n}$ (solid line) multilayer thin films (n = 1, 3 and 5). (e) Comparison of electrochemical performance of all multilayer films with varying architecture toward MOR. Yellow and blue Tafel region corresponds to $(GO/Au)_n$ and $(GO/Pd)_n$, respectively. All measurements were measured in 0.10 M KOH with 1.0 M CH_3OH in a saturated N_2 at a scan rate of 20 mV s^{-1}.

Figure 3.1.17. Schematic representation of a controllable electrochemical mechanism between mass and charge transfer. Red and gray arrows indicate the diffusion flows on Au and Pd NPs, respectively in LbL assembled $(GO/Au)_3/(GO/Pd)_3$ and $(GO/Pd)_3/(GO/Au)_3$ multilayer thin films.

Figure 3.1.18. Nyquist plots of impedance on $(GO/Au/GO/Pd)_3$, $(GO/Au)_3/(GO/Pd)_3$, and $(GO/Pd)_3/(GO/Au)_3$ multilayer thin films at 0.35 V. Inset represents an equivalent circuit.

Figure 3.1.19. CV of $(GO/Au/GO/Pd)_3$, $(GO/Au)_n/(GO/Pd)_{6-n}$, $(GO/Pd)_n/(GO/Au)_{6-n}$ multilayer thin films (n = 1, 3 and 5) in 0.10 M KOH in a saturated N_2 at a scan rate of 20 mV s^{-1}.

Figure 3.1.20. CV of commercial 30 wt.% Pd/C in 0.10 M KOH with 1.0 M CH_3OH in a saturated N_2 at a scan rate of 20 mV s^{-1}.

Figure 3.2.1. Schematic representation of layer-by-layer (LbL)-assembled $(GO/Pd)_n$ multilayer thin film electrodes with varying GO sheet size (LGO, MGO, and NGO) toward methanol oxidation reaction in bulk electrolyte solution. The black and red dotted arrows indicate the diffusion of methanol molecules in electrolyte and the 3D LbL electrodes, respectively. The yellow arrows indicate the charge transfer from the 3D LbL electrodes.

Figure 3.2.2. Representative AFM images of (a) LGO, (b) MGO, and (c) NGO sheets with corresponding line scan profiles and size distribution histograms. The average values were collected

over 40 samples.

Figure 3.2.3. FT-IR spectra of LGO, MGO, and NGO sheets.

Figure 3.2.4. Raman spectra of LGO, MGO, and NGO sheets.

Figure 3.2.5. TEM images with a corresponding size distribution histogram of DMAP-Pd NPs suspension.

Figure 3.2.6. (a) UV/vis absorbance spectra of representative $(LGO/Pd)_n$ multilayer thin films. The inset image shows the samples prepared with the corresponding number of bilayers (BLs, *n*). (b) Film thickness measured by surface profiler and (c) quartz crystal microbalance (QCM) analysis of all multilayer thin film electrodes as a function of the number of BLs (*n*). The inset in Figure b shows the corresponding UV/vis absorbance maxima at 215 nm for all multilayer electrodes. (d) Mass ratio of GO to Pd and volumetric mass of Pd in each multilayer thin film.

Figure 3.2.7. UV/vis absorbance spectra of (a) $(MGO/Pd)_n$ and (b) $(NGO/Pd)_n$ multilayer thin films. Inset image represents the samples prepared.

Figure 3.2.8. Representative SEM (left) and AFM (right) images of (a) $(LGO/Pd)_4$, (b) $(MGO/Pd)_4$, and (c) $(NGO/Pd)_4$ multilayer thin film electrodes. The scale bar in the SEM images is 1 μm and the R_{rms} values of the AFM images are averaged over a 5 × 5 μm^2 area.

Figure 3.2.9. (a – c) Representative cross-sectional high-resolution TEM images of (a) $(LGO/Pd)_6$, (b) $(MGO/Pd)_6$, and (c) $(NGO/Pd)_6$ multilayer thin film electrodes. (d) Representative cross-sectional HAADF-STEM image of $(LGO/Pd)_6$ with (e) EELS line scan and extracted EELS analysis of (f) LGO and (g) Pd NPs corresponding to the multilayer films.

Figure 3.2.10. (a – c) Cyclic voltammograms (CVs) of (a) $(LGO/Pd)_n$, (b) $(MGO/Pd)_n$, and (c) $(NGO/Pd)_n$ multilayer thin film electrodes. (d) Comparison of the electrochemical performance toward the MOR as a function of the number of BLs. The inset in Figure d shows the maximum number of BLs for all multilayer thin films and the current density at 4 BLs. All CVs were recorded in N_2 saturated 0.10 M KOH with 1.0 M CH_3OH at a scan rate of 20 mV/s.

Figure 3.2.11. Chronoamperogram (CA) of $(LGO/Pd)_{10}$, $(MGO/Pd)_{10}$ and $(NGO/Pd)_{10}$ multilayer thin films at 0 V (vs. Hg/HgO) in N_2 saturated 0.10 M KOH with 1.0 M CH_3OH.

Figure 3.2.12. (a) Nyquist plots of impedance of $(LGO/Pd)_4$, $(MGO/Pd)_4$, and $(NGO/Pd)_4$ multilayer thin films at -0.1 V with an equivalent circuit. (b) The calculated tortuosity and (c) diffusion length of $(LGO/Pd)_n$, $(MGO/Pd)_n$, and $(NGO/Pd)_n$ multilayer thin films with cross-sectional schematic representation of multilayer thin films, where *n* is above 6. The inset in Figure b and c shows the magnified tortuosity and diffusion length of $(NGO/Pd)_n$ with respect to the bilayer numbers (*n*),

represent the Mn^{2+} ions, and the ethylene carbonate solvent is shown as a transparent surface for clarity. Deconvoluted high-resolution Mn 2p XPS spectra of (g) PP/PE/PP, (h) CNF, and (i) TPY-CNF with Mn^{2+} ions.

Figure 5.1.7. A photograph showing the structural disruption of the electrospun mat after the mat was immersed in a liquid electrolyte (1.0 M $LiPF_6$ in EC/DEC = 1/1 (v/v)): (a) PVP electrospun mat and (b) PVP/PAN electrospun mat.

Figure 5.1.8. Variation in the XPS spectra (characteristic peak of nitrogen atoms) of PVP/PAN or PAN films after the films were swelled in a liquid electrolyte (1.0 M $LiPF_6$ in EC/DEC = 1/1 v/v) containing dissolved HF (100 ppm): (a) PVP/PAN film and (b) PAN film.

Figure 5.1.9. Characterization of the separator properties. (a) Linear sweep voltammograms. (b) Electrolyte wettability. (c) Effect of polar electrolyte (here, 1.0 M $LiPF_6$ in EC/PC = 1/1 (v/v)) on wettability of separators and charge/discharge profiles of cells incorporating PP/PE/PP separator and c-mat separator. (d) Thermal shrinkage after exposure to 150 ºC/0.5 h.

Figure 5.1.10. Comparison of the cell performance (at room temperature) of the c-mat and PP/PE/PP separators: (a) Discharge rate capability (LMO cathode/Li metal anode), (b) Discharge rate capability (LCO cathode/natural graphite anode), and (c) Cycling performance (LMO cathode/Li metal anode).

Figure 5.1.11. Cell performance of the c-mat and PP/PE/PP separators. (a) Charge/discharge profiles with cycling (100 cycles) at 60 °C. (b) High-temperature (60 °C) capacity retention as a function of cycle number. (c) AC impedance spectra after 100 cycles at 60 °C. (d) Amount of Mn^{2+} ions captured by separators and deposited on the Li metal anode (estimated from ICP-MS analysis). FT-IR spectra of the (e) TPY-CNF side and (f) PVP/PAN side of the c-mat separator after 100 cycles at 60 °C.

Figure 5.1.12. (a) Impedance spectra and (b) summary of the fitting results for the c-mat and PP/PE/PP separators after cycling (at 60 ºC). The inset in part (a) represents the equivalent circuit. Units of R_b, R_{sf} and R_{ct} are in ohms. R_b is the bulk resistance, R_{sf} is the surface resistance, and R_{ct} is the charge transfer resistance. CPE_{sf} and CPE_{ct} are the constant phase elements at high and low frequencies, respectively.

Figure 5.1.13. SEM images showing the long-term structural stability (after 100 charge/discharge cycles at 60 °C) of the c-mat separator: (a) TPY-CNF top layer and (b) PVP/PAN support layer.

Figure 5.1.14. Comparison of high-temperature (60 ºC) cycling performance between the cell (I) and cell (II), in which the TPY-CNF top layer was in contact with the LMO cathode (for cell (I)) and positioned toward the Li metal anode (for cell (II)).

Figure 5.2.1. Schematic representation of layer-by-layer (LbL) assembled $(PAH/PAA)_n$ multilayer

coated PE separator for inhibiting the shuttle effect of polysulfide across the separator in a Li-S battery.

Figure 5.2.2. a) Thickness growth curve of the $(PAH/PAA)_n$ multilayer thin films on a silicon wafer with respect to the assembly pH conditions and b) schematic representation of the internal structure of $(PAH/PAA)_n$ multilayer thin films assembled at different pH conditions. Thickness was measured in five independent measurements with ellipsometry.

Figure 5.2.3. Contact angle and SEM images of a) bare PE and b) O_2-plasma treated PE separator.

Figure 5.2.4. ATR-IR spectra of $(PAH/PAA)_5$ multilayer coated PE-separator at each assembly pH.

Figure 5.2.5. SEM images of PAH/PAA 1, 3, and 5 bilayer (BL) coated on separator by LbL assembly at a) pH 3/3, b) pH 6/3 and c) pH 8.5/8.5. The scale bar of each image is 1 μm.

Figure 5.2.6. Cyclic voltammograms (CV) of $(PAH/PAA)_n$ multilayer of pH 3/3 coated on ITO glass by LbL assembly in an aqueous 0.50 M Na_2SO_4 electrolyte solution containing 5.0 mM of a) $Ru(NH_3)_6^{3+}$ as the cationic and b) $Fe(CN)_6^{3-}$ as the anionic probes, respectively. Inset image shows the schematic representation of the cation exchange property of LbL thin films. c) The comparison of anodic peak current density of each ion species. d) Calculated permselectivity, P^+, (selectivity ratio of cation to anion) with different numbers of bilayers and pH conditions.

Figure 5.2.7. Cyclic voltammograms (CV) of $(PAH/PAA)_n$ multilayer of (a-b) pH 6/3 and (d-e) pH 8.5/8.5 coated on ITO glass by LbL assembly in aqueous 0.5 M Na_2SO_4 neutral electrolyte solution containing 5.0 mM of (a, d) $Ru(NH_3)_6^{3+}$ as the cationic and (b, e) $Fe(CN)_6^{3-}$ as the anionic probes, respectively. Comparison of the anodic peak current density of each ion species at c) pH 6/3 and f) pH 8.5/8.5.

Figure 5.2.8. a) Cationic retention and b) anionic retention of 1, 3, 5 BL of $(PAH/PAA)_n$ assembled at pH 3/3, 6/3, and 8.5/8.5.

Figure 5.2.9. Voltage profiles of the a) bare PE separator and b) $(PAH/PAA)_5$ coated PE separator at pH 3/3. c) Cycle performance and d) Coulombic efficiency of the $(PAH/PAA)_5$ coated separator at each pH and comparison to bare PE separator.

Figure 5.2.10. Voltage versus specific discharge capacity profiles of the $(PAH/PAA)_5$ at a) pH 6/3 and b) pH 8.5/8.5.

Chapter 6.

Figure 6.1. Schematic illustration of GAP multilayer conductors. Composite-by-composite (CbC) assembly of polyurethane (PU)-based stretchable multilayer of high and low gradient conductors with

different concentration of Au NPs in stretchable layer. Photograph showing the resulting GAP multilayer conductor under 100% strain.

Figure 6.2. (a) Schematic illustration and TEM image with a corresponding size distribution histogram of citrate-stabilized Au NPs. (b) Polymer structure of water-dispersed PU.

Figure 6.3. Characterization of single layer. (a) Stress-strain curves and (b) Young's modulus and rupture point for pure PU and single-layered AuPU nanocomposite films. (c) Normalized resistance of 90 wt% AuPU film as decreasing the bending radius and (d) bending durability test for 100 cycles at bending radius of 0.3 mm. Photograph showing the bending test of 90 wt% AuPU film.

Figure 6.4. Resistance of single-layered AuPU and pure PU films.

Figure 6.5. Architecture controlled GAP multilayer conductors. Schematic illustrations and representative cross-sectional SEM images with composed elemental mapping images of carbon and Au of (a) high and (b) low gradient multilayer conductors as increasing the number of layers. The scale bar in all SEM images is 20 μm.

Figure 6.6. TGA of (a) high GAP, (b) low GAP conductors and (c) AuPU nanocomposite films. (d) The resulting content of Au in all electrode examined in this study.

Figure 6.7. Mechanical and electrical properties of GAP multilayer conductors. (a) Stress-strain curves for all GAP multilayer conductors. (b, c) Young's modulus and rupture point of low and high GAP multilayer conductors. (d) Normalized resistance on top-surface of high and low GAP multilayer conductors of 3 L and 9 L under different strain conditions. (e) Change of resistance on top-surface of high GAP multilayer conductors of 9 L under different strains during 1000 cycles.

Figure 6.8. SEM of 9 L high GAP conductor under strain

Figure 6.9. Cross-sectional SEM of 9 L high GAP conductor under strain.

Figure 6.10. Finite element analysis (FEA) representing von Mises stress distribution of (a) horizontal and (b) vertical direction in 5 L and 9 L low GAP conductors under 50% strain.

Figure 6.11. Calculation of Z-directional conductivity of low GAP conductors as increasing the number of layers.

Figure 6.12. SAXS and simulation analysis for percolation network of Au NPs in PU matrix under strain. (a) Schematic illustration showing experimental setup of in situ SAXS measurement. (b) 2D SAXS patterns at selected uniaxial strains of 0%, 50%, and 100% for the pure PU and 50 wt% AuPU nanocomposite films. We summarized the behavior of the Au NPs in the matrix and change in electrical pathway under strain with corresponding schematic illustrations of the behaviour of Au NPs

(yellow sphere) and electrical pathway (red line) under strain through SAXS analysis. (c) Calculated Hermans orientation factor, *f*, under strain.

Figure 6.13. Characterization of anode materials. (a) Chemical reaction for synthesis of PI. (b) SEM images of synthesized PI on CNT. (c) FT-IR spectra and (d) TGA of CNT and PI/CNT.

Figure 6.14. Characterization of cathode materials. (a) SEM image and (b) TEM image of synthesized LMO/CNT. (c) XRD of MnO_2/CNT and LMO/CNT. (d) TGA of LMO/CNT.

Figure 6.15. Electrochemical performance of stretchable aqueous rechargeable lithium-ion battery based on GAP multilayer conductor as a current collector. (a) Cyclic voltammetry profiles of GAP anode (PI/CNT) and GAP cathode (LMO/CNT) at various C-rates in three electrode systems with 1 M Li_2SO_4 electrolyte. (b,c) Galvanotactic charge-discharge curves of GAP cathode and GAP anode, respectively. (d) Cycling performance of full battery at a rate of 15 C between 0.0 and 2.0 V in 1 M Li_2SO_4 for 1000 cycles. (e) Schematic illustration of the stretchable aqueous rechargeable lithium-ion battery that was fabricated by using the GAP anode and cathode with coplanar layout. (f) Cycle performance of the stretchable full cell at a rate of 15 C under various strains from 0% to 30% for 100 cycles.

Figure 6.16. Cycling performance of (a) the cathode and (b) the anode of half cell at 100 C over 200 cycles.

Figure 6.17. Galvanostatic charge-discharge curve of the full cell at various C-rate

Figure 6.18. Fatigue test of the stretchable battery under 50 % strain for 100 cycles.

List of Tables

Chapter 1.
Introduction of Graphene-based Multilayer Nanocomposites

1.1 Graphene oxide

Graphene, a two-dimensional single-layered carbon network, is an interesting platform material for the preparation of nanocomposites owing to its unique properties such as its large surface area (2600 m^2 g^{-1}), high conductivity (electron mobility: 15 000 cm^2 V^{-1} s^{-1}), and excellent mechanical stability (Young's modulus: 1100 GPa).[1–3] These remarkable intrinsic properties have attracted widespread interest from diverse research fields.[4–6] However, the preparation of pristine graphene is only possible through a limited number of methods, such as mechanical exfoliation[7] and chemical vapor deposition,[8,9] and both result in poor yields. The discovery of graphene oxide (GO), a product of chemical oxidation and exfoliation of graphite,[10–13] has opened an indirect pathway for utilizing the properties of graphene, albeit with some modified properties (**Figure 1.1**). Chemically exfoliated GO sheets are well dispersed in aqueous solution due to their charged functional groups such as carboxylic acids and alcohol groups. The carboxylic acids in GO can be also easily replaced with amine groups by the formation of amides using ethylenediamine, resulting in highly stable aqueous suspensions with high ζ-potential (**Figure 1.2**). Moreover, their chemical stability and high conductivity in addition to their high surface area allows these 2D sheets to act as excellent substrates for hosting and growing functional nanomaterials, including other carbon allotropes, inorganic nanostructures, polyelectrolytes, and biomolecules. Although the intrinsic structural defects often lead to a deterioration of the material properties and performance compared with pristine graphene, GO can offer a versatile platform for innovative hybrid materials with unique properties.

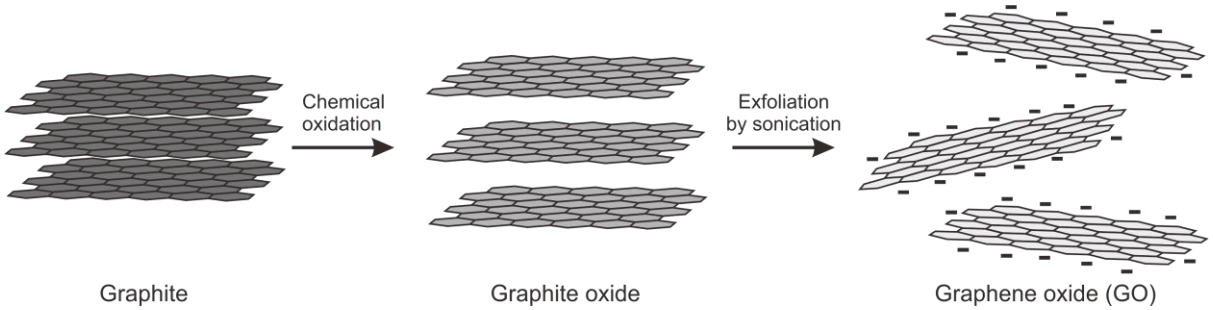

Figure 1.1. Schematic illustration of the synthesis of graphene oxide from graphite through the chemical oxidation and exfoliation process.

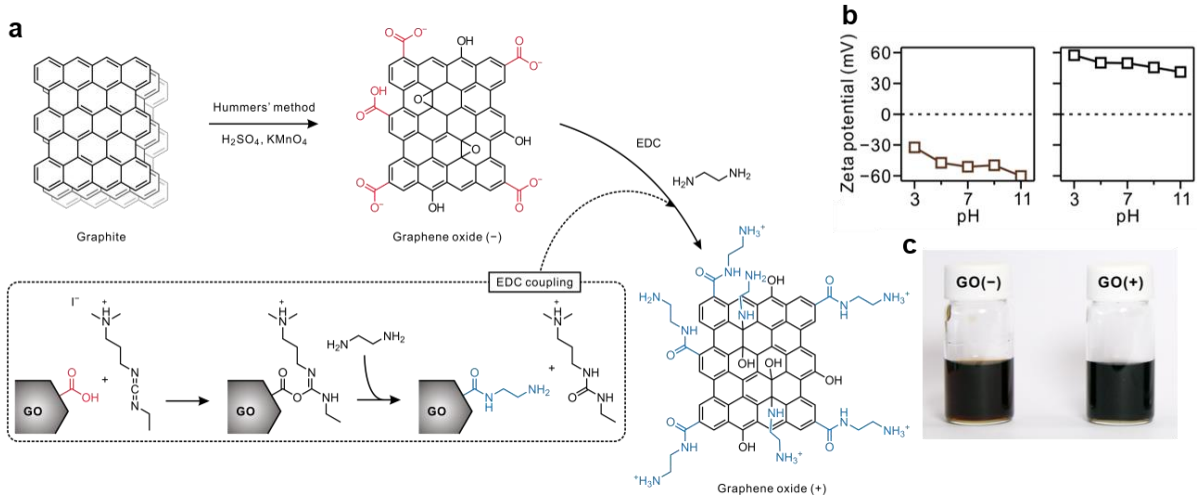

Figure 1.2. (a) Synthetic procedure for GO and amine-functionalized GO. (b) ζ-potential under different pH conditions and (c) photographs of GO(–) and GO(+) suspensions.

1.2 Layer-by-layer (LbL) assembly

The initial idea of LbL assembly was first presented by Iler in 1966, who demonstrated the deposition of oppositely charged silica and alumina particles.[14] Decher and co-workers revived LbL assembly by making thin films via the alternate adsorption of oppositely charged polyelectrolytes (**Figure 1.3a**).[15] Until recently, LbL approaches have attracted substantial attention due to the versatility of readily tailoring the size, composition, porosity, stability, and surface functionality of the resulting thin films by incorporating multiple functionalities using a facile and inexpensive process.

LbL-assembled thin films are prepared via the sequential adsorption of different macromolecular components exhibiting attractive forces such as electrostatic interactions, hydrogen bonding, van der Waals forces, and charge transfer complexes.[16] Graphene-based LbL assembly was first demonstrated by using non-exfoliated graphite oxide platelets and polyeletrolyte by Kotov et al. in 1996.[17] Three years later, a well-exfoliated individual graphite oxide sheet was used with cationic polymer for LbL growth by Mallouk and Kovtyukhova.[18] A remarkable achievement on the physical properties of graphene sheets by Geim, Novoselov, and others renewed significant interests in graphene-based layered materials.[1] The essentials of this thesis are to show that the introduction of functional groups into graphene during the exfoliation process together with additional chemical modification enables graphene derivatives to be incorporated within LbL-assembled structure by electrostatic interactions, hydrogen bonding, and van der Waals interactions even without the aid of other heterogeneous materials, which is not possible in pristine graphene. Especially, we focus on graphene-based LbL films prepared by the electrostatic attractions between negatively charged GO and positively charged materials (carbon nanomaterials, polymers, and inorganic nanomaterials). These thin film composites prepared by the hierarchical organization would be beneficial for reliable applications over other conventional methods such as vacuum-assisted filtration and Langmuir−Blodgett method. Vacuum-assisted filtration is advantageous to rapid and scale-up fabrication of layered films and has no limitation for selection of materials because the films can be manufactured through the physical trapping of materials using vacuum force.[16,19] Langmuir−Blodgett film deposition is also preferable for achieving uniform and dense packing of monolayers.[20,21] However, since the LbL assembly guarantees a nanoscale uniformity of composites and does not require relatively specialized skills and instrumentation, it is the most appropriate method to tunable hybrid architecture with a nanoscale precision.

With the progress of LbL assembly, many efficient and commercially feasible deposition methods have been developed (**Figure 1.3b**). Beyond the most popular and traditional dipping method (**Figure 1.4**), spin- and spray-assisted LbL assemblies have been introduced as alternative methods.[22-25] These new assembly methods often result in well-defined multilayer films as well as a highly ordered internal structure within a very short deposition period. In both methods, besides the electrostatic interactions, various forces such as centrifugal forces, air-shear forces, and flow rate could affect the quality of the resulting LbL films. In particular, spray-assisted LbL deposition is a powerful tool for

preparing multilayer films not only on 2D but also on 3D substrates such as complex textile fabrics. The advancement in these different deposition methods has significantly accelerated the applications of LbL assembly to various fields.

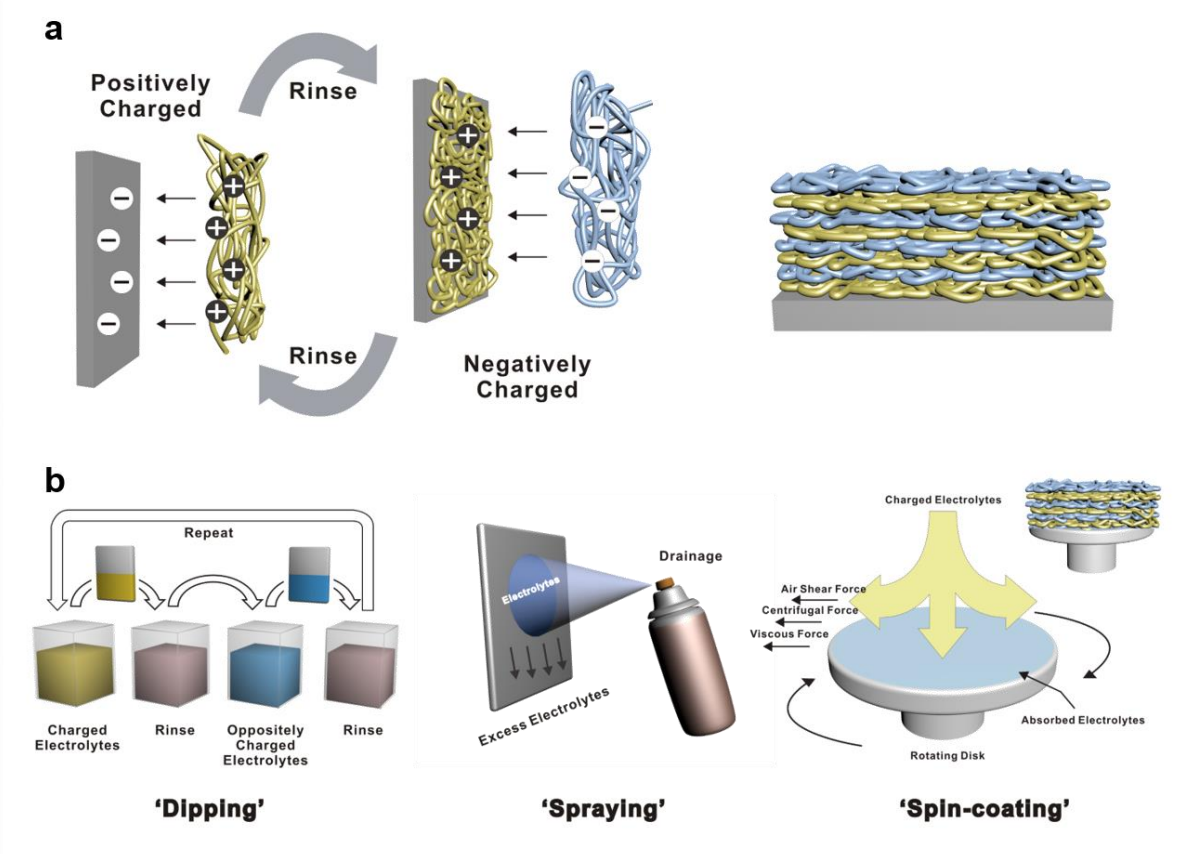

Figure 1.3. (a) Schematic illustration of the layer-by-layer (LbL) assembled multilayer films based on electrostatic interaction with (b) varying coating methods such as dipping, spraying and spin-coating.

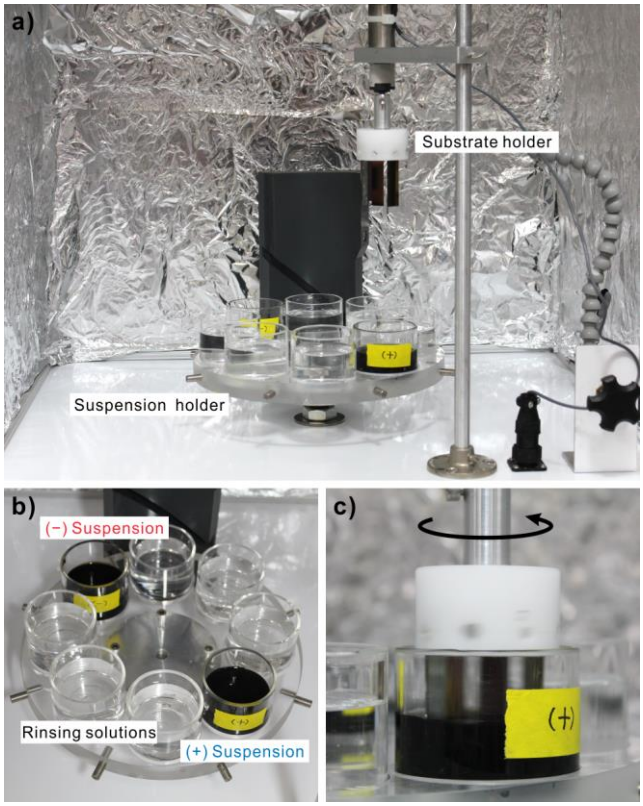

Figure 1.4. (a) Automated LbL assembly setup for graphene-based LbL assembly (nanoStrata). (b) Suspensions for (+) and (−) components with rinsing solutions. (c) Spin-dipping assembly.

1.3 Graphene-based hybrid composites

Several studies have reported that graphene-based hybrid composites exhibit superior performance compared with the individual components because of the synergistic effects between each component. As a representative example, the addition of graphene into hybrid composites provides 2D conducting channels for charge transfer during the electrochemical reactions.[26-28] Simultaneously, graphene employed as a large surface area support, which was easily exposed to the electrolyte and oxygen as well as effectively accelerating reactant, ion, and electron transport. Thus, the formation of graphene-based composites is greatly advantageous to the design of a new type of versatile material for high-performance TCFs, field-effect transistors (FETs), sensors, supercapacitors, solar cells, lithium ion batteries, electrodes, drug carriers, gas barriers, photocatalysts, and photoconductors. In many cases, however, graphene-based composites are highly disordered, leading to difficulties in demonstrating their reproducible performance and analyzing the contribution of each material to the device characteristics. One possible route to achieve nanoscale uniformity of these composites while preserving the unique characteristics of their constituents is to use layer-by-layer (LbL) assembly. The LbL technique is achieved through the sequential adsorption of oppositely charged components by attractive forces such as electrostatic interactions, hydrogen bonding, etc. Thus, the highly ordered and multilayered architectures by LbL assembly can be manufactured reproducibly, allowing nanoscale-level control of the thickness and composition of hybrid composite materials. Moreover, the graphene nanocomposites are complexed with the counterpart such as other carbon nanomaterials, polymers, and inorganic nanomaterials, in various device applications, including flexible electrodes, supercapacitor, batteries, and sensors (**Figure 1.5**).

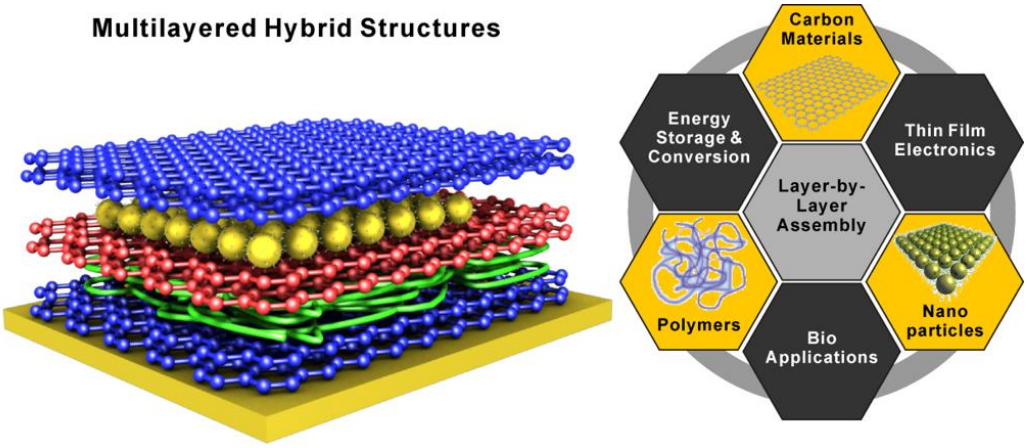

Figure 1.5. Schematic illustration of graphene multilayered hybrid nanocomposites with the counterparts and potential application.

1.3.1 Carbon nanomaterials

The hybridization of the unique electrical/chemical properties of carbon nanomaterials with the exceptional versatility of the nanoscale construction of multilayer LbL films has opened up wide research opportunities. In addition, various functionalities can be achieved by the carbon nanomaterials through a facile chemical modification, which makes it easy to host and grow the functional nanomaterials on the surface of carbon nanomaterials. This approach offers virtually unlimited opportunities for expanding the material selection for LbL deposition.[29–31] Thus, the utilization of both advantages of the intrinsic properties of functionalized carbon nanomaterials and precise control of the LbL system offers a unique potential platform for advanced electronic, energy, and sensor applications.

1.3.2 Polymers

Polymeric materials have been widely used in LbL assembly due to their functional groups for electrostatic interactions or hydrogen bonding.[32–35] In general, as-prepared GO is negatively charged in aqueous solution because of its functional groups, such as carboxylic acid and phenolic hydroxyl groups. Thus, positively charged polyelectrolytes have been selected for the counter component in graphene−polymer LbL assembly.[18,36–40] In addition to the conventional electrostatic interaction in LbL assembly, hydrogen bonding can act as an attractive force between GO and the polymer due to abundant oxygen-functional groups in GO.[19,41] Weak van der Waals interactions can also work in LbL assembly between GO and biopolymer and maximize its interactions along with other strong interactions, leading to the ultrarobust mechanical properties.[42,43] The reduction of GO sheets in LbL film has been performed by thermal treatment, chemical reduction, and electrochemical reaction to restore the unique properties of graphene, while keeping the structure of polymer counterparts intact. Due to the outstanding mechanical properties of graphene, graphene–polymer nanocomposites have been widely studied for high performance materials by using graphene derivatives as nanofillers.

1.3.3 Inorganic nanoparticles

Even though many applicable nanoparticles exhibit superior electronic and catalytic properties as well as mechanically strong reinforcing effects, these nanoparticles often undergo a significant loss of intrinsic properties due to irreversible aggregation. Therefore, because graphene and nanoparticles can complement each other, graphene can be a favorable supporting material of nanoparticles. Furthermore, graphene/ nanoparticle multilayered composites synthesized by the nanometer-scale control of LbL assembly exhibited improved performance compared with simply mixed hybrids. Using metal and oxide-based nanoparticles, many studies have been performed to apply LbL-assembled graphene/nanoparticle composites to diverse energy-related fields such as catalysts,[44–47] supercapacitors,[48–50] Li-ion batteries,[51] sensors,[52–55] solar cells,[56–59] and field-effect transistors.[60]

1.4 Electrochemistry in LbL assembled electrode

With various multi-dimensional (D) nanomaterials such as 2D graphene derivative, 1D polymer and carbon nanotube (CNT), and 0D metal nanoparticle, all of which can be composited with 2D GO nanosheets as a basic building block to afford electroactive 2D planar ultrathin films. Furthermore, we can easily fabricate from the 2D planar ultrathin films to 3D nanoporous electrode as increasing the number of bilayers and layer sequence by using the LbL assembly (**Figure 1.6**). As some representative examples, Hammond and Shao-Horn groups demonstrated that LbL assembled all multiwalled CNT film-based electrodes show significantly high gravimetric energy with its high capacity and high electronic conductivity.[29,31] With this CNT-based LbL electrode toward Li-ion battery, it was demonstrated that the LbL system can be not only used to design ideal electrochemical electrode such as supercapacitors, batteries and fuel cells, but also opened the possibility of bridging the performance gap between electrochemical double layer capacitor (i.e. governed by non-faradaic reaction) and Li-ion battery (i.e. governed by faradaic reaction).[61] In addition, these two different electroactive materials which have faradaic and non-faradaic mechanism can be individually used as cationic and anionic materials in LbL system. For example, polyaniline (PANI) is one of most popular conducting polymer which has faradaic capacitance. As a result, the combination of PANI and CNT showed the better performance than all CNT multilayer films owing to faradaic capacitance of conducting PANI.[62] Kim group also showed this feature of PANI with GO support, emphasizing the strengths of 2D graphene nanosheets.[63] This paper indicated that although the overall capacitance increases with the number of bilayers, capacitance gradually decreases beyond 10 bilayers because the electron transfer from the electrode as well as the ionic transport from the electrolyte can be restricted in the thicker thickness. This phenomenon was also found in another works that are LbL assembled electrocatalyst using metal nanoparticles.[44] Lutkenhaus group reported PANI/vanadium pentoxide assembled LbL electrode for Li-ion battery, in which they hypothesized that it is caused by a shift from a surface-confined process to a diffusion-limited process.[64]

In this regard, it is very important to achieve high performance and understand such electrochemical behavior on LbL assembled 3D electrode by changing the number of bilayers and layer sequence. As a result, this electroactive LbL films sensitively affected to rate-determining step of whole electrochemical reaction on electrode. Therefore, LbL assembled electrode can be good study model of mass and charge transfer system with respect to classic electrochemistry (**Figure 1.7**).

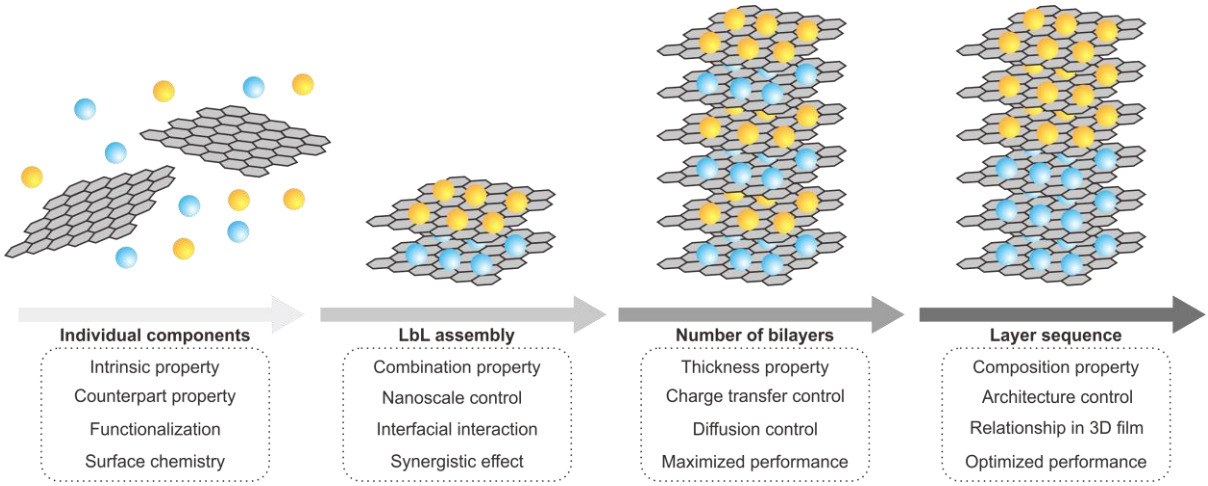

Figure 1.6. Properties and characterizations of LbL assembled 3D electrode for electrochemical analysis.

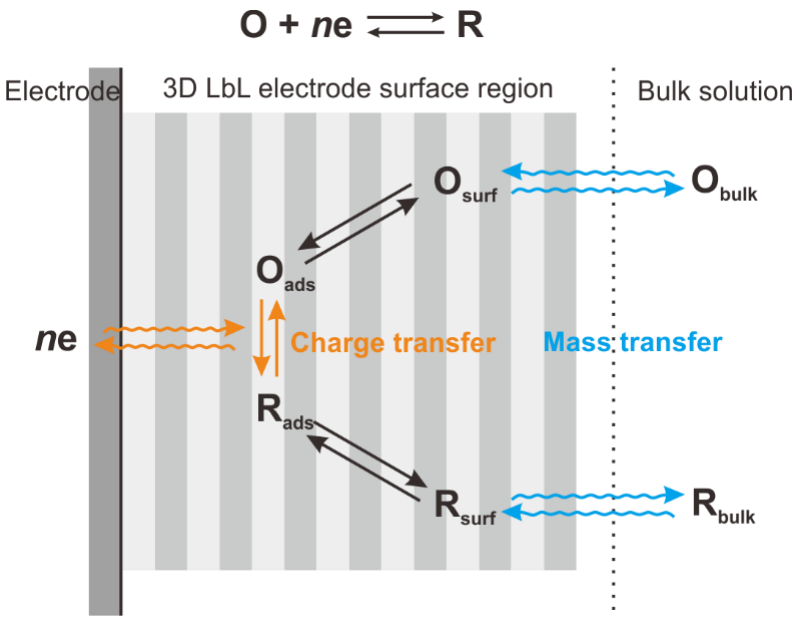

Figure 1.7. Electrochemical reaction based on mass and charge transfer within 3D LbL assembled multilayer electrode in electrolyte.

1.5 Application of graphene-based multilayer nanocomposites

Taking advantages of the versatility of LbL assembly, we can create multifunctional composite platforms by selecting the diverse counterpart materials and controlling the LbL engineering. This methodology is highly applicable to a wide range of energy conversion and storage fields such as electrocatalyst photocatalyst, battery and supercapacitor.[16] We explored the various applications of LbL-assembled graphene nanocomposites based on different combinations of graphene and functional materials and evaluated their performance as a function of the film thickness (i.e., number of BL). The optimum performance of each graphene nanocomposite is strongly correlated to the selection of materials and the film thickness. This finding indicates that precise control of the desired functionalities of multilayered films is necessary and possible by taking advantage of the LbL-based nanoscale engineering of the electrode. Although we mainly utilize the LbL-assembled graphene nanocomposites for energy applications, they have enormous potential in many fields of science and engineering owing to their tailorable architectures, compositions, and tunable properties. Considering the simplicity and versatility of this methodology, we anticipate that the LbL approach will emerge as the attractive platform technique for the design and fabrication of diverse hybrid nanocomposites with tailored functionalities (**Figure 1.8**).

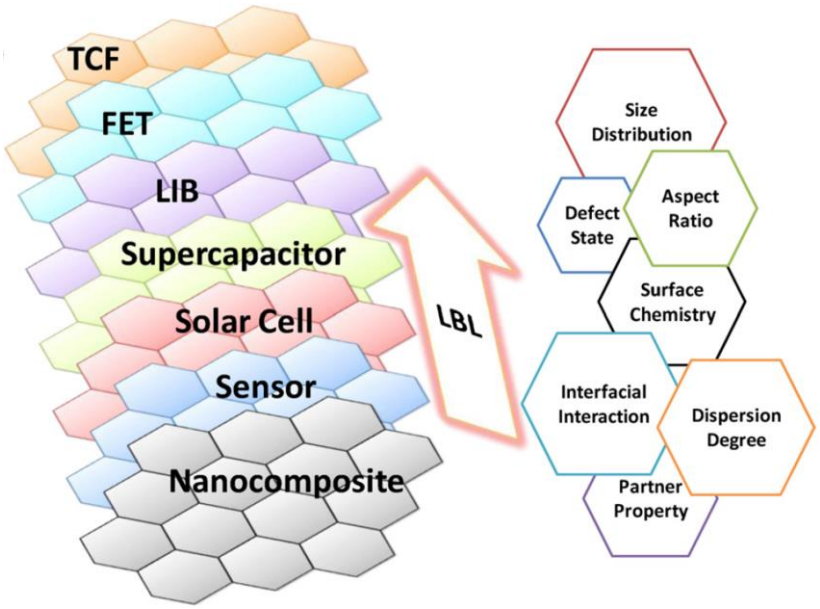

Figure 1.8. Summary of the application of LbL assembled graphene multilayer and the key factors toward better performance. Reprinted with permission from ref. 16. Copyright 2012 Elsevier.

1.6 Overview of Thesis

This thesis, comprised of 7 chapters, describes the importance of controlling the architecture in nanocomposites which are fabricated by various assembly techniques such as LbL assembly, vacuum filtration, and wet-spinning method for their potential application in energy conversion and storage systems.

Chapter 1 introduces the general description of nanomaterials such as graphene, and its hierarchically assembled hybrid multilayer nanocomposites based on carbon nanomaterials, polymer, and inorganic nanoparticles with respect to electrochemistry.

Chapter 2 presents an ultrathin supercapacitor electrode based on reduced graphene oxide (rGO) nanosheets functionalized with a conducting polymer that were assembled using a photo-cross-linkable polymer. Herein we study that the layer-dependence of the conversion of electrochemical operating principle from a surface-confined process to a diffusion-limited process as the film thickness was increased.

Chapter 3 unravels the importance of controlled architecture in bimetallic graphene multilayer electrode toward efficient electrocatalyst with the positively charged Au and Pd nanoparticles. In addition, we further investigate highly tunable electrocatalytic activity of multilayer thin film electrode assembled with Pd nanoparticles and varying graphene nanosheets toward methanol oxidation as a model reaction. Specifically, a significantly tunable electrocatalytic effect of multilayer electrode with a given set of the materials was demonstrated owing to the controllable diffusion pathways for reactants into uniquely designed three-dimensional films as well as charge transfer by different chemical properties of graphene sheets.

From chapter 4 to 6, we illustrate practical application of the architecture-controlled nanocomposites toward Li-ion battery systems, covering all components from electroactive materials, functional separators, and electrical conductors.

In specific, chapter 4 presents a fabrication of double-locked coaxial core/shell silicon (Si)-graphene fibers prepared by dual nozzle- induced wet-spinning assembly for high-performance Si anode by graphene nanocomposites. This core/shell graphene-based Si fibers not only alleviated large volume change, but also markedly improved the electrical conductivity of Si nanoparticles.

Chapter 5 provides a heterolayered nanomat-based hierarchical/asymmetric porous separator for lithium-ion battery using lithium manganese oxide materials as cathode. This functional separator is composed of a thin nanoporous mat of terpyridine-functionalized cellulose as the top layer deposited on an electrospun thick macroporous mat as the support layer, resulting to exhibit synergistically coupled chemical functional activity. In addition, a novel ion-permselective functional separator to inhibit the shuttle effect of polysulfides in lithium–sulfur battery is demonstrated by taking advantage of the pH-responsive weak polyelectrolytes, benefiting from fine tuning of the internal charge density of the multilayer thin films.

Chapter 6 demonstrates a gradient assembled polyurethane-based stretchable multilayer conductor with fine-controlled internal architecture assembled with Au nanoparticles as a conductive filler. Herein we propose a new assembly protocol, denoted composite-by-composite (CbC) assembly, which integrates the advantages of both conventional vacuum-assisted filtration and layer-by-layer (LbL) assembly.

Finally, chapter 7 summarizes the architecture-controlled nanocomposites in multilayer systems using diverse materials, regardless of the chemical compositions (e.g., organic, inorganic, carbon, and metal) and their dimensions (e.g., 0-, 1-, 2-, and 3D). We anticipate that fundamental electrochemical studies and design strategies for multilayered nanocomposites to be offered with new insights in the design for future energy conversion and storage devices as well as advanced flexible and wearable electronics.

1.7 References

(1) Geim, A. K.; Novoselov, K. S. The Rise of Graphene. *Nat. Mater.* **2007**, *6*, 183−191.

(2) Nair, R. R.; Blake, P.; Grigorenko, A. N.; Novoselov, K. S.; Booth, T. J.; Stauber, T.; Peres, N. M. R.; Geim, A. K. Fine Structure Constant Defines Visual Transparency of Graphene. *Science* **2008**, *320*, 1308.

(3) Sun, Y.; Wu, Q.; Shi, G. Graphene Based New Energy Materials. *Energy Environ. Sci.* **2011**, *4*, 1113−1132.

(4) Huang, X.; Qi, X.; Boey, F.; Zhang, H. Graphene-Based Composites. *Chem. Soc. Rev.* **2012**, *41*, 666−686.

(5) Chung, C.; Kim, Y.-K.; Shin, D.; Ryoo, S.-R.; Hong, B. H.; Min, D.-H. Biomedical Applications of Graphene and Graphene Oxide. *Acc. Chem. Res.* **2013**, *46*, 2211−2224.

(6) Raccichini, R.; Varzi, A.; Passerini, S.; Scrosati, B. The Role of Graphene for Electrochemical Energy Storage. *Nat. Mater.* **2014**, *14*, 271−279.

(7) Novoselov, K. S.; Geim, A. K.; Morozov, S. V.; Jiang, D.; Zhang, Y.; Dubonos, S. V.; Grigorieva, I. V.; Firsov, A. A. Electric Field Effect in Atomically Thin Carbon Films. *Science* **2004**, *306*, 666−669.

(8) Kim, K. S.; Zhao, Y.; Jang, H.; Lee, S. Y.; Kim, J. M.; Ahn, J.-H.; Kim, P.; Choi, J.-Y.; Hong, B. H.; Kim, K. S. Large-Scale Pattern Growth of Graphene Films for Stretchable Transparent Electrodes. *Nature* **2009**, *457*, 706−710.

(9) Bae, S.; Kim, H.; Lee, Y.; Xu, X.; Park, J.-S.; Zheng, Y.; Balakrishnan, J.; Lei, T.; Ri Kim, H.; Song, Y. Il; Kim, Y.-J.; Kim, K. S.; Özyilmaz, B.; Ahn, J.-H.; Hong, B. H.; Iijima, S. Roll-to-Roll Production of 30-Inch Graphene Films for Transparent Electrodes. *Nat. Nanotechnol.* **2010**, *5*, 574−578.

(10) Hummers, W. S.; Offeman, R. E. Preparation of Graphitic Oxide. *J. Am. Chem. Soc.* **1958**, *80*, 1339−1339.

(11) Lotya, M.; Hernandez, Y.; King, P. J.; Smith, R. J.; Nicolosi, V.; Karlsson, L. S.; Blighe, F. M.; De, S.; Wang, Z.; McGovern, I. T.; Duesberg, G. S.; Coleman, J. N. Liquid Phase Production of Graphene by Exfoliation of Graphite in Surfactant/Water Solutions. *J. Am. Chem. Soc.* **2009**, *131*, 3611−3620.

(12) Loh, K. P.; Bao, Q.; Ang, P. K.; Yang, J. The Chemistry of Graphene. *J. Mater. Chem.* **2010**, *20*, 2277−2289.

(13) Marcano, D. C.; Kosynkin, D. V.; Berlin, J. M.; Sinitskii, A.; Sun, Z.; Slesarev, A.; Alemany, L. B.; Lu, W.; Tour, J. M. Improved Synthesis of Graphene Oxide. *ACS Nano* **2010**, *4*, 4806−4814.

(14) Iler, R. K. Multilayers of Colloidal Particles. *J. Colloid Interface Sci.* **1966**, *21*, 569−594.

(15) Decher, G. Fuzzy Nanoassemblies: Toward Layered Polymeric Multicomposites. *Science* **1997**, *277*, 1232−1237.

(16) Yang, M.; Hou, Y.; Kotov, N. A. Graphene-based Multilayers: Critical Evaluation of Materials Assembly Techniques. *Nano Today* **2012**, *7*, 430−447.

(17) Kotov, N. A.; Dékány, I.; Fendler, J. H. Ultrathin Graphite oxide−Polyelectrolyte Composites Prepared by Self-assembly: Transition between Conductive and Non-Conductive States. *Adv. Mater.* **1996**, *8*, 637−641.

(18) Kovtyukhova, N. I.; Ollivier, P. J.; Martin, B. R.; Mallouk, T. E.; Chizhik, S. A.; Buzaneva, E. V.; Gorchinskiy, A. D. Layer-by-Layer Assembly of Ultrathin Composite Films from Micron-Sized Graphite Oxide Sheets and Polycations. *Chem. Mater.* **1999**, *11*, 771−778.

(19) Zhu, J.; Zhang, H.; Kotov, N. A. Thermodynamic and Structural Insights into Nanocomposites Engineering by Comparing Two Materials Assembly Techniques for Graphene. *ACS Nano* **2013**, *7*, 4818−4829.

(20) Ariga, K.; Yamauchi, Y.; Mori, T.; Hill, J. P. 25th Anniversary Article: What Can Be Done with the Langmuir-Blodgett Method? Recent Developments and its Critical Role in Materials Science. *Adv. Mater.* **2013**, *25*, 6477−6512.

(21) Ma, R.; Sasaki, T. Nanosheets of Oxides and Hydroxides: Ultimate 2D Charge-Bearing Functional Crystallites. *Adv. Mater.* **2010**, *22*, 5082−5104.

(22) Hwang, H.; Joo, P.; Kang, M. S.; Ahn, G.; Han, J. T.; Kim, B.-S.; Cho, J. H. Highly Tunable Charge Transport in Layer-by-Layer Assembled Graphene Transistors. *ACS Nano* **2012**, *6*, 2432−2440.

(23) Cho, J.; Char, K.; Hong, J. D.; Lee, K. B. Fabrication of Highly Ordered Multilayer Films Using a Spin Self-Assembly Method. *Adv. Mater.* **2001**, *13*, 1076−1078.

(24) Schlenoff, J. B.; Dubas, S. T.; Farhat, T. Sprayed Polyelectrolyte Multilayers. *Langmuir* **2000**, *16*, 9968−9969.

(25) Krogman, K. C.; Lowery, J. L.; Zacharia, N. S.; Rutledge, G. C.; Hammond, P. T. Spraying Asymmetry into Functional Membranes Layer-by-Layer. *Nat. Mater.* **2009**, *8*, 512−518.

(26) Chen, P.; Xiao, T.-Y.; Qian, Y.-H.; Li, S.-S.; Yu, S.-H. A Nitrogen- Doped Graphene/Carbon Nanotube Nanocomposite with Synergistically Enhanced Electrochemical Activity. *Adv. Mater.* **2013**, *25*, 3192−3196.

(27) Yu, D.; Yang, Y.; Durstock, M.; Baek, J.-B.; Dai, L. Soluble P3HTGrafted Graphene for Efficient Bilayer−Heterojunction Photovoltaic Devices. *ACS Nano* **2010**, *4*, 5633−5640.

(28) Kholmanov, I. N.; Domingues, S. H.; Chou, H.; Wang, X.; Tan, C.; Kim, J.-Y.; Li, H.; Piner, R.; Zarbin, A. J. G.; Ruoff, R. S. Reduced Graphene Oxide/Copper Nanowire Hybrid Films as High-Performance Transparent Electrodes. *ACS Nano* **2013**, *7*, 1811−1816.

(29) Lee, S. W.; Kim, B.-S.; Chen, S.; Shao-Horn, Y.; Hammond, P. T. Layer-by-Layer Assembly of All Carbon Nanotube Ultrathin Films for Electrochemical Applications. *J. Am. Chem. Soc.* **2008**, *131*, 671−679.

(30) Kim, B.-S.; Lee, S. W.; Yoon, H.; Strano, M. S.; Shao-Horn, Y.; Hammond, P. T. Pattern Transfer Printing of Multiwalled Carbon Nanotube Multilayers and Application in Biosensors. *Chem. Mater.* **2010**, *22*, 4791−4797.

(31) Lee, S. W.; Yabuuchi, N.; Gallant, B. M.; Chen, S.; Kim, B.-S.; Hammond, P. T.; Shao-Horn, Y. High-Power Lithium Batteries from Functionalized Carbon-Nanotube Electrodes. *Nat. Nanotechnol.* **2010**, *5*, 531−537.

(32) Shiratori, S. S.; Rubner, M. F. pH-Dependent Thickness Behavior of Sequentially Adsorbed Layers of Weak Polyelectrolytes. *Macromolecules* **2000**, *33*, 4213−4219.

(33) Chen, W.; McCarthy, T. J. Layer-by-Layer Deposition: A Tool for Polymer Surface Modification. *Macromolecules* **1997**, *30*, 78−86.

(34) Nguyen, C. A.; Argun, A. A.; Hammond, P. T.; Lu, X.; Lee, P. S. Layer-by-Layer Assembled Solid Polymer Electrolyte for Electrochromic Devices. *Chem. Mater.* **2011**, *23*, 2142−2149.

(35) Kharlampieva, E.; Koziovskaya, V.; Sukhishvili, S. A. Layer-by-Layer Hydrogen-Bonded Polymer Films: From Fundamentals to Applications. *Adv. Mater.* **2009**, *21*, 3053−3065.

(36) Yang, Y. H.; Bolling, L.; Priolo, M. A.; Grunlan, J. C. Super gas barrier and selectivity of graphene oxide-polymer multilayer thin films. *Adv. Mater.* **2013**, *25*, 503−508.

(37) Chen, J. T.; Fu, Y. J.; An, Q. F.; Lo, S. C.; Huang, S. H.; Hung, W. S.; Hu, C. C.; Lee, K. R.; Lai, J. Y. Tuning Nanostructure ofGraphene Oxide/Polyelectrolyte LbL Assemblies by Controlling pH of GO Suspension to Fabricate Transparent and Super Gas Barrier Films. *Nanoscale* **2013**, *5*, 9081−9088.

(38) Chen, D.; Wang, X.; Liu, T.; Wang, X.; Li, J. Electrically Conductive Poly(vinyl alcohol) Hybrid Films Containing Graphene and Layered Double Hydroxide Fabricated via Layer-by-Layer Self-Assembly. *ACS Appl. Mater. Interfaces* **2010**, *2*, 2005−2011.

(39) Kurapati, R.; Raichur, A. M. Graphene Oxide Based Multilayer Capsules with Unique Permeability Properties: Facile Encapsulation of Multiple Drugs. *Chem. Commun.* **2012**, *48*, 6013−6015.

(40) Wang, D.; Wang, X. Self-Assembled Graphene/Azo Polyelectrolyte Multilayer Film and Its Application in Electrochemical Energy Storage Device. *Langmuir* **2011**, *27*, 2007−2013.

(41) Zhao, X.; Zhang, Q.; Hao, Y.; Li, Y.; Fang, Y.; Chen, D. Alternate Multilayer Films of Poly(vinyl alcohol) and Exfoliated Graphene Oxide Fabricated via A Facial Layer-by-Layer Assembly. *Macromolecules* **2010**, *43*, 9411−9416.

(42) Hu, K.; Gupta, M. K.; Kulkarni, D. D.; Tsukruk, V. V. Ultra-Robust Graphene Oxide-Silk Fibroin Nanocomposite Membranes. *Adv. Mater.* **2013**, *25*, 2301−2307.

(43) Hu, K.; Tolentino, L. S.; Kulkarni, D. D.; Ye, C.; Kumar, S.; Tsukruk, V. V. Written-in Conductive Patterns on Robust Graphene Oxide Biopaper by Electrochemical Microstamping. *Angew. Chem., Int. Ed.* **2013**, *52*, 13784−13788.

(44) Choi, Y.; Gu, M.; Park, J.; Song, H.-K.; Kim, B.-S. Graphene Multilayer Supported Gold Nanoparticles for Efficient Electrocatalysts Toward Methanol Oxidation. *Adv. Energy Mater.* **2012**, *2*, 1510−1518.

(45) Xiao, F.-X.; Miao, J.; Liu, B. Layer-by-Layer Self-Assembly of CdS Quantum Dots/Graphene Nanosheets Hybrid Films for Photoelectrochemical and Photocatalytic Applications. *J. Am. Chem. Soc.*

2014, *136*, 1559−1569.

(46) Zhu, C.; Guo, S.; Zhai, Y.; Dong, S. Layer-by-Layer Self-Assembly for Constructing a Graphene/Platinum Nanoparticle Three-Dimensional Hybrid Nanostructure Using Ionic Liquid as a Linker. *Langmuir* **2010**, *26*, 7614−7618.

(47) Yao, Z.; Yue, R.; Zhai, C.; Jiang, F.; Wang, H.; Du, Y.; Wang, C.; Yang, P. Electrochemical Layer-by-Layer Fabrication of A Novel Three-Dimensional Pt/Graphene/Carbon Fiber Electrode and Its Improved Catalytic Performance for Methanol Electrooxidation In Alkaline Medium. *Int. J. Hydrogen Energy* **2013**, *38*, 6368−6376.

(48) Dong, X.; Wang, L.; Wang, D.; Li, C.; Jin, J. Layer-by-Layer Engineered Co-Al Hydroxide Nanosheets/Graphene Multilayer Films as Flexible Electrode for Supercapacitor. *Langmuir* **2012**, *28*, 293−298.

(49) Li, Z.; Wang, J.; Liu, X.; Liu, S.; Ou, J.; Yang, S. Electrostatic Layer-by-Layer Self-Assembly Multilayer Films Based on Graphene and Manganese Dioxide Sheets as Novel Electrode Materials for Supercapacitors. *J. Mater. Chem.* **2011**, *21*, 3397−3403.

(50) Niu, Z.; Du, J.; Cao, X.; Sun, Y.; Zhou, W.; Hng, H. H.; Ma, J.; Chen, X.; Xie, S. Electrophoretic Build-Up of Alternately Multilayered Films and Micropatterns Based on Graphene Sheets and Nanoparticles and their Applications in Flexible Supercapacitors. *Small* **2012**, *8*, 3201−3208.

(51) Xia, F.; Hu, X.; Sun, Y.; Luo, W.; Huang, Y. Layer-by-Layer Assembled MoO2-Graphene Thin Film as A High-Capacity and Binder-Free Anode for Lithium-Ion Batteries. *Nanoscale* **2012**, *4*, 4707−4711.

(52) Yu, Y.; Yang, Y.; Gu, H.; Yu, D.; Shi, G. Size-Controllable Preparation of Palladium Nanoparticles Assembled on TiO2/Graphene Nanosheets and Their Electrocatalytic Activity for Glucose Biosensing. *Anal. Methods* **2013**, *5*, 7049−7057.

(53) Lange, U.; Hirsch, T.; Mirsky, V. M.; Wolfbeis, O. S. Hydrogen Sensor Based on A Graphene - Palladium Nanocomposite. *Electrochim. Acta* **2011**, *56*, 3707−3712.

(54) Zhang, X.; Li, S.; Jin, X.; Zhang, S. A New Photoelectrochemical Aptasensor for The Detection of Thrombin Based on Functionalized Graphene and CdSe Nanoparticles Multilayers. *Chem. Commun.* **2011**, *47*, 4929−4931.

(55) Xi, Q.; Chen, X.; Evans, D. G.; Yang, W. Gold Nanoparticle-Embedded Porous Graphene Thin Films Fabricated via Layer-by-Layer Self-Assembly and Subsequent Thermal Annealing for Electrochemical Sensing. *Langmuir* **2012**, *28*, 9885−9892.

(56) Manga, K. K.; Zhou, Y.; Yan, Y.; Loh, K. P. Multilayer Hybrid Films Consisting of Alternating Graphene and Titania Nanosheets with Ultrafast Electron Transfer and Photoconversion Properties. *Adv. Funct. Mater.* **2009**, *19*, 3638−3643.

(57) Guo, C. X.; Yang, H. B.; Sheng, Z. M.; Lu, Z. S.; Song, Q. L.; Li, C. M. Layered Graphene/Quantum Dots for Photovoltaic Devices. *Angew. Chem., Int. Ed.* **2010**, *49*, 3014−3017.

(58) Yao, H.-B.; Wu, L.-H.; Cui, C.-H.; Fang, H.-Y.; Yu, S.-H. Direct Fabrication of Photoconductive Patterns on LBL Assembled Graphene Oxide/PDDA/Titania Hybrid Films by Photothermal and Photocatalytic Reduction. *J. Mater. Chem.* **2010**, *20*, 5190−5195.

(59) Wang, K.; Wan, S.; Liu, Q.; Yang, N.; Zhai, J. CdS Quantum Dot-Decorated Titania/Graphene Nanosheets Stacking Structures for Enhanced Photoelectrochemical Solar Cells. *RSC Adv.* **2013**, *3*, 23755−23761.

(60) Li, H.; Pang, S.; Wu, S.; Feng, X.; Müllen, K.; Bubeck, C. Layerby-Layer Assembly and UV Photoreduction of Graphene−Polyoxometalate Composite Films for Electronics. *J. Am. Chem. Soc.* **2011**, *133*, 9423−9429.

(61) Lee, S. W.; Gallant, B. M.; Byon, H. R.; Hammond, P. T.; Shao-Horn, Y. Nanosctuctured Carbon-based Electrodes: Bridging the Gap Between the Thin-Film Lithium-Ion Batteries and Electrochemical Capacitors. *Energy Environ. Sci.* **2011**, *4*, 1972–1985

(62) Hyder, M. N.; Lee, S. W.; Cebeci, F. C.; Schmidt, D. J.; Shao-Horn, Y.; Hammond, P. T. Layer-be-Layer Assembled Polyaniline Nanofiber/Multiwall Carbon Nanotube Thin Film Electrodes for High-Power and High-Energy Storage Applications. *ACS Nano* **2011**, *5*, 8552–8561.

(63) Lee, T.; Yun, T.; Park, B.; Sharma, B.; Song, H.-K.; Kim, B.-S. Hybrid Multilayer Thin Film Supercapacitor of Graphene Nanosheets with Polyaniline: Importance of Establishing Intimate Electronic Contact through Nanoscale Blending. *J. Mater. Chem.* **2012**, *22*, 21092–21099.

(64) Shao, L.; Jeon, J.-W.; Lutkenhaus, J. L. Polyaniline/Vanadium Pentoxide Layer-by-Layer Electrodes for Energy Storage. *Chem. Mater.* **2012**, *24*, 181–189.

Chapter 2.

Ultrathin Supercapacitor Electrode Based on Reduced Graphene Oxide Nanosheets Assembled with Photo-Cross-Linkable Polymer: Conversion of Electrochemical Kinetics in Ultrathin Films

2.1 Abstract

An ultrathin supercapacitor electrode based on reduced graphene oxide (rGO) nanosheets is prepared using Layer-by-Layer (LbL) assembly. The rGO nanosheets functionalized with a conducting polymer, poly(3,4-ethylene dioxythiophene):poly(styrenesulfonate) (PEDOT:PSS), were assembled using a photo-cross-linkable diazoresin (DR). The unique photo-cross-linking property of the DR polymer enabled the conversion of the ionic bonds in the LbL assembled film to covalent bonds upon UV irradiation, significantly enhancing the overall electrochemical activity of the resulting ultrathin supercapacitor electrode. In particular, electrochemical measurements suggested that a charge transfer process is facilitated after cross-linking, which resulted in a considerable increase in the volumetric capacitance. The hybrid thin film of the rGO supercapacitor exhibited a capacitance of 354 F/cm^3 at a scan rate of 20 mV/s and maintained a capacitance of 300 F/cm^3 even at a high scan rate of 200 mV/s, thus outperforming many other thin film supercapacitors.

** Chapter 2 is reproduced in part with permission of "K. Jo,† M. Gu,† and B.-S. Kim* Chemistry of Materials **2015**, 27, 7982–7989". Copyright 2015 American Chemical Society*

2.2 Introduction

Layer-by-Layer (LbL) assembly has been widely used as a simple yet versatile method of fabricating controlled nanostructures on a surface.[1,2] In this method, a substrate is sequentially dipped into positively and negatively charged colloidal suspensions, which enables the creation of highly tunable, functional thin films with nanometer-level control of the structure, composition, and properties. With new advances in LbL assembly, a wide variety of materials other than simple polyelectrolytes, including polymeric micelles, biomolecules, carbon nanotubes, and graphene, have been explored for use as active building blocks.[1,3−5] Incorporation of a broader range of nanomaterials using LbL assembly has expanded the potential applications of LbL structures in various fields ranging from energy and electrochemical devices to biological materials.[4,6,7] Typically, LbL assemblies rely on electrostatic interactions, which are stronger than many other types of intermolecular interactions used, such as hydrogen bonding,[8,9] charge-transfer interactions,[10] and coordination bonding.[11,12] Nevertheless, these interactions are weakened by high ionic strength, extreme pH, and strongly polar solvents, which consequently limit the applications of the assembled thin films in specific fields.

Alternatively, the stability of LbL multilayer thin films can be greatly enhanced by the conversion of electrostatic interactions into covalent interactions. Kotov and co-workers employed the covalent cross-linking strategy to impart intrinsic strength to a polymer−single-walled carbon nanotube (SWNT) composite.[13] They also found that the tensile strength of cross-linked composites was several times higher than that of a similar SWNT composite prepared by a simple mixing process. In this context, diazoresins (DRs), which are products of polycondensation of a diarylamine-4-diazonium salt or its derivatives with formaldehyde, are particularly attractive.[14] Integration of positively charged DRs into multilayer thin films with other anionic polyelectrolytes has been demonstrated to yield films with high stability due to the conversion of ionic linkages into covalent bonds upon UV treatment.[15]

Incorporation of active carbon nanomaterials such as graphene and carbon nanotubes into various hybrid materials is attracting significant interest because of their unique electrical, optical, and mechanical properties of such nanomaterials.[16] In particular, a thin film supercapacitor composed of active carbon materials such as reduced graphene oxide (rGO) offers an intriguing opportunity for capacitive behavior because of its high electrical conductivity, mechanical stability, and large surface area.[17−19] Furthermore, rGO can contribute to the enhancement of the electrochemical stability of pseudocapacitive materials, which generate electrochemical current through a direct redox reaction. Because pseudocapacitive materials are generally severely degraded with the number of pseudocapacitive cycles, rGO can provide a stable framework for such materials. Moreover, graphene itself shows capacitance because of the formation of an electric double layer, as it facilitates physical accumulation of charges on the solid−liquid interface because of its high electrical conductivity and large surface area.[18,20] Despite these favorable features, the use of graphene and related carbon materials in supercapacitors is still limited due to their low capacitance (typically in the range of 10−102 F g^{-1}),

as the electric double-layer capacitance (EDLC) is typically much lower than that of pseudocapacitance resulting from the faradaic redox reaction.[21] Thus, hybrid materials that exhibit pseudocapacitance have been actively introduced to complement the performance of rGO. Much effort has been devoted to integrate rGO with other electrochemically active components such as metal oxides, metals, semiconductors, and nanoparticles, with the aim of exploiting both the EDLC and the pseudocapacitance.[22–26] For example, a hybrid electrode consisting of an electric double-layer capacitor of graphene nanosheets and a pseudocapacitor of the conducting polymer polyaniline exhibits a synergistic effect with excellent electrochemical performance for flexible thin film supercapacitors. In these hybrid structures, pseudocapacitance is the major contributor to the total capacitance, although to the best of our knowledge, there has been no precise and quantitative analysis regarding this issue in the context of multilayers with graphene.[27,28]

In this study, rGO nanosheets functionalized with a conducting polymer [poly(3,4-ethylene dioxythiophene):poly-(styrenesulfonate) (PEDOT:PSS)] via noncovalent interactions (rGO-PEDOT:PSS) were integrated into a multilayer film with a photo-cross-linkable DR (**Figure 2.1**). Because of the unique photo-cross-linking property of the DR polymer, the electrochemical activity of the resulting ultrathin supercapacitor electrode based on the rGO-PEDOT:PSS film was significantly enhanced. Furthermore, we investigated the transfer mechanisms upon photo-cross-linking with respect to the film thickness in ultrathin film-based capacitive behavior.

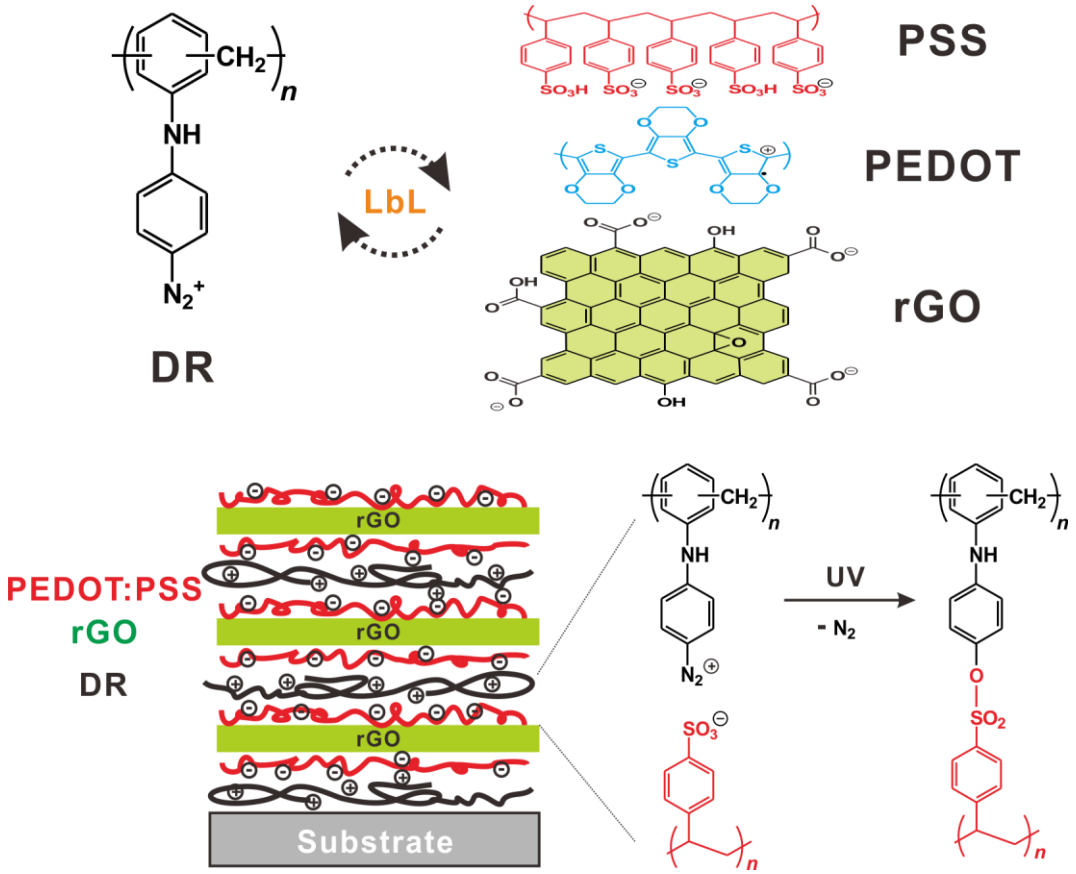

Figure 2.1. Layer-by-layer assembly of photo-crosslinkable DR and rGO-PEDOT:PSS.

2.3 Experimental

2.3.1 Synthesis of graphene oxide (GO) nanosheet.

Graphite oxide was initially synthesized from graphite powder (Aldrich) by the modified Hummers method and immersed in deionized water.[29] Ultrasonication was subsequently performed to exfoliate the graphite oxide into a brown disper-sion of graphene oxide (GO). The concentration of the dispersion was set to 0.50 mg/mL.

2.3.2 LbL assembly.

The LbL thin film was assembled on a silicon wafer, quartz slide, ZnSe slide, or indium tin oxide (ITO)-coated glass slide. All substrates were cleaned extensively before the LbL deposition. Each substrate was first treated with O2 plasma for 2 min before use. The substrate was then dipped into a positively charged DR solution (0.50 mg/mL, pH 3.5) for 10 min, followed by three sequential rinsing steps with pH-adjusted water for 1 min each. Finally, the substrate was dipped into an rGO-PEDOT:PSS suspension (0.50 mg/mL, pH 4.5) for 10 min and subjected to the same rinsing steps as described above. This cycle provided a bilayer of DR and rGO-PEDOT:PSS; herein, the notation $(DR/rGO\text{-}PEDOT:PSS)_1$ will be used, where the numerical subscript indicates the number of bilayers. The dipping process was repeated until the desired number of bilayers was formed (n = 1 – 10). All fabrication processes were performed in the dark, and the prepared thin films were kept in the dark to prevent potential degradation of DR. Each sample was irradiated with UV light (at a wavelength of 365 nm) for 10 min, using a 100 W black incandescent lamp (365 nm Blak-Ray B-100AP High Intensity UV Lamp, UVP) placed 20 cm from the sample.

2.3.3 Characterization.

The absorbance of the samples was measured by UV/vis spectroscopy (Cary 5000, Varian). The thickness of the samples on the silicon substrates was obtained by ellipsometry (J. A. Woollam Co. Inc., EC-400 and M-2000V). An LbL film on a ZnSe substrate was used to measure the IR spectra on an Fourier transform infrared (FT-IR) equipment (670-IR, Varian). Raman meas-urements (WITec alpha300R) were conducted with a 532 nm laser (1.0 mW). Surface morphology images were collected by a scanning electron microscope (SEM; Cold FE-SEM, Hitachi). All electrochemical measurements were performed with the potentiostat VSP from Bio-Logic Science Instruments, using a standard three-electrode cell. For electrochemical measurement, 1.0 M H_2SO_4 solution and Ag/AgCl electrode were utilized as electrolyte and reference electrode, respectively.

2.4 Results and Discussion

2.4.1 Film Growth and Morphology Analysis

DR was first synthesized according to previously published protocols.[14,30] The rGO nanosheets were functionalized with the conventional conducting polymer PEDOT:PSS through noncovalent interactions as demonstrated in a previous report.[31] Briefly, a GO nanosheet was chemically reduced to rGO by hydrazine treatment in the presence of PEDOT:PSS (weight ratio of 1:10) to give a stable suspension of rGO-PEDOT:PSS at a concentration of 0.50 mg/mL. The ζ-potential of the rGOPEDOT:PSS recorded −57 mV, suggesting successful formation of highly charged PSS layers surrounding the rGO nanosheets.

Elemental analysis showed that the rGO nanosheet content in the rGO/PEDOT:PSS nanocomposite was around 30%. Given these two stable suspensions, multilayer films of (DR/rGO-PEDOT:PSS)*n* (*n* = number of bilayers, BL) were assembled on a glass slide or silicon wafer by means of the electrostatic interactions between the positively charged DR (DR-N_2^+) and the negatively charged rGO-PEDOT:PSS, using LbL assembly.

Figure 2.2a shows the UV/vis absorbance spectra of the assembled $(DR/rGO\text{-}PEDOT:PSS)_n$ with different numbers of bilayers. The absorbance of the multilayer film increased linearly with the number of bilayers. The absorbance at 380 nm was attributed to the π−π* transition of the diazonium group, whereas the absorbance at 270 nm corresponded to the conjugated backbone of the rGO nanosheets.[31−33] This result indicated that the deposition was uniform and that a similar amount of DR was deposited in each layer. Moreover, a constant mass of rGO nanosheets was assembled, as evidenced by the linear increase in the absorbance at 270 nm with the number of bilayers. Ellipsometry measurements further yielded an average thickness of about 10.7 nm for the 10 BL film, that is, a thickness of about 1.07 nm per bilayer considering the linear growth profile of the $(DR/rGO\text{-}PEDOT:PSS)_n$ multilayer film (**Figure 2.2b**). The control experiment performed on the multilayer film assembled without the rGO nanosheets, $(DR/PEDOT:PSS)_n$, also demonstrated a linear growth profile with an average bilayer thickness of 0.82 nm, which was slightly smaller than that of the $(DR/rGO\text{-}PEDOT:PSS)_n$ multilayer film.

Independent from the growth of the multilayers, Raman spectroscopy was examined to verify that all of the components were integrated within the multilayer (**Figure 2.3**). For example, the rGO nanosheet exhibited D and G peaks at 1300 and 1600 cm^{-1}, respectively, whereas Raman-inactive DR did not show any signals. PEDOT also displayed a characteristic Raman peak corresponding to the symmetric C=C vibration at ∼1475 cm^{-1}, as previously reported.[34] The surface morphology of the multilayers was observed in the SEM (**Figure 2.4**). rGO multilayers were visible with a large coverage of more than several tens of micrometers with characteristic surface wrinkles on the graphene structure.

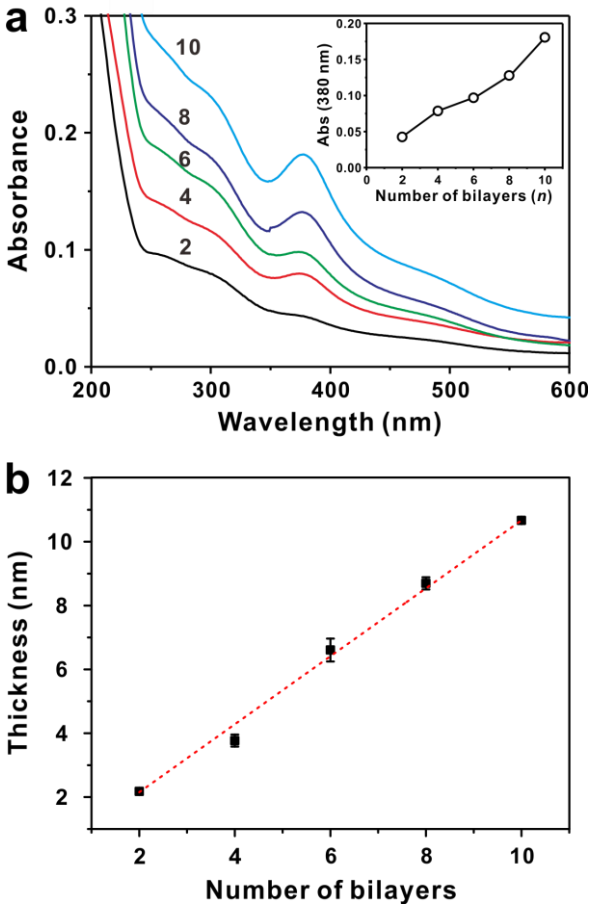

Figure 2.2. (a) Growth curve of (DR/rGO-PEDOT:PSS)$_n$ multi-layer thin film with different numbers of bilayers. The number on each curve represents the number of bilayers. Inset shows the linear relationship between the absorbance of the film at 380 nm and the number of bilayers. (b) The thickness of (DR/rGO-PEDOT:PSS)$_n$ samples measured by ellipsometer.

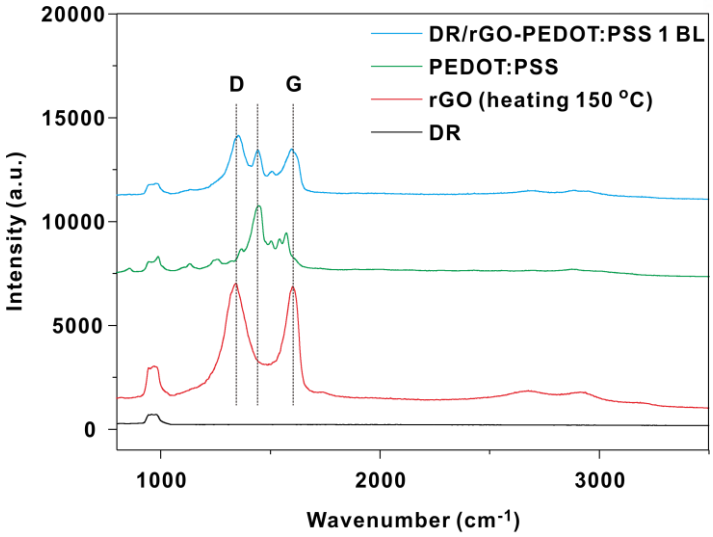

Figure 2.3. Raman spectra of $(DR/RGO\text{-}PEDOT:PSS)_{20}$ multilayer thin film (top) before, (bottom) after the UV irradiation.

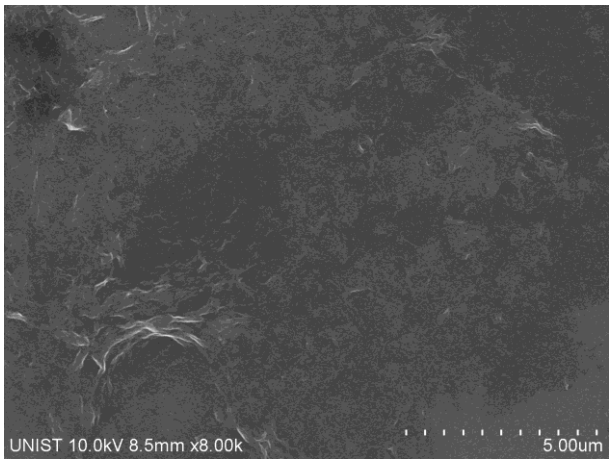

Figure 2.4. Representative SEM image of $(DR/rGO\text{-}PEDOT:PSS)_{10}$ multilayer film.

2.4.2 Electrochemical Analysis.

The capacitive performance of the photo-cross-linked $(DR/rGO\text{-}PEDOT:PSS)_{10}$ thin film supercapacitor was evaluated using cyclic voltammetry (CV) at potential intervals from −0.2 to 1.0 V, using a Ag/AgCl electrode as the reference electrode and a platinum wire as the counter electrode. Volumetric capacitance (F/cm^3) and areal capacitance values (F/cm^2) were extracted using the following equation (1):

$$C_V = \frac{1}{\nu \Delta V A t} \oint i dV \qquad (1)$$

where v is the scan rate (V/s), ΔV is the potential range (V), A is the area (cm^2), and t is the thickness (cm) obtained from ellipsometry measurements. The electrochemical performance of the $(DR/PEDOT:PSS)_{10}$ control film was also investigated to understand the contribution of rGO to the capacitive behavior. The hybrid supercapacitor based on rGO nanosheets functionalized with the conducting polymer PEDOT:PSS exhibited broad redox peaks in the potential ranges investigated, indicating typical pseudocapacitive behavior (**Figure 2.5a**). Interestingly, UV irradiation resulted in a remarkable increase in the current density and the corresponding volumetric capacitance reaching 306 F/cm^3 by 54%, illustrating that photo-crosslinking between DR and PSS improved the capacitive performance (**Figure 2.5b**). On the other hand, the $(DR/PEDOT:PSS)_{10}$ film showed a modest decrease of 27% from 119 to 87.3 F/cm^3 in capacitance upon photo-crosslinking (**Figure 2.5c**). It is of note that the volumetric capacitance values were calculated throughout -0.2 – 0.8 V to exclude contribution of irreversible oxidation within 0.8 – 1.0 V to non-faradaic region. Taking these results together, we can account for the higher capacitance by the presence of the rigid rGO framework, which firmly protects the PEDOT:PSS structure during the redox reaction.

Furthermore, we hypothesized that rGO prevents side reactions, especially not directional crosslinking between DR and PEDOT. Because the photo-crosslinking reaction is very fast such side reactions are inevitable. To prove this hypothesis, we separated the capacitance value into non-faradaic and faradaic components, which are the EDLC and pseudocapacitance, respectively (**Figure 2.5b, c**). The $(DR/rGO\text{-}PEDOT:PSS)_{10}$ set displayed a 160% increase in pseudocapacitance, whereas $(DR/PEDOT:PSS)_{10}$ showed a 48% decrease in pseudocapacitance because of the damage to the PEDOT during the crosslinking process. On the other hand, PEDOT:PSS combined with rGO maintained the redox peak because of the alternative bonding of various functional groups in rGO with DR when the amount of PSS was insufficient. Note that the number of PSS groups is also important for photo-crosslinking, because a lack of PSS results in a similar degradation of the capacitance (**Figure 2.6**). When a low proportion of PEDOT:PSS was used to prepare the rGO-PEDOT:PSS, for example, a 1:1 weight ratio of rGO to PEDOT:PSS, the electrochemical activity was significantly degraded after

UV exposure. Moreover, the EDLC increased slightly by 30%, indicating that the formation of covalent bonds between rGO and DR contributes to the enhancement of the EDLC. Because the backbone of PEDOT:PSS is tightly bound to rGO by π=π interactions, degradation of the capacitance can be considerably prevented. As a result, owing to the formation of covalent bonds after UV treatment, the specific capacitance reached 354 F/cm^3 at a scan rate of 20 mV/s, and a capacitance of 300 F/cm^3 was observed even at a higher scan rate of 200 mV/s. On the other hand, the film without UV treatment showed severely degraded capacitance as the scan rate was increased (**Figure 2.7**). The capacitance values are comparable to previously determined values, indicating that the thin film prepared in the current study can be used in practical supercapacitors.[15, 18, 35-37]

To further elucidate the transfer mechanisms in ultrathin film-based capacitive behavior, which is governed by two types of rate-determining steps: a diffusion limited mass transfer process and a surface-confined charge transfer process,[38] CV curves of the (DR/rGO-PEDOT:PSS)$_n$ (n = 2–10) films were collected, and volumetric capacitances were extracted (**Figure 2.5d**, and **Figure 2.8a**). The 10 BL sample was found to have the maximum areal capacitance, whereas the 4 BL sample had the highest volumetric capacitance. This variance may be due, in part, to the increase in thickness. Under this nanoscale thickness where the mass transfer is negligible, a surface-confined system is established, and charge transfer becomes the main rate-determining step, called by charge-transfer-limited system. However, as the number of bilayers increases, diffusion of the electrolyte provides another source of resistance. As a result, the capacitive behavior of a thick film is governed mainly by diffusion-limited mass transfer processes. As indicated in **Figure 2.5d**, the diffusion-limited resistance is negligible in thin films (up to 4 BL), whereas it dramatically diminishes the volumetric capacitance of thicker (6 – 10 BL) films. On the basis of these results, it can be inferred that the resistance from a mass transfer process significantly degrades the electrochemical activity as the thickness increases. Clearly, it is interesting to observe that the trade-off between the two processes is optimally balanced in the 4 BL film.

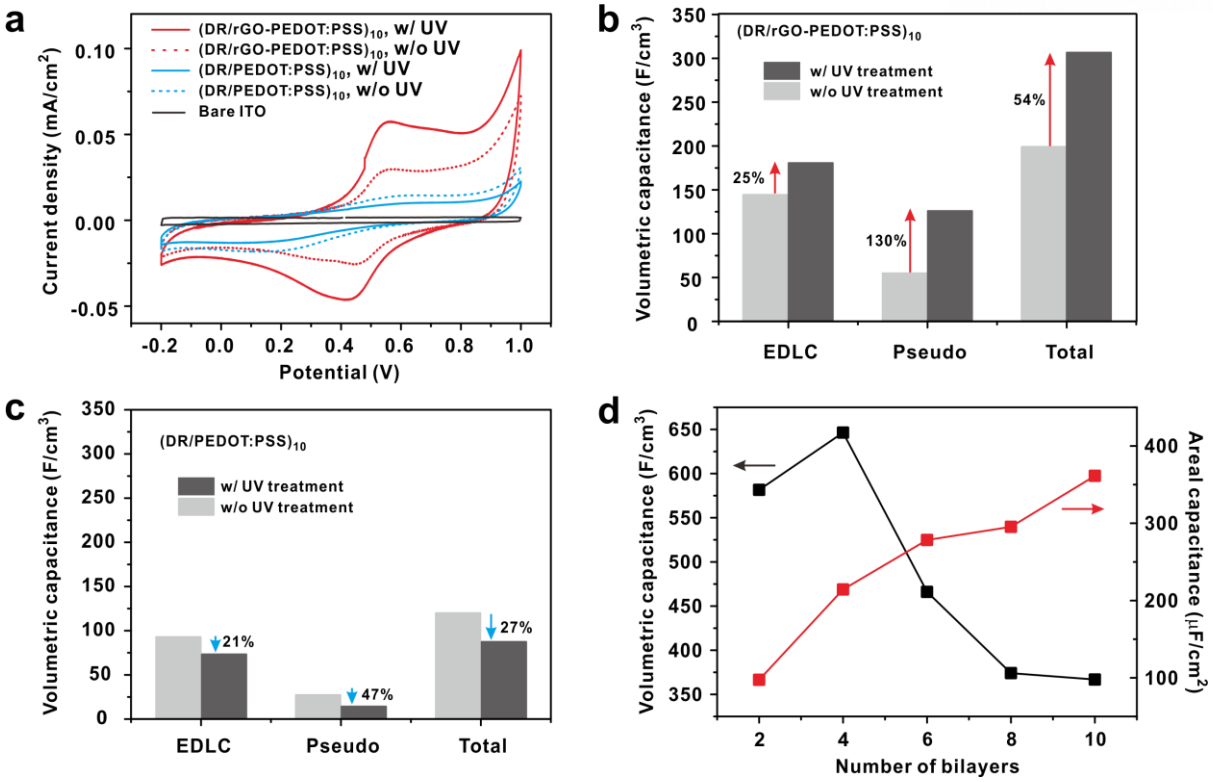

Figure 2.5. (a) Representative cyclic voltammogram curves of $(DR/rGO\text{-}PEDOT:PSS)_{10}$ and $(DR/PEDOT:PSS)_{10}$ at 100 mV/s before (dotted line) and after (solid line) UV treatment. Bare ITO-glass substrate was included for comparison. (b,c) EDLC and pseudocapacitance portions of $(DR/rGO\text{-}PEDOT:PSS)_{10}$ and $(DR/PEDOT:PSS)_{10}$, respectively. To eliminate irreversible oxidation region, the capacitance values were calculated in the range from −0.2 to 0.8 V. (d) Volumetric and areal capacitance of each layer after UV treatment.

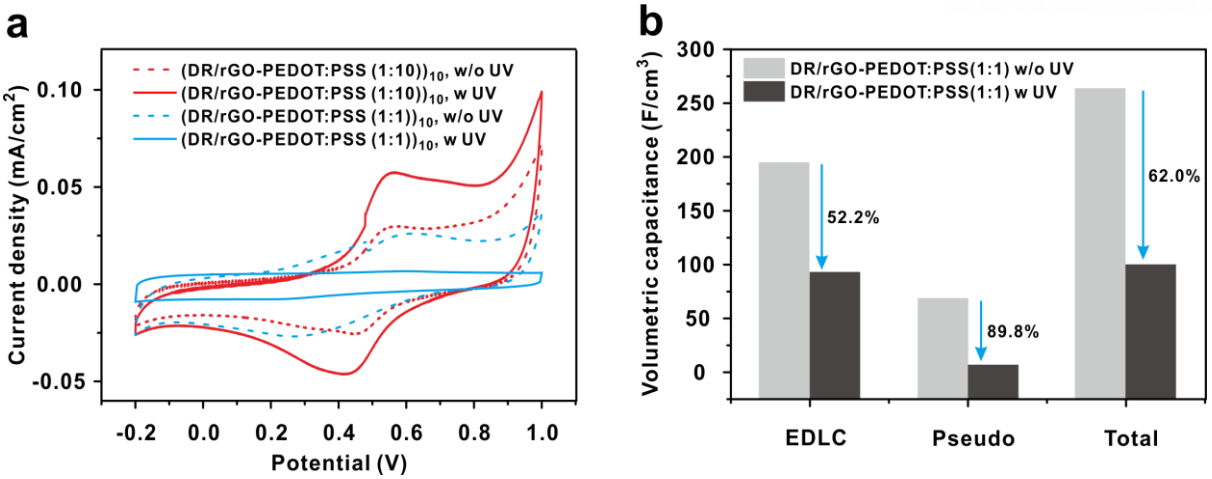

Figure 2.6. (a) Cyclic voltammogram curves of $(DR/rGO\text{-}PEDOT:PSS)_{10}$ with respect to weight ratio of PEDOT:PSS to rGO (1 - 10) measured at a scan rate of 100 mV/s. rGO-PEDOT:PSS (1:10) was used for data in the manuscript. (b) Deconvoluted volumetric capacitance of $(DR/rGO\text{-}PEDOT:PSS(1:1))_{10}$ at 100 mV/s.

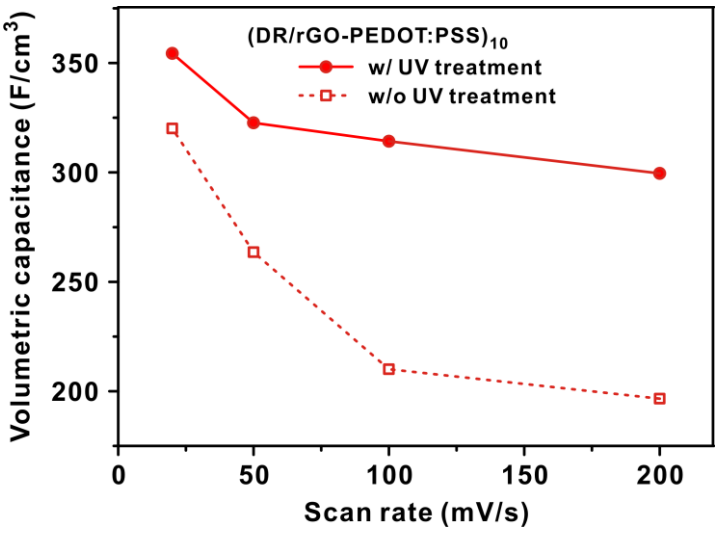

Figure 2.7. Volumetric capacitance of 10 BL film versus scan rate before (dotted line) and after (solid line) UV treatment. The electrolyte employed was 1.0 M H_2SO_4, and the third scan was used for comparison.

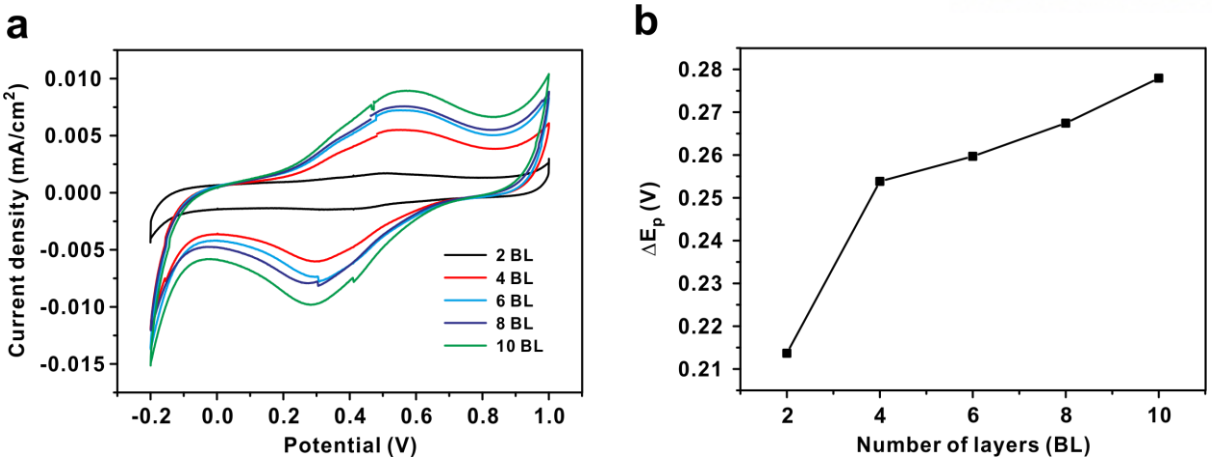

Figure 2.8. (a) Cyclic voltammogram curves of $(DR/rGO\text{-}PEDOT:PSS)_n$ (n = 2 - 10) at a scan rate of 20 mV/s. (b) Anodic/cathodic peak to peak separation with respect to number of layers.

Furthermore, because the bonding characteristics and charge balance change after UV treatment, the origin of the capacitance variation after UV treatment can be elucidated if quantitative comparison is possible. For that purpose, we introduced a simple relationship for a quantitative analysis of the rate-determining step in the samples. First, the diffusion-limited process is described by the Randles–Sevcik equation, which expresses the peak current density in a reversible redox reaction as follows (2):

$$i = (2.69 * 10^5) n^{3/2} A D_O^{1/2} C_O^* v^{1/2} \qquad (2)$$

where n is the number of electrons transferred during the redox reaction, A is the area (cm^2), D_O is the diffusion coefficient (cm^2/s), and C_O* is the bulk concentration of redox components (mol/cm^3), and v is the scan rate (V/s). According to this relationship, the peak current density is proportional to $v^{1/2}$, and the diffusion process mainly limits the capacitive currents ($i \propto v^{1/2}$).[39] In addition, as the multilayer film is extremely thin, current from the redox reaction is not influenced by diffusion; therefore, the diffusion coefficient is insignificant in the system. For this reason, it can be assumed that only adsorbed electroactive components react on the surface of the film; such a system is referred to as a surface-confined system. In a reversible and extremely thin system, the peak current density is given as follows (3):

$$i = \frac{n^2 F^2 v A \Gamma_O^*}{4RT} \qquad (3)$$

where F is the Faraday constant (C/mol), Γ_O* is the amount of redox components (mol/cm^2), R is the ideal gas constant (J/K·mol), and T is the temperature (K). This relationship reveals that the peak current density is directly proportional to the scan rate when the film is sufficiently thin ($i \propto v$).[40,41] To evaluate the rate-determining process for each set, plots of the peak current density versus the scan rate were obtained (**Figure 2.9**). The p value collected from the fitting of the data of the $(DR/rGO\text{-}PEDOT:PSS)_{10}$ film was significantly altered after UV treatment (**Table 2.1**). The film before UV treatment had a p value of 0.474, which is fairly close to the ideal value of 0.5; capacitive current was conducted mainly through a typical mass-transfer-limited process. Interestingly, after UV treatment, the film yielded an increased p value of 0.656 (**Figure 2.9a,c**). Although the main transfer limit still originates from mass transfer, this result suggests that the formation of covalent bonds facilitates the charge transfer process. Considering the increase in the volumetric capacitance, especially pseudocapacitance and p value after UV treatment, charge transfer facilitation due to crosslinking in the $(DR/rGO\text{-}PEDOT:PSS)_{10}$ film clearly results in a significant increase in the capacitance value. Further,

the capacitance value of the 4 BL film showed a p value of ca. 1.0, so the charge transfer process predominantly determines the electrochemical activity (**Figure 2.9b,d**). This trend is in good agreement with **Figure 2.5d** in terms of the transition of the electrochemical-current-limiting mechanism from charge transfer to mass transfer. Interestingly, the trade-off thickness for charge transfer to mass transfer as the dominant process, ~4 nm, is much lower than that previously reported; for example, a 195 nm thick film composed of vanadium contained small molecules.[40] This may be due to the unique characteristic of the layered architecture by 2-dimentional building block of GO sheets. The CV curves for various numbers of bilayers also agree well with the above trend. The anodic/cathodic peak-to-peak separation (ΔE_p) gradually increases from 0.21 to 0.28 with increasing number of bilayers (**Figure 2.8b**). Because a higher overpotential is necessary for a large mass transfer resistance, mass transfer becomes more critical than charge transfer as the number of layers increases. Similarly, impedance data also reveals the charge transfer resistance reduces as the number of layers increases (**Table 2.2** and **Figure 2.10**). Comparing R_{ct} value of each set, UV treatment reduces charge transfer resistance in both 4 and 10 BL sets. In that regards, charge transfer is facilitated through photo-crosslinking. Charge/discharge curves from galvanostat accord with previous description on influence of UV treatment enhancing the performance of electrode (**Figure 2.11**). Although there was no considerable difference in the internal resistance values upon photo-crosslinking, the difference became significant with increase in the number of layers. From this observation, we argue that mass transfer resistance takes a significant role in determining overall internal resistance by interfering ionic diffusion in charging/discharging process as the number of layer increases.

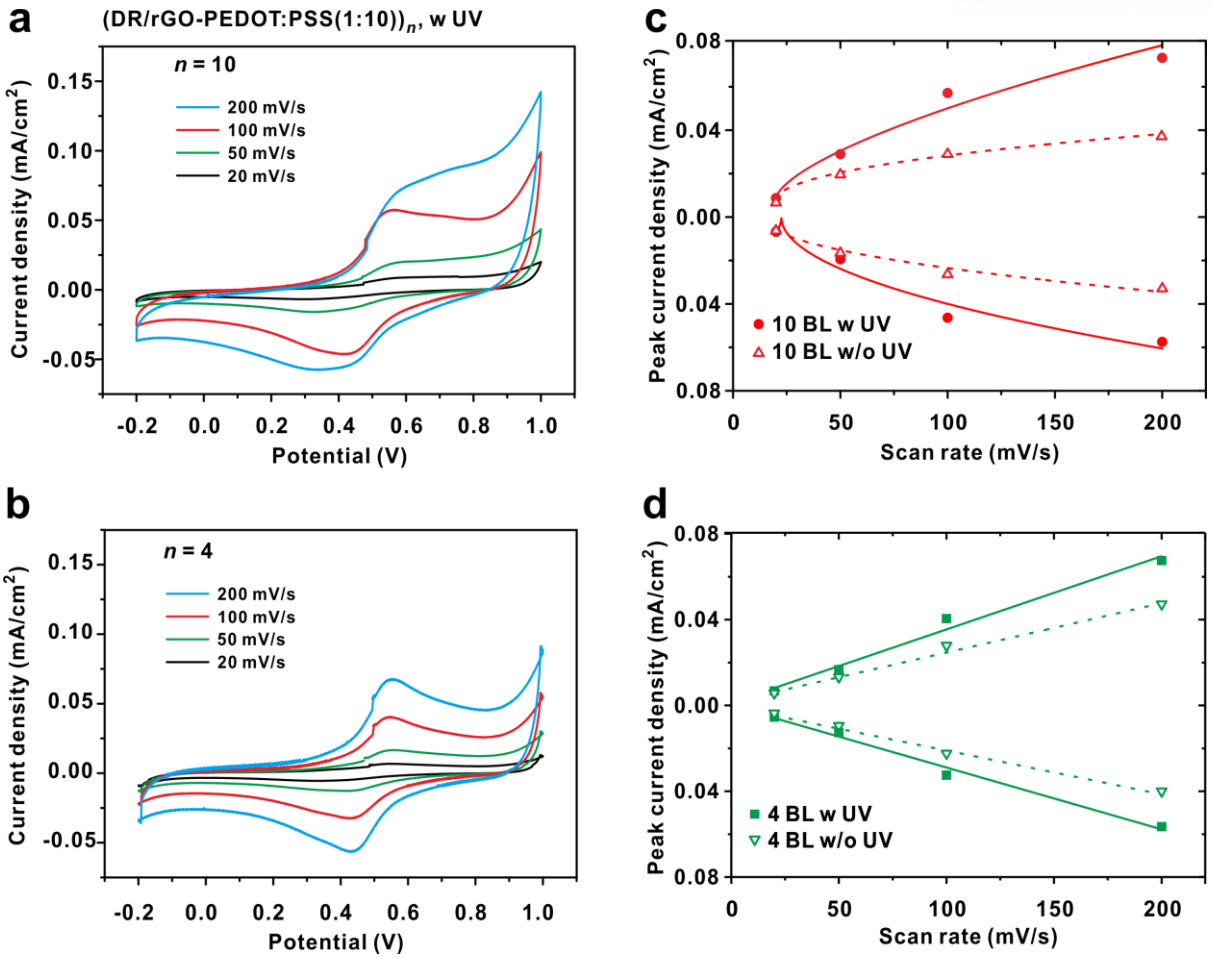

Figure 2.9. Cyclic voltammograms of (a) 10 BL and (b) 4 BL set with respect to scan rates. Current density versus scan rate plots for (DR/rGOPEDOT: PSS)$_n$ at (a) n = 10 BL and (b) n = 4 BL before (dotted line) and after (solid line) UV treatment.

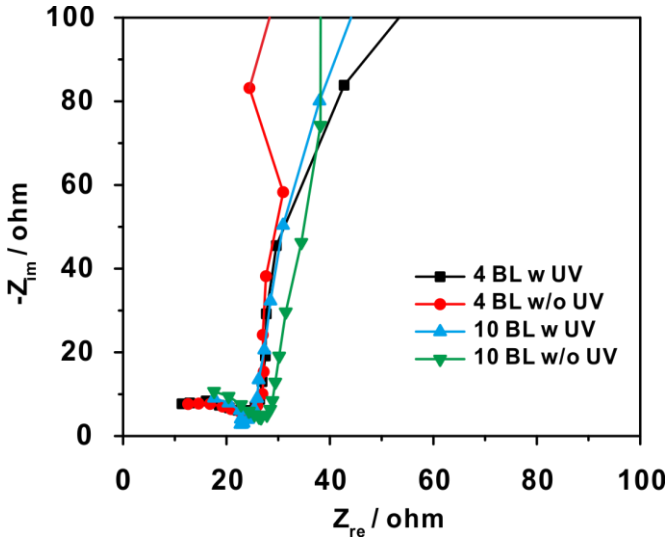

Figure 2.10. Impedance data of $(DR/rGO\text{-}PEDOT:PSS)_n$ film before and after UV treatment.

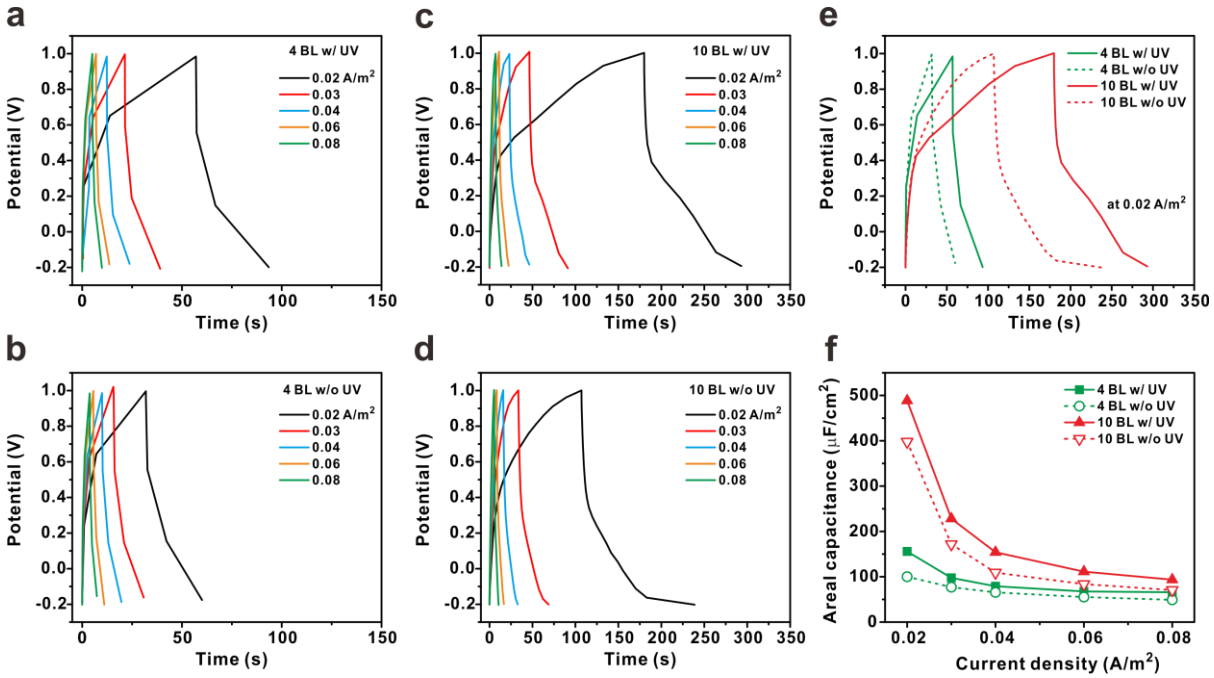

Figure 2.11. (a-d) Galvanostat charge/discharge curves of (a, b) 4 BL and (c, d) 10 BL of $(DR/rGO\text{-}PEDOT:PSS)_n$ sample with and without UV treatment measured at various current density values. (e) Representative charge/discharge curves at 0.02 A/m^2 (f) corresponding areal capacitance of 4 and 10 BL electrodes.

Table 2.1. p values of (DR/rGO-PEDOT:PSS)$_n$ (n = 4, 10) films. Fitting relation of $y = y_o + A(x-x_o)^p$ was employed.

Samples	**4 BL**	**10 BL**
w/o UV	0.976	0.474
w/ UV	1.02	0.656

Table 2.2. R_{ct} values of (DR/rGO-PEDOT:PSS)$_n$ film before and after UV treatment.

R_{ct} (ohm)	**4 BL**	**10 BL**
w/o UV	19.2	18.2
w/ UV	17.2	10.9

2.5 Conclusion

An ultrathin supercapacitor electrode was fabricated by solution-processable LbL assembly of rGO nanosheets with a photo-cross-linkable polymer. UV treatment triggered crosslinking of DR with PEDOT:PSS, causing pure electrostatic interactions to convert to covalent bonds. The $(DR/rGOPEDOT:PSS)_{10}$ film exhibited a large volumetric capacitance value of 354 F/cm^3, which is attributed to significant enhancement of the pseudocapacitance from PEDOT:PSS. Furthermore, electrochemical measurements suggested that photo-cross-linking between DR and PEDOT:PSS facilitates charge transfer, yielding a fairly large capacitance value of 300 F/cm^3 even at a high scan rate of 200 mV/s. Through solution processable LbL assembly, various colloidal building blocks can be incorporated via electrostatic interactions, so future applications to thin film supercapacitors can be developed. Furthermore, we anticipate that the study will offer a model system to elucidate the electrochemical pathways governing the development of high-performance thin film supercapacitors.

2.6 References

(1) Decher, G. Fuzzy Nanoassemblies: Toward Layered Polymeric Multicomposites. *Science* **1997,** *277*, 1232-1237.

(2) Hammond, P. T. Form and Function in Multilayer Assembly: New Applications at the Nanoscale. *Adv. Mater.* **2004,** *16*, 1271-1293.

(3) Kim, B.-S.; Smith, R. C.; Poon, Z.; Hammond, P. T. Mad (Multiagent Delivery) Nanolayer: Delivering Multiple Therapeutics from Hierarchically Assembled Surface Coatings. *Langmuir* **2009,** *25*, 14086-14092.

(4) Lee, S. W.; Kim, B. S.; Chen, S.; Shao-Horn, Y.; Hammond, P. T. Layer-by-Layer Assembly of All Carbon Nanotube Ultrathin Films for Electrochemical Applications. *J. Am. Chem. Soc.* **2009,** *131*, 671-679.

(5) Hong, T.-K.; Lee, D. W.; Choi, H. J.; Shin, H. S.; Kim, B.-S. Transparent, Flexible Conducting Hybrid Multi Layer Thin Films of Multiwalled Carbon Nanotubes with Graphene Nanosheets. *ACS Nano* **2010,** *4*, 3861-3868.

(6) DeMuth, P. C.; Moon, J. J.; Suh, H.; Hammond, P. T.; Irvine, D. J. Releasable Layer-by-Layer Assembly of Stabilized Lipid Nanocapsules on Microneedles for Enhanced Transcutaneous Vaccine Delivery. *ACS Nano* **2012,** *6*, 8041-8051.

(7) Tang, Z. Y.; Wang, Y.; Podsiadlo, P.; Kotov, N. A. Biomedical Applications of Layer-by-Layer Assembly: From Biomimetics to Tissue Engineering. *Adv. Mater.* **2006,** *18*, 3203-3224.

(8) Lee, H.; Mensire, R.; Cohen, R. E.; Rubner, M. F. Strategies for Hydrogen Bonding Based Layer-by-Layer Assembly of Poly(Vinyl Alcohol) with Weak Polyacids. *Macromolecules* **2012,** *45*, 347-355.

(9) Wang, L. Y.; Wang, Z. Q.; Zhang, X.; Shen, J. C.; Chi, L. F.; Fuchs, H. A New Approach for the Fabrication of an Alternating Multilayer Film of Poly(4-Vinylpyridine) and Poly(Acrylic Acid) Based on Hydrogen Bonding. *Macromol. Rapid Commun.* **1997,** *18*, 509-514.

(10) Shimazaki, Y.; Ito, S.; Tsutsumi, N. Adsorption-Induced Second Harmonic Generation from the Layer-by-Layer Deposited Ultrathin Film Based on the Charge-Transfer Interaction. *Langmuir* **2000,** *16*, 9478-9482.

(11) Xiong, H.; Cheng, M.; Zhou, Z.; Zhang, X.; Shen, J. A New Approach to the Fabrication of a Self-Organizing Film of Heterostructured Polymer/Cu2s Nanoparticles. *Adv. Mater.* **1998,** *10*, 529-532.

(12) Schutte, M.; Kurth, D. G.; Linford, M. R.; Colfen, H.; Mohwald, H. Metallosupramolecular Thin Polyelectrolyte Films. *Angew. Chem. Int. Ed.* **1998,** *37*, 2891-2893.

(13) Mamedov, A. A.; Kotov, N. A.; Prato, M.; Guldi, D. M.; Wicksted, J. P.; Hirsch, A. Molecular Design of Strong Single-Wall Carbon Nanotube/Polyelectrolyte Multilayer Composites. *Nat. Mater.* **2002,** *1*, 190-194.

(14) Cao, W. X.; Zhao, C.; Cao, J. W. Synthesis and Characterization of 3-Methoxydiphenylamine-4-Diazonium Salt and Its Diazoresin. *J. Appl. Polym. Sci.* **1998,** *69*, 1975-1982.

(15) Xiong, Z.; Gu, T.; Wang, X. Self-Assembled Multi Layer Films of Sulfonated Graphene and Polystyrene-Based Diazonium Salt as Photo-Cross-Linkable Supercapacitor Electrodes. *Langmuir* **2014,** *30*, 522-532.

(16) Lee, T.; Min, S. H.; Gu, M.; Jung, Y. K.; Lee, W.; Lee, J. U.; Seong, D. G.; Kim, B.-S. Layer-by-Layer Assembly for Graphene-Based Multi Layer Nanocomposites: Synthesis and Applications. *Chem. Mater.* **2015,** *27*, 3785-3796.

(17) Hong, J.; Han, J. Y.; Yoon, H.; Joo, P.; Lee, T.; Seo, E.; Char, K.; Kim, B.-S. Carbon-Based Layer-by-Layer Nanostructures: From Films to Hollow Capsules. *Nanoscale* **2011,** *3*, 4515-4531.

(18) Zhang, L. L.; Zhou, R.; Zhao, X. S. Graphene-Based Materials as Supercapacitor Electrodes. *J. Mater. Chem.* **2010,** *20*, 5983-5992.

(19) Park, S.; Ruoff, R. S. Chemical Methods for the Production of Graphenes. *Nat. Nanotechnol.* **2009,** *4*, 217-224.

(20) Yoo, J. J.; Balakrishnan, K.; Huang, J. S.; Meunier, V.; Sumpter, B. G.; Srivastava, A.; Conway, M.; Reddy, A. L. M.; Yu, J.; Vajtai, R.; Ajayan, P. M. Ultrathin Planar Graphene Supercapacitors. *Nano Lett.* **2011,** *11*, 1423-1427.

(21) Simon, P.; Gogotsi, Y. Materials for Electrochemical Capacitors. *Nat. Mater.* **2008,** *7*, 845-854.

(22) Wu, Z. S.; Wang, D. W.; Ren, W.; Zhao, J.; Zhou, G.; Li, F.; Cheng, H. M. Anchoring Hydrous Ruo2 on Graphene Sheets for High-Performance Electrochemical Capacitors. *Adv. Func. Mater.* **2010,** *20*, 3595-3602.

(23) Guo, S.; Dong, S.; Wang, E. Three-Dimensional Pt-on-Pd Bimetallic Nanodendrites Supported on Graphene Nanosheet: Facile Synthesis and Used as an Advanced Nanoelectrocatalyst for Methanol Oxidation. *ACS Nano* **2010,** *4*, 547-555.

(24) Bai, H.; Li, C.; Shi, G. Q. Functional Composite Materials Based on Chemically Converted Graphene. *Adv. Mater.* **2011,** *23*, 1089-1115.

(25) Kou, R.; Shao, Y.; Mei, D.; Nie, Z.; Wang, D.; Wang, C.; Viswanathan, V. V.; Park, S.; Aksay, I. A.; Lin, Y.; Wang, Y.; Liu, J. Stabilization of Electrocatalytic Metal Nanoparticles at Metal-Metal Oxide-Graphene Triple Junction Points. *J. Am. Chem. Soc.* **2011,** *133*, 2541-2547.

(26) Qu, Q.; Yang, S.; Feng, X. 2d Sandwich-Like Sheets of Iron Oxide Grown on Graphene as High Energy Anode Material for Supercapacitors. *Adv. Mater.* **2011,** *23*, 5574-5580.

(27) Dong, X.; Cao, Y.; Wang, J.; Chan-Park, M. B.; Wang, L.; Huang, W.; Chen, P. Hybrid Structure of Zinc Oxide Nanorods and Three Dimensional Graphene Foam for Supercapacitor and Electrochemical Sensor Applications. *RSC Adv.* **2012,** *2*, 4364-4369.

(28) Yan, J.; Fan, Z. J.; Wei, T.; Qian, W. Z.; Zhang, M. L.; Wei, F. Fast and Reversible Surface Redox Reaction of Graphene-Mno2 Composites as Supercapacitor Electrodes. *Carbon* **2010,** *48*, 3825-3833.

(29) Hummers, W. S.; Offeman, R. E. Preparation of Graphitic Oxide. *J. Am. Chem. Soc.* **1958,** *80*, 1339-1339.

(30) Cao, W. X.; Ye, S. J.; Cao, S. G.; Zhao, C. Novel Polyelectrolyte Complexes Based on Diazo-Resins. *Macromol. Rapid Commun.* **1997,** *18*, 983-989.

(31) Jo, K.; Lee, T.; Choi, H. J.; Park, J. H.; Lee, D. J.; Lee, D. W.; Kim, B.-S. Stable Aqueous Dispersion of Reduced Graphene Nanosheets Via Non-Covalent Functionalization with Conducting Polymers and Application in Transparent Electrodes. *Langmuir* **2011,** *27*, 2014-2018.

(32) Zhao, S.; Li, X. F.; Yang, M.; Sun, C. Q. Fabrication and Characterization of Covalently Attached Multilayer Films Containing Iron Phthalocyanine and Diazo-Resins. *J. Mater. Chem.* **2004,** *14*, 840-844.

(33) Qin, S. H.; Qin, D. Q.; Ford, W. T.; Zhang, Y. J.; Kotov, N. A. Covalent Cross-Linked Polymer/Single-Wall Carbon Nanotube Multilayer Films. *Chem. Mater.* **2005,** *17*, 2131-2135.

(34) Sakamoto, S.; Okumura, M.; Zhao, Z. G.; Furukawa, Y. Raman Spectral Changes of Pedot-Pss in Polymer Light-Emitting Diodes Upon Operation. *Chem. Phys. Lett.* **2005,** *412*, 395-398.

(35) Tao, Y.; Xie, X.; Lv, W.; Tang, D.-M.; Kong, D.; Huang, Z.; Nishihara, H.; Ishii, T.; Li, B.; Golberg, D.; Kang, F.; Kyotani, T.; Yang, Q.-H. Towards Ultrahigh Volumetric Capacitance: Graphene Derived Highly Dense but Porous Carbons for Supercapacitors. *Sci. Rep.* **2013,** *3*, 2975-2982.

(36) Centeno, T. A.; Stoeckli, F. The Volumetric Capacitance of Microporous Carbons in Organic Electrolyte. *Electrochem. Commun.* **2012,** *16*, 34-36.

(37) Murali, S.; Quarles, N.; Zhang, L. L.; Potts, J. R.; Tan, Z.; Lu, Y.; Zhu, Y.; Ruoff, R. S. Volumetric Capacitance of Compressed Activated Microwave-Expanded Graphite Oxide (a-Mego) Electrodes. *Nano Energy* **2013,** *2*, 764-768.

(38) Bard, A. J.; Faulkner, L. R., *Electrochemical Methods Fundamentals and Applications*. 2nd ed.; John Wiley & Sons: New York, 2000.

(39) Choi, Y.; Gu, M.; Park, J.; Song, H.-K.; Kim, B.-S. Graphene Multilayer Supported Gold Nanoparticles for Efficient Electrocatalysts toward Methanol Oxidation. *Adv. Energy Mater.* **2012,** *2*, 1510-1518.

(40) Fernandes, D. M.; Teixeira, A.; Freire, C. Multielectrocatalysis by Layer-by-Layer Films Based on Pararosaniline and Vanadium-Substituted Phosphomolybdate. *Langmuir* **2015,** *31*, 1855-1865.

(41) Fernandes, D. M.; Freire, C. Hybrid Photochromic Multilayer Films Based on Chitosan and Europium Phosphomolybdate. *J. Appl. Electrochem.* **2014,** *44*, 655-665.

Chapter 3.
Electrocatalytic Multilayer Nanoelectrode by Layer-by-Layer Assembly

3.1 Bimetallic Graphene Multilayer Electrode toward Efficient Electrocatalyst

3.1.1 Abstract

Even though traditional electrode fabrication methods such as simple mixing process have been used in various energy storage and conversion devices due to its handiness, these methods could not fully utilize and maximize the intrinsic properties of each active material. With the limited control over the internal structure of the electrode, it also often poses a significant challenge to elucidate the structure-property relationship between components within the electrode. Taking advantages of versatile layer-by-layer (LbL) assembly which can tailor nano-architecture of hybrid electrodes, here we report electrocatalytic thin films for methanol oxidation by adjusting the assembly sequence of LbL films composed of the Au and Pd nanoparticles (NPs) and graphene oxide (GO) nanosheets. In case of co-assembled bimetallic LbL structure of $(GO/Au/GO/Pd)_n$ where respective Au and Pd NPs are supported with GO nanosheets, the electrocatalytic activity is significantly higher than that of respective monometallic LbL electrode (i.e. $(GO/Au)_n$ and $(GO/Pd)_n$). To further investigate the architecture effect on the electrochemical behavior, Au and Pd NPs are assembled with GO in a different relative position of hybrid multilayer electrodes. It is proved that the electrocatalytic activity can be highly tunable by the position of metal NPs in the LbL structure, suggesting the structural dependence of charge and mass transfer between the electrolyte and the electrode, which is otherwise impossible to investigate in a simple conventional electrode fabrication method. Because of the highly tunable properties of LbL assembled electrodes coupled with electrocatalytic NPs, we anticipate that the general concept presented here will offer new insights in the nanoscale control over the architecture of the electrode toward development of novel electroactive catalysts.

3.1.2 Introduction

The rapid depletion of fossil fuels and growing environmental concerns have created an enormous worldwide demand for alternative technologies of clean and renewable energies.[1,2] Therefore, there have been significant researches for electrochemical energy conversion technology, as following that the design of electrodes with high conversion efficiency becomes very important. Typically, various electroactive materials with conductive supports are fabricated into electrodes of energy conversion devices by simple mixing process;[3] however, these traditional electrode fabrication methods not only could not fully utilize the intrinsic properties of each active material, but also limit analyzing the contribution of individual materials to the overall performance of the electrode. For this reason, a more concerted approach to fabricate the nanostructured electrode with a fine structural control is gaining more attention.[4,5]

Among many assembly strategies for these nanostructured electrode with two or more components, layer-by-layer (LbL) assembly is one of the most versatile nanoscale blending methods to assemble diverse materials on various surfaces.[6-10] The LbL assembly is often achieved through the sequential adsorption of materials with complementary functional groups employing electrostatic interactions, hydrogen bonding, or other intermolecular interactions.[11,12] Thus, highly ordered multilayered architectures can be manufactured reproducibly, allowing nanoscale-level control over both composition and structure of hybrid multilayers with the choice of materials and sequence of layering. With these unique opportunities, there are active researches on LbL assembled thin films for various energy storage and conversion applications, including lithium ion battery, supercapacitor, fuel cell, solar cell and electrocatalyst.[13-19] Along with the development of hybrid electrodes, there have been approaches, including our own, to couple unique physical and chemical properties of 2-dimensional (2D) nanomaterials such as graphene nanosheets with the versatility of LbL assembly for electronic and biomaterial surfaces;[20-31] for example, we found that the graphene oxide (GO) nanosheets not only serve as a structural component of the multilayer thin films, but also potentially improve the utilization of metal NPs within the electrode, emphasizing the critical role of graphene as a chemically stable support in preserving the catalytic active surface of Au NPs.[18] It is also interesting to observe that the electrocatalytic activity of hybrid electrode is highly tunable with respect to the number of layers. Onda et al. have previously reported the importance of well-organized layered structures with different performance through sequential reaction in the design of multi-enzyme reactors using glucose oxidase and glucoamylase as biocatalysts.[32] However, there is no report on the investigation of electrochemical activity of multilayer electrode and the associated electrochemical communication between active materials with respect to the internal architecture (i.e. controlled by layering sequence) when more than two active components are involved.

In that regard, herein we report the creation of 3D hybrid electrocatalytic thin films with varying internal architectures that are composed of two electroactive Au and Pd NPs integrated with graphene

nanosheets with LbL assembly. In specific, we focused on the elucidation of architecture-property relationship of hybrid electrodes toward methanol oxidation reaction (MOR) as a model electrocatalytic reaction (**Figure 3.1.1**).

We found that the electrocatalytic activity is highly tunable by the number and the position of metal NPs in the LbL structure, suggesting the considerable structural dependence of mass transfer of the electrolyte within the 3D hybrid electrode. Moreover, even with the identical composition of constituent NPs, the hybrid electrode exhibited highly tunable electrocatalytic activity depending on the electrode architecture, which is otherwise impossible to investigate with a simple electrode fabrication method. Considering the versatile nature of LbL assembly coupled with electroactive NPs, the approach developed here will offer new insights in the design of the nanoscale electrodes for advanced energy conversion devices.

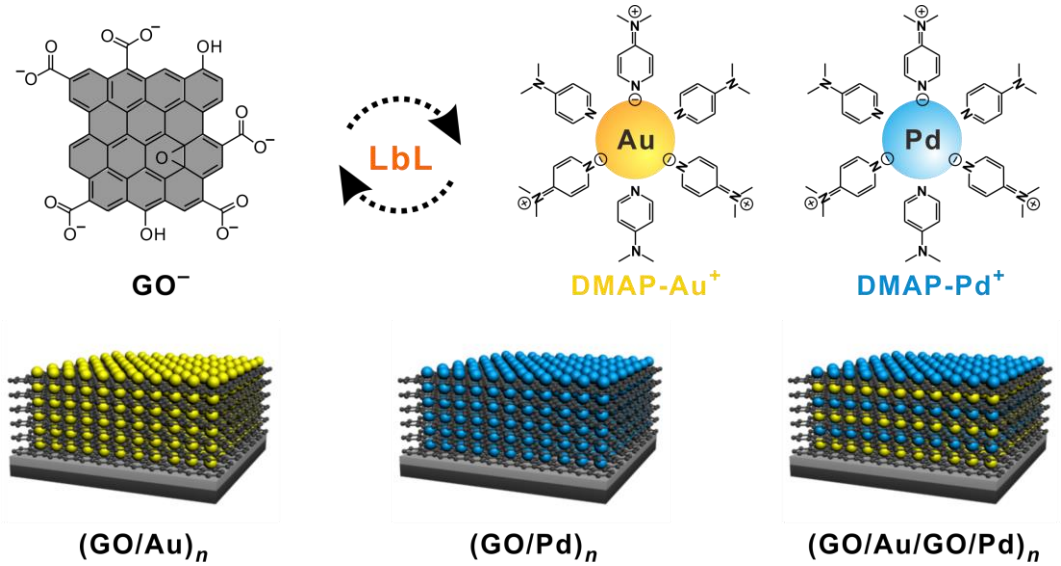

Figure 3.1.1. Schematic representation of layer-by-layer (LbL) assembled monometallic $(GO/Au)_n$, and $(GO/Pd)_n$ and bimetallic $(GO/Au/GO/Pd)_n$ multilayer thin films for methanol oxidation reaction.

3.1.3 Experimental

3.1.3.1 Preparation of GO

Graphite oxide was synthesized from graphite powder (Sigma-Aldrich) by modified Hummers method and exfoliated to give a brown dispersion of graphene oxide (GO) under ultrasonication at a concentration of 0.50 mg/mL.[33, 34]

3.1.3.2 Preparation of Au and Pd NPs

The 4-(dimethylamino)pyridine (DMAP)-stabilized Au and Pd NPs were prepared by using the spontaneous phase transfer from organic solvent according to a literature method.[35]

3.1.3.3 LbL of hybrid electrode films

ITO-coated glass substrate was cleaned by sonication in deionized (DI) water, acetone and ethanol for 10 min. Silicon and quartz substrates were cleaned by piranha solution to remove any organic contamination and subsequently treated with (3-aminopropyl)triethoxysilane to introduce positively charged hydrophilic surface. These substrates were first dipped into negatively charged GO solution (0.50 mg/mL) at pH 4 for 10 min. It was then dipped into DI water for 1 min three times to remove loosely bound GO. Subsequently, the substrate was then dipped into positively charged DMAP-coated Au or Pd NPs suspension at pH 11 for 10 min, and washed with DI water three times for 1 min, which afforded one-bilayer film of $(GO/Au)_1$ or $(GO/Pd)_1$, respectively. The above procedures were repeated to achieve the desired number of bilayers (n). Multicomponent assembly was conducted using the identical procedure with both Au and Pd NP suspensions. All as-assembled multilayer films were subjected to thermal reduction at 150 ºC for 12 h in an oven. For comparison, a commercial 30 wt.% palladium nanoparticles supported by carbon black (Pd/C, Sigma-Aldrich) was used as a control. Pd/C ink was prepared by dispersing 20 mg of Pd/C powder in 2.0 mL of DI water and 40 μL of 5 wt.% Nafion solution (Sigma-Aldrich). 5 μL of the Pd/C ink was dropped on a glassy carbon electrode (diameter: 3 mm).

3.1.3.4 Electrochemical analysis.

Electrochemical experiments were performed using a standard three electrode cell configuration (Biologic science instrument, VSP). A platinum wire was used as a counter electrode and Hg/HgO as a reference. The working electrode was multilayer thin film assembled on ITO-coated glass. Cyclic voltammetry (CV) was performed between -0.60 to 0.60 V in 0.10 M KOH solution with 1.0 M methanol solution at room temperature in a saturated N_2 at a scan rate of 20 mV s^{-1}. The current density was calculated by dividing the geometric area (cm^2) of as-prepared LbL electrodes. The values of potential were converted from versus Hg/HgO to versus the reversible hydrogen electrode (RHE) by: Hg/HgO + 0.879 V = RHE. For the correction, the potential difference between Hg/HgO and RHE was

measured in a cell where platinum wires were used as the working and counter electrodes in a H_2-saturated aqueous electrolyte of 0.10 M KOH with Hg/HgO as the reference electrode (**Figure 3.1.2**). Linear sweep voltammetry (LSV) was carried out at a scan rate of 5 mV s^{-1}. Electrochemical impedance spectroscopy (EIS) measurements were carried out in the frequency range from 100 kHz to 100 mHz under AC stimulus of 10 mV in amplitude.

3.1.3.5 Characterizations.

The absorbance of the thin films was characterized by using UV/vis spectroscopy (VARIAN, Cary 5000). The thickness of the as-prepared samples on silicon substrates was measured by surface profiler (KLA Tencor, P-6). The surface morphology of the samples was investigated using scanning electron microscopy (Cold FE-SEM, Hitachi, S-4800) and atomic force microscopy (AFM, Nanoscope V, Veeco) via a tapping mode. The size and morphology of the prepared NPs were measured by transmission electron microscopy (Normal-TEM, JEOL, JEM-2100, accelerating voltage of 200 kV). The LbL films were analyzed by X-ray photoelectron spectroscopy (XPS, Thermo Fisher, K-alpha). The cross-sectional TEM samples were prepared by focus ion beam (FIB) technique (FEI, Quanta 3D FEG) and the cross-sectional images were obtained by high-resolution transmission electron microscopy (HR-TEM), high-angle annular dark field scanning transmission electron microscopy (HAADF-STEM), and energy dispersive X-ray spectroscopy (EDXS) (JEOL, JEM-2100F, accelerating voltage of 200 kV). The active mass of each material adsorbed onto the film surface was analyzed by a quartz crystal microbalance (QCM, Stanford Research System, QCM200), using the following Sauerbrey equation (1, 2):

$$\Delta F(\mathrm{Hz}) = -\frac{2F_o^2}{A\sqrt{\rho_q \mu_q}}\Delta m \quad (1)$$

$$\Delta F(\mathrm{Hz}) = -56.6 \times \Delta m \quad (2)$$

where ΔF is the resonant frequency change (Hz), Δm is the mass change per unit area of the quartz crystal (μg/cm^2), F_o (5 MHz) is the fundamental resonance frequency of the crystal, A is the area of the Au-Cr electrode, ρ_q (2.65 g·cm^{-3}) is the density of quartz crystal and μ_q (2.95×10^{11} g·cm^{-1}·s^{-2}) is the shear modulus. Consequently, the specific current can be calculated by dividing the peak current by the active mass of metal NPs.

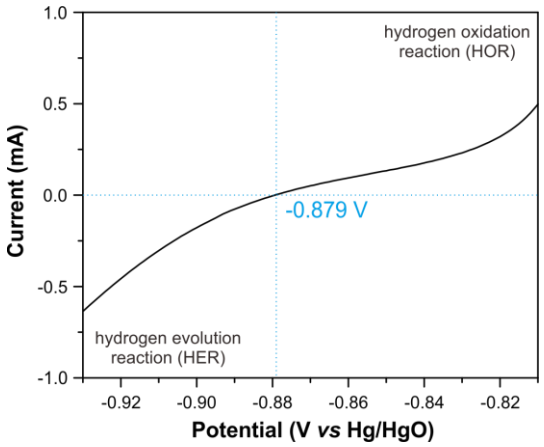

Figure 3.1.2. RHE calibration in H_2-saturated 0.10 M KOH electrolyte at a potential scan rate of 5 mV s^{-1}. The open circuit potential was measured at -0.879 V.

3.1.4 Results and Discussion

3.1.4.1 Fabrication of hybrid LbL electrodes

Highly stable aqueous suspensions of GO and the electrocatalytic metal NPs are necessary to fabricate 3D LbL assembled electrocatalyst films. Negatively charged GO suspension possessing many oxygen-containing functional groups such as carboxyl acids, hydroxyl, and epoxide groups was initially prepared using the modified Hummers method.[33, 34] Subsequently, positively charged Au and Pd NPs were prepared by using the spontaneous phase transfer from organic solvent with 4-(dimethylamino)pyridine (DMAP) ligand.[35] We employed the identical ligand for the synthesis of both NPs to minimize the ligand effect on the electrocatalytic activity. The average diameter of Au and Pd NPs was determined to be 5.8 nm and 3.4 nm (**Figure 3.1.3**). With these stable suspensions of the positively charged NPs as electroactive species and the negatively charged GO as a stable support, we fabricated three types of multilayer films by LbL assembly onto a silicon wafer, quartz and ITO-coated glass slide, respectively. In specific, homogeneous monometallic hybrid electrodes consisting of GO and respective metal NPs (either Au or Pd NPs) were assembled in an architecture of substrate/$(GO/Au)_n$ or substrate/$(GO/Pd)_n$ (n = number of bilayer (BL), typically n = 2 - 8). Moreover, heterogeneous bimetallic electrodes composed of GO and both metal NPs were assembled in the format of substrate/$(GO/Au/GO/Pd)_n$ (n = number of tetralayer (TL), typically n = 1 - 4).

The successful growth of each multilayer was monitored by the gradual increase of absorbance upon increasing the number of layers in UV/vis spectra (**Figure 3.1.4a** and **3.1.5**). The linear growth curve corresponding absorbance maxima of GO at 215 nm clearly demonstrates the uniform multilayer formation after each assembly (**Figure 3.1.4b**). Interestingly, we found that the absorbance sum of each $(GO/Au)_n$ and $(GO/Pd)_n$ multilayer was similar to that of bimetallic $(GO/Au/GO/Pd)_n$ films, suggesting the precise control over the thickness and composition of multilayers without significantly altering the internal structures. In other case, the surface plasmon absorbance of Au NPs at 600 nm within heterostructured $(GO/Au/GO/Pd)_n$ was matching exactly to that of Au NPs within $(GO/Au)_n$ multilayer films (inset in **Figure 3.1.4b**). Despite two different NPs are alternatively deposited within $(GO/Au/GO/Pd)_n$ multilayer, it is interesting to observe that the amount of Au NPs is constant with the $(GO/Au)_n$ multilayer films owing to the identical charge density of Au NPs. The corresponding thickness of each multilayer film shows a linear growth with respect to the number of deposition steps with an average bilayer thickness corresponding to 8.82 nm, 4.77 nm for a single bilayer of $(GO/Au)_n$ and $(GO/Pd)_n$ multilayer, respectively, and 14.2 nm for a single tetralayer of $(GO/Au/GO/Pd)_n$ films (**Figure 3.1.4c**). The average thickness of a single tetralayer is in accord with the sum of the average bilayer thickness of two monometallic films, which demonstrates the high fidelity of the LbL assembly in building hybrid electrodes.

We further analyzed the adsorption behavior of GO, Au and Pd NPs in $(GO/Au/GO/Pd)_n$ multilayer films using a quartz crystal microbalance (QCM). **Figure 3.1.4d** shows the stepwise

measurement of the mass deposited after each layer, indicating the amount of each component in the multilayer structure quantitatively; for example, the average mass was found to be 0.55 μg/cm^2, 4.31 μg/cm^2 and 1.38 μg/cm^2 for GO, Au and Pd NPs, respectively, within a single tetralayer. The adsorption of metal NPs was the higher than that of GO sheets, implying that it would be advantageous in respect to catalytic effect on metal by high mass loading per unit area. In addition, the amount of Au NPs was higher than that of Pd NPs, resulting in accord with the growth curves in UV/vis spectra and thickness data.

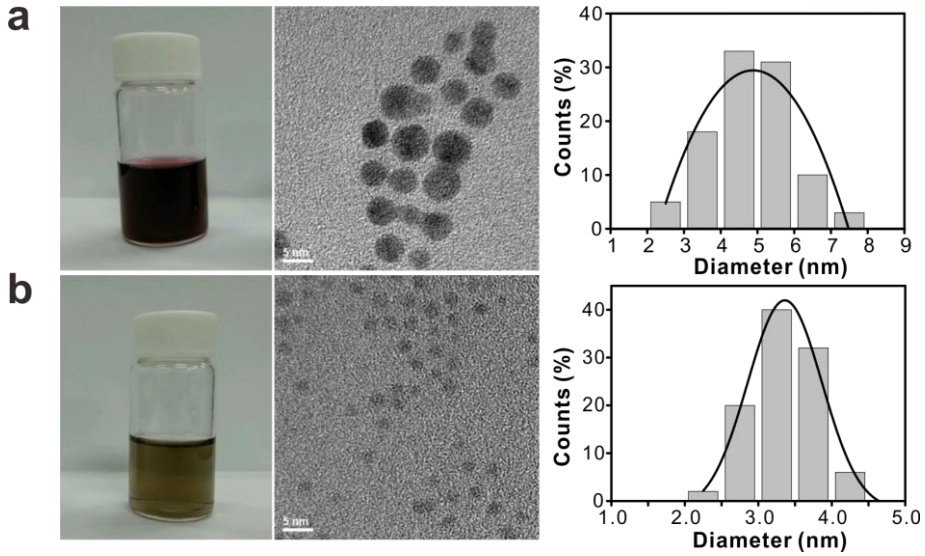

Figure 3.1.3. Photograph and TEM image with a corresponding size distribution histogram of (a) DMAP-Au NPs suspension and (b) DMAP-Pd NPs suspension.

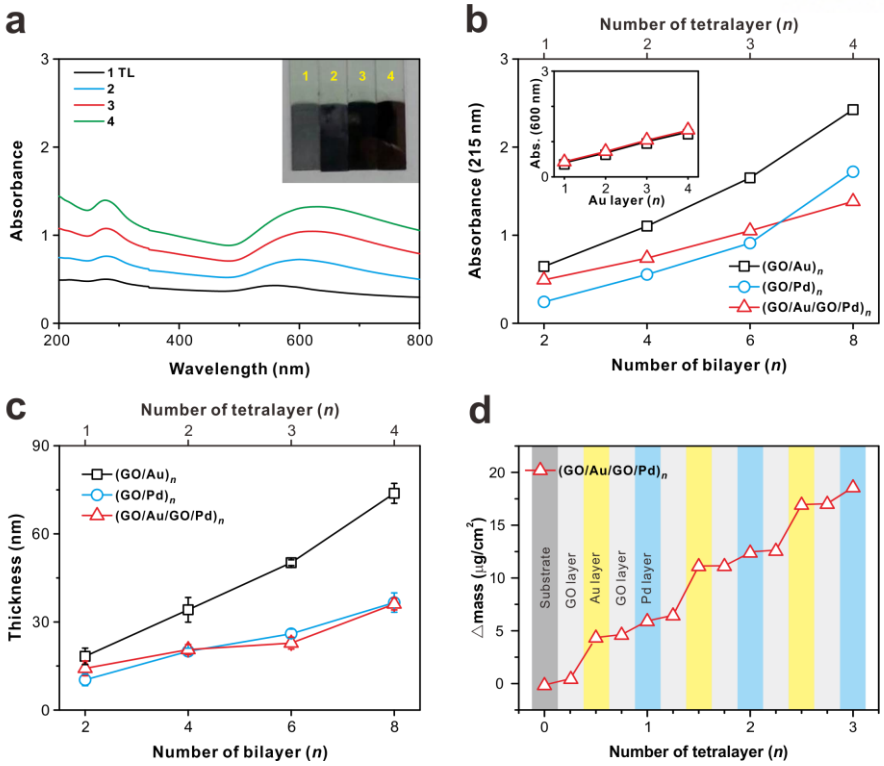

Figure. 3.1.4. Films growth characteristics of LbL assembled multilayer electrodes. (a) UV/vis absorbance spectra of $(GO/Au/GO/Pd)_n$ multilayer thin films. Inset image represents the samples prepared. (b) The corresponding absorbance maxima of multilayer films at 215 nm with $(GO/Au)_n$ and $(GO/Pd)_n$. Inset represents the corresponding absorbance maxima of multilayer films at 600 nm. (c) The thickness of each film measured by a surface profiler. (d) Mass change by QCM analysis as a function of the number of tetralayer of $(GO/Au/GO/Pd)_n$ multilayer thin films.

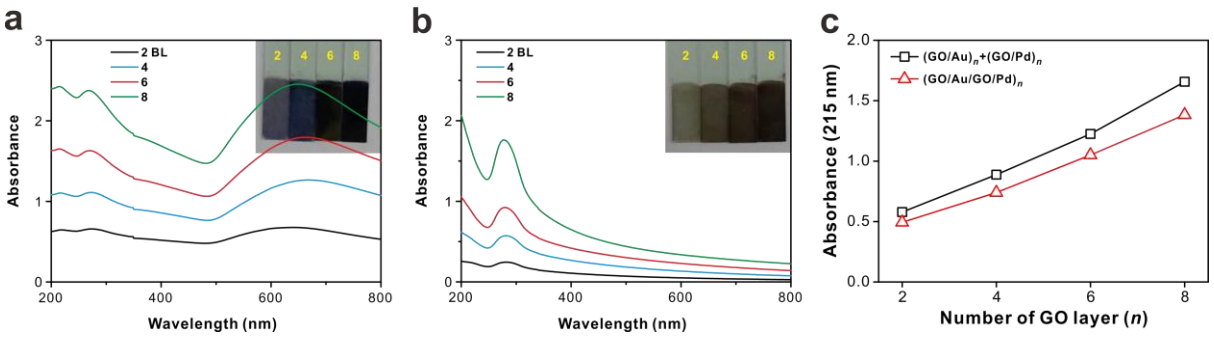

Figure 3.1.5. UV/vis absorbance spectra of (a) $(GO/Au)_n$ and (b) $(GO/Pd)_n$ multilayer thin films. (c) Comparison of absorbance of GO layer at 215 nm in (red triangle) bimetallic $(GO/Au/GO/Pd)_n$ multilayer and (black square) the sum of two individual monometallic $(GO/Au)_n$ and $(GO/Pd)_n$ multilayers.

3.1.4.2 Effect of co-assembly of Au and Pd NPs

As we found that the thermally treated multilayer films at 150 ºC exhibited superior electrocatalytic activity for methanol oxidation in our previous study, each multilayer film underwent the thermal reduction process before investigating the electrochemical characteristics. Thermal reduction not only restores the electrical conductivity of GO, but also eliminates the excess DMAP ligands, which would prevent the effective electrocatalytic reaction on the surfaces of Au and Pd NPs. However, the thermal treatment higher than 150 ºC for further reduction of GO did not improve the electrocatalytic activity toward the methanol oxidation significantly, suggesting the ligand mobility atop Au NPs is more critical in enhancing the overall electrocatalytic activity.[18]

The anodic peak potential of Pd NPs was observed at around 0 V and the current density of $(GO/Pd)_n$ multilayer films showed the highest value of 3.45 mA/cm^2 at 6 BL at 0.01 V which is approximately 6 times higher than that of $(GO/Au)_6$ multilayer films (0.54 mA/cm^2) (**Figure 3.1.6a**). This result indicates the methanol oxidation on Pd NPs is more effective than on Au NPs in alkaline electrolyte as known in the previous literatures.[36,37] It is of note that the peak current (i_p) increased gradually due to the increased concentration of active Pd NPs upon LbL assembly with electrochemical surface areas (ECSAs) (**Figure 3.1.7**), which then decreased after the 6 BL as similarly observed in $(GO/Au)_n$ multilayers.[18] The decreased peak current above 6 BL is explained due to the limited diffusion of methanol into the 3D electrode as related to the layered architecture of GO nanosheets. The barrier effect of 2D GO sheets in the multilayer film was demonstrated similarly in gas barrier film.[38]

To evaluate this commonly observed phenomenon in LbL electrode, logarithmic current with respect to various scan rates (v) was plotted to calculate an exponent of scan rate, which represents a transfer mechanism governed by a diffusion-limited mass transfer and a surface-confined charge transfer process (**Figure 3.1.8**).[39] In an ultrathin layer system where only adsorbed electroactive species react on the surface of film, the peak current (i_p) is given as follows in equation (3):

$$i_p = \frac{\alpha F^2 A v \Gamma_O^*}{2.718RT} \qquad (3)$$

where α is the transfer coefficient, F is the Faraday constant (C/mol), v is the scan rate (V/s), A is the area (cm^2), Γ_O^* is the amount of electroactive components (mol/cm^2), R is the ideal gas constant (J/K·mol), and T is the temperature (K). This relation reveals that the peak current density is directly proportional to v. As increasing the films thickness, however, the mass transfer from electrolyte becomes a limiting factor and the peak current (i_p) is given as follows in equation (4):

$$i_p = FAC_O^* D_O^{1/2} v^{1/2} \left(\frac{\alpha F}{RT}\right)^{1/2} \pi^{1/2} \chi(bt) \qquad (4)$$

where D_O is the diffusion coefficient (cm^2/s), $\chi(bt)$ is a function for the normalized current for irreversible system, and C_O^* is the bulk concentration of electroactive components (mol/cm^3). According to this relationship, the peak current is proportional to $v^{1/2}$. Based on these electrochemical kinetics on electrode, the slope was gradually decreased from 0.71 to 0.60 as increasing the number of bilayer, indicating electrochemical behavior in LbL assembled electrode changed from surface-confined to diffusion-limited process. In a separate study, Lutkenhaus group reported that the shift was caused by a transition from a surface-confined process to a diffusion-limited process within the LbL assembled electrode of polyaniline /vanadium pentoxide.[40] Eventually, a balance between mass and charge transfer at 6 BL was optimized, leading to the observed electrocatalytic behavior.

On the basis of maximum catalytic effect of monometallic system at 6 BL film through a fine balance between the methanol diffusion and electron transfer process, we evaluated the catalytic effect of bimetallic system, where both Au and Pd NPs are alternatively assembled within heterogeneous $(GO/Au/GO/Pd)_3$ films (**Figure 3.1.6b**). As a control, we also prepared individual $(GO/Au)_3$ and $(GO/Pd)_3$ monometallic electrodes. The successful fabrication of co-assembled bimetallic electrode was also monitored by the presence of respective Au 4f and Pd 3d signals in $(GO/Au/GO/Pd)_3$ films comparing to respective monometallic $(GO/Au)_3$ and $(GO/Pd)_3$ electrodes in high-resolution X-ray photoelectron spectroscopy (XPS) (**Figure 3.1.9**). To our surprise, the peak current (i_p) of co-assembled bimetallic $(GO/Au/GO/Pd)_3$ films at 0.34 V increased to 10.3 mA/cm^2, significantly higher than 0.20 mA/cm^2 and 1.22 mA/cm^2 of individual monometallic $(GO/Au)_3$ and $(GO/Pd)_3$ electrode, respectively. It is also of note that the co-assembled bimetallic $(GO/Au/GO/Pd)_3$ electrode exhibits three times higher peak current than that of $(GO/Pd)_6$ film even at a lower content of Pd NPs. This observation clearly suggests that there exists a synergistic effect on the enhancement of electrocatalytic effect within heterogeneous bimetallic 3D multilayer electrode. In addition, the electrocatalytic activity of $(GO/Au/GO/Pd)_3$ film did not alter when the sequence of layering is reversed as in $(GO/Pd/GO/Au)_3$ films (**Figure 3.1.10**).

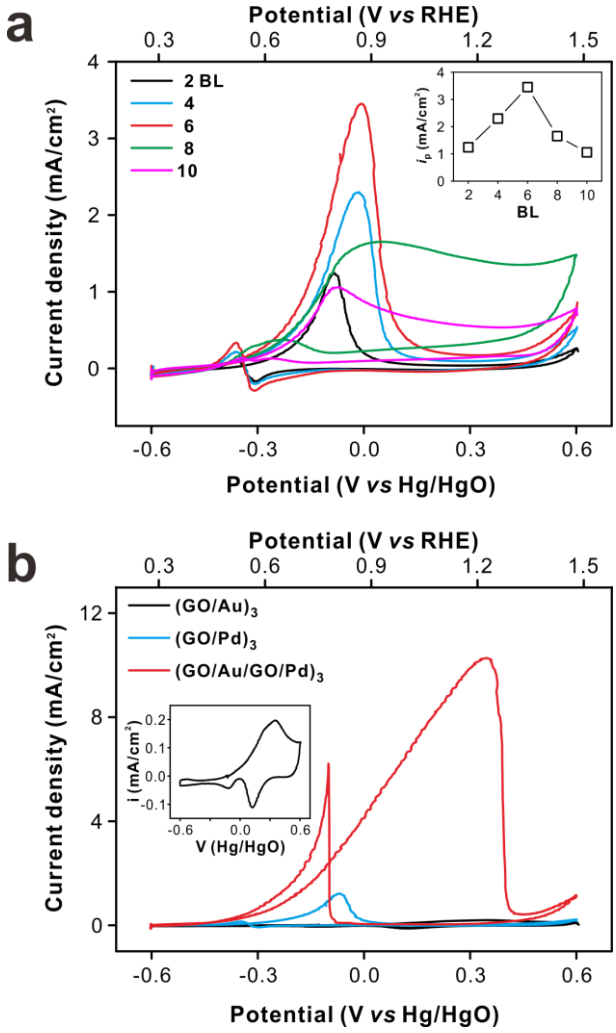

Figure 3.1.6. Catalytic effect for methanol oxidation reaction. Cyclic voltammograms (CVs) of (a) $(GO/Pd)_n$ multilayer thin films with an inset of the current density plot as a function of number of bilayer (BL) in $(GO/Pd)_n$ multilayer films. (b) Comparison of electrocatalytic activity of $(GO/Au)_3$, $(GO/Pd)_3$ and $(GO/Au/GO/Pd)_3$ films. Inset in Figure b shows a magnified CV of $(GO/Au)_3$. All measurements were performed in 0.10 M KOH with 1.0 M CH_3OH in a saturated N_2 at a scan rate of 20 mV s^{-1}.

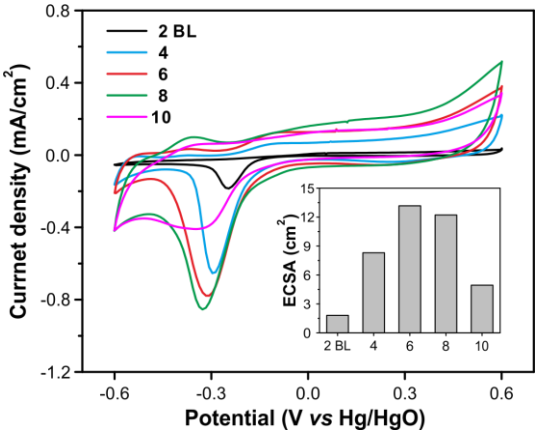

Figure 3.1.7. CV of $(GO/Pd)_n$ multilayer thin films (n = 2, 4, 6, 8 and 10) in 0.10 M KOH in a saturated N_2 at a scan rate of 20 mV s^{-1}. Inset shows corresponding electrochemical surface areas (ECSA) calculated by using following equation (1).

$$ECSA = \frac{\int IdV}{a \cdot v} \qquad (1)$$

where I is current (mA), V is the applied potential (V), integration is conducted from the reduction peaks of Pd NPs, v is a scan rate (V/s) and a is 0.424 mC/cm^2 for Pd NPs.

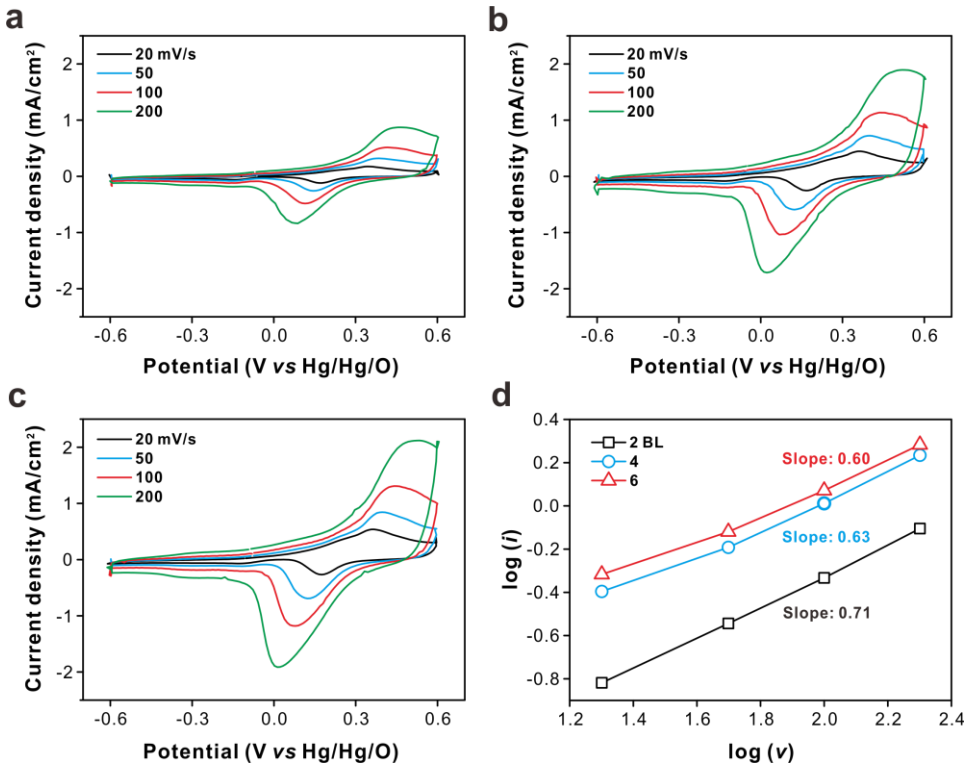

Figure 3.1.8. CV of $(GO/Au)_n$ multilayer thin films of (a) 2 BL, (b) 4 BL and (c) 6 BL in 0.10 M KOH and 1.0 M CH_3OH solution under a saturated N_2 at various scan rates. (d) Plots of log i_p vs log v to determine the reaction kinetics. The slope is reduced from 0.71 to 0.60 as the film thickness increases.

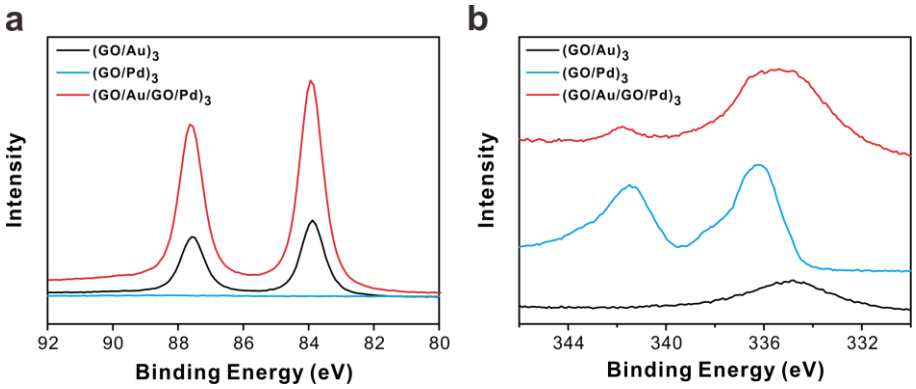

Figure 3.1.9. High-resolution XPS spectra of (a) Au 4f and (b) Au 4d and Pd 3d for $(GO/Au)_3$, $(GO/Pd)_3$ and $(GO/Au/GO/Pd)_3$ multilayer thin films.

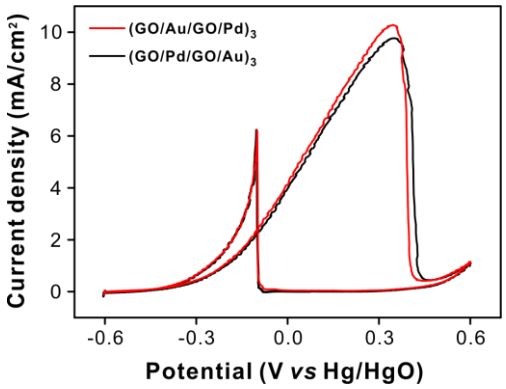

Figure 3.1.10. CV of bimetallic multilayer electrodes prepared under different sequence of layering. (red) $(GO/Au/GO/Pd)_3$ and (black) $(GO/Pd/GO/Au)_3$ in 0.10 M KOH and 1.0 M CH_3OH solution under a saturated N_2 at a scan rate of 20 mV s^{-1}.

Furthermore, as a long-term stability is a critical requirement in development of efficient electrocatalyst, we performed a stability test of $(GO/Au/GO/Pd)_3$ electrode through multiple electrocatalytic cycles (**Figure 3.1.11**). The anodic peak current continuously increased initially from first to 30^{th} cycles, which then followed by a slight decrease afterwards. The increase in initial cycling was due to full activation for diffusion of methanol molecules into undermost layer from interface of electrolyte and the 3D electrode, in accordance with other report employing porous graphene aerogel electrode.[41] Bimetallic $(GO/Au/GO/Pd)_3$ hybrid film exhibited a superior electrochemical stability over 100 cycles with a retention of 90%, owing to the stable graphene sheets support for electroactive metal NPs as well as the improved electron pathway within 3D interconnected LbL films. Another source of the improved cyclic stability is the interplay of Au and Pd NPs, as demonstrated in the poor cycle retention of only 5% of $(GO/Pd)_6$ film over 100 cycles. It is known that Au NP displays a poisoning tolerance for byproduct during MOR such as CO through further oxidation of the CO.[42,43] As a result, Au NPs can provide sites to Pd NPs for effective MOR by regenerating contaminated metal surface through CO removal.

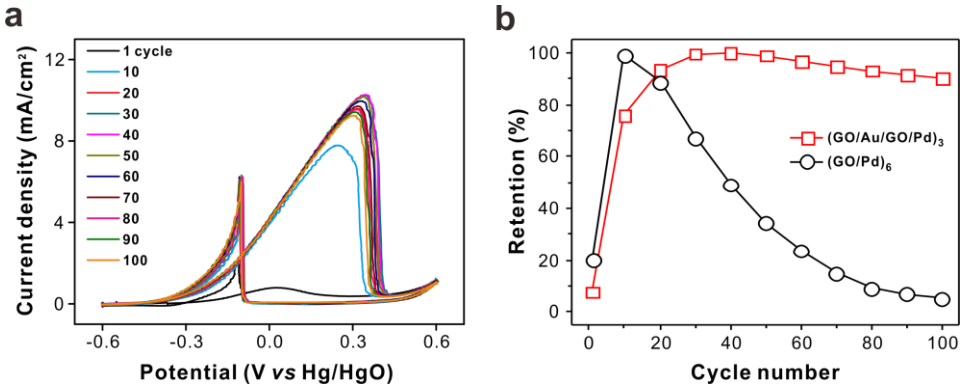

Figure 3.1.11. Stability test of bimetallic $(GO/Au/GO/Pd)_3$ thin film electrode through (a) CV and (b) corresponding cycle retention, comparing with monometallic $(GO/Pd)_6$ thin film for 100 cycles measured in 0.10 M KOH with 1.0 M CH_3OH in a saturated N_2 at a scan rate of 20 mV s^{-1}.

3.1.4.3 Effect of LbL architecture

Until now, we investigated highly improved catalytic effect by co-assembly with Au and Pd NPs and the conversion of electrochemical operating principles above certain layer thickness. We then examined the impact of the electrode architecture on the electrochemical behavior of hybrid films more in detail, such that the role of GO within the multilayer in controlling the diffusion pathways as well as the influence of relative position of metal NPs in terms of tailoring the electrochemical reactions because adsorbates such as methanol molecules from electrolyte are more accessible to surface of electrode. Thus, we fabricated three types of multilayer films using different sequence of layering to afford 3D hybrid electrodes of varying architecture (**Figure 3.1.12**): fully alternating Au and Pd NPs, $(GO/Au/GO/Pd)_3$, Pd layered on top of Au NPs, $(GO/Au)_3/(GO/Pd)_3$, and Au layered over Pd NPs, $(GO/Pd)_3/(GO/Au)_3$, respectively. The location of the NPs within the multilayer electrode was determined in consideration of balance between electrode (inner-layer) and electrolyte (outer-layer). In addition, all electrodes were fixed at 6 BL due to the optimized balance of mass and charge transfer as studied in a previous section. It is worth noting that the precision in engineering the architecture of electrode can be achieved simple by changing the sequence of the deposition steps during the assembly, highlighting the versatile nature of the LbL assembly in building the 3D electrode.

The successful fabrication of respective 3D electrodes is confirmed by cross-sectional high-resolution transmission electron microscopy (TEM) (**Figure 3.1.12**). The multilayer films of different architectures are clearly observed with the aid of the contrast difference between Au and Pd NPs (**Figure 3.1.3**). The junction between GO and NPs is also demonstrated with a distinct morphology of graphene sheet within the layers (**Figure 3.1.13**). Furthermore, the associated elemental information within the hybrid electrode was elucidated by high-angle annular dark field scanning transmission electron microscopy (HAADF-STEM). The HAADF-STEM images indicate the homogeneous lateral distribution of each corresponding element within LbL films. As shown in **Figure 3.1.12a**, Au and Pd NPs were distributed in the entire films of $(GO/Au/GO/Pd)_3$, whereas each NPs are localized in the respective position in the separated films of $(GO/Au)_3/(GO/Pd)_3$ and $(GO/Pd)_3/(GO/Au)_3$ (**Figure 3.1.12b,c**); however, it is also of note that the interlayer diffusion of the smaller Pd NPs within the multilayer is also observed as often demonstrated in some LbL systems.[44,45]

The analysis of the surfaces of each film also supports the hierarchically assembled films. According to the atomic force microscopy (AFM) images, surface root-mean-square roughness (R_{rms}) values (averaged over 10×10 μm^2) of $(GO/Au/GO/Pd)_3$, $(GO/Au)_3/(GO/Pd)_3$ and $(GO/Pd)_3/(GO/Au)_3$ films were determined to be 6.05, 5.31 and 9.48 nm, respectively (**Figure 3.1.14**). When Au NPs are deposited on outer-layers of films, the surface roughness increases because the size of Au NPs is larger than that of Pd NPs. In contrast, the films terminating with smaller sized Pd NPs display smoother morphology in general. Additionally, the scanning electron microscopy (SEM) images illustrate the successful deposition of Au and Pd NPs on top of the GO sheets (**Figure 3.1.15**).

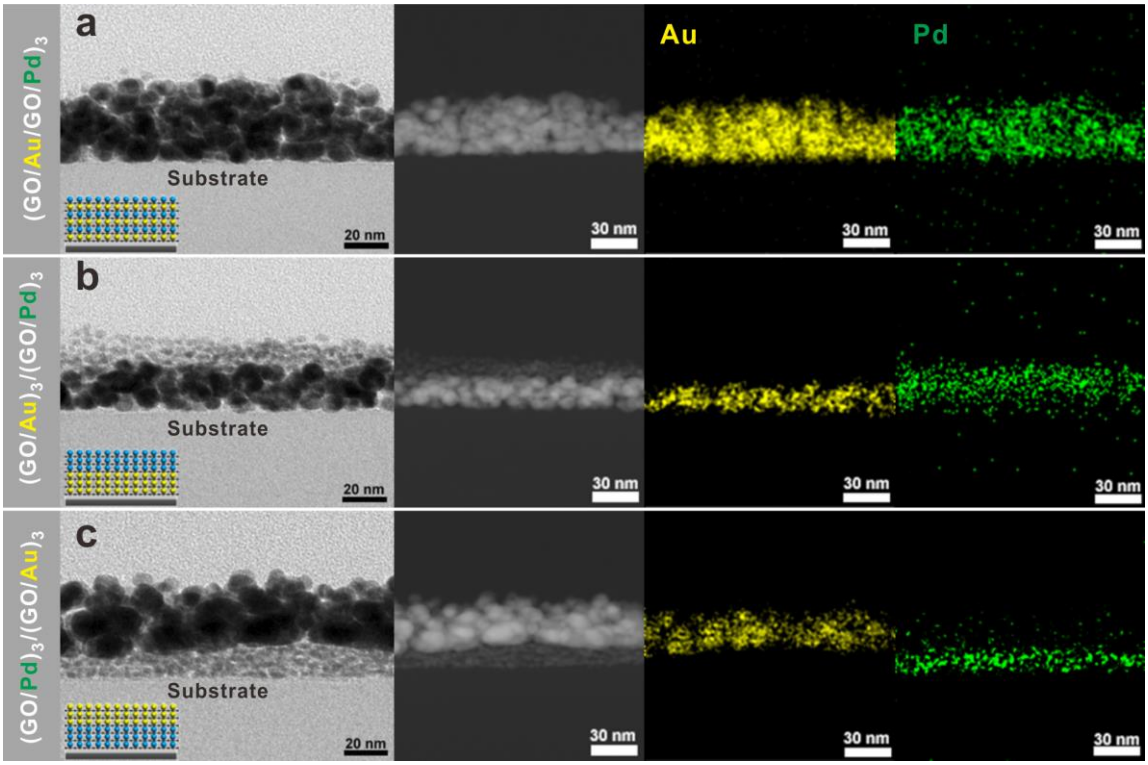

Figure 3.1.12. Architecture controlled multilayer thin films. Representative cross-sectional high-resolution TEM and HAADF-STEM images with composed elemental mapping images of Au and Pd of (a) $(GO/Au/GO/Pd)_3$, (b) $(GO/Au)_3/(GO/Pd)_3$ and (c) $(GO/Pd)_3/(GO/Au)_3$ multilayer thin films.

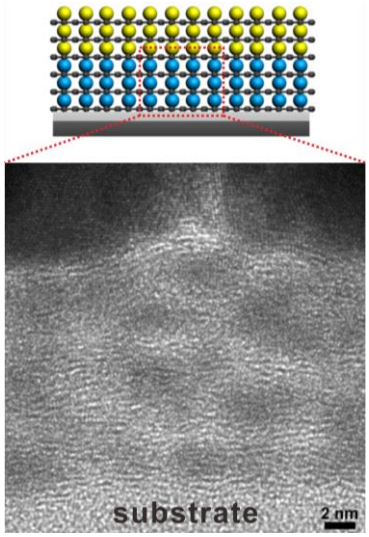

Figure 3.1.13. Representative cross-sectional high-resolution TEM of $(GO/Pd)_3/(GO/Au)_3$ multilayer thin film with a schematic illustration.

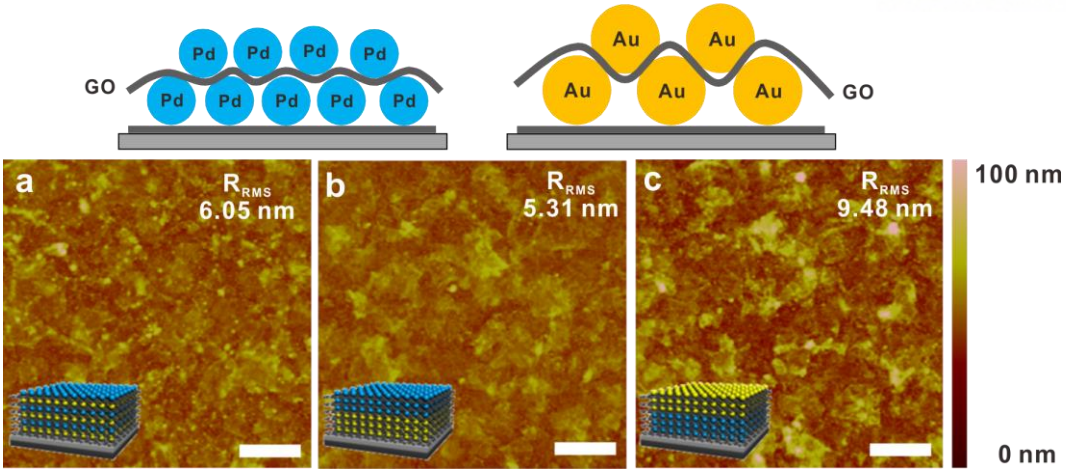

Figure 3.1.14. AFM images of (a) $(GO/Au/GO/Pd)_3$, (b) $(GO/Au)_3/(GO/Pd)_3$ and (c) $(GO/Pd)_3/(GO/Au)_3$ multilayer thin films with schematic illustrations. The scale bar of each image is 1.0 μm.

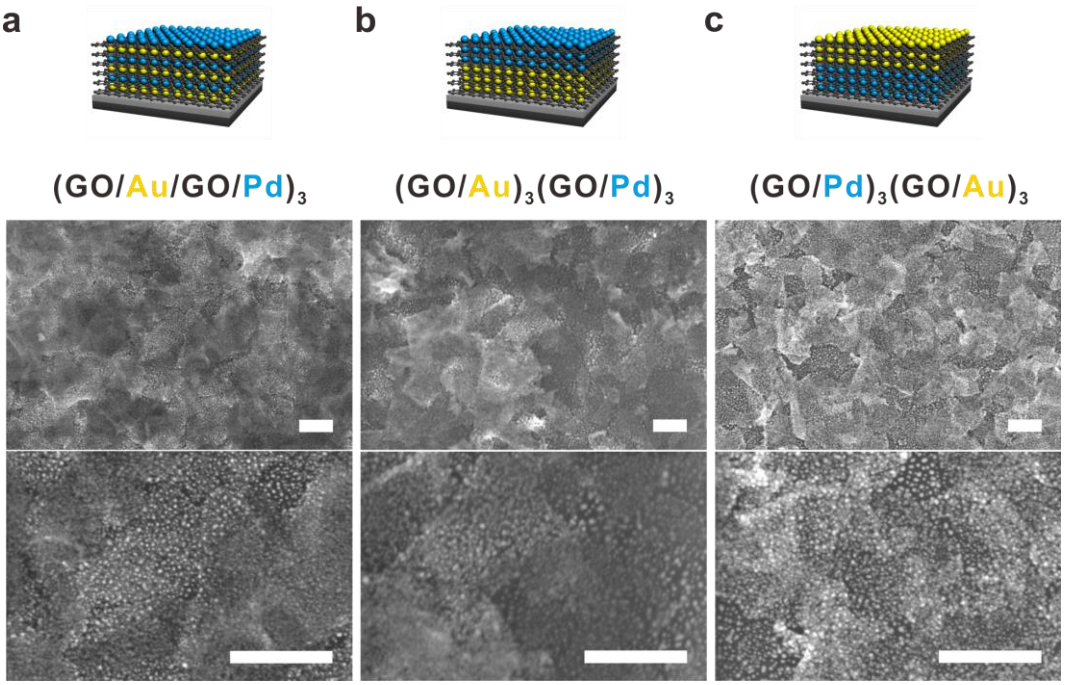

Figure 3.1.15. SEM images of (a) $(GO/Au/GO/Pd)_3$, (b) $(GO/Au)_3/(GO/Pd)_3$ and (c) $(GO/Pd)_3/(GO/Au)_3$ multilayer thin films with schematic illustrations. The scale bar of each image is 400 nm.

3.1.4.4 Electrocatalytic activity of hybrid LbL electrodes.

The electrochemical measurements were carried out to investigate the influence of electrode architecture on the electrochemical performance toward MOR. Besides the heterostructured $(GO/Au)_3/(GO/Pd)_3$, $(GO/Pd)_3/(GO/Au)_3$ and $(GO/Au/GO/Pd)_3$ multilayer films with different structures, respective homogeneous $(GO/Au)_3$ and $(GO/Pd)_3$ multilayers were assembled for comparison (**Figure 3.1.16a**). As shown in **Figure 3.1.6**, all of Au and Pd NPs co-assembled bimetallic electrodes showed remarkably increased peak current values comparing to control sets of monometallic $(GO/Au)_3$ and $(GO/Pd)_3$ multilayer films. However, most interestingly, there was a definite difference of electrochemical activity between hybrid films of opposite sequence of layering such as $(GO/Au)_3/(GO/Pd)_3$ and $(GO/Pd)_3/(GO/Au)_3$. For example, the anodic peak current of $(GO/Pd)_3/(GO/Au)_3$ (10.3 mA/cm^2) is approximately 1.7 times higher than that of $(GO/Au)_3/(GO/Pd)_3$ (5.9 mA/cm^2). This difference clearly demonstrates that the structural difference on 3D electrode significantly influences on the electrochemical catalytic effect by the surface reaction.

In order to elucidate the origin of this structural effect on the kinetics of heterogeneous multilayer films, the Tafel plot of each electrode was displayed (**Figure 3.1.16b**). The Tafel region of $(GO/Au)_n$ and $(GO/Pd)_n$, following a negligible mass transfer process, is limited by charge transfer for the dissociation of methanol by C-H bond breaking. This region has distinct linear ranges from 0 to 0.25 V (yellow region in **Figure 3.1.16b**) and from -0.35 to -0.10 V (blue region in **Figure 3.1.16b**) with a Tafel slope of 311 and 192 mV/dec, respectively. The lower Tafel slope of $(GO/Pd)_n$ indicates the faster kinetics than $(GO/Au)_n$ during MOR, resulting the higher anodic peak current in applied potential as shown in **Figure 3.1.6b**. The non-linear Tafel region in the potential range from 0 to 0.25 V of $(GO/Pd)_n$ films indicates that mass transfer limited system begins to dominate due to high overpotential to overcome the restricted charge transfer. In bimetallic electrode, therefore, each rate-determining step of MOR is overlapped between mass transfer limited system by $(GO/Pd)_n$ and charge transfer limited system by $(GO/Au)_n$ films in potential window from 0 to 0.25 V, and the whole kinetics of bimetallic multilayer films is affected as which metal NPs are outer-layered because of the concentration gradient of reactants in 3D electrode by different electrochemical kinetics. Generally, methanol oxidation is catalyzed on Au NPs with the adsorption of OH^- (OH^-_{ad}) in alkaline media by the following reactions (5), where the charge transfer coefficient λ varies between 0 and 1:[18]

$$Au + OH^- \rightarrow Au\text{-}OH_{ad}^{(1-\lambda)-} + \lambda e^-$$

$$CH_3OH + Au\text{-}OH_{ad}^{(1-\lambda)-} + 4OH^- \rightarrow Au + HCOO^- + 4H_2O + (4-\lambda)e^- \quad (5)$$

The formate species produced on Au NPs can then serve as a reactive intermediate on Pd NPs with the concomitant adsorption of formate ($HCOO^-_{ad}$) in alkaline media by following reactions (6):[36]

$$Pd + HCOO^- \rightarrow Pd\text{-}HCOO_{ad}^{(1-\lambda)-} + \lambda e^-$$

$$Pd\text{-}HCOO_{ad}^{(1-\lambda)-} + OH^- \rightarrow Pd + CO_2 + H_2O + (2-\lambda)e^- \quad (6)$$

In other words, Au NPs can supply additional reactant to Pd NPs, resulting in the enhanced mass transfer by alleviating the reactant depletion in 3D electrode. Therefore, when Au NPs are located in the outer-layer of hybrid films, such as $(GO/Pd)_3/(GO/Au)_3$, it displayed the higher current density by a larger overpotential applied until 0.4 V due to the enhanced mass transfer into inner-layered Pd NPs. On the other hand, when Pd NPs are located in outer-layer of multilayer film, such as $(GO/Au)_3/(GO/Pd)_3$, oxidation rate on Au NPs is limited by mass transfer due to methanol depletion via outer-layered Pd NPs although the current density was increased until 0.16 V by supplying a small amount of formate from inner-layered Au NPs (**Figure 3.1.17**).

The improved catalytic activity of the primary active metal Pd in the presence of adsorbed OH (OH_{ad}) on the secondary metal Au has been commonly explained by a bifunctional mechanism via the Langmuir-Hinshelwood (L-H) pathway (7):[42]

$$Pd + CH_3OH + 4OH^- \rightarrow Pd\text{-}CO_{ad} + 4H_2O + 4e^-$$

$$Pd\text{-}CO_{ad} + Au\text{-}OH_{ad} + OH^- \rightarrow Pd + Au + CO_2 + H_2O + e^- \quad (7)$$

It is recently reported that $Ni(OH)_2$ can facilitate the oxidative removal of carbonaceous poisons from adjacent Pt sites by supplying sufficient OH_{ad} through L-H pathway.[46] This bifunctional mechanism is attributed to the enhanced catalytic effect of partly contacted metals in our LbL bimetallic system; however, the enhanced mass transfer via the dual reaction pathway by both formate and CO as reactant is more considerable than the synergistic effect by bifunctional mechanism.

We calculated a αn (α is the transfer coefficient and n is the number of electrons) of each LbL assembled electrode to further demonstrate the competitive mass and charge transfer mechanism analysis in the potential range from 0 to 0.25 V.[47] Negative αn value out of the range of 0 to 1 suggests that it does not follow the charge transfer limited system any longer. In range of each charge transfer limited system, $(GO/Pd)_3$ film, showing a lower Tafel slope, has higher αn values from 0.25 to 0.40 (blue region in **Figure 3.1.16c**), while the $(GO/Au)_3$ films is lower in the range of 0.10 to 0.25 (yellow region in **Figure 3.1.16c**). This observation commonly indicates that the first charge transfer in MOR is the rate-determining step.[48,49] Interestingly, all bimetallic hybrid electrodes showed continuous αn in the entire potential ranges, indicating that electrochemical reaction kinetics on bimetallic electrode follows the kinetics of monometallic electrode at each potential range. As a result, competitive mass

and charge transfer between Pd and Au NPs in range from 0 to 0.25 V was determined mainly by outer-layered metal NPs interfacing with the electrolytes.

Another factor that can influence on the electrocatalytic effect of 3D electrode with varying architectures can be the interface between outermost layer and electrolyte due to the morphological difference in LbL films (**Figure 3.1.12**, **3.1.14** and **3.1.15**). The relatively rough surfaces in $(GO/Pd)_3/(GO/Au)_3$ multilayer not only provide more reaction sites of the electrode, but also enhance the mobility of methanol molecules into 3D electrode. To address the effect of morphological difference, electrochemical impedance spectroscopy (EIS) measurement was performed (**Figure 3.1.18**). The charge transfer resistance (R_{CT}) values ascribed to semicircle of Nyquist plot of $(GO/Au)_3/(GO/Pd)_3$, $(GO/Pd)_3/(GO/Au)_3$ and $(GO/Au/GO/Pd)_3$ multilayer films correspond to 5346, 3899 and 2534 Ω at 0.35 V, respectively. The surface roughness can also enhance the interactions between NPs within the multilayer and electrolyte, eventually leading to a decrease in the contact resistance, R_{CT}. In addition, the more increment of the contact layers between Au and Pd NPs within fully co-assembled $(GO/Au/GO/Pd)_3$ multilayer could be attributed to a lower R_{CT}.[50,51]

In order to further explore and feature the importance of LbL assembly in terms of controlling over the architecture of the electrode in achieving the best performance with a given set of component, we have fabricated co-assembled multilayers of Au and Pd NPs with GO in structures of $(GO/Au)_n/(GO/Pd)_{6-n}$ and $(GO/Pd)_n/(GO/Au)_{6-n}$ (n = 1, 3 and 5) (**Figure 3.1.16d**). In general, multilayers with outer Au NPs such as $(GO/Pd)_3/(GO/Au)_3$ and $(GO/Pd)_5/(GO/Au)_1$ showed a higher current density than those with outer-layered Pd NPs films with an exception of $(GO/Pd)_1/(GO/Au)_5$. The countertrend in $(GO/Pd)_1/(GO/Au)_5$ can also be speculated as follows: (i) the amount of single-layered Pd NPs as primary active sites than Au NPs is insufficient to the whole catalytic effect on LbL assembled 3D electrode; and (ii) the effect of outer-layered Pd NPs in direct contact with reactant methanol on topmost layer is more influential than that of aforementioned enhanced interaction in undermost layer by surface roughness of outer-layered Au NPs. Given the fact that the ECSA between same compositional films showed no significant difference (**Figure 3.1.19**), this result also supports our explanation of the architectural effect by the enhanced mass transfer of outer-layered Au NPs as well as morphological difference, which affords more preferential interaction of electrode surface from electrolyte.

Finally, **Figure 3.1.16e** and **Table 3.1.1** summarize the electrochemical performance of all multilayer films with varying architecture toward MOR in this study. In monometallic films, Pd multilayer films showed the better electrocatalytic activity than Au multilayer films and electrocatalytic activity also increased with an increase in the number of bilayers. In bimetallic films, the anodic peak current increased highly with increasing the ratio of Pd as primary active sites and layering Au in outer-region of 3D multilayer films by the enhanced mass transfer. As a result, the $(GO/Pd)_5/(GO/Au)_1$ film showed the highest specific current (1105.6 mA/mg), considering the active mass of metal NPs based

on QCM analysis as well as anodic peak current (12.4 mA/cm^2) than any of the other multilayer films although commercial Pd/C catalyst showed a similar current density of 12.3 mA/cm^2 at a low peak potential of 0.08 V (**Figure 3.1.20**). It is interesting that there is no distinct current density difference among bimetallic films at -0.07 V, which is a peak potential of $(GO/Pd)_3$ in spite of the enhanced catalytic activity than monometallic films, indicating the influential architecture effect in 3D electrode as well as synergetic effect of co-assembled Au and Pd NPs. It should be again emphasized that the highly tunable nature of LbL assembly only can afford the fabrication of the 3D electrode with an ultimate control over the structures to understand the electrochemical activity within the electrode and should be readily applied to the practical electrochemical electrodes.

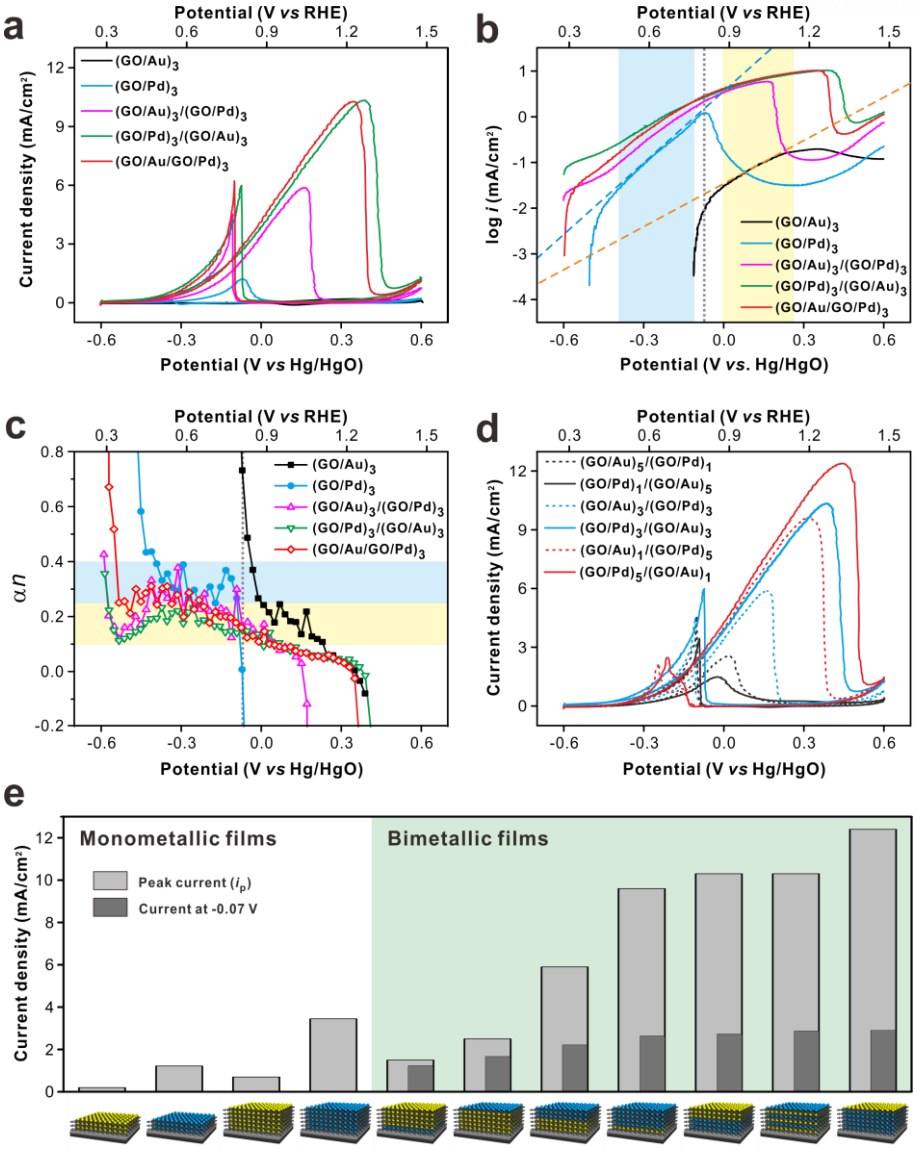

Figure 3.1.16. Architectural effect in 3D multilayer electrode for methanol oxidation. (a) Cyclic voltammograms, (b) corresponding Tafel plots and (c) calculated αn, product of transfer coefficient (α) and number of electrons (n) of $(GO/Au)_3$, $(GO/Pd)_3$, $(GO/Au)_3/(GO/Pd)_3$, $(GO/Pd)_3/(GO/Au)_3$ and $(GO/Au/GO/Pd)_3$ multilayer films. (d) Cyclic voltammograms of $(GO/Au)_n/(GO/Pd)_{6-n}$ (dotted line), $(GO/Pd)_n/(GO/Au)_{6-n}$ (solid line) multilayer thin films (n = 1, 3 and 5). (e) Comparison of electrochemical performance of all multilayer films with varying architecture toward MOR. Yellow and blue Tafel region corresponds to $(GO/Au)_n$ and $(GO/Pd)_n$, respectively. All measurements were measured in 0.10 M KOH with 1.0 M CH_3OH in a saturated N_2 at a scan rate of 20 mV s^{-1}.

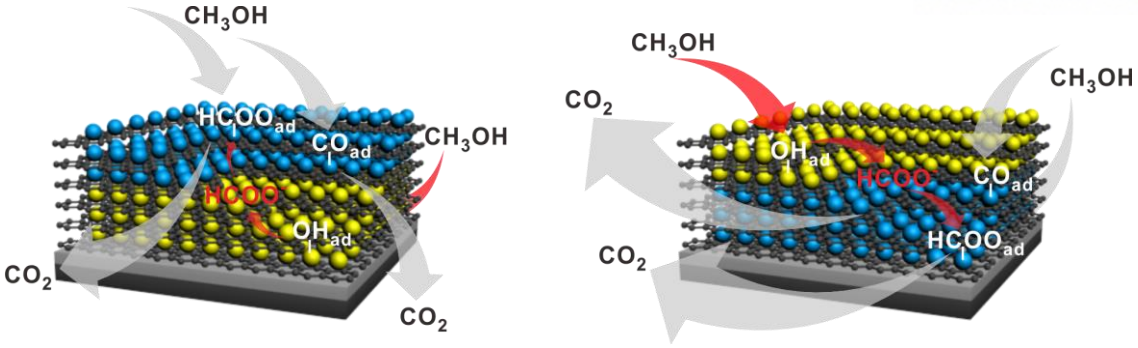

Figure 3.1.17. Schematic representation of a controllable electrochemical mechanism between mass and charge transfer. Red and gray arrows indicate the diffusion flows on Au and Pd NPs, respectively in LbL assembled $(GO/Au)_3/(GO/Pd)_3$ and $(GO/Pd)_3/(GO/Au)_3$ multilayer thin films.

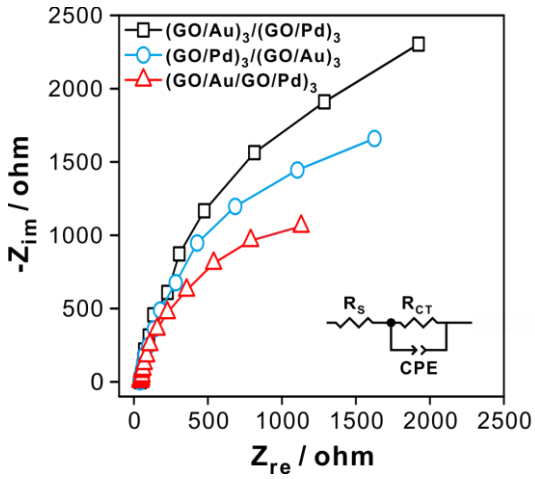

Figure 3.1.18. Nyquist plots of impedance on $(GO/Au/GO/Pd)_3$, $(GO/Au)_3/(GO/Pd)_3$, and $(GO/Pd)_3/(GO/Au)_3$ multilayer thin films at 0.35 V. Inset represents an equivalent circuit.

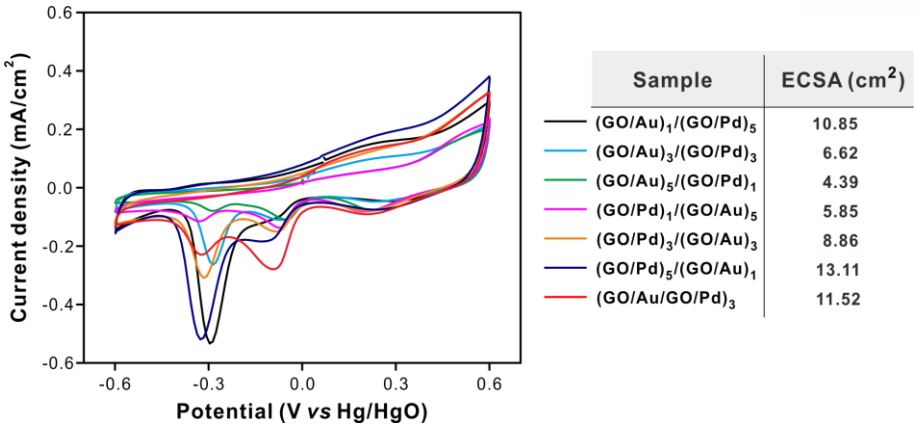

Figure 3.1.19. CV of $(GO/Au/GO/Pd)_3$, $(GO/Au)_n/(GO/Pd)_{6-n}$, $(GO/Pd)_n/(GO/Au)_{6-n}$ multilayer thin films (n = 1, 3 and 5) in 0.10 M KOH in a saturated N_2 at a scan rate of 20 mV s^{-1}. CV curves were selected at the 5th scan of voltammetry. The ECSAs were calculated by using following equation (8).

$$ECSA = \frac{\int IdV}{a_{Pd} \cdot v} + \frac{\int IdV}{a_{Au} \cdot v} \qquad (8)$$

where I is current (mA), V is the applied potential (V), integration is conducted from the reduction peaks of Pd NPs and Au NPs at around -0.3 V and -0.1 V, respectively, v is a scan rate (V/s) and a is 0.424 mC/cm^2 and 0.386 mC/cm^2 for Pd NPs and Au NPs, respectively.

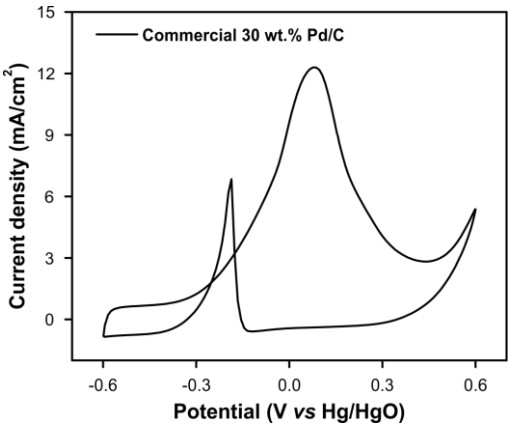

Figure 3.1.20. CV of commercial 30 wt.% Pd/C in 0.10 M KOH with 1.0 M CH_3OH in a saturated N_2 at a scan rate of 20 mV s^{-1}.

Table 3.1.1. Summary of electrocatalytic properties of all samples in this study.

	Anodic peak potential (V)	**Anodic peak current (mA/cm^2)**	**Specific current (mA/mg)**	**I_f/I_b**	**Cycle retention (%)**
$(GO/Au/GO/Pd)_3$	0.34	10.3	601.8	1.60	90
$(GO/Au)_1/(GO/Pd)_5$	0.32	9.6	859.2	4.57	85
$(GO/Au)_3/(GO/Pd)_3$	0.16	5.9	344.2	1.31	91
$(GO/Au)_5/(GO/Pd)_1$	0.02	2.5	110.9	0.54	44
$(GO/Pd)_1/(GO/Au)_5$	-0.02	1.5	64.5	0.44	76
$(GO/Pd)_3/(GO/Au)_3$	0.40	10.3	605.3	1.70	95
$(GO/Pd)_5/(GO/Au)_1$	0.45	12.4	1105.6	5.17	85

Cycle retention was calculated by anodic peak current for 100 cycles divided by anodic maximum peak current. Anodic peak current in the forward scan (I_f) is associated with a process by the oxidation of freshly chemisorbed species coming from methanol adsorption, while that in backward scan (I_b) is related to the removal of the incompletely oxidized carbonaceous species formed during the forward scan. The larger value of ratio of I_f to I_b (I_f/I_b) implies the relatively predominant tolerance towards poisoning species and has been used as an indicator for the assessment of the electrocatalytic behavior of NPs toward MOR. The I_f/I_b values were proportional to the ratio of Pd to Au NPs, indicating Au NPs generated more incompletely oxidized carbonaceous species during MOR than Pd NPs although Au NPs enhance the activity and CO poisoning tolerance. This ratio also affects to the stability of the multilayers toward MOR as evidenced in $(GO/Au)_5/(GO/Pd)_1$ and $(GO/Pd)_1/(GO/Au)_5$ films with a relatively low cycle retention of 44% and 76%, respectively. As a result, the relative ratio of Au NPs and Pd NPs is a critical parameter to the bimetallic heterogeneous catalytic system.

3.1.5 Conclusion

In conclusion, we presented electrocatalytic thin films for methanol oxidation by adjusting the assembly sequence of LbL films. This 3D electrode prepared by the LbL assembly offers precise control not only over the thickness, but also the catalytic effect by changing the number of bilayers with two different NP catalysts on graphene supports. As a result, the heterogeneous $(GO/Au/GO/Pd)_n$ multilayers showed the highly enhanced catalytic effect for MOR than homogeneous $(GO/Au)_n$ and $(GO/Pd)_n$ multilayers because of not only the synergetic effect between Au and Pd NPs with the graphene sheets support, but also the oxidative removal effect of poisons on Pd NPs by neighboring Au NPs. Furthermore, owing to the tunable transition of thin firms from surface confined to diffusion limited process, LbL assembled electrode could provide a study model of mass and charge transfer system with respect to electrochemistry. The structural difference of Au and Pd NPs within the relative position of multilayer electrode affords highly tunable electrocatalytic activity, and thus confirming a novel versatility of LbL assembly to tailor the nanoarchitecture of hybrid electrodes.

3.1.6 References

(1) Turner, J. A. Realizable Renewable Energy Future. *Science* **1999,** *285*, 687-689.

(2) Chu, S.; Majumdar, A. Opportunities and Challenges for a Sustainable Energy Future. *Nature* **2012,** *488*, 294-303.

(3) Larcher, D.; Tarascon, J. M. Towards Greener and More Sustainable Batteries for Electrical Energy Storage. *Nat. Chem.* **2015,** *7*, 19-29.

(4) Ariga, K.; Ji, Q.M.; Nakanishi, W. ; Hill, J.P.; Aono, M. Nanoarchitectonics: a New Materials Horizon for Nanotechnology. *Mater. Horiz.* **2015**, *2* 406–413.

(5) Abe, H.; Liu, J.; Ariga, K. Catalytic Nanoarchitectonics for Environmentally Compatible Energy Generation. *Mater. Today* **2016**, *19*, 12–18.

(6) Richardson, J. J.; Bjoernmalm, M.; Caruso, F. Technology-Driven Layer-by-Layer Assembly of Nanofilms. *Science* **2015,** *348*, aaa2491.

(7) Decher, G. Fuzzy Nanoassemblies: Toward Layered Polymeric Multicomposites. *Science* **1997,** *277*, 1232-1237.

(8) Hammond, P. T. Form and Function in Multilayer Assembly: New Applications at the Nanoscale. *Adv. Mater.* **2004,** *16*, 1271-1293.

(9) Jiang, C. Y.; Tsukruk, V. V. Freestanding Nanostructures via Layer-by-Layer Assembly. *Adv. Mater.* **2006,** *18*, 829-840.

(10) Ariga, K.; Li, J. B.; Fei, J. B.; Ji, Q. M.; Hill, J. P. Nanoarchitectonics for Dynamic Functional Materials from Atomic-/Molecular-Level Manipulation to Macroscopic Action. *Adv. Mater.* **2016,** *28*, 1251-1286.

(11) Quinn, J. F.; Johnston, A. P. R.; Such, G. K.; Zelikin, A. N.; Caruso, F. Next Generation, Sequentially Assembled Ultrathin Films: Beyond Electrostatics. *Chem. Soc. Rev.* **2007,** *36*, 707-718.

(12) Kharlampieva, E.; Kozlovskaya, V.; Sukhishvili, S. A. Layer-by-Layer Hydrogen-Bonded Polymer Films: From Fundamentals to Applications. *Adv. Mater.* **2009,** *21*, 3053-3065.

(13) Kovtyukhova, N. I.; Ollivier, P. J.; Martin, B. R.; Mallouk, T. E.; Chizhik, S. A.; Buzaneva, E. V.; Gorchinskiy, A. D. Layer-by-Layer Assembly of Ultrathin Composite Films from Micron-Sized Graphite Oxide Sheets and Polycations. *Chem. Mater.* **1999,** *11*, 771-778.

(14) Li, H.; Pang, S.; Wu, S.; Feng, X.; Muellen, K.; Bubeck, C. Layer-by-Layer Assembly and UV Photoreduction of Graphene-Polyoxometalate Composite Films for Electronics. *J. Am. Chem. Soc.* **2011,** *133*, 9423-9429.

(15) Jo, K.; Gu, M.; Kim, B.-S. Ultrathin Supercapacitor Electrode Based on Reduced Graphene Oxide Nanosheets Assembled with Photo-Cross-Linkable Polymer: Conversion of Electrochemical Kinetics in Ultrathin Films. *Chem. Mater.* **2015,** *27*, 7982-7989.

(16) Yang, M.; Hou, Y.; Kotov, N. A. Graphene-Based Multilayers: Critical Evaluation of Materials Assembly Techniques. *Nano Today* **2012,** *7*, 430-447.

(17) Rydzek, G.; Ji, Q.; Li, M.; Schaaf, P.; Hill, J. P.; Boulmedais, F.; Ariga, K. Electrochemical Nanoarchitectonics and Layer-by-Layer Assembly: From Basics to Future. *Nano Today* **2015,** *10*, 138-167.

(18) Choi, Y.; Gu, M.; Park, J.; Song, H.-K.; Kim, B.-S. Graphene Multilayer Supported Gold Nanoparticles for Efficient Electrocatalysts Toward Methanol Oxidation. *Adv. Energy Mater.* **2012,** *2*, 1510-1518.

(19) Chen, Y.H.; Chen, T.; Dai, L. Layer-by-Layer Growth of $CH_3NH_3PbI_{3-x}Cl_x$ for Highly Efficient Planar Heterojunction Perovskite Solar Cells. *Adv. Mater.* **2015**, *27*, 1053–1059.

(20) Lee, T.; Yun, T.; Park, B.; Sharma, B.; Song, H.-K.; Kim, B.-S. Hybrid Multilayer Thin Film Supercapacitor of Graphene Nanosheets with Polyaniline: Importance of Establishing Intimate Electronic Contact through Nanoscale Blending. *J. Mater. Chem.* **2012,** *22*, 21092-21099.

(21) Gu, M.; Lee, J.; Kim, Y.; Kim, J. S.; Jang, B. Y.; Lee, K. T.; Kim, B.-S. Inhibiting the Shuttle Effect in Lithium-Sulfur Batteries using a Layer-by-Layer Assembled Ion-Permselective Separator. *RSC Adv.* **2014,** *4*, 46940-46946.

(22) Hong, T.-K.; Lee, D. W.; Choi, H. J.; Shin, H. S.; Kim, B.-S. Transparent, Flexible Conducting Hybrid Multilayer Thin Films of Multiwalled Carbon Nanotubes with Graphene Nanosheets. *ACS Nano* **2010,** *4*, 3861-3868.

(23) Kim, B.-S.; Lee, S. W.; Yoon, H.; Strano, M. S.; Shao-Horn, Y.; Hammond, P. T. Pattern Transfer Printing of Multiwalled Carbon Nanotube Multilayers and Application in Biosensors. *Chem. Mater.* **2010,** *22*, 4791-4797.

(24) Hong, J.; Char, K.; Kim, B.-S. Hollow Capsules of Reduced Graphene Oxide Nanosheets Assembled on a Sacrificial Colloidal Particle. *J. Phys. Chem. Lett.* **2010,** *1*, 3442-3445.

(25) Lee, D. W.; Hong, T.-K.; Kang, D.; Lee, J.; Heo, M.; Kim, J. Y.; Kim, B.-S.; Shin, H. S. Highly Controllable Transparent and Conducting Thin Films using Layer-by-Layer Assembly of Oppositely Charged Reduced Graphene Oxides. *J. Mater. Chem.* **2011,** *21*, 3438-3442.

(26) Yang, S. H.; Lee, T.; Seo, E.; Ko, E. H.; Choi, I. S.; Kim, B.-S. Interfacing Living Yeast Cells with Graphene Oxide Nanosheaths. *Macromol. Biosci.* **2012,** *12*, 61-66.

(27) Hwang, H.; Joo, P.; Kang, M. S.; Ahn, G.; Han, J. T.; Kim, B.-S.; Cho, J. H. Highly Tunable Charge Transport in Layer-by-Layer Assembled Graphene Transistors. *ACS Nano* **2012,** *6*, 2432-2440.

(28) Joo, P.; Kim, B. J.; Jeon, E. K.; Cho, J. H.; Kim, B.-S. Optical Switching of the Dirac Point in Graphene Multilayer Field-Effect Transistors Functionalized with Spiropyran. *Chem. Comm.* **2012,** *48*, 10978-10980.

(29) Kim, S.-M.; Joo, P.; Ahn, G.; Cho, I. H.; Kim, D. H.; Song, W. K.; Kim, B.-S.; Yoon, M.-H. Transparent Conducting Films Based on Reduced Graphene Oxide Multilayers for Biocompatible Neuronal Interfaces. *J. Biomed. Nanotechnol.* **2013,** *9*, 403-408.

(30) Jung, Y. K.; Lee, T.; Shin, E.; Kim, B.-S. Highly Tunable Aptasensing Microarrays with Graphene

Oxide Multilayers. *Sci. Rep.* **2013,** *3*, 3367.

(31) Lee, T.; Min, S. H.; Gu, M.; Jung, Y. K.; Lee, W.; Lee, J. U.; Seong, D. G.; Kim, B.-S. Layer-by-Layer Assembly for Graphene-Based Multi layer Nanocomposites: Synthesis and Applications. *Chem. Mater.* **2015,** *27*, 3785-3796.

(32) Onda, M.; Lvov, Y.; Ariga, K.; Kunitake, T. Sequential Reaction and Product Separation on Molecular Films of Glucoamylase and Glucose Oxidase Assembled on and Ultrafilter. *J. Ferment. Bioeng.* **1996,** *82*, 502-506.

(33) Hummers, W. S.; Offeman, R. E. Preparation of Graphitic Oxide. *J. Am. Chem. Soc.* **1958,** *80*, 1339-1339.

(34) Jo, K.; Lee, T.; Choi, H. J.; Park, J. H.; Lee, D. J.; Lee, D. W.; Kim, B.-S. Stable Aqueous Dispersion of Reduced Graphene Nanosheets via Non-Covalent Functionalization with Conducting Polymers and Application in Transparent Electrodes. *Langmuir* **2011,** *27*, 2014-2018.

(35) Gittins, D. I.; Caruso, F. Spontaneous Phase Transfer of Nanoparticulate Metals from Organic to Aqueous Media. *Angew. Chem. Int. Ed.* **2001,** *40*, 3001-3004.

(36) Yang, Y.-Y.; Ren, J.; Zhang, H.-X.; Zhou, Z.-Y.; Sun, S.-G.; Cai, W.-B. Infrared Spectroelectrochemical Study of Dissociation and Oxidation of Methanol at a Palladium Electrode in Alkaline Solution. *Langmuir* **2013,** *29*, 1709-1716.

(37) Gao, F.; Goodman, D. W. Pd-Au Bimetallic Catalysts: Understanding Alloy Effects from Planar Models and Supported Nanoparticles. *Chem. Soc. Rev.* **2012,** *41*, 8009-8020.

(38) Yang, Y.-H.; Bolling, L.; Priolo, M. A.; Grunlan, J. C. Super Gas Barrier and Selectivity of Graphene Oxide-Polymer Multilayer Thin Films. *Adv. Mater.* **2013,** *25*, 503-508.

(39) Bard, A. J.; Faulkner, L. R., *Electrochemical Methods Fundamentals and Applications*. 2nd ed.; John Wiley & Sons: New York, 2000.

(40) Shao, L.; Jeon, J. W.; Lutkenhaus, J. L. Polyaniline/Vanadium Pentoxide Layer-by-Layer Electrodes for Energy Storage. *Chem. Mater.* **2012,** *24*, 181-189.

(41) Tsang, C.-H. A.; Hui, K. N.; Hui, K. S.; Ren, L. Deposition of Pd/Graphene Aerogel on Nickel Foam as a Binder-Free Electrode for Direct Electro-oxidation of Methanol and Ethanol. *J. Mater. Chem. A* **2014,** *2*, 17986-17993.

(42) Wang, X.; Tang, B.; Huang, X.; Ma, Y.; Zhang, Z. High Activity of Novel Nanoporous Pd-Au Catalyst for Methanol Electro-oxidation in Alkaline Media. *J. Alloys Compd.* **2013,** *565*, 120-126.

(43) Rodriguez, P.; Kwon, Y.; Koper, M. T. M. The Promoting Effect of Adsorbed Carbon Monoxide on the Oxidation of Alcohols on a Gold Catalyst. *Nat. Chem.* **2012,** *4*, 177-182.

(44) Lavalle, P.; Voegel, J. C.; Vautier, D.; Senger, B.; Schaaf, P.; Ball, V. Dynamic Aspects of Films Prepared by a Sequential Deposition of Species: Perspectives for Smart and Responsive Materials. *Adv. Mater.* **2011,** *23*, 1191-1221.

(45) Picart, C.; Mutterer, J.; Richert, L.; Luo, Y.; Prestwich, G. D.; Schaaf, P.; Voegel, J. C.; Lavalle, P.

Molecular Basis for the Explanation of the Exponential Growth of Polyelectrolyte Multilayers. *Proc. Natl. Acad. Sci. U. S. A.* **2002,** *99*, 12531-12535.

(46) Huang, W.; Wang, H.; Zhou, J.; Wang, J.; Duchesne, P. N.; Muir, D.; Zhang, P.; Han, N.; Zhao, F.; Zeng, M.; Zhong, J.; Jin, C.; Li, Y.; Lee, S.-T.; Dai, H. Highly Active and Durable Methanol Oxidation Electrocatalyst Based on the Synergy of Platinum-Nickel Hydroxide-Graphene. *Nat. Commun.* **2015,** *6*, 10035.

(47) Mustain, W. E.; Prakash, J. Kinetics and Mechanism for the Oxygen Reduction Reaction on Polycrystalline Cobalt-Palladium Electrocatalysts in Acid Media. *J. Power Sources* **2007,** *170*, 28-37.

(48) Kowal, A.; Li, M.; Shao, M.; Sasaki, K.; Vukmirovic, M. B.; Zhang, J.; Marinkovic, N. S.; Liu, P.; Frenkel, A. I.; Adzic, R. R. Ternary Pt/Rh/SnO_2 Electrocatalysts for Oxidizing Ethanol to CO_2. *Nat. Mater.* **2009,** *8*, 325-330.

(49) Luo, J.; Njoki, P. N.; Lin, Y.; Mott, D.; Wang, L. Y.; Zhong, C. J. Characterization of Carbon-Supported AuPt Nanoparticles for Electrocatalytic Methanol Oxidation Reaction. *Langmuir* **2006,** *22*, 2892-2898.

(50) Xiao, F.-X.; Miao, J.; Liu, B. Layer-by-Layer Self-Assembly of CdS Quantum Dots/Graphene Nanosheets Hybrid Films for Photoelectrochemical and Photocatalytic Applications. *J. Am. Chem. Soc.* **2014,** *136*, 1559-1569.

(51) Wang, H.; Ishihara, S.; Ariga, K.; Yamauchi, Y. All-Metal Layer-by-Layer Films: Bimetallic Alternate Layers with Accessible Mesopores for Enhanced Electrocatalysis. *J. Am. Chem. Soc.* **2012,** *134*, 10819-10821.

3.2 Diffusion Controlled Nanoelectrode via Sized Graphene Oxide Nanosheets

3.2.1 Abstract

Controlling the architecture of hybrid nanomaterial electrodes is critical for understanding their fundamental electrochemical mechanisms and applying these materials in future energy conversion and storage systems. Herein, we report highly tunable electrocatalytic multilayer electrodes, composed of palladium nanoparticles (Pd NPs) supported by graphene sheets of varying lateral size, employing a versatile layer-by-layer (LbL) assembly method. We demonstrate that the electrocatalytic activity is highly tunable through control of the diffusion and electron pathways within the 3-dimensional multilayer electrodes. A larger-sized-graphene-supported electrode exhibited its maximum performance with a thinner film, due to facile charge transfer by the mass transfer limited in early stage, while a smaller-sized-graphene-supported electrode exhibited its highest current density with higher mass loading in the thicker films by enabling facile mass transfer through increased diffusion pathways. These findings of tortuous-path effect on electrocatalytic electrode supported by varying sized graphene provides new insights and a novel design principle in electrode engineering that will be beneficial for the development of effective electrocatalysts.

3.2.2 Introduction

The rapidly approaching energy crisis necessitates efficient conversion and storage technologies for sustainable and renewable energy to diminish the current environmental concerns that are growing unabated.[1] In this regard, energy devices with superior performance have been developed such as fuel cells, metal-air batteries, and water electrolyzers, all of which use highly efficient and cost-effective electrocatalysts during electrochemical operation.[2-5] Thus, there has been significant progresses in the development of various electrocatalysts such as novel metal nanoparticles (NPs) and carbon-based nanomaterials.[5,6] These active materials are generally applied in the form of composites combined with conductive supports and binders to compensate for their drawbacks such as volume expansion, low electrical conductivity, and poor cycling performance. Catalytic supports are critical in the performance of electrocatalysts and, consequently, there are continuing efforts to develop effective conductive supports.[7, 8]

Graphene oxide (GO), a chemically exfoliated graphene analogue, serves as a unique electrocatalytic support with its large surface area, chemical functionality, and remarkable mechanical/chemical stability.[9-11] Owing to the atomically thin 2-dimensional (2D) sheet structure of GO, significant efforts have been devoted to enhancing the catalytic performance of various electroactive nanomaterials, such as metals, metal oxides, and semiconductors, on the surface of GO.[12-14] Furthermore, the importance of controlling the GO sheet size has recently been illustrated by their size-dependent electrochemical activity; for example, the Li group demonstrated that the large size of chemically synthesized graphene quantum dots showed the increased electrocatalytic activity toward the oxygen reduction reaction.[15] Conversely, the Chen group reported that using smaller GO sheets improved the heterogeneous electron transfer kinetics in the reduction of redox probes within electrode, which was correlated with an increased defect density in smaller GO sheets.[16] Consequently, using GO nanosheets with a well-defined lateral size is important when utilizing GO electrode materials in electrochemical reactions. However, as-synthesized GO products often have a wide size distribution due to the uncontrolled breakage of large sheets into small sheets during the oxidation and exfoliation processes. There are outstanding contributions to controlling the size fractionation of GO nanosheets that exploit differences in the molecular weight and charge density between GO nanosheets of different sizes using methods such as centrifugation, pH-assisted sedimentation, and dispersibility in polar solvents.[16-19]

Utilizing electrode fabrication techniques that allow nanoscale blending of materials is also important when investigating the nanoscopic electrochemical activity of graphene-supported hybrid nanomaterials. This is in contrast to bulk graphene composites that are traditionally prepared by a simple mixing process. Layer-by-layer (LbL) assembly is one of the most versatile tools used to assemble multifunctional nanoscale materials with nanoscale control over their composition and structure.[20-23] Generally, LbL-assembled films are formed by depositing alternating layers of oppositely charged

materials. Due to its simplicity and versatility as a method, LbL-assembled thin films have been examined for various energy conversion and storage devices.[11, 24-29] For example, the Shao-Horn and Lutkenhaus groups independently showed the tunable electrocatalytic activity of LbL-assembled electrodes, emphasizing the excellent charge-storage capability of carbon nanotubes and GO nanosheets.[30, 31] Interestingly, these studies indicate that the electrochemical activity can be tuned by varying the number of bilayers (i.e. thickness). This phenomenon is attributed to the balance between electron transfer into the inner electrode surface and ionic transport from the electrolyte that are restricted with increasing multilayer film thickness.[32] In another notable example, our group found that the performance of graphene-supported metal NPs-based electrocatalysts exhibited the maximum performance at a specific thickness and optimized layer sequence within the multilayer electrodes.[33, 34] Although there are some examples, including our own efforts, demonstrating the electrocatalytic performance of the 3D multilayer electrodes, there are few researches achieving such fine control over the electrocatalytic be-havior simply by changing the dimension of the individu-al components with unraveling the underlying electro-chemical mechanism between mass and charge transfer thus far.

Herein, we report the fabrication of elaborately designed electrodes using an LbL assembly method that enables control over the internal electrode structure and mass-transfer pathways by varying the size of the GO building blocks. Specifically, to investigate the influence of controlled diffusion pathways within the 3D LbL-assembled electrodes on their electrocatalytic activity, we prepared three GO suspensions with different GO sheet size distributions and assembled them with Pd NPs to fabricate hybrid electrocatalytic electrodes. We then used the methanol oxidation reaction (MOR) as a model reaction to investigate their activity (**Figure 3.2.1**). The electrocatalytic activity toward the MOR is highly affected by the balance between the mass-transfer pathway and charge transfer within the electrode, which varies with the GO sheet dimensions. This interesting model system offers a unique opportunity to understand the fundamental electrochemical mechanisms of hybrid multilayer electrodes composed of identical components, which is vital for designing high-performance electrocatalysts.

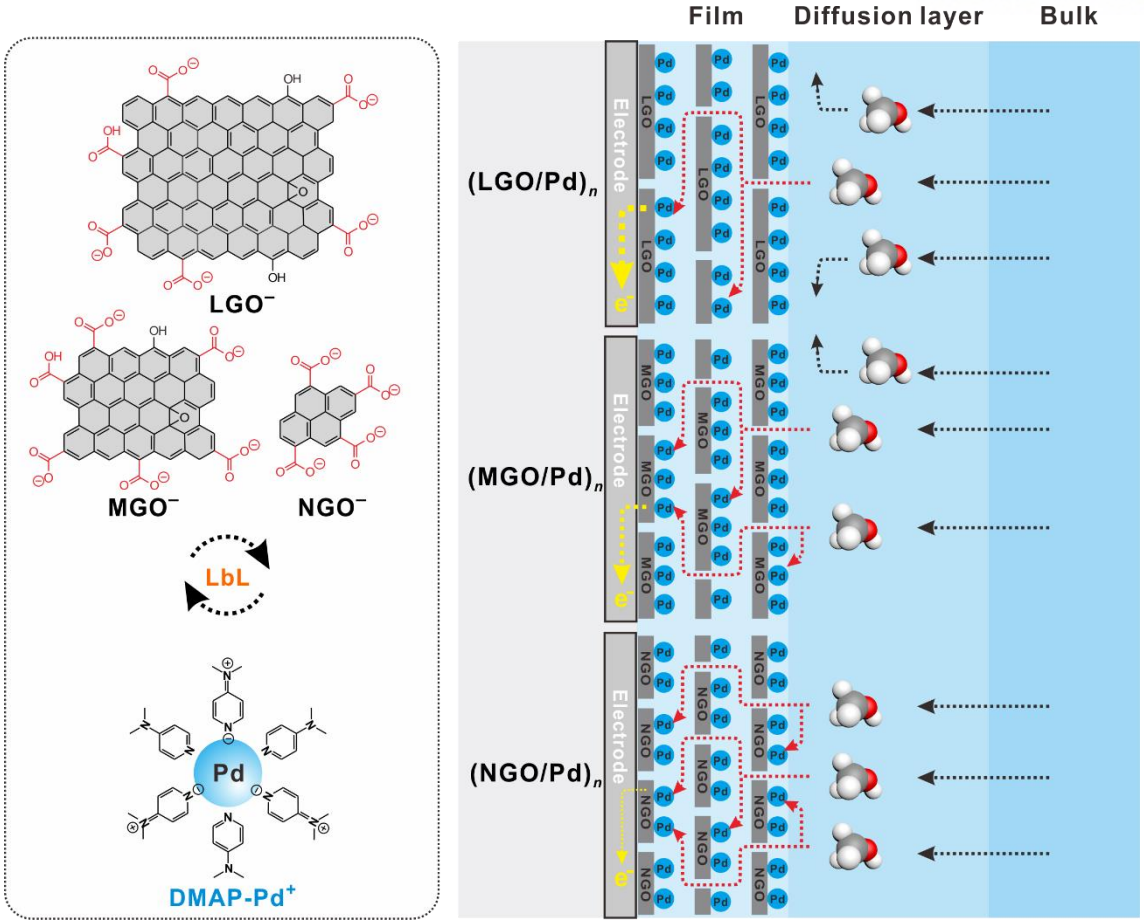

Figure 3.2.1. Schematic representation of layer-by-layer (LbL)-assembled $(GO/Pd)_n$ multilayer thin film electrodes with varying GO sheet size (LGO, MGO, and NGO) toward methanol oxidation reaction in bulk electrolyte solution. The black and red dotted arrows indicate the diffusion of methanol molecules in electrolyte and the 3D LbL electrodes, respectively. The yellow arrows indicate the charge transfer from the 3D LbL electrodes.

3.2.3 Experimental

3.2.3.1 Preparation of LGO.

Graphite oxide was synthesized from graphite powder by modified Hummers method and exfoliated to give a brown dispersion of LGO under homogenizer (WiseTis, HG-15D) at a concentration of 0.50 mg/mL.[35,36]

3.2.3.2 Preparation of MGO.

Graphite oxide was exfoliated under ultrasonication (Sonics & Materials Inc., VC 750) at a concentration of 0.50 mg/mL.[37]

3.2.3.3 Preparation of NGO.

NGO was synthesized from graphite nanofibers (Catalytic Materials, United States) according to a literature method under ultrasonication at a concentration of 0.50 mg/mL.[38]

3.2.3.4 Preparation of Pd NPs.

The 4-(dimethylamino)pyridine (DMAP)-stabilized Pd NPs were prepared by using the spontaneous phase transfer from organic solvent according to a literature method.[39]

3.2.3.5 LbL of hybrid electrode films.

ITO-coated glass substrate was cleaned by sonication in deionized (DI) water, acetone and ethanol for 10 min. Silicon and quartz substrates were cleaned by piranha solution to remove any organic contamination and subsequently treated with (3-aminopropyl)triethoxysilane to introduce positively charged hydrophilic surface. These substrates were first dipped into negatively charged GO solution (0.50 mg/mL) at pH 4 for 10 min. It was then dipped into DI water for 1 min three times to remove loosely bound GO. Subsequently, the substrate was then dipped into positively charged DMAP-coated Pd NPs suspension at pH 11 for 10 min, and washed with DI water three times for 1 min, which afforded one-bilayer film of $(GO/Pd)_1$, respectively. The above procedures were repeated to achieve the desired number of bilayers (BLs, *n*).

3.2.3.6 Electrochemical analysis.

As-assembled multilayer films were subjected to thermal reduction process at 150 ºC for 12 h in an oven before investigating the electrochemical properties. Electrochemical experiments were performed using a standard three electrode cell configuration (Biologic Science Instrument, VSP). A platinum wire was used as a counter electrode and Hg/HgO as a reference. The working electrode was multilayer thin film assembled on ITO-coated glass. Cyclic voltammetry (CV) was performed between -0.60 to 0.60 V in 0.10 M KOH solution with 1.0 M methanol solution at room temperature in a saturated

N_2 at a scan rate of 20 mV/s. Electrochemical impedance spectroscopy (EIS) measurements were carried out in the frequency range from 100 kHz to 50 mHz under AC stimulus of 10 mV in amplitude. Chronoamperometry (CA) was measured at 0 V in N_2 saturated 0.10 M KOH with 1.0 M CH_3OH.

3.2.3.7 Characterizations.

FT-IR (Varian, 670-IR) and Raman spectroscopy (WITec, alpha300R) were used to determine the chemical structure of varying GO sheets. The size and morphology of the prepared NPs were measured by transmission electron microscopy (Normal-TEM, JEOL, JEM-2100, accelerating voltage of 200 kV). The absorbance of the thin films was characterized by using UV/vis spectroscopy (Varian, Cary 5000). The thickness of the as-prepared samples on silicon substrates was measured by surface profiler (Veeco, Dektak 150). The surface morphology of the samples was investigated using scanning electron microscopy (Cold FE-SEM, Hitachi, S-4800) and atomic force microscopy (AFM, Veeco, Dimension D3100) via a tapping mode. The active mass of each material adsorbed onto the film surface was analyzed by a quartz crystal microbalance (QCM, Stanford Research System, QCM200), using the following Sauerbrey equation (1, 2):

$$\Delta F(\mathrm{Hz}) = -\frac{2F_o^2}{A\sqrt{\rho_q \mu_q}}\Delta m \quad (1)$$

$$\Delta F(\mathrm{Hz}) = -56.6 \times \Delta m \quad (2)$$

where ΔF is the resonant frequency change (Hz), Δm is the mass change per unit area of the quartz crystal (μg/cm^2), F_o (5 MHz) is the fundamental resonance frequency of the crystal, A is the area of the Au-Cr electrode, ρ_q (2.65 g/cm^{-3}) is the density of quartz crystal and μ_q (2.95×10^{11} g/cm·s^2) is the shear modulus.

3.2.4 Results and Discussion

Highly stable aqueous GO suspensions and electrocatalytic Pd NPs are prerequisites for fabricating 3D LbL multilayer electrodes based on electrostatic interactions. In order to prepare GO suspensions of varying size, graphite powder was initially oxidized according to the modified Hummers method to obtain graphite oxide, which contains various chemical functional groups such as carboxyl acid, hydroxyl, and epoxide groups.[35, 36] We then utilized two different exfoliation methods using homogenizer and ultrasonication to prepare GO suspensions with different size distributions. Homogenizer was used as a mild exfoliation method to produce a lower-defect GO by shear stress, resulting in a suspension of large-sized graphene sheets (LGO), while medium-sized GO sheets (MGO) were prepared using ultrasonication, which tears the graphene sheets and introduces more damages.[37] In addition, we prepared nanosized graphene sheets (NGO) according to a literature method using exfoliation from a graphite nanofiber precursor, which has smaller carbon domains than conventional graphite powder.[38]

The successful synthesis of the three GO sheet suspensions was confirmed by atomic force microscopy (AFM) and Fourier-transform infrared (FT-IR) spectroscopy measurements. Representative AFM images revealed that all of the GO suspensions were mainly comprised of single-layer GO sheets, with a thickness of ~1.4 nm (**Figure 3.2.2**). Each GO suspension exhibited a distinct lateral-size distribution, with average dimensions of 52.61 ± 50.88, 0.57 ± 0.22, and $0.38 \times 10^{-3} \pm 0.17 \times 10^{-3}$ μm^2 for LGO, MGO, and NGO, respectively. This indicates that using the different exfoliation processes and precursors was successful in controlling the GO sheet size.

FT-IR spectroscopy was employed to characterize the chemical functionalities present in LGO, MGO, and NGO (**Figure 3.2.3**). All three GO products showed the carbonyl-stretching vibration peaks associated with carboxylic acid (COOH, at 1722 cm^{-1}) and carboxylate groups (COO$^-$, at 1600 cm^{-1}). The relative fraction of carboxylate to carboxylic acid at pH 4 was determined to be 0.75, 1.20, and 3.86 for LGO, MGO, and NGO, respectively. This indicates that the ionization of the GO sheets is significantly affected by the density of chemical functional groups on the GO sheets due to the structural difference induced by the number of defects within the GO sheets.

Raman spectroscopy analysis was used to further investigate the structural differences between the three GO products (**Figure 3.2.4**). Generally, GO displays two prominent peaks at 1344 and 1601 cm^{-1}, which corresponded to the symmetry A_{1g} mode of the D band and the E_{2g} mode of the sp^2 carbon atoms of the G band, respectively.[40] It is well established that the D band corresponds to structural defects, amorphous structures, or edges that break the sp^2-carbon-lattice symmetry, while the G band is associated with graphitic sp^2-carbon domains. A strong D-band intensity indicates a high defect density and the presence of edge functional groups in GO. The D-to-G-band intensity ratio (I_D/I_G) was 0.99, 1.04, and 1.09 for LGO, MGO, and NGO, respectively, suggesting that the sp^2-carbon structure becomes more damaged with decreasing GO sheet dimensions.

In parallel, a positively charged Pd NP suspension was prepared based on the spontaneous phase transfer of organic-soluble Pd NPs into an aqueous phase using 4-(dimethylamino)pyridine (DMAP), a readily available organic ligand that affords the necessary stability in aqueous solutions.[40] The resulting DMAP-coated Pd NPs had an average diameter of 3.4 ± 0.5 nm (**Figure 3.2.5**).

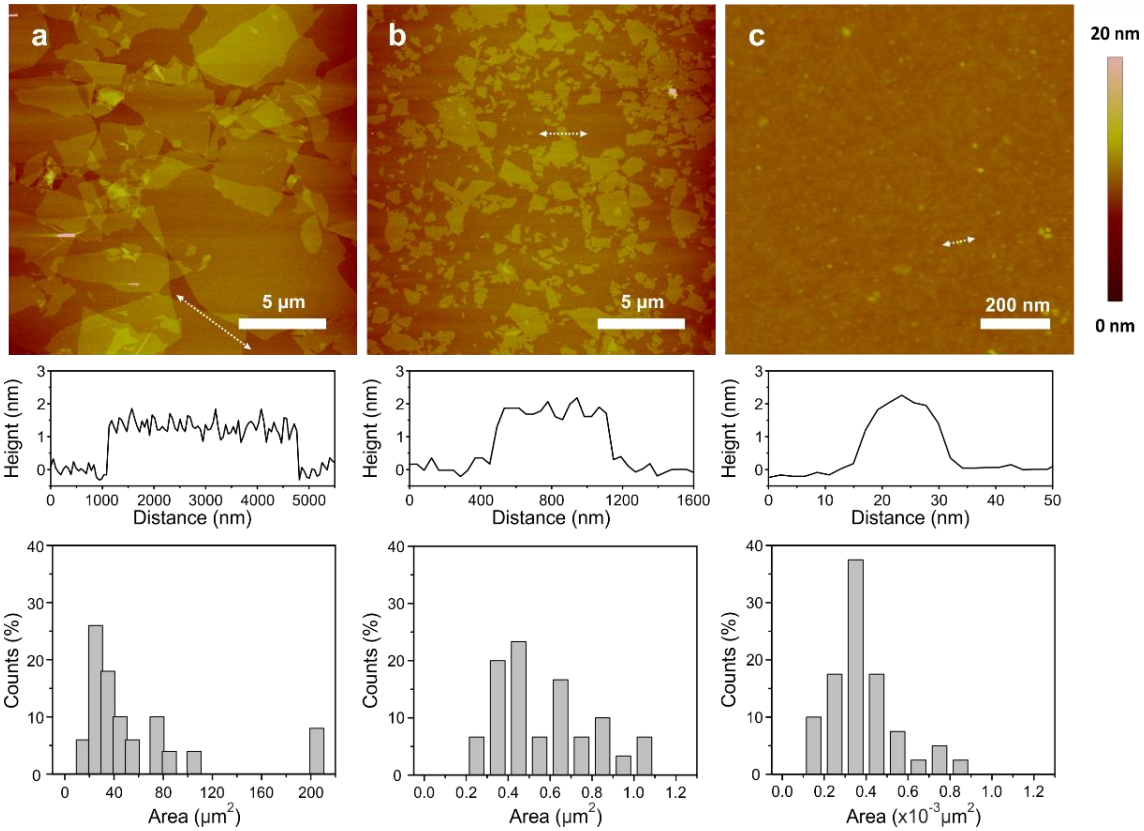

Figure 3.2.2. Representative AFM images of (a) LGO, (b) MGO, and (c) NGO sheets with corresponding line scan profiles and size distribution histograms. The average values were collected over 40 samples.

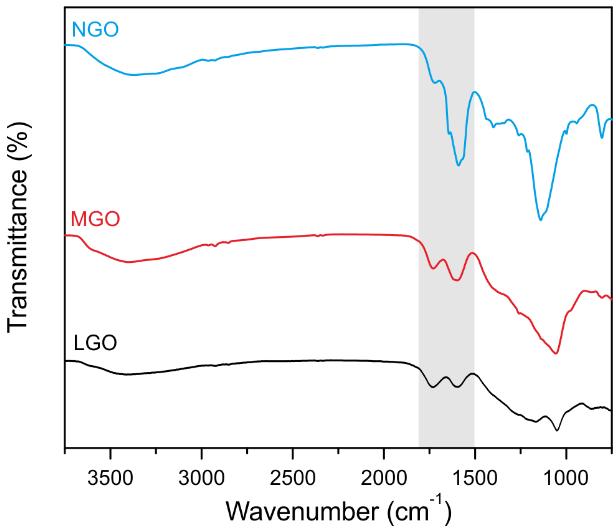

Figure 3.2.3. FT-IR spectra of LGO, MGO, and NGO sheets.

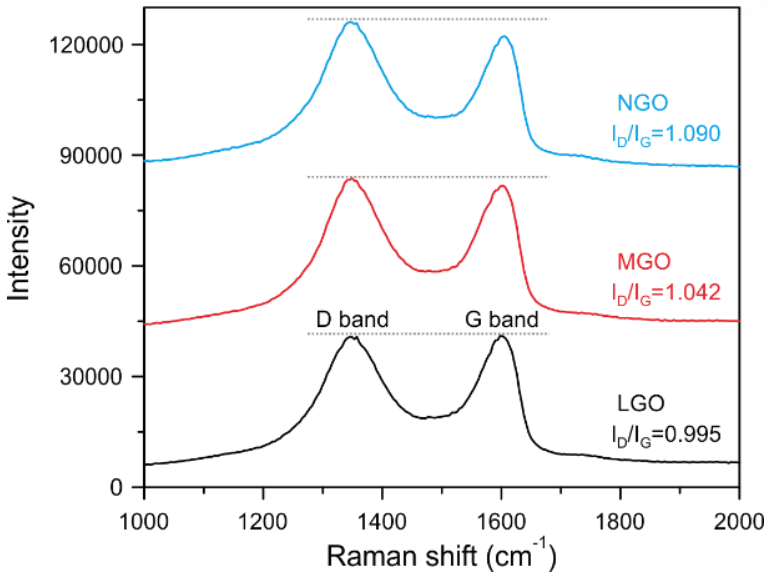

Figure 3.2.4. Raman spectra of LGO, MGO, and NGO sheets.

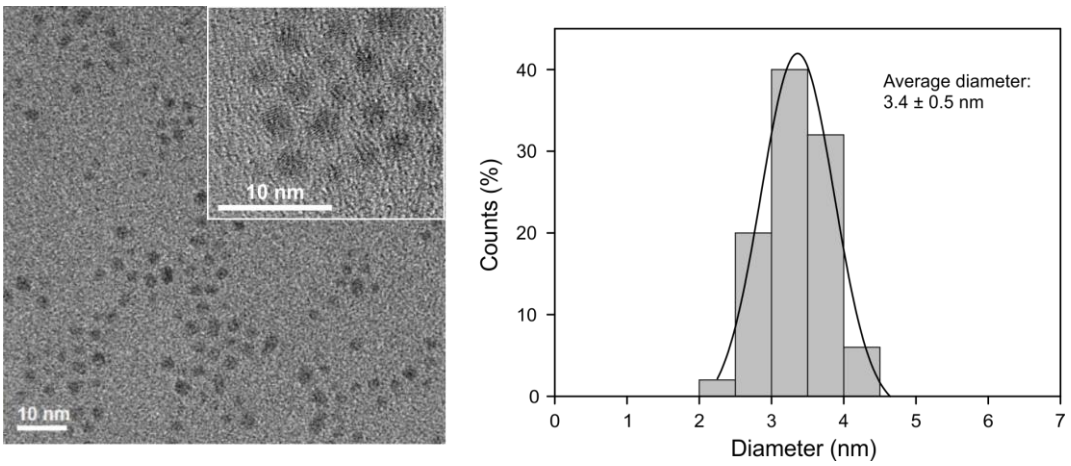

Figure 3.2.5. TEM images with a corresponding size distribution histogram of DMAP-Pd NPs suspension.

With these stable suspensions of the positively charged Pd NPs (ζ-potential of +35 mV) as electroactive species and the negatively charged GO suspension (ζ-potential of −40 mV) as a stable catalytic support, we fabricated three types of multilayer electrodes by LbL assembly using LGO, MGO, and NGO. The resulting multilayer architectures were denoted $(LGO/Pd)_n$, $(MGO/Pd)_n$, and $(NGO/Pd)_n$, where n is the number of GO/Pd bilayers (BLs, typically 2−10). UV/vis spectroscopy was used to monitor the successful growth of each multilayer (**Figure 3.2.6a** and **3.2.7**). The absorbance gradually increased with increasing number of layers, indicating the successful assembly of GO-supported-Pd NPs multilayer electrodes. Moreover, the linear growth of the characteristic GO absorbance peak at 215 nm clearly demonstrated the uniform formation of multilayers with respect to the number of BLs. The corresponding thickness of each multilayer film grew linearly with the number of BLs and the average bilayer thickness was 8.5, 8.5, and 10.1 nm for a single bilayer of $(LGO/Pd)_n$, $(MGO/Pd)_n$, and $(NGO/Pd)_n$, respectively (**Figure 3.2.6b**). These similar film thicknesses are attributed to the well-exfoliated nature of the single-layer GO regardless of the sheet size. It should be noted that the internal architecture of the hybrid electrodes could be controlled precisely by the LbL assembly method with high accuracy.

We further analyzed the sequential adsorption behavior of GO and Pd NPs in each multilayer electrode using a quartz crystal microbalance (QCM). **Figure 3.2.6c** shows the stepwise measurement of the mass deposited after each layer, which quantifies the amount of each component in the multilayer structure. The adsorption of Pd NPs was greater than that of the GO sheets, with the relative mass ratio of GO to Pd NPs within each multilayer found to be 0.146, 0.219, and 0.341 on the surface of LGO, MGO, and NGO, respectively (**Figure 3.2.6d**). This could be attributed to decreasing GO sheet density per single-layer unit area with decreasing GO sheet size. In addition, we calculated the volumetric mass of Pd NPs within each multilayer based on the film thickness determined. The volumetric mass of Pd NPs within each layer decreased from 1.89 to 1.45 as the GO sheet size decreased from LGO to NGO, indicating a change in the 3D multilayer electrode morphology from relatively densely packed films to porous films.

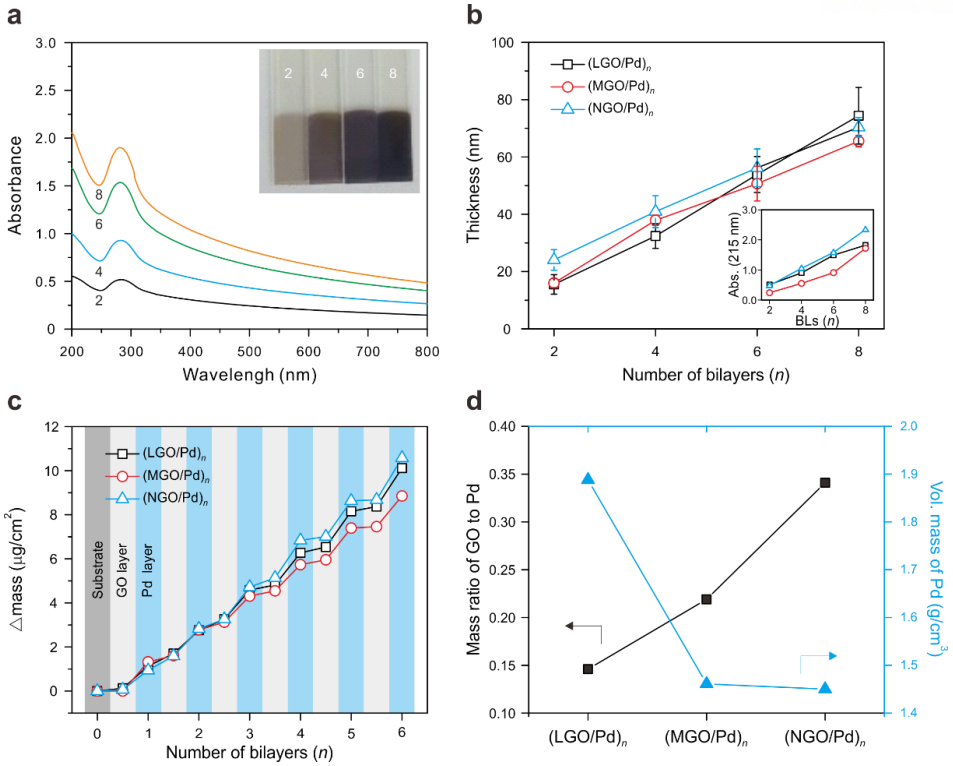

Figure 3.2.6. (a) UV/vis absorbance spectra of representative $(LGO/Pd)_n$ multilayer thin films. The inset image shows the samples prepared with the corresponding number of bilayers (BLs, *n*). (b) Film thickness measured by surface profiler and (c) quartz crystal microbalance (QCM) analysis of all multilayer thin film electrodes as a function of the number of BLs (*n*). The inset in Figure b shows the corresponding UV/vis absorbance maxima at 215 nm for all multilayer electrodes. (d) Mass ratio of GO to Pd and volumetric mass of Pd in each multilayer thin film.

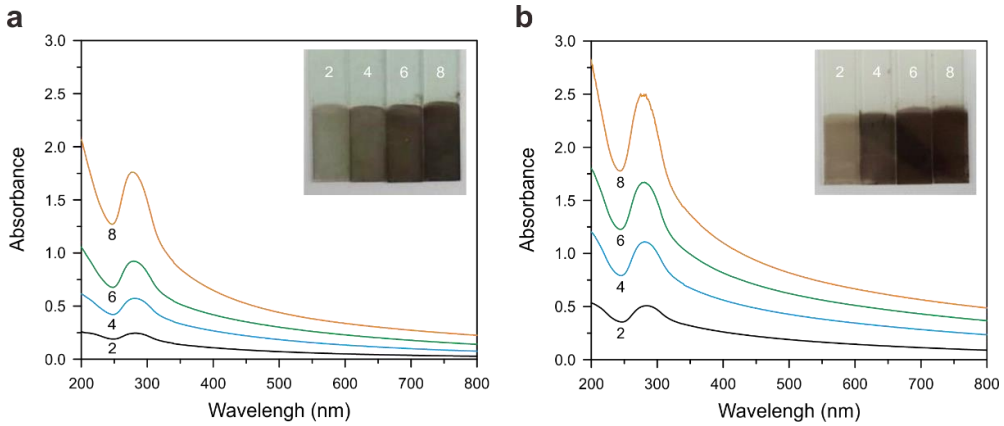

Figure 3.2.7. UV/vis absorbance spectra of (a) $(MGO/Pd)_n$ and (b) $(NGO/Pd)_n$ multilayer thin films. Inset image represents the samples prepared.

Analyzing the surface morphology of each film also supports the assembled multilayer films (**Figure 3.2.8**). Scanning electron microscopy (SEM) measurements showed that the substrate surface was successfully covered with uniformly deposited Pd NPs on top of GO sheets in multilayers films for $(LGO/Pd)_n$, $(MGO/Pd)_n$, and $(NGO/Pd)_n$. The surface morphology of the assembled films exhibited characteristic wrinkled GO sheets of varying sizes, distributed over the entire film surface. In addition, the films assembled with NGO nanosheets displayed a relatively rough morphology, with root-mean-squared roughness (R_{rms}) values of 5.9, 9.7, and 21.2 nm determined from the AFM measurements for the $(LGO/Pd)_4$, $(MGO/Pd)_4$, and $(NGO/Pd)_4$ films, respectively.

The change of surface roughness by graphene sheet size was further confirmed by cross-sectional high-resolution transmission electron microscopy (HR-TEM), clearly indicating the different surface morphology with respect to the dimension of GO sheets within the multilayers (**Figure 3.2.9**). In addition, the identification of the precise nanoscale architecture was elucidated by a cross-sectional high-angle annular dark field scanning transmission electron microscopy (HAADF-STEM) with a corresponding electron energy loss spectroscopy (EELS). The HAADF-STEM image demonstrated the homogeneous lateral distribution of respective components with the corresponding EELS line scan analysis of $(LGO/Pd)_6$ multilayer film clearly distinguished the alternate deposition of LGO sheets and Pd NPs layers through a sequential nanoscale control enabled by LbL assembly.

An increased electrode surface roughness can enhance the interactions between the Pd NPs within the multilayer and the electrolyte, leading to increased diffusion pathways for the reactants into the inner multilayer electrode. This tortuous-path effect created by the layered architecture of the 2D materials in the multilayer films has been similarly demonstrated in barrier films that block the diffusion of permeable gases or liquids.[41-42] However, the effect on electrocatlytic films by the tortuous-path has not been studied intensively with quantitative electrochemical comparison such as mass-transfer process of electroactive species from diffusion layer of electrolyte into the surface of electrode.

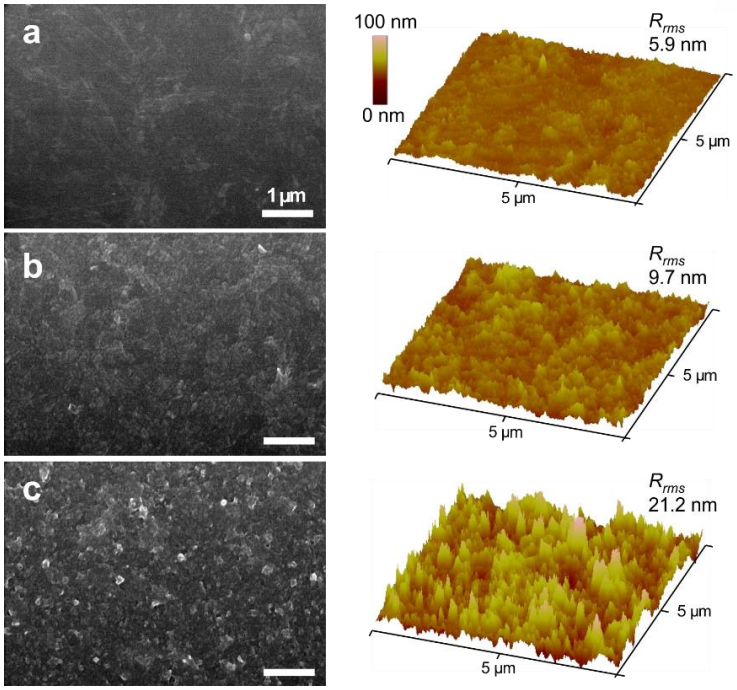

Figure 3.2.8. Representative SEM (left) and AFM (right) images of (a) $(LGO/Pd)_4$, (b) $(MGO/Pd)_4$, and (c) $(NGO/Pd)_4$ multilayer thin film electrodes. The scale bar in the SEM images is 1 μm and the R_{rms} values of the AFM images are averaged over a 5 × 5 μm^2 area.

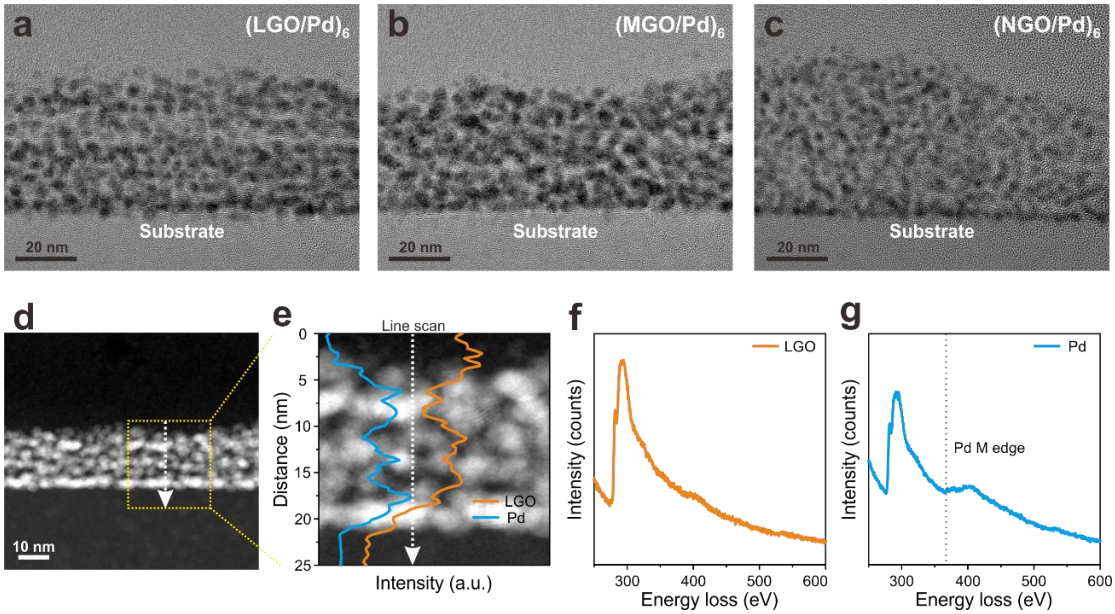

Figure 3.2.9. (a – c) Representative cross-sectional high-resolution TEM images of (a) $(LGO/Pd)_6$, (b) $(MGO/Pd)_6$, and (c) $(NGO/Pd)_6$ multilayer thin film electrodes. (d) Representative cross-sectional HAADF-STEM image of $(LGO/Pd)_6$ with (e) EELS line scan and extracted EELS analysis of (f) LGO and (g) Pd NPs corresponding to the multilayer films.

In order to electrochemically investigate the influence of increased diffusion pathways with varying GO sizes, cyclic voltammetry was performed to evaluate the electrochemical performance of the multilayer electrodes toward the MOR (**Figure 3.2.10**). The MOR is a particularly interesting model reaction, as it allows the assessment of the mass transfer (diffusion of methanol molecules from the electrolyte) and charge transfer (dissociation of methanol molecules by C-H bond breaking) properties of 3D electrodes with respect to the electrochemical process. Compared to the fast kinetics of a redox probe such as ferricyanide, the methanol oxidation kinetics are sluggish. Additionally, the diffusion of the methanol molecules into the inner electrode significantly influences the overall catalytic performance.[33,34,43,44] In our previous study, the maximum catalytic effect for methanol oxidation was found at a specific number of BLs in graphene-supported metallic multilayers due to the limited diffusion of methanol into the 3D electrode by the layered architecture of 2D GO sheet building blocks, resulting in a conversion from a surface-confined process to a diffusion-limited process as the film thickness was increased.[45] It is of note that this layer-dependence of the electrochemical operating principle is a unique characteristic of LbL-assembled multilayer electrodes.

Interestingly, in this study, the larger-sized GO sheet-supported $(LGO/Pd)_n$ multilayers showed a maximum current density of 3.55 mA/cm^2 at only 4 BLs (**Figure 3.2.10a**). This indicates that the methanol diffusion pathways were limited at an early stage by the balance between the mass and charge transfer processes, compared to that of the $(MGO/Pd)_n$ films that saturated at 6 BLs (**Figure 3.2.10b**). Most interestingly, the $(NGO/Pd)_n$ films, which have many more diffusion pathways, yielded the highest current value of 9.74 mA/cm^2 at 12 BLs (**Figure 3.2.10c**). Accordingly, we found a higher number of BLs were required for the maximum catalytic effect in smaller-sized NGO. This highlights the enhanced mass transfer of the methanol reactants resulting from facile diffusion through the multiple pathways created within the multilayer electrodes integrated with NGO The chronoamperometric measurement of electrocatalytic performance is in accord with the current density values measured in CVs. It also exhibited the high stability owing to the stable graphene nanosheet supports for electroactive metal NPs (**Figure 3.2.11**).

Figure 3.2.10d summarizes the relationship between mass and charge transfer with varying GO sheet size. In terms of charge transfer processes, it is generally reported that GO sheets of a smaller size have a lower conductivity than that of large-sized GO sheets because of the increased degree of oxidation. As a result, the current density of all multilayer electrodes at 4 BLs, at which the $(LGO/Pd)_n$ films displayed their maximum current density, decreased with decreasing GO sheet size, indicating a trade-off between the mass and charge transfer properties of the graphene-based multilayer electrodes.

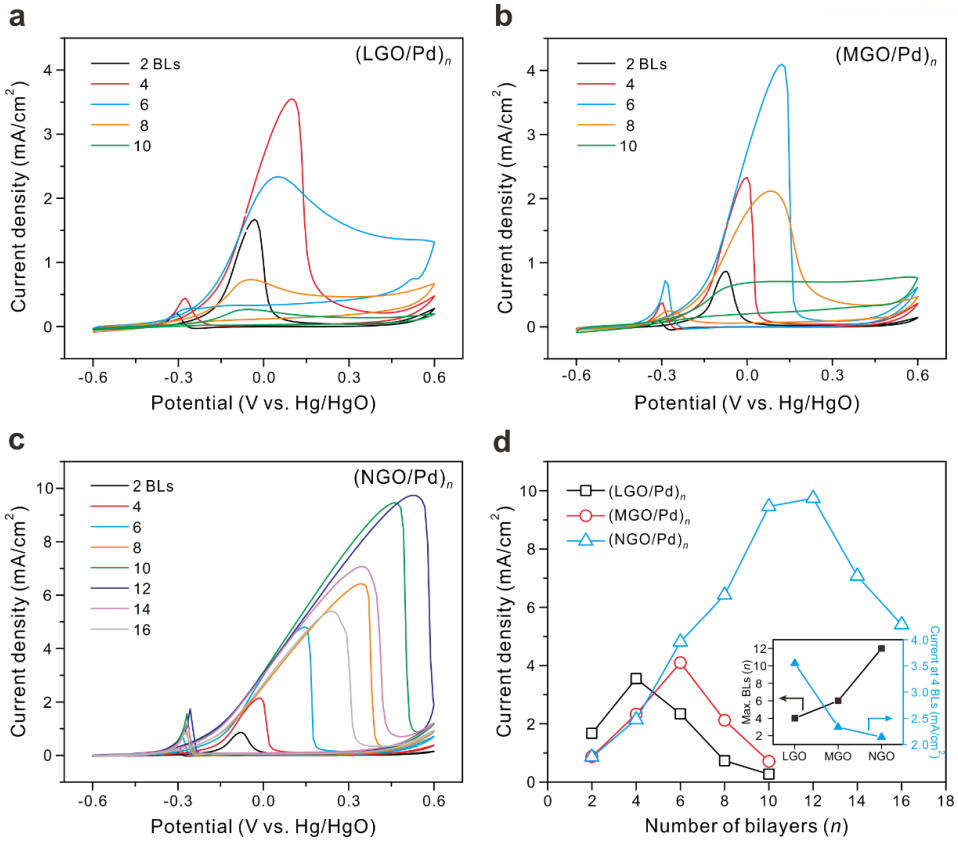

Figure 3.2.10. (a – c) Cyclic voltammograms (CVs) of (a) $(LGO/Pd)_n$, (b) $(MGO/Pd)_n$, and (c) $(NGO/Pd)_n$ multilayer thin film electrodes. (d) Comparison of the electrochemical performance toward the MOR as a function of the number of BLs. The inset in Figure d shows the maximum number of BLs for all multilayer thin films and the current density at 4 BLs. All CVs were recorded in N_2 saturated 0.10 M KOH with 1.0 M CH_3OH at a scan rate of 20 mV/s.

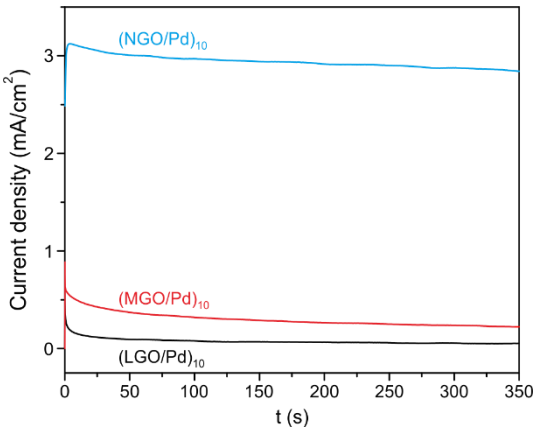

Figure 3.2.11. Chronoamperogram (CA) of $(LGO/Pd)_{10}$, $(MGO/Pd)_{10}$ and $(NGO/Pd)_{10}$ multilayer thin films at 0 V (vs. Hg/HgO) in N_2 saturated 0.10 M KOH with 1.0 M CH_3OH.

Electrochemical impedance spectroscopy (EIS) was performed to evaluate the electrochemical kinetics and interfacial resistance with respect to the charge transfer processes that are critical in electrochemical reactions (**Figure 3.2.12a**). The charge-transfer resistance (R_{CT}) values obtained from the Nyquist plot semicircles of the $(LGO/Pd)_4$, $(MGO/Pd)_4$, and $(NGO/Pd)_4$ multilayer films were 122, 1115, and 900 Ω, respectively, at -0.1 V. These results demonstrate that the $(LGO/Pd)_4$ film exhibits a higher current density than the $(MGO/Pd)_4$ and $(NGO/Pd)_4$ films due to facile charge transfer resulting from the higher conductivity of larger-sized GO sheets with a lower defect density. This is in accordance with the defect densities determined from FT-IR measurements and the low I_D/I_G ratio of the LGO sheets determined from Raman spectroscopy measurements.

Conversely, with regards to the mass-transfer process, the number of BLs at which the films displayed their maximum current density increased with decreasing GO sheet size. Additionally, the electrode assembled with smaller GO sheets also displayed their highest current density at a larger overpotential than other films, which was attributed to the alleviation of reactant depletion by enhancing the methanol mobility into the 3D electrode through increased diffusion pathways within the multilayer. In order to quantitatively determine the effects of enhanced mass transfer, the diffusion coefficient (D) was calculated for the $(LGO/Pd)_n$, $(MGO/Pd)_n$, and $(NGO/Pd)_n$ multilayer electrodes, where n is above 6 because the thin layer films such as 2 and 4 BLs are not governed by the diffusion-limited process, but the surface-confined charge-transfer process as similarly demonstrated in our previous study.[34] For an irreversible diffusion-limited process such as MOR, the current (i) and peak current (i_p) are given by equations (3,4):

$$i = FAC_O^* D_O^{1/2} \nu^{1/2} \left(\frac{\alpha F}{RT}\right)^{1/2} \pi^{1/2} \chi(bt) \qquad (3)$$

$$i_p = (2.99 \times 10^5) \alpha^{1/2} A C_O^* D^{1/2} \nu^{1/2} \qquad (4)$$

where F is the Faraday constant (C/mol), A is the area (cm^2), C_O^* is the bulk concentration of electroactive components (mol/cm^3), ν is the scan rate (V/s), R is the ideal gas constant (J/K·mol), T is the temperature (K), $\chi(bt)$ is a function for the normalized current for irreversible system, and α is the transfer coefficient. The function $\chi(bt)$ becomes a maximum at $\pi^{1/2}\chi(bt) = 0.4958$ for peak current (i_p) and α values were calculated from Tafel slopes, where the number of electrons transferred during the redox reaction, n, was assumed to be 1 because the first charge transfer is the rate determining step in MOR (**Figure 3.2.13, 3.2.14** and **Table 3.2.1**). $(NGO/Pd)_n$ films shows the significantly higher D values as 160 and 1400 times at 10 BLs than that of the $(MGO/Pd)_n$ and $(LGO/Pd)_n$ films, respectively. Owing to its superior diffusion properties with a considerably higher D value, the inferior charge-transfer kinetics exhibited by the NGO multilayer electrodes can be overcome by increasing the number

of BLs with a high Pd NPs mass loading and the overpotential through alleviating reactant depletion at diffusion-limited region above 0 V, resulting in increased electrocatalytic performance (**Figure 3.2.15**).

Furthermore, we also calculated two parameters such as tortuosity (τ) and diffusion length (L) of each multilayer film based on the equation (5):

$$\tau = \frac{D}{D_O} = \frac{L}{T} \qquad (5)$$

where D_O is diffusion coefficient of commercial Pd/C catalysts, T is the films thickness. As a result, τ of $(NGO/Pd)_n$ films was found to be significantly smaller than other multilayer films in the order of NGO < MGO < LGO as in **Figure 3.2.12b**; for example, as a fixed number of bilayers, the $(NGO/Pd)_{10}$ displayed τ value of merely 2 in comparison to that of $(LGO/Pd)_{10}$ film with a considerably higher τ of 2917 (**Table 3.2.1**). This result suggests that all reactants are directly accessible into the inner catalytic surface of films without taking a detour. In contrast, the $(LGO/Pd)_n$ films should experience considerably longer and tortuous path which corresponds to longer L with respect to the number of BLs as in **Figure 3.2.12c**. Although developing the electron pathway by increasing the electrical conductivity has been mainly emphasized in the literature when designing efficient electrocatalysts,[46] achieving a facile diffusion pathway is also a critical issue that has not been the subject of intensive study so far. The results presented here reaffirm that the establishing the high diffusion pathways, as well as increasing the conductivity, is essential for designing high-performance nanomaterial electrodes.

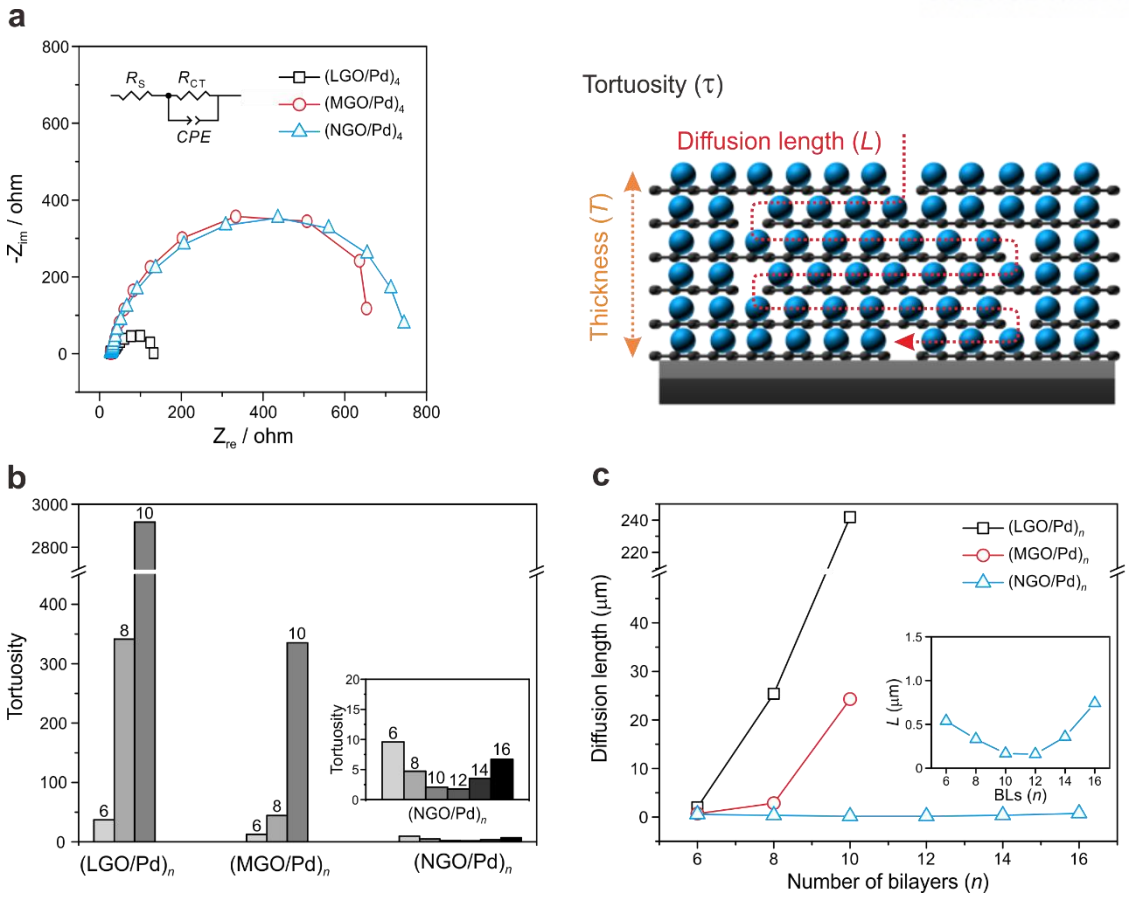

Figure 3.2.12. (a) Nyquist plots of impedance of $(LGO/Pd)_4$, $(MGO/Pd)_4$, and $(NGO/Pd)_4$ multilayer thin films at -0.1 V with an equivalent circuit. (b) The calculated tortuosity and (c) diffusion length of $(LGO/Pd)_n$, $(MGO/Pd)_n$, and $(NGO/Pd)_n$ multilayer thin films with cross-sectional schematic representation of multilayer thin films, where n is above 6. The inset in Figure b and c shows the magnified tortuosity and diffusion length of $(NGO/Pd)_n$ with respect to the bilayer numbers (n), respectively.

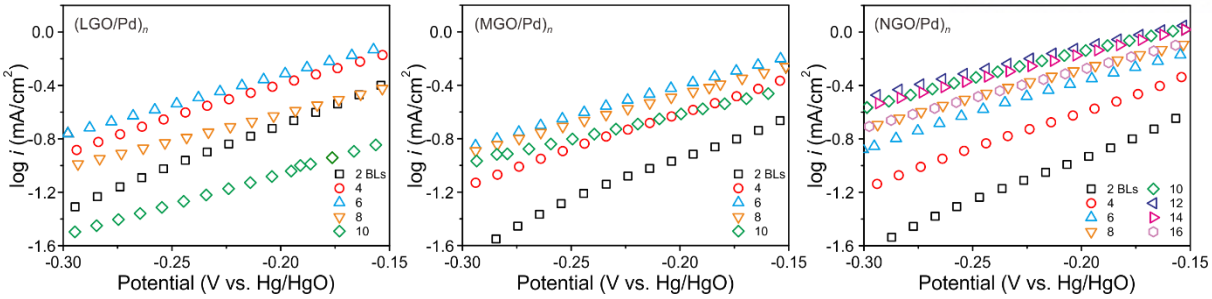

Figure 3.2.13. Tafel plots of $(LGO/Pd)_n$, $(MGO/Pd)_n$, and $(NGO/Pd)_n$ multilayer thin films. Tafel slopes and the corresponding αn were calculated in the Tafel region from -0.30 to -0.15 V.

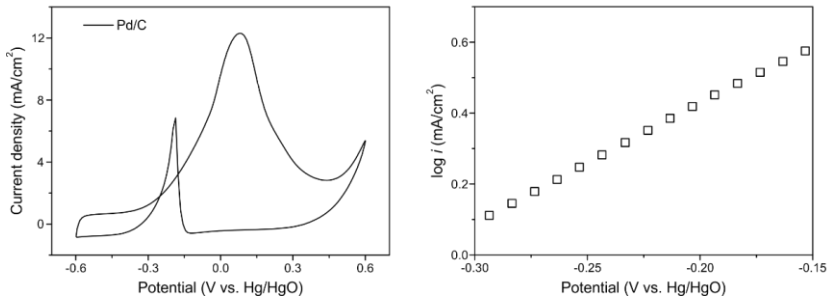

Figure 3.2.14. CV and Tafel plots of commercial 30 wt% Pd/C in N_2 saturated 0.10 M KOH with 1.0 M CH_3OH.

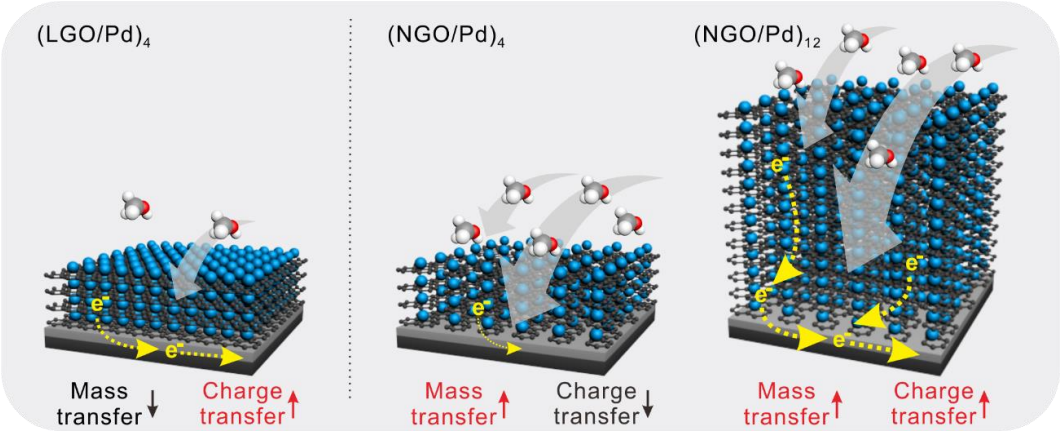

Figure 3.2.15. Schematic representation of the tunable electrocatalytic activity of multilayer electrodes, consisting of Pd NPs assembled with graphene sheets of varying sizes, toward the MOR. The gray and yellow arrows indicate the mass transfer of methanol molecules and the charge transfer, respectively, in the 3D LbL electrodes.

Table 3.2.1. Properties related to charge and mass-transfer of $(LGO/Pd)_n$, $(MGO/Pd)_n$, and $(NGO/Pd)_n$ multilayer thin films comparing to commercial Pd/C.

Multilayer films	*BLs*	*Tafel slope* (mV/dec)	*nα*	*Diffusion coefficient* (*D*, m^2/s)	*Tortuosity, (τ)*	*Diffusion length (L, nm)*
$(LGO/Pd)_n$	6	223	0.264	1.16×10^{-6}	37	1995
	8	249	0.237	1.26×10^{-7}	341	25390
	10	213	0.277	1.47×10^{-8}	2917	241838
$(MGO/Pd)_n$	6	216	0.274	3.44×10^{-6}	12	690
	8	227	0.260	9.66×10^{-7}	44	2837
	10	268	0.220	1.28×10^{-7}	335	24285
$(NGO/Pd)_n$	6	204	0.289	4.48×10^{-6}	10	538
	8	233	0.254	9.09×10^{-6}	5	332
	10	244	0.242	2.07×10^{-5}	2	167
	12	270	0.219	2.43×10^{-5}	2	160
	14	255	0.231	1.21×10^{-5}	4	357
	16	232	0.255	6.40×10^{-6}	7	742
Pd/C		299	0.197	4.29×10^{-5}	1	

3.2.5 Conclusion

In conclusion, we developed hybrid electrocatalytic multilayer electrodes for the methanol oxidation reaction composed of Pd NPs supported by GO sheets of varying lateral dimensions. The facile LbL assembled nanoelectrode offers precise control over not only over the electrode thickness and composition, but also its catalytic effect by changing the number of BLs. We found that the catalytic activity of multilayered $(GO/Pd)_n$ hybrid electrodes could be tuned by varying the number of BLs and the GO sheet size. The larger-sized GO support showed facile charge transfer in the thinner electrode films, while the smaller-sized graphene support exhibited enhanced mass transfer in the thicker electrode films, indicating a trade-off between the mass and charge transfer within these multilayer electrodes. With this structural control, as well as the versatile nature of the LbL assembly method for building 3D electrodes, we anticipate that this new design will offer a unique opportunity to understand the fundamental electrochemical kinetics of various electrode designs for future energy conversion and storage systems.

3.2.6 References

(1) Turner, J. A. A Realizable Renewable Energy Future *Science* **1999**, *285*, 687-689.

(2) Debe, M. K. Electrocatalyst Approaches and Challenges for Automotive Fuel Cells *Nature* **2012**, *486*, 43-51.

(3) Choi, N. S.; Chen, Z. H.; Freunberger, S. A.; Ji, X. L.; Sun, Y. K.; Amine, K.; Yushin, G.; Nazar, L. F.; Cho, J.; Bruce, P. G. Challenges Facing Lithium Batteries and Electrical Double-Layer Capacitors *Angew. Chem., Int. Ed.* **2012**, *51*, 9994-10024.

(4) Larcher, D.; Tarascon, J. M. Towards Greener and More Sustainable Batteries for Electrical Energy Storage *Nat. Chem.* **2015**, *7*, 19-29.

(5) Asefa, T. Metal-Free and Noble Metal-Free Heteroatom-Doped Nanostructured Carbons as Prospective Sustainable Electrocatalysts *Acc. Chem. Res.* **2016**, *49*, 1873-1883.

(6) Hu, C. G.; Dai, L. M. Carbon-Based Metal-Free Catalysts for Electrocatalysis beyond the ORR *Angew. Chem., Int. Ed.* **2016**, *55*, 11736-11758.

(7) Lam, E.; Luong, J. H. T. Carbon Materials as Catalyst Supports and Catalysts in the Transformation of Biomass to Fuels and Chemicals *ACS Catal.* **2014**, *4*, 3393-3410.

(8) Kamat, P. V. Graphene-Based Nanoarchitectures. Anchoring Semiconductor and Metal Nanoparticles on a Two-Dimensional Carbon Support *J. Phys. Chem. Lett.* **2010**, *1*, 520-527.

(9) Dreyer, D. R.; Park, S.; Bielawski, C. W.; Ruoff, R. S. The Chemistry of Graphene Oxide *Chem. Soc. Rev.* **2010**, *39*, 228-240.

(10) Krishnan, D.; Kim, F.; Luo, J. Y.; Cruz-Silva, R.; Cote, L. J.; Jang, H. D.; Huang, J. X. Energetic Graphene Oxide: Challenges and Opportunities *Nano Today* **2012**, *7*, 137-152.

(11) Lee, T.; Min, S. H.; Gu, M.; Jung, Y. K.; Lee, W.; Lee, J. U.; Seong, D. G.; Kim, B. S. Layer-by-Layer Assembly for Graphene-Based Multilayer Nanocomposites: Synthesis and Applications *Chem. Mater.* **2015**, *27*, 3785-3796.

(12) Choi, H. J.; Jung, S. M.; Seo, J. M.; Chang, D. W.; Dai, L. M.; Baek, J. B. Graphene for Energy Conversion and Storage in Fuel Cells and Supercapacitors *Nano Energy* **2012**, *1*, 534-551.

(13) Chang, D. W.; Baek, J. B. Nitrogen-Doped Graphene for Photocatalytic Hydrogen Generation *Chem. Asian J.* **2016**, *11*, 1125-1137.

(14) Lightcap, I. V.; Kamat, P. V. Graphitic Design: Prospects of Graphene-Based Nanocomposites for Solar Energy Conversion, Storage, and Sensing *Acc. Chem. Res.* **2013**, *46*, 2235-2243.

(15) Li, Q. Q.; Zhang, S.; Dai, L. M.; Li, L. S. Nitrogen-Doped Colloidal Graphene Quantum Dots and Their Size-Dependent Electrocatalytic Activity for the Oxygen Reduction Reaction *J. Am. Chem. Soc.* **2012**, *134*, 18932-18935.

(16) Zhang, B.; Fan, L. X.; Zhong, H. W.; Liu, Y. W.; Chen, S. L. Graphene Nanoelectrodes: Fabrication and Size-Dependent Electrochemistry *J. Am. Chem. Soc.* **2013**, *135*, 10073-10080.

(17) Wang, X. L.; Bai, H.; Shi, G. Q. Size Fractionation of Graphene Oxide Sheets by pH-Assisted

Selective Sedimentation *J. Am. Chem. Soc.* **2011**, *133*, 6338-6342.

(18) Zhang, W. J.; Zou, X. F.; Li, H. R.; Hou, J. J.; Zhao, J. F.; Lan, J. W.; Feng, B. L.; Liu, S. T. Size Fractionation of Graphene Oxide Sheets by the Polar Solvent-Selective Natural Deposition Method *RSC Adv.* **2015**, *5*, 146-152.

(19) Qi, X. D.; Zhou, T. N.; Deng, S.; Zong, G. Y.; Yao, X. L.; Fu, Q. Size-Specified Graphene Oxide Sheets: Ultrasonication Assisted Preparation and Characterization *J. Mater. Sci.* **2014**, *49*, 1785-1793.

(20) Decher, G. Fuzzy Nanoassemblies: Toward Layered Polymeric Multicomposites *Science* **1997**, *277*, 1232-1237.

(21) Richardson, J. J.; Bjornmalm, M.; Caruso, F. Technology-Driven Layer-by-Layer Assembly of Nanofilms *Science* **2015**, *348*, aaa2491.

(22) Ahn, E.; Lee, T.; Gu, M.; Park, M.; Min, S. H.; Kim, B.-S. Layer-by-Layer Assembly for Graphene-Based Multilayer Nanocomposites: The Field Manual *Chem. Mater.* **2017**, *29*, 69-79.

(23) Rydzek, G.; Ji, Q. M.; Li, M.; Schaaf, P.; Hill, J. P.; Boulmedais, F.; Ariga, K. Electrochemical Nanoarchitectonics and Layer-by-Layer assembly: From Basics to Future *Nano Today* **2015**, *10*, 138-167.

(24) Yang, M.; Hou, Y.; Kotov, N. A. Graphene-Based Multilayers: Critical Evaluation of Materials Assembly Techniques *Nano Today* **2012**, *7*, 430-447.

(25) Gu, M.; Lee, J.; Kim, Y.; Kim, J. S.; Jang, B. Y.; Lee, K. T.; Kim, B. S. Inhibiting the Shuttle effect in Lithium-Sulfur Batteries using a Layer-by-Layer assembled Ion-Permselective Separator *RSC Adv.* **2014**, *4*, 46940-46946.

(26) Lee, S. W.; Kim, B.-S.; Chen, S.; Shao-Horn, Y.; Hammond, P. T. Layer-by-Layer Assembly of All Carbon Nanotube Ultrathin Films for Electrochemical Applications *J. Am. Chem. Soc.* **2009**, *131*, 671-679.

(27) Choi, Y.; Choi, S.; Jeong, H. Y.; Liu, M.; Kim, B.-S.; Kim, G. Highly Efficient Layer-by-Layer-Assisted Infiltration for High-Performance and Cost-Effective Fabrication of Nanoelectrodes *ACS Appl. Mater. Interfaces* **2014**, *6*, 17352-17357.

(28) Bucur, C. B.; Muldoon, J.; Lita, A. A Layer-by-Layer Supramolecular Structure for a Sulfur Cathode *Energy Environ. Sci.* **2016**, *9*, 992-998.

(29) Ko, Y.; Shin, D.; Koo, B.; Lee, S. W.; Yoon, W. S.; Cho, J. Ultrathin Supercapacitor Electrodes with High Volumetric Capacitance and Stability using Direct Covalent-Bonding between Pseudocapacitive Nanoparticles and Conducting Materials *Nano Energy* **2015**, *12*, 612-625.

(30) Lee, S. W.; Gallant, B. M.; Byon, H. R.; Hammond, P. T.; Shao-Horn, Y. Nanostructured Carbon-Based Electrodes: Bridging the Gap Between Thin-Film Lithium-Ion Batteries and Electrochemical Capacitors *Energy Environ. Sci.* **2011**, *4*, 1972-1985.

(31) Jeon, J. W.; Kwon, S. R.; Lutkenhaus, J. L. Polyaniline Nanofiber/Electrochemically Reduced Graphene Oxide Layer-by-Layer Electrodes for Electrochemical Energy Storage *J. Mater. Chem. A*

2015, *3*, 3757-3767.

(32) Lee, T.; Yun, T.; Park, B.; Sharma, B.; Song, H. K.; Kim, B. S. Hybrid Multilayer Thin Film Supercapacitor of Graphene Nanosheets with Polyaniline: Importance of Establishing Intimate Electronic Contact Through Nanoscale Blending *J. Mater. Chem.* **2012**, *22*, 21092-21099.

(33) Choi, Y.; Gu, M.; Park, J.; Song, H. K.; Kim, B. S. Graphene Multilayer Supported Gold Nanoparticles for Efficient Electrocatalysts Toward Methanol Oxidation *Adv. Energy Mater.* **2012**, *2*, 1510-1518.

(34) Gu, M.; Kim, B. S. Unraveling the Importance of Controlled Architecture in Bimetallic Multilayer Electrode Toward Efficient Electrocatalyst *Nano Energy* **2016**, *30*, 658-666.

(35) Hummers, W. S.; Offeman, R. E. Preparation of Graphitic Oxide *J. Am. Chem. Soc.* **1958**, *80*, 1339-1339.

(36) Niu, L. Y.; Coleman, J. N.; Zhang, H.; Shin, H.; Chhowalla, M.; Zheng, Z. J. Production of Two-Dimensional Nanomaterials via Liquid-Based Direct Exfoliation *Small* **2016**, *12*, 272-293.

(37) Chang, M. S.; Kim, Y. S.; Kang, J. H.; Park, J.; Sung, S. J.; So, S. H.; Park, K. T.; Yang, S. J.; Kim, T.; Park, C. R. Guidelines for Tailored Chemical Functionalization of Graphene *Chem. Mater.* **2017**, *29*, 307-318.

(38) Luo, J.; Cote, L. J.; Tung, V. C.; Tan, A. T. L.; Goins, P. E.; Wu, J.; Huang, J. Graphene Oxide Nanocolloids *J. Am. Chem. Soc.* **2010**, *132*, 17667-17669.

(39) Gittins, D. I.; Caruso, F. Spontaneous Phase Transfer of Nanoparticulate Metals from Organic to Aqueous Media *Angew. Chem., Int. Ed.* **2001**, *40*, 3001-3004.

(40) Park, M.; Song, K.; Lee, T.; Cha, J.; Lyo, I.; Kim, B.-S. Tailoring Graphene Nanosheets for Highly Improved Dispersion Stability and Quantitative Assessment in Nonaqueous Solvent *ACS Appl. Mater. Interfaces* **2016**, *8*, 21595-21602.

(41) Priolo, M. A.; Holder, K. M.; Guin, T.; Grunlan, J. C. Recent Advances in Gas Barrier Thin Films via Layer-by-Layer Assembly of Polymers and Platelets *Macromol. Rapid Commun.* **2015**, *36*, 866-879.

(42) Choi, J. H.; Park, Y. W.; Park, T. H.; Song, E. H.; Lee, H. J.; Kim, H.; Shin, S. J.; Lau Chun Fai, V.; Ju, B.-K. Fuzzy Nanoassembly of Polyelectrolyte and Layered Clay Multicomposite toward a Reliable Gas Barrier *Langmuir* **2012**, *28*, 6826-6831.

(43) Kim, J.; Lee, S. W.; Hammond, P. T.; Shao-Horn, Y. Electrostatic Layer-by-Layer Assembled Au Nanoparticle/MWNT Thin Films: Microstructure, Optical Property, and Electrocatalytic Activity for Methanol Oxidation *Chem. Mater.* **2009**, *21*, 2993-3001.

(44) Wang, D.; Wang, J.; Liu, Z.-e.; Yang, X.; Hu, X.; Deng, J.; Yang, N.; Wan, Q.; Yuan, Q. High-Performance Electrochemical Catalysts Based on Three-Dimensional Porous Architecture with Conductive Interconnected Networks *ACS Appl. Mater. Interfaces* **2016**, *8*, 28265-28273.

(45) Jo, K.; Gu, M.; Kim, B.-S. Ultrathin Supercapacitor Electrode Based on Reduced Graphene Oxide Nanosheets Assembled with Photo-Cross-Linkable Polymer: Conversion of Electrochemical Kinetics

in Ultrathin Films *Chem. Mater.* **2015**, *27*, 7982-7989.

(46) Lee, D. G.; Gwon, O.; Park, H. S.; Kim, S. H.; Yang, J.; Kwak, S. K.; Kim, G.; Song, H. K. Conductivity-Dependent Completion of Oxygen Reduction on Oxide Catalysts *Angew. Chem., Int. Ed.* **2015**, *54*, 15730-15733.

Chapter 4.

Double Locked Silver-Coated Silicon Nanoparticle/Graphene Core/Shell Fiber for High-Performance Lithium-Ion Battery Anodes

4.1 Abstract

We present a fabrication of scalable coaxial core/shell silicon (Si)-graphene fiber prepared by dual nozzle- induced wet-spinning assembly for high-performance Si anode. Over 50 wt% of Si nanoparticles mixed with graphene oxide suspension can be incorporated in the core with the outstanding dispersibility of unique silver-coated Si nanoparticles in aqueous media. The core fiber is further encapsulated by graphene shell which not only provides conducting pathways, but also alleviates severe volume expansion of Si core. This novel core/shell Si anode with double locked graphene architecture delivers more stable cycle performance and superior rate capability than anodes composed of simple mixture of Si-graphene composites.

** Chapter 4 is reproduced in part with permission of "M. Gu,† S. Ko,† S. Yoo,† E. Lee, S. H. Min, S. Park,* and B.-S. Kim* Journal of Power Sources* **2015**, *300*, 351–357*". Copyright 2015 Elsevier*

4.2 Introduction

Lithium-ion batteries (LIBs) have been intensively developed as one of the most promising energy storage devices. The potential uses of LIBs to power future portable electronic devices, electrical vehicles, and smart grids have prompted the development of novel materials and systems to enhance the energy density and cycle life of LIBs.[1,2] However, conventional graphite anodes with a low theoretical capacity (372 mA h g^{-1}) in LIBs cannot meet the demand for high power and energy density for future advanced devices and large-scale energy storage systems.

As an alternative, silicon (Si) has received considerable attention recently as a next-generation anode material because of its highest theoretical specific capacity of *ca.* 3500 mA h g^{-1} as well as low lithiation potential, low cost, and environmental safety.[3–5] Despite these favorable features, commercialization of Si-based anodes is still not realized owing to their low intrinsic electrical conductivity and significant challenges such as a considerable volume change (>300%) during the lithiation–delithiation process and safety issues related to lithiated Si. In particular, the volume change causes high stress and pulverization, and eventually breaks down the electrical contact from the current collector or other conductive phases, resulting in degradation of the electrode and a limited cycle life.[6–8] Therefore, extensive research efforts have endeavored to alleviate the aforementioned challenges, and thereby to improve the electrochemical performance of Si-based anode materials.

Nanostructured Si anode materials with various morphologies such as nanoparticles, nanotubes, nanowires, and thin films have been developed to overcome the problem of volume change, and to improve cycle performance.[9–11] These nanostructured Si anodes offer potential solutions by providing a smaller absolute volume change, as well as additional benefit of the short diffusion path of the Li^+ ion that enhances kinetic performance. However, there are problems associated with the intrinsic nanoscale dimensions of these anodes: their large surface areas and low packing density are responsible for serious side reactions with the electrolyte and low volumetric energy density, respectively. Thus, Si composites with carbon supporting materials (e.g., carbon black and carbon nanotubes) have exploited to realize considerably enhanced cell performance: the outstanding multi-functionality of the composites enables protection of the Si surface from electrolyte and imparts superior conductive properties and mechanical flexibility that is sufficient to alleviate extensive volume expansion.[12,13]

Among various carbon supporting materials, in particular, graphene and its derivatives have been actively employed owing to their superior electrical, thermal, and mechanical strength. For example, there have been reports of synthesizing composites of Si and graphene by a number of different methods, including electrostatic attraction,[14–16] freeze-drying,[17] vacuum filtration,[18–20] ultrasonication,[21] cross-linking,[22,23] plasma-assisted ball-milling,[24,25] electrospinning,[26,27] and layer-by-layer assembly.[28,29] These approaches demonstrate that graphene acts as an elastic buffer to accommodate the volume expansion of Si nanoparticles and as a good electron conductor. However, it is still highly desirable to develop a simple, scalable, and effective strategy that can utilize the strength

of carbon materials such as graphene to overcome the limitations of Si anodes.

Herein, we developed a large-scale solution-processable fabrication method to produce core/shell structured graphene fiber with silver-coated Si (Si@Ag) nanoparticles for high performance anodes by a dual-nozzle wet-spinning assembly strategy (**Figure 4.1**). Si@Ag nanoparticles were used to provide outstanding conductivity and improved cycle life as demonstrated in our previous report.[30] We further examined the architectural effect of core/shell structures by comparing the performance between coaxial core/shell fibers and simple mixtures. The coaxial fibers showed highly improved electrochemical performance not only with high charge-discharge capacities, but also with excellent rate capabilities even at a high rate of 10 C due to the improved mechanical strength and electron pathway between Si nanoparticles and graphene sheets. Finally, we demonstrated that the uniquely interconnected core/shell structure exhibited electrical conductivity without any conducting agents such as super P carbon black.

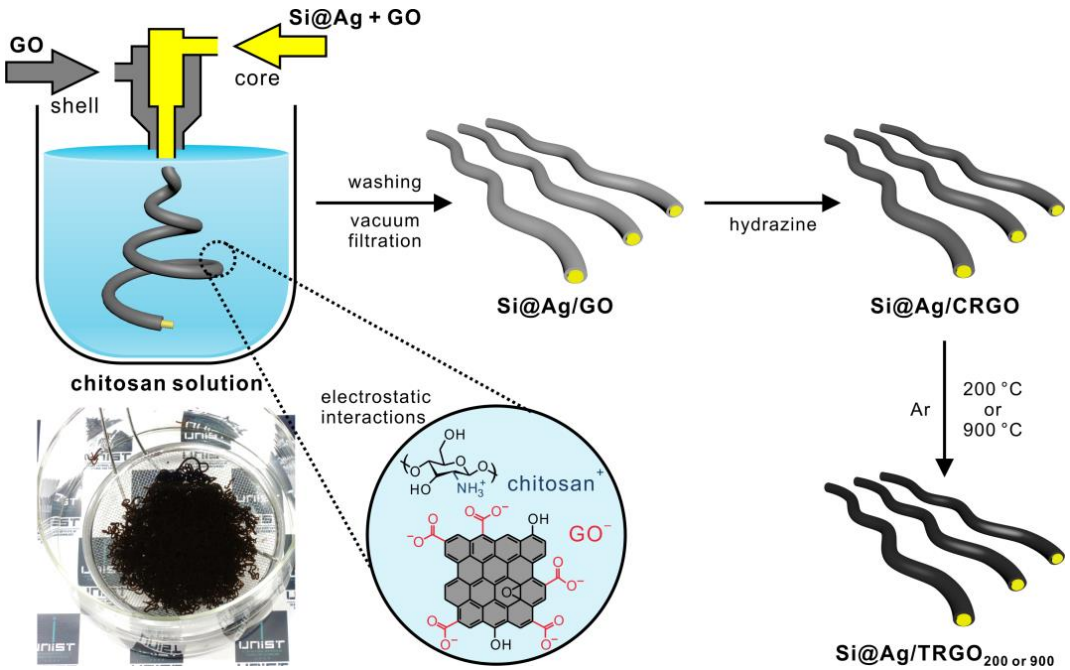

Figure 4.1. Schematic illustration of coaxial Ag coated Si–graphene fibers by wet-spinning process.

4.3 Experimental

4.3.1 Synthesis of Si@Ag nanoparticles

The Si@Ag nanoparticles were prepared according to previous literature [30]. In brief, 0.25 g of Si powder (average diameter of 50 nm, 99.9%, Aldrich) was dispersed into 20 mL of ethanol at 50 °C in a propylene reactor. Subsequently, 5.0 mM of silver nitrate ($AgNO_3$, Aldrich) and 5.0 mM of n-butylamine (Aldrich) was added to the solution with stirring for 10 min. As-synthesized Si@Ag nanoparticles were rinsed with ethanol to remove excess Ag precursor. Finally, it was filtered out and dried at 80 °C for 12 h in a vacuum oven.

4.3.2 Synthesis of graphene oxide suspension

Graphite oxide was synthesized from graphite powder by modified Hummers method and exfoliated to give a brown dispersion of graphene oxide (GO) under ultrasonication.[31,32]

4.3.3 Preparation of core/shell structured Si@Ag/GO fibers by wet-spinning

Core/shell structured Si@Ag/GO fibers were fabricated by wet-spinning method using dual-nozzle. Si@Ag nanoparticles dissolved in deionized water (200 mg/mL) were mixed with GO dispersion (20 mg/mL) (Si@Ag:GO = 1:1, v/v) to enhance the conductivity among Si@Ag nanoparticles. This homogenously mixed solution was transferred to a syringe which is connected to the core channel of spinneret, while the separate GO dispersion (20 mg/mL) was connected to the shell channel of spinneret. The core (at a rate of 10 mL/h) and shell (at a rate of 60 mL/h) solutions are injected to coagulation solution containing chitosan solution (0.50 wt% in 0.50 wt% acetic acid). After immersion for 30 min in a coagulation bath, the as-prepared Si@Ag/GO fibers were dipped into 0.50 wt% acetic acid for 3 h and then finally washed with deionized water for 3 h to remove the residual coagulation solution. The washed Si@Ag/GO fibers were collected by vacuum filtration.

4.3.4 Reduction of Si@Ag/GO fibers

The chemical reduction of the Si@Ag/GO fibers was typically carried out with a hydrazine vapor treatment at 80 °C for 24 h to afford chemically reduced Si@Ag/GO fibers (hereafter, Si@Ag/CRGO). The thermal reduction was further performed by heating the sample in a quartz furnace under an argon atmosphere. The temperature was raised to 200 or 900 °C at a rate of 5 °C/min, maintained for 1 h, and slowly cooled down to room temperature to provide thermally reduced Si@Ag/CRGO fibers of Si@Ag/$TRGO_{200}$ and Si@Ag/$TRGO_{900}$, respectively.

4.3.5 Characterizations

Inductively coupled plasma-mass spectrometer (ICP-MS; Perkin Elmer, ELAN DRC-II) analysis was used to confirm the content of Ag on the Si nanoparticles. Field emission scanning electron

microscopy (FE-SEM; Hitachi, S-4800) was used to observe surface morphologies of wet-spun samples. Thermogravimetric analysis (TGA; TA instruments, Q50) was used to calculate the mass content of Si and GO. The microstructures of samples were studied using a high power X-ray diffractometer (XRD) and a Cu Kα source (Rigaku, D/MAZX 2500V/PC).

4.3.6 Electrochemical analysis

The electrochemical properties of simple mixture and coaxial fiber electrodes were tested by galvanostatic discharging and charging processes in coin-type half cells (2016 R-type) with 20 mm in diameter and 1.6 mm in thickness. The cells were composed of active material/super P carbon black/binder composite as a working electrode and lithium metal as a counter electrode, and prepared in an argon-filled glove box. The electrode consisting of active material (simple mixture or coaxial fiber, 80 wt%), super P carbon black (conducting agent, 10 wt%, TIMCAL), and poly(acrylic acid)/sodium carboxymethyl cellulose (50/50, wt/wt, Aldrich) binder (10 wt%) with active mass loading amount of ~1 mg/cm^2. The resulting slurry was coated on a copper current collector and dried in a vacuum oven at 150 °C for 2 h. The electrolyte was composed of 1.3 M $LiPF_6$ in ethylene carbonate/diethyl carbonate (EC/DEC, 30/70 v/v, Panaxetec) with 10 wt% fluoroethylene carbonate (FEC). The cells were cycled at a rate of 0.05–10 C between 0.005–1.5 V (vs. Li/Li$^+$). All the electrochemical measurements were carried out with a WBCS-3000 battery cycler (Wonatech Co.) at room temperature. Electrochemical impedance spectroscopy (EIS) measurements were performed in the frequency range from 10 mHz to 1 MHz with an amplitude of 10 mV at the charged state (~1.5 V).

4.4 Results and Discussion

We introduced a dual-nozzle wet-spinning method to fabricate the core/shell-structured fibers using the Si@Ag nanoparticle solution for the core and the GO suspension for the shell nozzle (**Figure 4.1**). Electrically conductive Si@Ag nanoparticles were initially synthesized by the chemical reduction of Ag^+ ions in the presence of Si nanoparticles with a mild reducing agent, as reported in our previous paper.[30] This method provides the formation of Ag nanoparticles coated on the Si nanoparticles in an aqueous solution with an average diameter of 13 nm for Ag nanoparticles on 50 nm Si nanoparticles (**Figure 4.2**). The content of Ag nanoparticles was ~3 wt% as confirmed by inductively coupled plasma-mass spectrometer (ICP-MS) analysis. Owing to their good dispersion in aqueous solution, Si@Ag nanoparticles are compatible with the stable GO suspension prepared using the modified Hummers method.[31,32] The coaxial Si@Ag/GO fibers were produced by coagulation in a chitosan solution through polyionic complexation between negatively charged GO sheets and positively charged chitosan solution.[33] The as-prepared core/shell Si@Ag/GO fibers exhibit mechanical stability due to the electrostatic interaction between chitosan and GO. The robust mechanical properties of coaxial fibers were also demonstrated by winding fibers with lengths of several tens of centimeters long around a glass rod (**Figure 4.3**). It is also important to note that this method is highly scalable for mass production of graphene based composites, benefiting from the solution-processable wet-spinning method.

The scanning electron microscopy (SEM) image in **Figure 4.4a** shows the successful enveloping of Si@Ag nanoparticles by the GO shells. The diameter of the Si@Ag/GO fibers is about 380 μm, including 270 μm diameter of the Si@Ag core fibers. Once the coaxial fiber was produced, Si@Ag/GO underwent a reduction process by chemical and thermal protocols to enhance the electrical conductivity and the integrity of the resulting composite. As shown in **Figure 4.4b,c** and **4.5**, the diameter of Si@Ag/GO fibers decreased after the reduction process to 360 μm, including 233 ± 23.5 μm diameter of the core of Si@Ag fibers, and the shell thickness of the fibers was ranged from 15 to 65 μm with an average thickness of 39.1 μm. The magnified SEM image of core Si@Ag fibers revealed that Si@Ag nanoparticles were uniformly confined and well interconnected with graphene sheets within the core (**Figure 4.4d**). The graphene sheets within the Si core fiber can play a critical role of enhancing the electrical conductivity and further reinforcing the mechanical strength of the Si core fiber together with the additional graphene shell. As a result, the double locked graphene structure of the coaxial fiber can accommodate a large volume change of the Si nanoparticles and facilitate the electron conduction from Li^+ ions during the lithiation–delithiation process, by enhancing the interconnection between Si@Ag nanoparticles and graphene sheets in the core fiber and encapsulating the Si core fiber with the graphene shell.

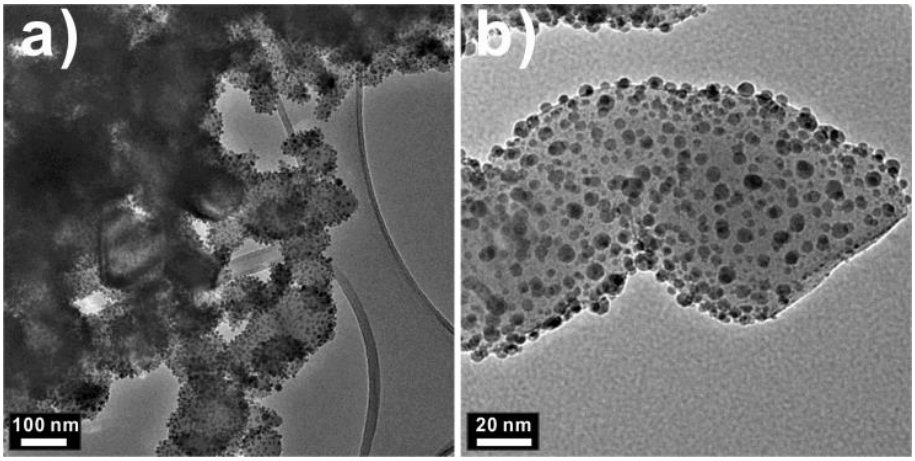

Figure. 4.2. (a) TEM image and (b) Magnified TEM image of Si@Ag particles. Ag particles with size of <20 nm were coated on the surface of Si particles and the content of Ag particles was ~3 wt% as confirmed by inductively coupled plasma (ICP) analysis.

Figure. 4.3. Photograph of winding Si@Ag/GO fibers around a glass rod.

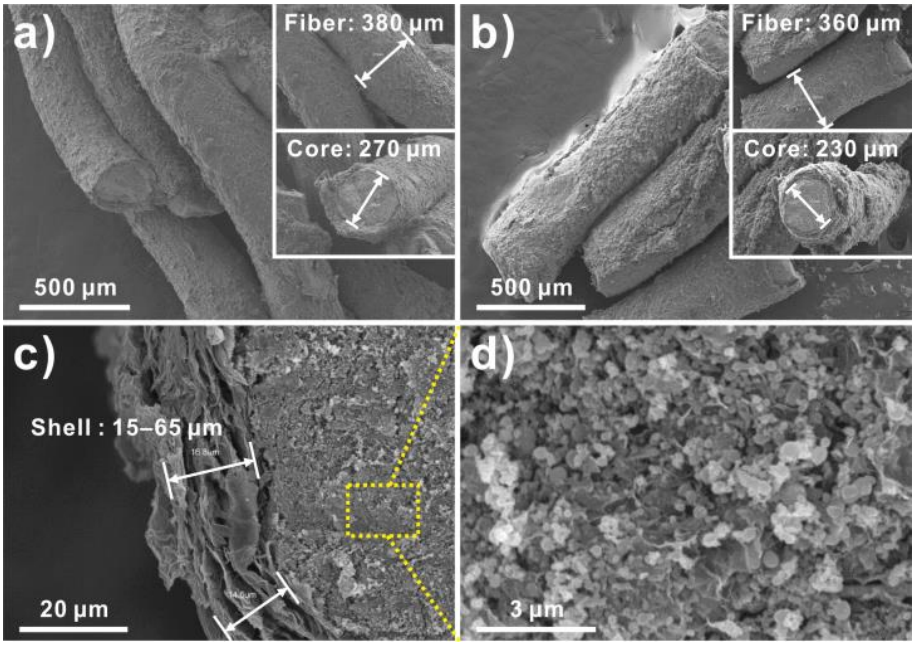

Figure. 4.4. SEM images of (a) as-prepared Si@Ag/GO fibers and (b–d) the Si@Ag/TRGO$_{900}$ fibers after chemical and thermal reduction. (d) Magnified SEM image of internal structure of the core fiber in part c.

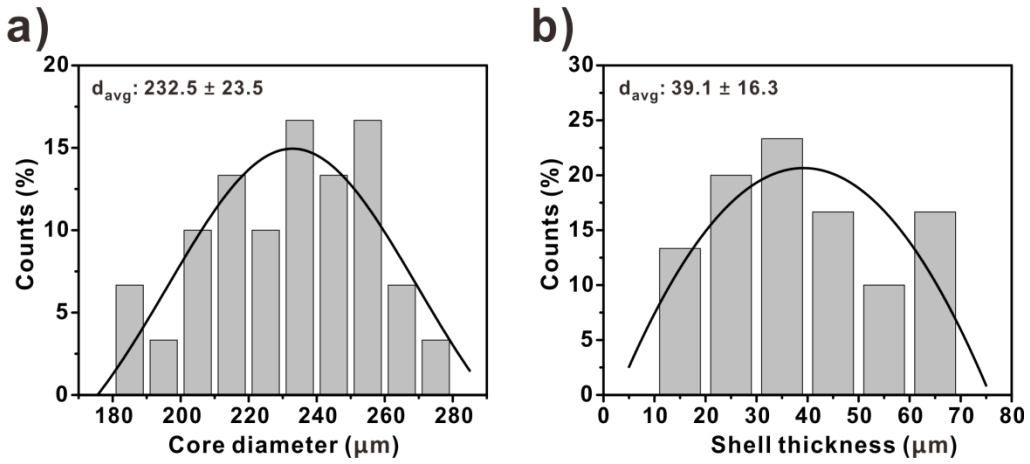

Figure. 4.5. A histogram of (a) core diameter and (b) shell thickness distribution of Si@Ag/TRGO$_{900}$.

Thermogravimetric analysis (TGA) was used to classify each contribution of Si and graphene in Si@Ag/TRGO$_{900}$ fibers in 60% O_2 and 40% N_2 condition. Si@Ag/TRGO$_{900}$ fibers showed decomposition at 500 ºC by degradation of graphene, remaining the amount of about 57% and mass fraction was subsequently increased above 500 °C due to the oxidation of containing Si@Ag nanoparticles in core fibers (**Figure 4.6a**). In order to confirm the compositional ratio in Si@Ag/TRGO$_{900}$, the individual Si@Ag nanoparticles and TRGO$_{900}$ fibers were also analyzed because each content can be calculated by a simple equation (1).[14]

$$W_{Si@Ag}X_{Si@Ag} + W_{TRGO900}(1 - X_{Si@Ag}) = W_{Si@Ag/TRGO900} \quad (1)$$

where $W_{Si@Ag}$, $W_{TRGO900}$, and $W_{Si@Ag/TRGO900}$ are residual weight percent of Si@Ag, TRGO$_{900}$, and the Si@Ag/TRGO$_{900}$ fibers, respectively. $X_{Si@Ag}$ is the Si@Ag content in the Si@Ag/TRGO$_{900}$ fibers. Si@Ag was partially oxidized above 500 °C in O_2 condition of TGA with a increase in mass (~115%). TRGO$_{900}$ fibers without Si@Ag did not show any increment above 500 °C with remaining 9% resultant. As a result, Si@Ag/TRGO$_{900}$ fibers contained approximately 48 wt% TRGO$_{900}$ and 52 wt% Si@Ag, respectively, without any residues. It shows that over 50 wt% of Si nanoparticles mixed with GO sheets were incorporated in the core because of the outstanding compatibility of aqueous Si@Ag nanoparticles with the stable GO suspension.

We could also confirm the degree of reduction of Si@Ag/GO as different reduction process through TGA. In the case of Si@Ag/GO fibers, many oxygen-containing functional groups of GO such as carboxyl, hydroxyl, and epoxide groups accounting for about 36 wt% were mainly decomposed at 200 °C (**Figure 4.7**). Some portion of oxygen-containing functional groups disappeared after hydrazine vapor reduction, but still remained (~16 wt%) in the 25–400 °C range of Si@Ag/CRGO fibers, while Si@Ag/TRGO$_{900}$ fibers did not show any decomposition of functional groups, indicating Si@Ag/GO fibers was entirely reduced. It means that additional thermal reduction is necessary for inhibiting the side reaction between functional groups and electrolyte as well as enhanced conductivity of fully reduced GO.

The successful reduction of the graphene fiber is also supported by X-ray diffraction (XRD) analysis as presented in **Figure 4.6b**. After reduction, the broad XRD peak of GO at 11.9° disappeared and the new peak at 26.4° appeared, corresponding to the *d*-spacing of 0.338 nm which is close to that of natural graphite (0.335 nm), while Si@Ag/TRGO$_{900}$ showed no significant change in the XRD characteristic peaks of Si and Ag.

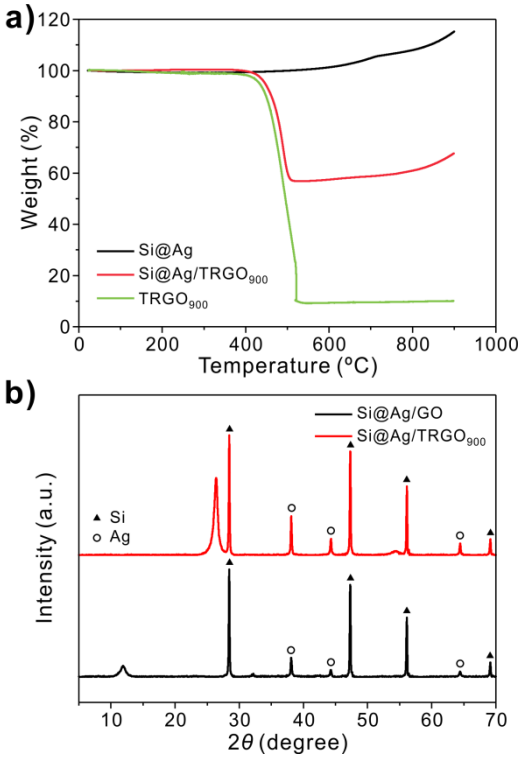

Figure. 4.6. (a) TGA of Si@Ag nanoparticles, Si@Ag/TRGO$_{900}$, and TRGO$_{900}$ fibers in 60% O_2 and 40% N_2 condition at a rate of 5 °C/min. (b) XRD of Si@Ag/GO and Si@Ag/TRGO$_{900}$ fibers with characteristic diffraction patterns of Si and Ag.

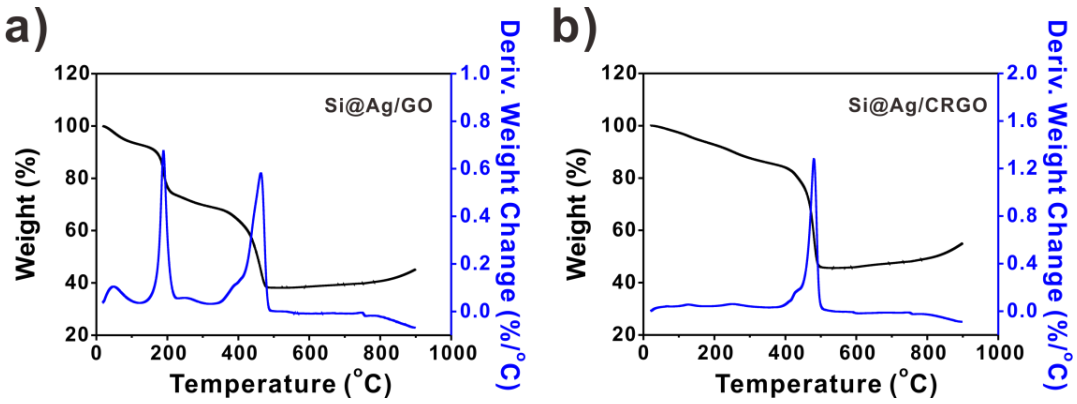

Figure. 4.7. TGA of (a) as-prepared Si@Ag/GO and (b) Si@Ag/CRGO. GO with many functional groups (e.g., carboxyl, hydroxyl and epoxide) in the Si@Ag/GO fibers was partially decomposed at 200 ºC and completely decomposed at above 500 ºC. In the case of Si@Ag/CRGO, some of functional groups were still remained in the range of 25-400 ºC.

In order to investigate the effect of the architecture of double locked graphene on the Si nanoparticles, electrochemical properties of Si@Ag/TRGO$_{900}$ and simple mixture of Si@Ag and TRGO$_{900}$ as the anodes in LIBs were evaluated using a coin-type half cell (2016R) within 0.005–1.5 V (vs. Li/Li$^+$). All samples were fabricated using the same composition. Simple mixed sample was physically mixed with two components, while Si@Ag/TRGO$_{900}$ was obtained by the wet-spinning process that enables graphene to be applied both in the core and shell of the coaxial fibers.

Figure 4.8 and **4.9** compare electrochemical performance for simple mixture and Si@Ag/GO fibers treated by different reduction processes. Si@Ag/TRGO$_{900}$ exhibited a relatively low discharge (charge) capacities of 1423 mA h g^{-1} (1124 mA h g^{-1}) with coulombic efficiency of 79.0% compared to simple mixed composite, 1603 mA h g^{-1} (1309 mA h g^{-1}) with coulombic efficiency of 81.7%, at first cycle at 0.05 C rate (**Figure 4.9a**). It is obvious that Si@Ag/TRGO$_{900}$ showed a better cycling performance with a charge capacity of 974 mA h g^{-1} after 100 cycles at 0.2 C rate, corresponding to 86.7% capacity retention, while simple mixture showed the specific charge capacity of 959 mA h g^{-1} after 100 cycles, corresponding to capacity retention of 73.3% through a normalized capacity by dividing the first charge capacity (**Figure 4.9b**). It is expected that the active Si materials in the simple mixture react more easily with Li ions by their large surface area exposed to the electrolyte, resulting in the high capacity at the first cycle. The cell with simple mixture, however, suffered from the severe capacity drop at initial few cycles due to the loss of active materials by significant structure destruction during continuous cycling. On the contrary, the cell with doubly protected Si@Ag/TRGO$_{900}$ displayed stable cycle retention without a noticeable decline in capacity, in spite of the low capacity at the first cycle for the hindrance of Li ion diffusion by graphene.[20,34,35]

Especially, the rate performance of Si@Ag/TRGO$_{900}$ was superior to that of the simple mixture. The rate capabilities of both electrodes are plotted in **Figure 4.9c**. The improved electrochemical performances can be explained as follows: (i) the dual graphene-protected core/shell structure plays a key role in alleviating the mechanical stress on the Si nanoparticles during large volume change in cycling; and (ii) the uniform dispersion of Si nanoparticles in graphene layers in core fiber leads to a significant enhancement in the electrical conductivity of Si nanoparticles with the highly improved electron pathway than that of simple mixed sample.

Reduction process has strongly affected the cell performance in Si@Ag/GO. Both Si@Ag/CRGO and Si@Ag/TRGO$_{200}$ showed lower charge capacity and coulombic efficiency than Si@Ag/TRGO$_{900}$ and simple mixture with TRGO$_{900}$, which was completely reduced with enhanced electrical conductivity as shown in **Figure 4.9a**. This may be attributed to the functional groups that remained on the graphene fiber surface, and it can cause serious side reactions during the lithiation process in carbonate-based electrolytes.[36] Even though all samples were fabricated via a wet-spinning process, the graphene layers irrespective of the position of the fibers were different depending on the reduction processes. Generally, poor electrochemical performance was observed when CRGO was used

as the anode in LIBs. However, the CRGO subjected to additional thermal reduction at high temperature showed much higher specific capacity, because functional groups on the GO surface was removed completely as confirmed by TGA analysis.[34,37,38] As a result, the side reaction of the Si@Ag/TRGO$_{900}$ was significantly decreased compared to that of other samples with much higher specific capacity and coulombic efficiency.

To verify excellent cycling and rate performances of Si@Ag/TRGO$_{900}$ fibers, the electrochemical impedance spectroscopy (EIS) measurements of the simple mixture and the Si@Ag/TRGO$_{900}$ were also performed on cycled (first and 50th) electrodes (**Figure 4.10**). According to the equivalent circuit, R_S is the ohmic series resistance that is associated with the cell components, such as the electrolyte or other components. R_{SEI} is the Li ion transfer resistance through the SEI layer, R_{CT} is the charge transfer resistance, and W is the Warburg impedance about the Li ion diffusion into the active materials. The capacitor components were replaced by the constant phase elements (CPE_1 and CPE_2). In the EIS spectra, the total cell resistance of the simple mixture and the Si@Ag/TRGO$_{900}$ were 88 and 78 Ω after the first cycle, respectively. After 50th cycles, the total resistance of the simple mixture was 122 Ω, while that of the Si@Ag/TRGO$_{900}$ was 102 Ω. Although the values of both electrodes increased after 50th cycles, the total resistance in the core/shell structured Si@Ag/TRGO$_{900}$ increased less than that in the simple mixture. It is attributed that the double locked graphene layers enhance the structural integrity and electrical conductivity of the Si@Ag/TRGO$_{900}$ electrodes during charge and discharge cycles. Another noticeable point is that most of surfaces of the electrodes consisting of Si and graphene were covered with SEI layers after long cycling. As the electrode was fabricated with a mixture of conducting agent and binder, it was hard to discern the architecture of coaxial fibers; nonetheless, we found that the overall electrode structure did not undergo severe volume changes causing deterioration of cycling performance (**Figure 4.11**).

Furthermore, we investigated electrochemical properties of Si@Ag/TRGO$_{900}$ electrodes without a conducting agent (**Figure 4.12**). In most of LIBs, the conducting agent has been used to facilitate electron transport between active materials. Since the cell does not operate in the absence of conducting agents in Si anode, the incorporation of conducting agent into Si anode materials is essential to overcome its low intrinsic electrical property. Thus, it would be meaningful to investigate cell performance of the electrode without conducting agent in Si anode system. Because TRGO$_{900}$ could provide a high electrical conductivity to Si nanoparticles, it was expected not to require additional conducting agent like super P carbon black.

As such, TRGO$_{900}$ fibers were used as the anode, the first discharge and charge capacities were 503 mA h g^{-1} and 210 mA h g^{-1}, respectively, with a coulombic efficiency of 41.7%. After 100 cycles at 0.2 C rate, the charge capacity was 196 mA h g^{-1}, corresponding to the capacity retention of 93.3% compared to the first cycle. In addition, the Si@Ag/TRGO$_{900}$ electrode without a conducting agent

showed discharge and charge capacities of 1204 mA h g^{-1} and 960 mA h g^{-1}, respectively, with a coulombic efficiency of 79.7% and the charge capacity was 766 mA h g^{-1} after 100 cycles, corresponding to the capacity retention of 79.8%. The charge capacity of Si@Ag with conducting agent after 100 cycles at 0.2 C rate was 1320 mA h g^{-1} with the first charge capacity of 1550 mA h g^{-1}; however without a conducting agent, it exhibited severe deterioration of cycling performance.[30] Although the specific capacity of Si@Ag/$TRGO_{900}$ without any other conducting agent was slightly lower than that of the Si@Ag and Si@Ag/$TRGO_{900}$ electrode with the conducting agent, it showed relatively good cycling retention, because $TRGO_{900}$ that provides an electrical pathway could compensate for the lower electrical conductivity of the Si nanoparticles. This result suggests that the double locked Si@Ag/$TRGO_{900}$ fiber electrode fabricated by wet-spinning exhibits enough electrical conductivity even in the absence of conducting agents leading to significantly improved electrochemical performances, including high specific capacity, stable cycling, and high rate capabilities.

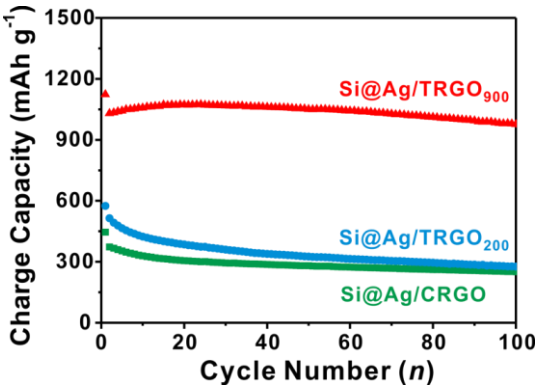

Figure. 4.8. Cycling performance of various reduced Si@Ag/GO electrodes at different temperatures.

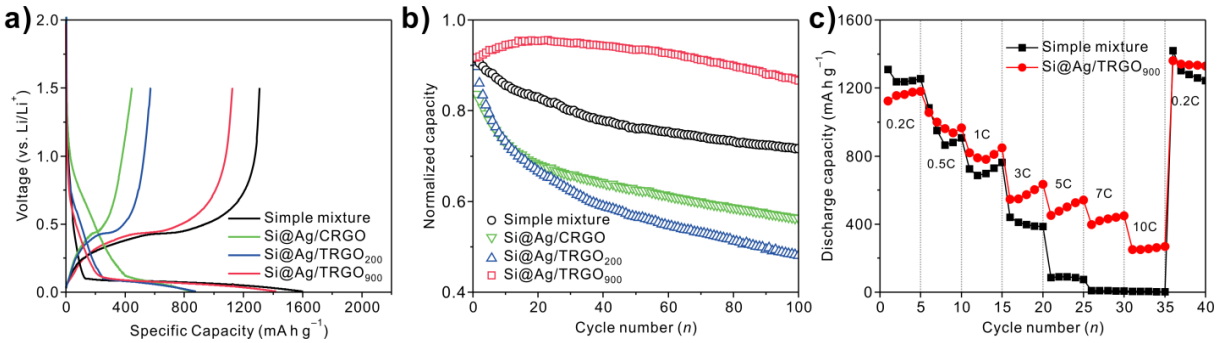

Figure. 4.9. Electrochemical evaluation of Si@Ag/CRGO, Si@Ag/TRGO fibers and a simple mixture of Si@Ag and $TRGO_{900}$: (a) First cycle and (b) charge capacity normalized cycling performance with different reduction processes. (c) Rate capabilities (0.2–10 C) of simple mixture and $Si@Ag/TRGO_{900}$. The first cycle voltage profiles were obtained at 0.05 C rate.

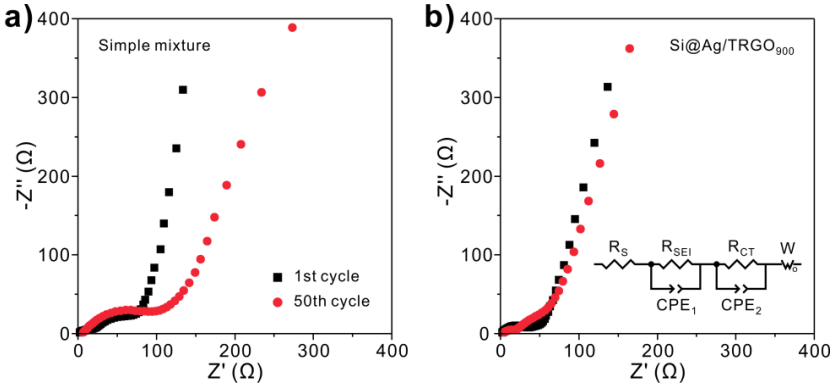

Figure. 4.10. Electrochemical impedance spectra (EIS) of (a) simple mixture and (b) core/shell structured $Si@Ag/TRGO_{900}$ electrodes after first and 50th cycles. The inset in part b represents the equivalent circuit.

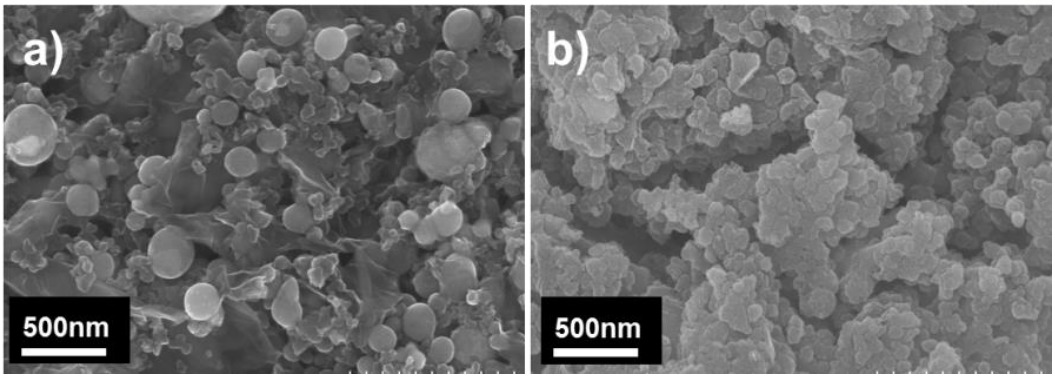

Figure. 4.11. SEM images of the Si@Ag/TRGO$_{900}$ electrodes (a) before and (b) after 100 cycles at 0.2 C.

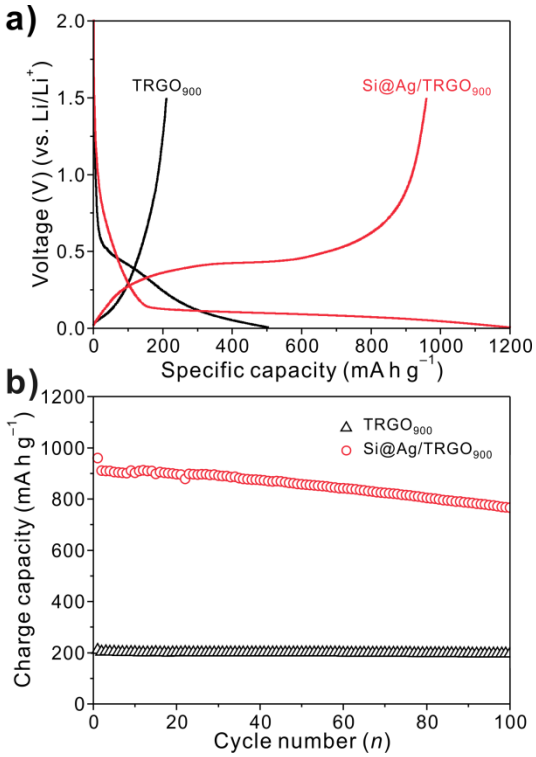

Figure. 4.12. Electrochemical evaluation of Si@Ag/TRGO$_{900}$ electrode prepared without a conducting agent. (a) First cycle voltage profiles of TRGO$_{900}$ and Si@Ag/TRGO$_{900}$ electrodes were obtained at 0.05 C rate in the voltage ranges of 0.005–1.5 V. (b) Cycling performances of TRGO$_{900}$ and Si@Ag/TRGO$_{900}$ electrodes obtained at the same voltage range at 0.2 C rate.

4.5 Conclusion

We presented a facile process based on wet spinning to fabricate graphene-enveloped Si@Ag fibers with a core/shell structure. After additional chemical and thermal reduction, the graphene sheets were found to have fewer structural defects with a significant enhancement in the electrical conductivity. This treatment led to improved electrochemical performances, including a high reversible capacity, stable cycling retention, and superior rate capabilities in LIBs. In addition, the double locked Ag-coated Si-graphene core/shell structure not only alleviated large volume change, but also markedly improved the electrical conductivity of Si nanoparticles. Furthermore, we demonstrated that Si@Ag/TRGO900 can be used without the addition of conducting agents. This simple and versatile method can be extended to other nanoparticles to synthesize high-performance anode materials for practical rechargeable battery applications.

4.6 References

(1) Tarascon, J. M.; Armand, M. Issues and Challenges Facing Rechargeable Lithium Batteries. *Nature* **2001**, *414*, 359–367.

(2) Bruce, P. G.; Scrosati, B.; Tarascon, J. M. Nanomaterials for Rechargeable Lithium Batteries. *Angew. Chem. Int. Ed.* **2008**, *47*, 2930–2946.

(3) Magasinski, A.; Dixon, P.; Hertzberg, B.; Kvit, A.; Ayala, J.; Yushin, G. High-Performance Lithium-Ion Anodes Using a Hierarchical Bottom-Up Approach. *Nat. Mater.* **2010**, *9*, 353–358.

(4) Wu, H.; Cui, Y. Designing Nanostructured Si anodes for High Energy Lithium Ion Batteries. *Nano Today* **2012**, *7*, 414–429.

(5) Bang, B. M.; Kim, H.; Song, H.-K.; Cho, J.; Park, S. Scalable Approach to mMlti-Dimensional Bulk Si Anodes via Metal-Assisted Chemical Etching. *Energy Environ. Sci.* **2011**, *4*, 5013–5019.

(6) Obrovac, M. N.; Krause, L. J. Reversible Cycling of Crystalline Silicon Powder. *J. Electrochem. Soc.* **2007**, *154*, A103–A108.

(7) Choi, N.-S.; Chen, Z.; Freunberger, S. A.; Ji, X.; Sun, Y.-K.; Amine, K.; Yushin, G.; Nazar, L. F.; Cho, J.; Bruce, P. G. Challenges Facing Lithium Batteries and Electrical Double-Layer Capacitors. *Angew. Chem. Int. Ed.* **2012**, *51*, 9994–10024.

(8) Szczech, J. R.; Jin, S. Nanostructured Silicon for High Capacity Lithium Battery Anodes. *Energy Environ. Sci.* **2011**, *4*, 56–72.

(9) Su, X.; Wu, Q. L.; Li, J. C.; Xiao, X. C.; Lott, A.; Lu, W. Q.; Sheldon, B. W.; Wu, J. Silicon-Based Nanomaterials for Lithium-Ion Batteries: A Review. *Adv. Energy Mater.* **2014**, *4*, 1300882

(10) Goriparti, S.; Miele, E.; De Angelis, F.; Di Fabrizio, E.; Zaccaria, R. P.; Capiglia, C. Review on Recent Progress of Nanostructured Anode Materials for Li-Ion Batteries. *J. Power Sources* **2014**, *257*, 421–443.

(11) Wu, H.; Chan, G.; Choi, J. W.; Ryu, I.; Yao, Y.; McDowell, M. T.; Lee, S. W.; Jackson, A.; Yang, Y.; Hu, L.; Cui, Y. Stable Cycling of Double-Walled Silicon Nanotube Battery Anodes through Solid-Electrolyte Interphase Control. *Nat. Nanotechnol.* **2012**, *7*, 310–315.

(12) Xin, S.; Guo, Y. G.; Wan, L. J. Nanocarbon Networks for Advanced Rechargeable Lithium Batteries. *Acc. Chem. Res.* **2012**, *45*, 1759–1769.

(13) Terranova, M. L.; Orlanducci, S.; Tamburri, E.; Guglielmotti, V.; Rossi, M. Si/C Hybrid Nanostructures for Li-Ion Anodes: An Overview. *J. Power Sources* **2014**, *246*, 167–177.

(14) Zhou, X.; Yin, Y.-X.; Wan, L.-J.; Guo, Y.-G. Self-Assembled Nanocomposite of Silicon Nanoparticles Encapsulated in Graphene through Electrostatic Attraction for Lithium-Ion Batteries. *Adv. Energy Mater.* **2012**, *2*, 1086–1090.

(15) Yi, R.; Zai, J.; Dai, F.; Gordin, M. L.; Wang, D. Dual Conductive Network-Enabled Graphene/Si-C Composite Anode with High Areal Capacity for Lithium-Ion Batteries. *Nano Energy* **2014**, *6*, 211–218.

(16) Zhou, M.; Pu, F.; Wang, Z.; Cai, T.; Chen, H.; Zhang, H.; Guan, S. Facile Synthesis of Novel Si Nanoparticles-Graphene Composites as High-Performance Anode Materials for Li-Ion Batteries. *Phys. Chem. Chem. Phys.* **2013**, *15*, 11394–11401.

(17) Zhou, X.; Yin, Y.-X.; Wan, L.-J.; Guo, Y.-G. Facile Synthesis of Silicon Nanoparticles Inserted into Graphene Sheets as Improved Anode Materials for Lithium-Ion Batteries. *Chem. Comm.* **2012**, *48*, 2198–2200.

(18) Lee, S. E.; Kim, H.-J.; Kim, H.; Park, J. H.; Choi, D.-G. Highly Robust Silicon Nanowire/Graphene Core-Shell Electrodes without Polymeric Binders. *Nanoscale* **2013**, *5*, 8986–8991.

(19) Sun, F.; Huang, K.; Qi, X.; Gao, T.; Liu, Y.; Zou, X.; Wei, X.; Zhong, J. A Rationally Designed Composite of Alternating Strata of Si Nanoparticles and Graphene: a High-Performance Lithium-Ion Battery Anode. *Nanoscale* **2013**, *5*, 8586–8592.

(20) Lee, J. K.; Smith, K. B.; Hayner, C. M.; Kung, H. H. Silicon Nanoparticles-Graphene Paper Composites for Li Ion Battery Anodes. *Chem. Comm.* **2010**, *46*, 2025–2027.

(21) He, Y.-S.; Gao, P.; Chen, J.; Yang, X.; Liao, X.-Z.; Yang, J.; Ma, Z.-F. A Novel Bath Lily-like Graphene Sheet-Wrapped Nano-Si Composite as a High Performance Anode Material for Li-Ion Batteries. *RSC Adv.* **2011**, *1*, 958–960.

(22) Sun, C.; Deng, Y.; Wan, L.; Qin, X.; Chen, G. Graphene Oxide-Immobilized NH_2-Terminated Silicon Nanoparticles by Cross-Linked Interactions for Highly Stable Silicon Negative Electrodes. *ACS Appl. Mater. Interfaces* **2014**, *6*, 11277–11285.

(23) Wen, Y.; Zhu, Y.; Langrock, A.; Manivannan, A.; Ehrman, S. H.; Wang, C. Graphene-Bonded and -Encapsulated Si Nanoparticles for Lithium Ion Battery Anodes. *Small* **2013**, *9*, 2810–2816.

(24) Hu, R.; Sun, W.; Chen, Y.; Zeng, M.; Zhu, M. Silicon/Graphene based Nanocomposite Anode: Large-Scale Production and Stable High Capacity for Lithium Ion Batteries. *J. Mater. Chem. A* **2014**, *2*, 9118–9125.

(25) Sun, W.; Hu, R.; Liu, H.; Zeng, M.; Yang, L.; Wang, H.; Zhu, M. Embedding Nano-Silicon in Graphene Nanosheets by Plasma Assisted Milling for High Capacity Anode Materials in Lithium Ion Batteries. *J. Power Sources* **2014**, *268*, 610–618.

(26) Xu, Z.-L.; Zhang, B.; Kim, J.-K. Electrospun Carbon Nanofiber Anodes Containing Monodispersed Si Nanoparticles and Graphene Oxide with Exceptional High Rate Capacities. *Nano Energy* **2014**, *6*, 27–35.

(27) Zhou, X.; Guo, Y.-G. A PEO-Assisted Electrospun Silicon-Graphene Composite as an Anode Material for Lithium-Ion Batteries. *J. Mater. Chem. A* **2013**, *1*, 9019–9023.

(28) Chang, J.; Huang, X.; Zhou, G.; Cui, S.; Hallac, P. B.; Jiang, J.; Hurley, P. T.; Chen, J. Multilayered Si Nanoparticle/Reduced Graphene Oxide Hybrid as a High-Performance Lithium-Ion Battery Anode. *Adv. Mater.* **2014**, *26*, 758–764.

(29) Ji, L.; Zheng, H.; Ismach, A.; Tan, Z.; Xun, S.; Lin, E.; Battaglia, V.; Srinivasan, V.; Zhang, Y.

Graphene/Si Multilayer Structure Anodes for Advanced Half and Full Lithium-Ion Cells. *Nano Energy* **2012**, *1*, 164–171.

(30) Yoo, S.; Lee, J.-I.; Ko, S.; Park, S. Highly Dispersive and Electrically Conductive Silver-Coated Si Anodes Synthesized via a Simple Chemical Reduction Process. *Nano Energy* **2013**, *2*, 1271–1278.

(31) Hummers, W. S.; Offeman, R. E. Preparation of Graphitic Oxide. *J. Am. Chem. Soc.* **1958**, *80*, 1339–1339.

(32) Hong, T. K.; Lee, D. W.; Choi, H. J.; Shin, H. S.; Kim, B. S. Transparent, Flexible Conducting Hybrid Multilayer Thin Films of Multiwalled Carbon Nanotubes with Graphene Nanosheets. *ACS Nano* **2010**, *4*, 3861–3868.

(33) Zou, J.; Kim, F. Self-Assembly of Two-Dimensional Nanosheets Induced by Interfacial Polyionic Complexation. *ACS Nano* **2012**, *6*, 10606–10613.

(34) Xiang, H.; Zhang, K.; Ji, G.; Lee, J. Y.; Zou, C.; Chen, X.; Wu, J. Graphene/Nanosized Silicon Composites for Lithium Battery Anodes with Improved Cycling Stability. *Carbon* **2011**, *49*, 1787–1796.

(35) Paek, S.-M.; Yoo, E.; Honma, I. Enhanced Cyclic Performance and Lithium Storage Capacity of SnO2/Graphene Nanoporous Electrodes with Three-Dimensionally Delaminated Flexible Structure. *Nano Lett.* **2009**, *9*, 72–75.

(36) Fong, R.; Vonsacken, U.; Dahn, J. R. Studies of Lithium Intercalation into Ccarbons using Ninaqueous Electrochemical-Cells. *J. Electrochem. Soc.* **1990**, *137*, 2009–2013.

(37) Lian, P. C.; Zhu, X. F.; Liang, S. Z.; Li, Z.; Yang, W. S.; Wang, H. H. Large Reversible Capacity of High Quality Graphene Sheets as an Anode Material for Lithium-Ion Batteries. *Electrochim. Acta* **2010**, *55*, 3909–3914.

(38) Aurbach, D. Review of Selected Electrode-Solution Interactions which Determine the Performance of Li and Li Ion Batteries. *J. Power Sources* **2000**, *89*, 206–218.

Chapter 5.
Architecture-Controlled Functional Separators

5.1 Functionalized Nanocellulose-Integrated Heterolayered Nanomats toward Smart Battery Separators

5.1.1 Abstract

Alternative materials obtained from natural resources have recently garnered considerable attention as an innovative solution to bring unprecedented advances in various energy storage systems. Here, we present a new class of heterolayered nanomat-based hierarchical/asymmetric porous membrane with synergistically coupled chemical activity as a nanocellulose-mediated green material strategy to develop smart battery separator membranes far beyond their current state-of-the-art counterparts. This membrane consists of a terpyridine (TPY)-functionalized cellulose nanofibril (CNF) nanoporous thin mat as the top layer and an electrospun polyvinyl pyrrolidone (PVP)/polyacrylonitrile (PAN) macroporous thick mat as the support layer. The hierarchical/asymmetric porous structure of the heterolayered nanomat is rationally designed with consideration of the trade-off between leakage current and ion transport rate. The TPY (to chelate Mn^{2+} ions) and PVP (to capture hydrofluoric acid)-mediated chemical functionalities bring a synergistic coupling in suppressing Mn^{2+}-induced adverse effects, eventually enabling a substantial improvement in the high-temperature cycling performance of cells.

** Chapter 5.1 is reproduced in part with permission of "J.-H. Kim,† M. Gu,† D. H. Lee, J.-H. Kim, Y.-S. Oh, S. H. Min,* B.-S. Kim,* and S.-Y. Lee* Nano Letters* **2016**, *16*, 5533–5541*". Copyright 2016 American Chemical Society*

5.1.2 Introduction

The rapidly approaching smart energy era, which will enjoy the widespread popularity of electric vehicles (EVs), grid-scale energy storage systems (ESSs) and flexible/wearable electronics, is strongly pushing us to develop advanced rechargeable batteries with reliable electrochemical performance.[1-3] As an innovative solution to address this challenging issue and also to fuel the sustainable growth of battery technologies, natural-resource-based alternative materials beyond the current state-of-the-art synthetic products have recently drawn substantial attention. Among the various eco-friendly materials reported to date, cellulose has been highlighted as a promising building block because of its natural abundance, low cost, physicochemical robustness, biocompatibility, lightweight, and recyclability.[4,5] Enormous efforts have been undertaken to use cellulose as an alternative natural material for a wide variety of rechargeable power sources such as lithium-ion and sodium-ion batteries and supercapacitors, with a focus on potential applications in electrode binders, mechanical buffers of metallic anodes, porous current collectors and separator membranes.[6-9]

In the relentless pursuit of next-generation high-performance/high-safety batteries, a great deal of research interest should be devoted to the separator membranes as well as the electrodes and electrolytes. Internal short-circuit failure occurring between the electrodes, which is considered a primary cause of cell fires or explosions, can be prevented by separator membranes.[10-12] Meanwhile, as an essential prerequisite for activating the electrochemical reaction in batteries, ions should reach electrodes via the electrolyte-filled porous channels of the separator membrane. Given such an important function of separator membranes in the ion transport between electrodes, introducing novel chemical functionalities to separator membranes is expected to bring unprecedented benefits to battery performance. For example, unwanted by-products in electrolytes, such as manganese ions (Mn^{2+}) dissolved from lithium manganese oxide electrode materials[13,14] and hydrofluoric acid (HF) generated by side reactions between residual water and lithium salts,[15] are known to result in serious capacity loss during charge/discharge cycling. These by-products can be captured by separator membranes bearing suitable chemical functionality prior to reaching the electrodes. Unfortunately, very few studies have been performed to develop functionalized separator membranes, including the partial modification of polyolefin microporous membranes[16,17] and electrospun nonwovens.[18] In particular, the theoretical-understanding-based design and synthesis of chemically active groups in functional separator membranes, along with concurrent endeavors to promote ion transport kinetics, have not been reported.

Herein, intrigued by the facile functionalization of nanocellulose via its rich hydroxyl moieties, we propose a green material strategy for the development of next-generation separator membranes that can address the aforementioned long-standing challenges (i.e., internal short-circuit safety failure, ion transport kinetics, and chemical functionality). Specifically, we present a new class of heterolayered-nanomat-based hierarchical/asymmetric porous membranes with synergistically-coupled chemical activity (referred to as the c-mat separator). The c-mat separator is composed of a terpyridine (TPY)-

functionalized cellulose nanofibril (TPY-CNF) thin nanoporous mat as the top layer and an electrospun polyvinylpyrrolidone (PVP)/polyacrylonitrile (PAN) thick macroporous mat as the support layer. The TPY-CNF top layer is seamlessly integrated with the PVP/PAN support layer by a vacuum-assisted infiltration process. The TPY molecules, because of their electron-rich nitrogen groups in an array of π-conjugated geometries, readily coordinate with metals to form bis(terpyridine)/metal complexes $[M(TPY)_2]$.[19,20] In this study, Mn^{2+} ions (dissolved from $LiMn_2O_4$ (LMO) are chosen as model metal ions dissolved in liquid electrolytes. Notably, the Mn^{2+}-chelating capability of TPY in TPY-CNF is theoretically investigated using density functional theory (DFT) calculations and molecular dynamics (MD) simulations. The TPY-CNF, in conjunction with the PVP acting as a HF scavenger, provides synergistic coupling in suppressing Mn^{2+}-induced adverse effects. In addition to this unusual chemical functionality, another salient feature of the c-mat separator is the one-dimensional (1D) fiber-based heterolayered nanomat architecture, which enables the construction of a hierarchical/asymmetric porous structure. In the thin top layer, nanoscale pores are formed between densely piled TPY-CNFs, thereby preventing leakage current between the electrodes. The macroporous electrospun PVP/PAN mat allows fast and facile ion transport through its highly developed, micrometer-sized porous channels that function like ionic highways. Benefiting from the aforementioned structural/chemical uniqueness, the c-mat separator is anticipated to provide substantial improvements in battery performance far beyond that achievable with conventional separator technologies.

5.1.3 Experimental

5.1.3.1 Synthesis of terpyridine (TPY) ligand.

Potassium hydroxide (KOH) pellets (1.15 g) and 23 mL of ammonia (28%) were added to a mixture of 2-acetylpyridine (1.685 mL) and 4-cyanobenzaldehyde (0.98 g) in anhydrous ethanol (50 mL), and the resulting mixture was stirred for 24 h at 34 ºC. The mixture was subsequently cooled in an ice bath and processed using vacuum filtration with a washing step using ice-cold anhydrous ethanol. The filtered powder was recrystallized with anhydrous ethanol, resulting in a pure white powder. One gram of the obtained white powder dissolved in 35 mL of THF was slowly added via a syringe pump to a solution of lithium aluminium hydride (0.50 g) dissolved in 35 mL of THF. The mixture was stirred for 12 h at 25 ºC under a nitrogen atmosphere. After the reaction, an additional 50 mL of THF was added and the mixture was subsequently processed using vacuum filtration with vigorous washing with THF. The filtered yellowish solution was evaporated using a rotary evaporator. The resulting powder was dissolved in dichloromethane (DCM), and HCl gas was then pumped into the solution for 90 min. The formed precipitate was filtered and dissolved in deionized (DI) water. To further purify the synthesized TPY, a 0.10 M NaOH solution was added to the aqueous solution and extracted with DCM. The extract was evaporated and then dissolved in 0.10 M HCl solution to a concentration of 30 mg mL^{-1}.

5.1.3.2 Synthesis of functionalized nanocellulose with TPY (TPY-CNF).

The nanocellulose suspension was produced by repeated high-pressure homogenization of pretreated wood cellulose powders (particle size ~45 μm, KC Flock, Nippon Paper Chemicals) in water. The detailed procedure for preparing the CNF suspension is described in our previous publications.[2] To oxidize the nanocellulose, a 0.50 wt% cellulose suspension (100 mL) was mixed with 2,2,6,6-tetramethylpiperidine-1-oxyl (TEMPO, 14.75 mg), sodium bromide (NaBr, 162 mg) and 5 wt% sodium hypochlorite solution (NaClO, 10 mL) for 6 h. The resulting mixture was washed with DI water by centrifugation. This oxidized nanocellulose suspension (50 mL) was then reacted with the as-synthesized TPY solution (4.0 mL) for 12 h in the presence of *N*-ethyl-*N′*-(3-dimethylaminopropyl)carbodiimide methiodide (EDC, 238 mg). The resulting suspension was washed with DI water by centrifugation.

5.1.3.3 DFT calculations.

To compare the binding energy of Mn^{2+} complexes, we performed DFT calculations using the Gaussian 09 program.[3] $Mn^{2+}(PP_3)$, Mn^{2+}(Glc), and Mn^{2+}(TPY) were introduced as model complexes for the PP, CNF, and TPY, respectively. The spin multiplicity for the ground state of Mn^{2+} complexes was set to sextet. Geometry optimizations were calculated at the level of B3LYP/6-31G(d, p), and accurate single-point energies were obtained at the level of B3LYP/6-311+G(2d,2p) from the optimized

geometries. The basis set superposition error (BSSE) corrections were also considered in the binding energy calculations.

5.1.3.4 MD simulations.

To test the binding stability of Mn^{2+} ions, we performed all-atom MD simulations using the AMBER force field.[4,5] Microcrystalline models (approximately 6 nm in both length and width) of syndiotactic PP, cellulose Iβ, and cellulose Iβ with 4 TPY groups were placed in parallel with the *xy*-plane of the simulation box. In the case of cellulose, the (010) exposed surface was built using the Cellulose-Builder toolkit.[6] The Mn^{2+} ions were set to be positioned at each model surface, and the simulation box was then filled with 1,600 EC molecules and 8 PF_6^- ions. The generalized AMBER forcefield (GAFF) parameters[4] were used for the PP, EC, and TPY group, and the cellulose was parameterized by the GLYCAM06 forcefield.[5] The PF_6^- ion model was taken from the literature.[7] All partial charges on the PP, EC, and TPY group were calculated using the AM1-BCC method in AmberTools14.[8] The MD simulations and visualizations were performed using the Amber14 and VMD software packages,[9] respectively. After the energy of the initial conformation was minimized, each system was relaxed by a 100-ps canonical (NVT) and 500-ps isothermal-isobaric (NPT) MD simulation at 330 K. For the production run, long NPT MD simulations were calculated at 333 K and P = 1 bar using the Langevin thermostat with a collision frequency of 1.0 ps^{-1} and the Berendsen barostat with a coupling constant of 2.0 ps. The cutoff distance of 1.0 nm and the particle mesh Ewald (PME) method were applied to the short-range nonbonding interactions and the long-range electrostatic interactions, respectively. All bond lengths involving H atoms were constrained with the SHAKE algorithm,[10] and a time step of 2 fs was used.

5.1.3.5 Structural design and fabrication of the c-mat separator.

To fabricate the electrospun macroporous mat, we used electrospinning with PVP/PAN blends. The blended PAN (molecular weight = 150,000 g mol^{-1}) and PVP (molecular weight = 1,300,000 g mol^{-1}) solution was prepared by dissolving the polymers in dimethylacetamide (DMAc) at 70 ºC for 12 h, where the total polymer concentration was 20 wt.% and the relative composition ratio of PVP/PAN was 50/50 (w/w). The electrospinning conditions were 8.0 kV and a feed rate of 3.5 μL min^{-1}. The resulting electrospun PVP/PAN mat was collected on a stainless steel plate positioned 10 cm from the nozzles. After being roll-pressed at room temperature, a freestanding macroporous electrospun mat (thickness ~19 μm) was produced. The c-mat separators were fabricated via a simple vacuum-assisted infiltration process. The TPY-CNF suspension was poured onto a PVP/PAN mat positioned inside a porcelain Büchner funnel and then subjected to a vacuum to infiltrate the porous mat, leading to the formation of a hierarchical/asymmetric porous structure. The thickness of the TPY-CNF layer was

controlled by varying the amount of the TPY-CNF suspension. The final c-mat separator (thickness ~20 μm) was obtained with a 1-μm-thick TPY-CNF layer. A commercial PP/PE/PP separator (thickness ~20 μm, Celgard) was chosen as the control sample.

5.1.3.6 Characterizations of TPY-CNF.

The ^{1}H NMR spectra of TPY were acquired using a VNMRS 600 spectrometer operated at 600 MHz; the samples were dissolved in DMSO solvent. A mass analysis of TPY was carried by mass spectroscopy (450-GC & 320-MS, Bruker). Fourier transform infrared (FT-IR) spectra were collected using an FT-IR spectrophotometer (670-IR, Varian). X-ray photoelectron spectroscopy (XPS, Thermo Fisher, K-alpha) was used to detect the chemical state of TPY-CNF.

5.1.3.7 Physicochemical characterizations of the c-mat separator.

The surface and cross-sectional morphologies of the separators were characterized by field emission scanning electron microscopy (FE-SEM, Hitachi) in conjunction with energy-dispersive X-ray spectroscopy (EDS). The pore size distribution of the c-mat separator was measured using mercury intrusion porosimetry (AutoPore IV 9500, Micromeritics Instrument Corp.). The thermal shrinkage of the separators was evaluated by measuring their (area-based) dimensional change after exposure to 150 ^{o}C for 0.5 h. For the electrochemical characterization of the separators, a liquid electrolyte of 1 M $LiPF_6$ in EC/DEC (1/1 (v/v), Soulbrain) was employed. The electrolyte wettability of the separators was quantitatively estimated by measuring the separators' electrolyte immersion height.

5.1.3.8 Electrochemical properties of the c-mat separator.

The electrochemical stability window of the separators was measured by a linear sweep voltammetry experiment performed on a working electrode of stainless steel and a counter and reference electrode of lithium metal at a scan rate of 1.0 mV s^{-1}. The open-circuit voltage (OCV) drop in the fully charged cell (at a current density of 0.2 C) was monitored as a function of elapsed time. The ionic conductivity of the separator was examined by AC impedance analysis (VSP classic, Bio-Logic) over the frequency range from 10^{-2} to 10^{6} Hz. A pouch-type cell (width × length = 30 × 40 mm^2) was assembled by sandwiching a separator between the LMO cathode (LMO/carbon black/PVdF = 92/3/5 w/w/w, areal mass loading = 17 mg cm^{-2}) and the Li metal anode (the TPY-CNF top layer was in contact with the LMO cathode while the PVP/PAN support layer faced the Li metal anode), and the cell was activated by being filled with the liquid electrolyte (1 M $LiPF_6$ in EC/DEC = 1/1 v/v). The cell performance was investigated using a cycle tester (PNE Solution) at 25 and 60 °C under various charge/discharge conditions.

5.1.4 Results and Discussion

To produce TPY-functionalized CNFs (TPY-CNFs), we rationally designed the synthetic reaction steps as follows (**Figure 5.1.1a**). Pristine CNFs were obtained through the repeated high-pressure mechanical disintegration of wood pulp.[21,22] The surface modification of CNFs was conducted using TEMPO-mediated oxidation to generate carboxylic acid/carboxylate groups that act as reactive branching sites. Because of the presence of the more hydrophilic carboxylate moiety, the solubility of the oxidized CNFs was enhanced in the aqueous suspension, yielding a lower viscosity (3.00 ± 1.79 cP) compared to that of the pristine CNF suspension (8.46 ± 0.37 cP). Meanwhile, amine-containing TPY molecules were synthesized and confirmed by ^{1}H NMR and mass spectrometry (**Figure 5.1.2**). As-synthesized TPY was then conjugated with carboxylate groups on the oxidized CNFs in the presence of *N*-ethyl-*N*'-(3-dimethylaminopropyl) carbodiimide methiodide (EDC), eventually leading to the TPY-CNFs.

The functional groups of the synthesized TPY-CNFs were identified through analysis of the corresponding FT-IR spectra (**Figure 5.1.1b**). For both the oxidized CNFs and TPY-CNFs, the introduction of carboxylate groups caused the appearance of the C=O stretching vibration peak at 1,610 cm^{-1}, which was absent in the spectrum of the pristine CNFs. In the spectrum of the TPY-CNFs, new peaks were observed at 1,468 and 791 cm^{-1}, which were attributed to N–H bending and rocking of amide, respectively, indicating the successful amide coupling by EDC chemistry. The TPY molecule bonded to the CNFs was further verified by analyzing the XPS spectra (**Figure 5.1.1c**). The characteristic N 1s peaks of the TPY-CNFs were observed at 402.1 (amide) and 399.3 eV (pyridinic-N); these peaks were shifted upwards from those of the bare TPY molecules at 400.4 (amine) and 398.2 eV (pyridinic-N).

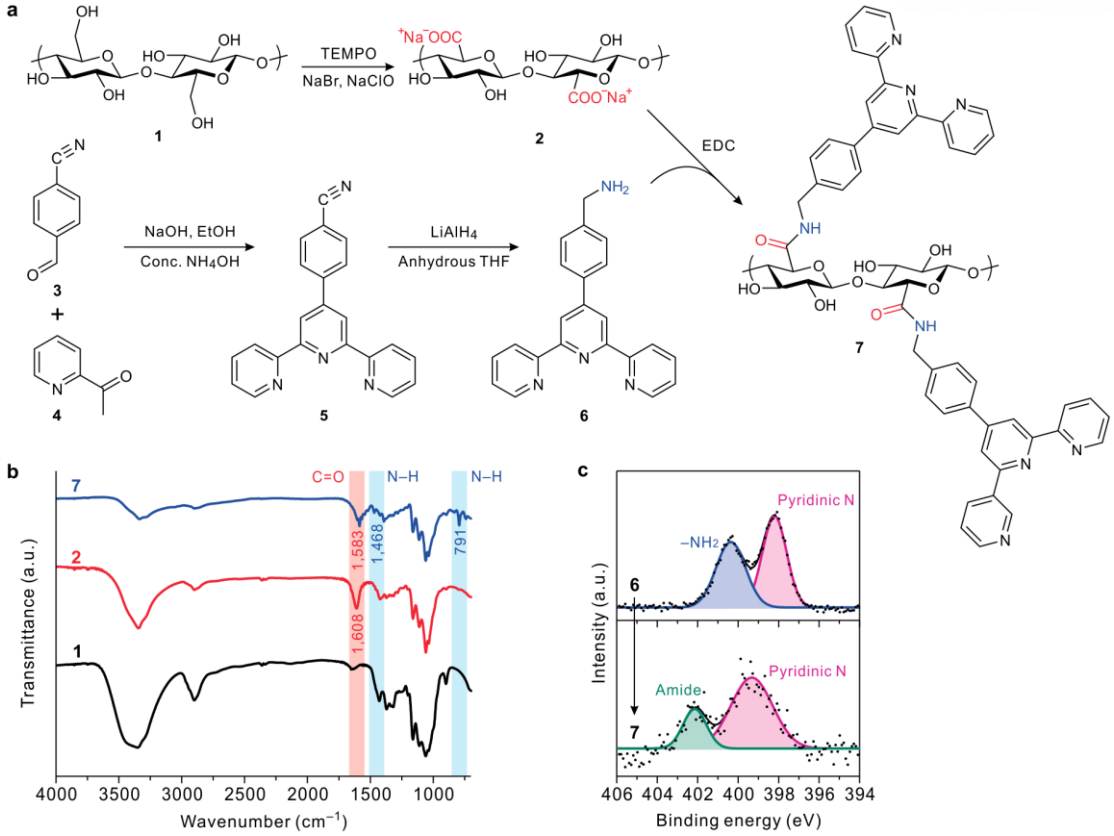

Figure 5.1.1. Synthesis of TPY-functionalized cellulose nanofibrils (CNFs). (a) Illustration of a TPY-functionalized CNF. (b) FT-IR spectra of CNF **1**, oxidized CNF **2**, and TPY-functionalized CNF **7**. (c) N 1s XPS spectra of TPY **6** and TPY-functionalized CNF **7**.

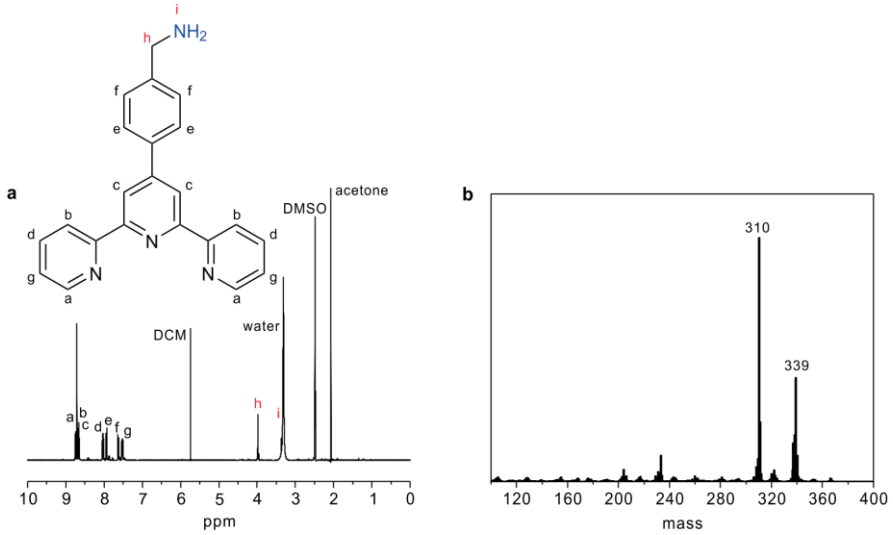

Figure 5.1.2. (a) ^{1}H NMR spectra and (b) mass analysis of TPY.

The c-mat separator was fabricated using a vacuum-assisted infiltration technique analogous to the traditional paper-making process.[23-25] The as-obtained TPY-CNF suspension was poured onto an electrospun PVP/PAN mat positioned inside a porcelain Büchner funnel. The uniform dispersion of the nanometre-scale TPY-CNF suspension is shown in the inset of **Figure 5.1.3a**. After the vacuum infiltration followed by solvent removal, a self-standing c-mat separator was successfully produced. A schematic depicting the overall fabrication procedure of the c-mat separator is provided in **Figure 5.1.3a**.

The structural uniqueness of the c-mat separator was characterized with a particular focus on its hierarchical/asymmetric porous morphology. A scanning electron microscopy (SEM) image of the c-mat separator shows that the 1D nanofibers (i.e., the TPY-CNFs) are densely packed and uniformly distributed over a wide area of the TPY-CNF mat, generating a number of nanoscale pores formed between the compactly piled TPY-CNFs (**Figure 5.1.3b**). Meanwhile, an EDS image reveals the presence of TPY molecules (their nitrogen atoms are represented in green) chemically linked to the CNFs. The opposite side of the c-mat separator was the electrospun PVP/PAN mat serving as a support layer (**Figure 5.1.3c**). Compared with the TPY-CNFs, the electrospun PVP/PAN fibers have a larger micron-sized diameter, thus yielding a highly interconnected macroporous structure in the resultant PVP/PAN support layer. A cross-sectional SEM image shows that the thin TPY-CNF mat (top layer) was integrated with the thick PVP/PAN mat (support layer) and that a hierarchical/asymmetric porous structure developed in the through-thickness direction (**Figure 5.1.3d**).

To check the structural/dimensional robustness of the c-mat separator, tape tests were conducted. No appreciable amount of TPY-CNFs or PVP/PAN fibers was detached from the c-mat separator (**Figure 5.1.3e**). Additionally, upon repeated crumpling/uncrumpling cycles, the c-mat separator maintained its dimensional stability without physically disintegrating into individual fibers (**Figure 5.1.3e**).

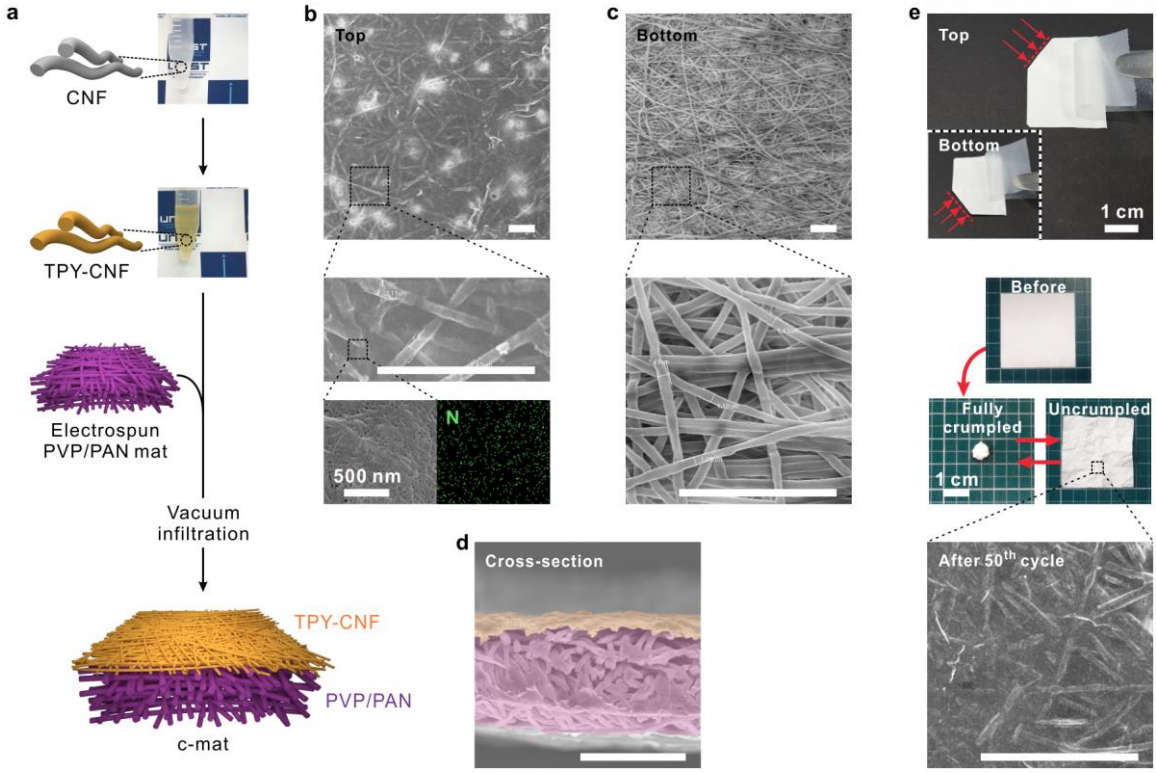

Figure 5.1.3. Fabrication and structural/physical characterizations of the c-mat separator. (a) Schematic depicting the overall fabrication procedure of the c-mat separator. SEM images of the (b) top, (c) bottom sides, and (d) cross-section of the asymmetric c-mat separator and an elemental mapping image of nitrogen. (e) A tape test using commercial Scotch tape, a crumpling test of the c-mat, and an SEM image after the 50th cycle. The scale bar of each SEM images is 20 μm.

We note again that a morphological feature of the c-mat separator is the heterolayered nanomat-enabled hierarchical/asymmetric porous structure (i.e., the combination of the nanoporous structure (the TPY-CNF top layer) and the macroporous one (the PVP/PAN support layer)). To elucidate the advantageous effect of this structural uniqueness on the electrochemical performance of cells, a PVP/PAN mat and a TPY-CNF mat were fabricated as model separators and subsequently compared with the c-mat separator. The porous morphology and pore size distribution (PSD) of the separator samples examined herein are shown in **Figure 3a–c**. The PVP/PAN separator (**Figure 5.1.4a**) clearly exhibited large-sized macropores, and the average diameter was estimated from the PSD to be ~1,000 nm. In comparison, the nanoporous structure (average diameter ~10 nm) formed from the densely packed TPY-CNFs was observed at the TPY-CNF separator (**Figure 5.1.4b**). Notably, the c-mat separator exhibited the hierarchical (nanoporous-macroporous)/asymmetric porous structure in the through-thickness direction (**Figure 5.1.4c**), which was further verified by the bimodal pore size distribution.

The drop in the open-circuit voltage (OCV) and the discharge C-rate capability of the cells assembled with the aforementioned separators were characterized; the results are discussed in terms of the separators' porous structures.[26] The OCV drop test (**Figure 5.1.4d**), which is known to be an indicator of self-discharge behaviour in cells, showed that the cell containing the macroporous PVP/PAN separator failed to maintain its charge voltage over time, revealing that the micrometer-scale pore size of the PVP/PAN separator is too large to sufficiently prevent leakage current between the electrodes. By contrast, no appreciable drop in the OCV was observed at the c-mat separator, which appeared to be comparable to that of a commercial PP/PE/PP separator. The OCV results demonstrate that the nanoporous TPY-CNF top layer in the c-mat separator plays a critical role in suppressing leakage current.

Despite the beneficial contribution of the TPY-CNF top layer, its nanoporous structure may limit the ionic flux through the layer, thus negatively affecting the electrochemical performance of cells. To address this concern, various c-mat separators with TPY-CNF top layers of various thicknesses were fabricated. **Figure 5.1.4e** shows the effect of the top layer thickness on the discharge capacity of cells assembled with c-mat separators, wherein half-cells (i.e., LMO cathode/separator/Li metal anode) were charged at a constant current density of 0.2 C and were discharged at various current densities (0.2 – 5.0 C) in the voltage range from 3.0 to 4.3 V. As the top layer thickness was increased from 1 to 10 μm, the discharge capacities tended to decrease; which became more pronounced at higher discharge current densities. Notably, a serious drop in discharge capacities was observed at a thickness of 10 μm. The detailed discharge profiles of the cells are provided in **Figure 5.1.5**. These results demonstrate that the TPY-CNF top layer, because of its relatively less-developed porous structure, acts as a resistive layer to ionic conduction; they also demonstrate that the excessively large thickness of the top layer causes

cell polarization, eventually deteriorating the discharge capacities, particularly at high current densities. One noteworthy finding is that the c-mat separator with the TPY-CNF top layer (thickness = 1 μm) delivered higher discharge capacities than the PP/PE/PP separator over a wide range of current densities, demonstrating that finely tuning the thickness of the nanoporous TPY-CNF top layer, in association with the integrated macroporous PVP/PAN support layer (acting as an ionic highway), allows fast/facile ion transport while simultaneously preventing the leakage current between the electrodes. In other words, under the condition that leakage current of cells is strictly suppressed, the thinner top layer is beneficial for achieving the faster ion transport, eventually leading to the superior cell performance. Future works will be devoted to fine-tuning porous structure of the top and support layers by material/process control, which is expected to allow additional decrease in the thickness of the top layer. Schematics depicting the effects of the porous structure of the separators on the leakage current and on the ion transport between the electrodes are presented in **Figure 5.1.4**.

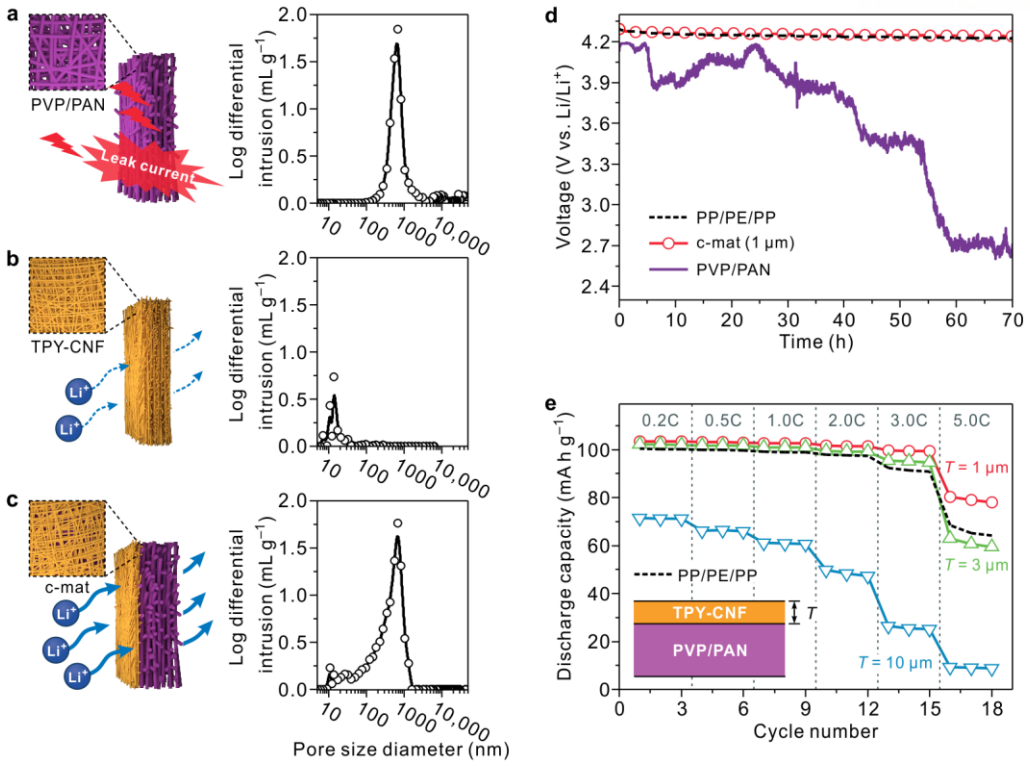

Figure 5.1.4. Comparison of the separators. Schematic and pore size distribution of the (a) PVP/PAN electrospun mat, (b) TPY-CNF, and (c) TPY-CNF on PVP/PAN (c-mat). (d) OCV profiles of the cells (LMO cathode/Li metal anode), where the cells were charged to 4.3 V at a constant current density of 0.2 C and their voltage drop was measured as a function of the elapsed time. (e) Discharge rate performance as a function of the thickness of the TPY-CNF layer.

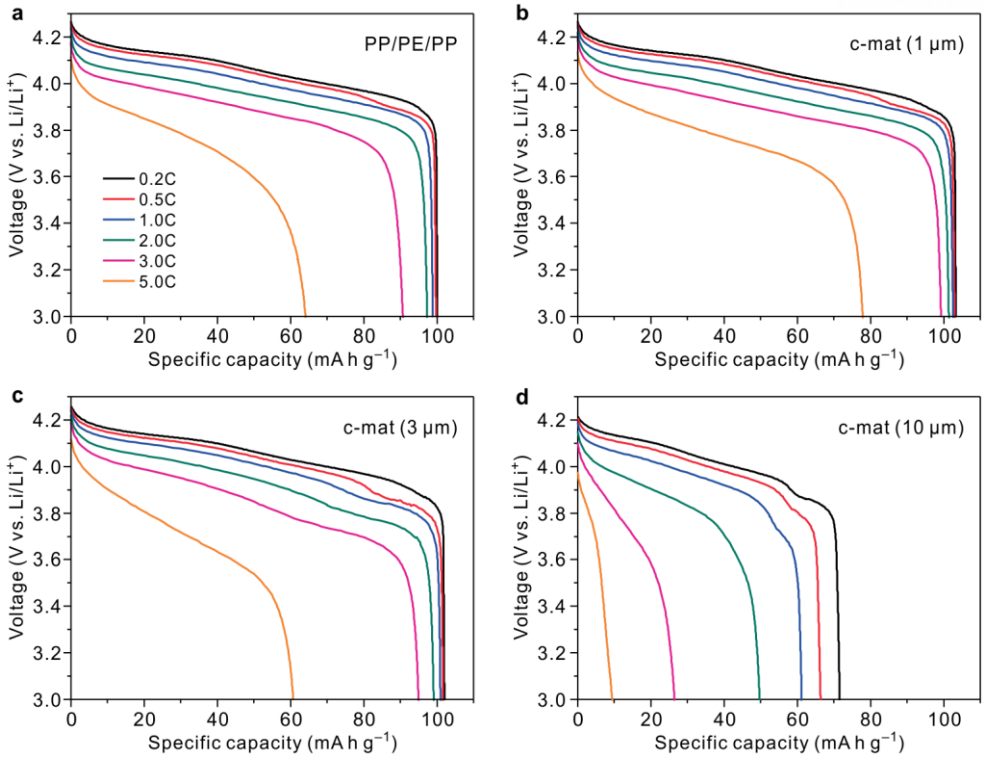

Figure 5.1.5. Discharge profiles of cells assembled with (a) PP/PE/PP separator and c-mat separator with TPY-CNF layers with thicknesses of (b) 1 μm, (c) 3 μm and (d) 10 μm.

In addition to the aforementioned structural uniqueness, another salient feature of the c-mat separator is the chemical functionalities achieved by TPY-CNFs (in the top layer) and PVP (in the support layer). We theoretically investigated the metal ion (here, Mn^{2+} ion) chelation of TPY-CNFs by performing DFT calculations. As a control, a plain PP separator was chosen. Considering the possible binding sites of Mn^{2+} ions, the PP, CNF, and TPY were simplified to trimers of PP (PP_3), α-D-glucose (Glc), and TPY molecules, respectively. The optimized geometries and binding energies of the Mn^{2+} complex were calculated at the B3LYP/6-311+G(2d,2p)//B3LYP/6-31G(d,p) level with BSSE corrections using the Gaussian 09 program.[27]

On the basis of the binding energy of the $Mn^{2+}(PP_3)$ complex, **Figure 5.1.6a–c** show that Mn^{2+}(Glc) and Mn^{2+}(TPY) complexes have large differences in their binding energies, which are 31.69 kcal mol^{-1} and 130.80 kcal mol^{-1}, respectively. Whereas the Mn–H interaction is dominant in the $Mn^{2+}(PP_3)$ complex, the optimized geometry of the Mn^{2+}(Glc) complex indicates a relatively strong interaction between the Mn^{2+} ion and the lone-pair electrons in the hydroxyl oxygen atom. In particular, the high binding energy of the Mn^{2+}(TPY) complex results from the electrostatic interactions and charge transfer between the Mn^{2+} ion and the pyridine groups in TPY with the coordinated structure.

The binding stability of the Mn^{2+} ions on the model surfaces of PP, CNFs, and TPY-CNFs was also investigated using MD simulations. The calculations were performed using the AMBER 14 software;[28] the detailed procedure is described in the Experimental section. The Mn^{2+} ions were initially positioned at each model surface on the basis of the geometries determined from the DFT calculations. In the NPT simulations of 400 ns at 333 K, the *z*-axis position of the Mn^{2+} ions was tracked during the last 100 ns.

As shown in **Figure 5.1.6d**, the Mn^{2+} ions were located in the region of the ethylene carbonate (EC) solvent while being detached from the PP surface. The probability of the *z*-axis position shows that Mn^{2+} ions could move freely in the EC solvent, representing the absence of specific interactions between the Mn^{2+} ions and the PP surface. By contrast, the nanocellulose surface still held a Mn^{2+} ion by the hydroxyl groups of the glucose unit after 400 ns (**Figure 5.1.6e**). The high probability around the CNF surface demonstrates that Mn^{2+} ions have relatively strong interactions with the CNF surface compared with that of PP. As expected, the terpyridine groups in the TPY-CNFs maintained their coordination structure with the Mn^{2+} ions during the MD simulation (**Figure 5.1.6f**) because of the high interaction energy between them. As a result, the probability of the *z*-axis position of the Mn^{2+} ions is obviously concentrated at the surface of the TPY-CNFs.

On the basis of the aforementioned simulation results, the Mn^{2+} ion binding capability of the TPY-CNFs was experimentally verified. The TPY-CNFs, along with the PP/PE/PP separator and the pristine CNFs, were soaked in 1 M $MnCl_2$ solution, and the change in their XPS Mn 2p spectra was analyzed (**Figure 5.1.6g–i**). The TPY-CNFs showed the appearance of Mn 2p peaks, whereas no appreciable Mn 2p peaks were observed at the PP/PE/PP separator or the pristine CNFs. Furthermore,

the deconvoluted peaks of the TPY-CNFs shifted downwards from 654.1 (Mn $2P_{1/2}$), 645.8 (MnO satellite) and 642.1 eV (Mn $2P_{3/2}$) to 653.4, 644.7 and 641.1 eV, respectively, verifying metal-ligand coordination via the electron-donating of the TPY ligands. The aforementioned theoretical (by DFT calculations and MD simulations) and experimental (by XPS spectra) analyses together demonstrate the exceptional functionality of the TPY-CNF in Mn^{2+} chelation, which is therefore anticipated to play a viable role as a chemically active component of the c-mat battery separator.

The pyrrolidone rings of PVP, enabled by their Lewis basicity, are known to effectively scavenge HF dissolved in the electrolyte solution.[29] However, the bare PVP mat (without a PAN component) was chemically vulnerable to the electrolyte solution, resulting in the loss of its dimensional stability (**Figure 5.1.7a**). This problem with PVP was resolved by exploiting a polymer blending strategy in which PAN was mixed with PVP. At the composition ratio of 50/50 (w/w), the resultant PVP/PAN mats maintained their dimensional integrity in the electrolyte solution (**Figure 5.1.7b**). As a supplementary experiment to identify the HF-scavenging capability, the PVP/PAN mat was soaked for 24 h in an electrolyte solution (1 M $LiPF_6$ in EC/diethyl carbonate (DEC) = 1/1 v/v) containing 100 ppm HF, and the change in its XPS spectra was monitored (**Figure 5.1.8**). The characteristic N 1s peak assigned to the nitrogen of pyrrolidone shifted upwards, and a new peak appeared at approximately 400.5 eV, indicating the possible formation of new N–H bonds between pyrrolidone and HF. In comparison, no appreciable change in the N 1s peak was observed for the electrolyte-soaked PAN mat. These results demonstrate the important role of PVP in chemically scavenging HF.

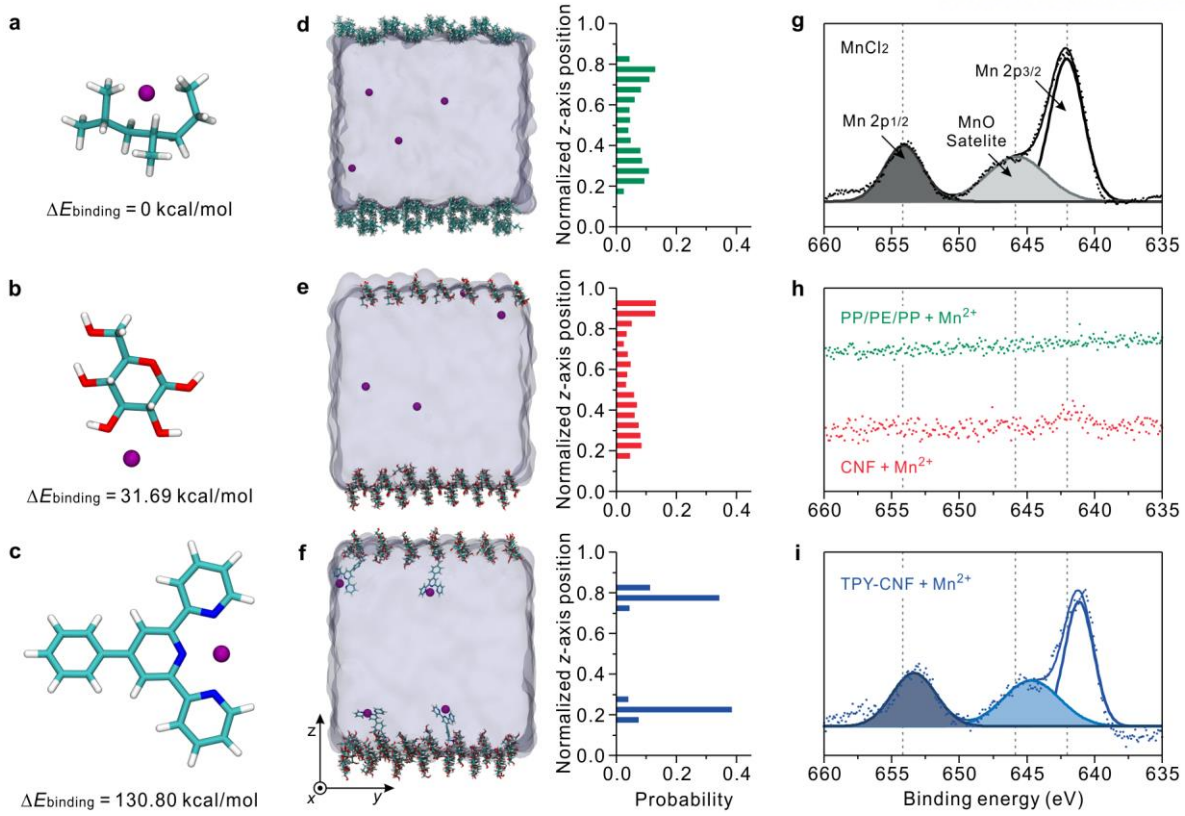

Figure 5.1.6. Mn^{2+} ion binding capability of TPY-CNF. B3LYP/6-31G(d,p)-optimized geometries of (a) $Mn^{2+}(PP_3)$, (b) Mn^{2+}(Glc), and (c) Mn^{2+}(TPY) complexes with the relative binding energies from DFT calculations at B3LYP/6-311+G(2d,2p) level, including BSSE corrections. Equilibrium morphologies after a 400 ns MD simulation at 333 K and normalized *z*-axis position probability of Mn^{2+} ions for the last 100 ns on the surface of (d) PP, (e) cellulose, and (f) TPY-cellulose. Violet beads represent the Mn^{2+} ions, and the ethylene carbonate solvent is shown as a transparent surface for clarity. Deconvoluted high-resolution Mn 2p XPS spectra of (g) PP/PE/PP, (h) CNF, and (i) TPY-CNF with Mn^{2+} ions.

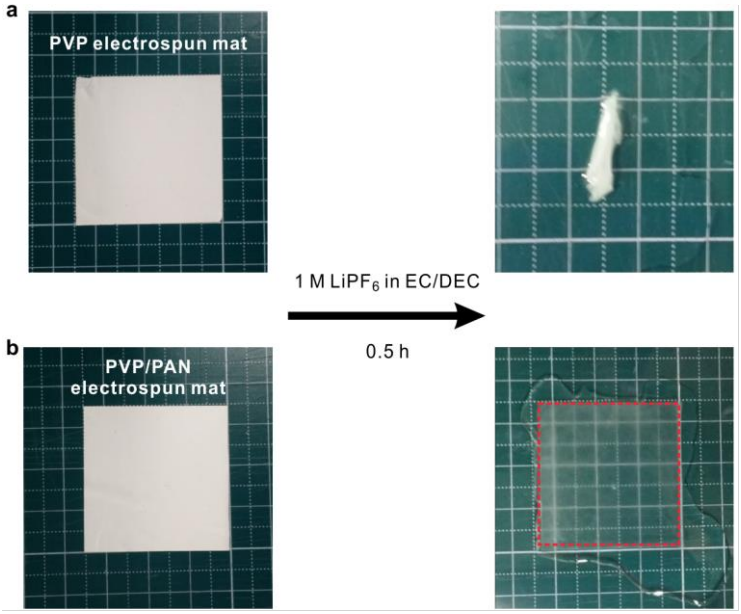

Figure 5.1.7. A photograph showing the structural disruption of the electrospun mat after the mat was immersed in a liquid electrolyte (1.0 M $LiPF_6$ in EC/DEC = 1/1 (v/v)): (a) PVP electrospun mat and (b) PVP/PAN electrospun mat.

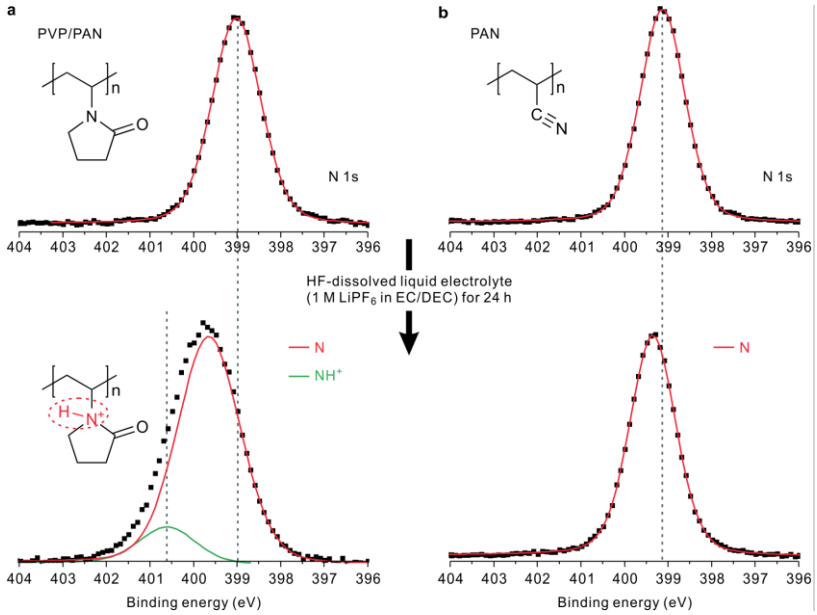

Figure 5.1.8. Variation in the XPS spectra (characteristic peak of nitrogen atoms) of PVP/PAN or PAN films after the films were swelled in a liquid electrolyte (1.0 M $LiPF_6$ in EC/DEC = 1/1 v/v) containing dissolved HF (100 ppm): (a) PVP/PAN film and (b) PAN film.

Prior to exploring the electrochemical performance of the c-mat separator for use in lithium-ion batteries, we characterized its basic membrane properties. The c-mat separator exhibited a higher ion conductivity than the PP/PE/PP separator, which was further confirmed by comparison of their air permeability (represented by the Gurley value) and their porosity (**Table 5.1.1**). These results demonstrate the c-mat separator's superior ionic flux stemming from its unusual hierarchical/asymmetric porous structure. The linear sweep voltammetry (LSV) results showed that the c-mat separator was electrochemically stable to 4.5 V (vs. Li/Li^+), comparable to the stability of the PP/PE/PP separator (**Figure 5.1.9a**). The c-mat separator, as a consequence of its polar components and well-developed porous structure, exhibited a higher electrolyte-immersion height (i.e., better electrolyte wettability) than the PP/PE/PP separator (**Figure 5.1.9b**). This superior wettability was further underscored by examining charge/discharge profiles of cells containing extremely polar electrolyte (here, 1 M $LiPF_6$ in EC/PC = 1/1 (v/v)) was chosen as a representative electrolyte). The cell (LMO cathode/separator/$Li_4Ti_5O_{12}$ anode) assembled with the c-mat separator showed the normal charge/discharge behavior and the stable cycling performance whereas the cell with the PP/PE/PP separator was unable to be electrochemically activated (**Figure 5.1.9c**). No thermal shrinkage was observed in the c-mat separator upon exposure to 150 ºC/0.5 h (**Figure 5.1.9d**), demonstrating its excellent thermal tolerance compared to that of the PP/PE/PP separator.

To investigate the effects of the c-mat separator on cell performance, a pouch-type cell (width × length = 30 × 40 mm^2) was assembled with a LMO cathode and a Li metal anode, in which the TPY-CNF top layer was in contact with the LMO cathode while the PVP/PAN support layer faced the Li metal anode. The c-mat separator, because of its faster ion transport rate (**Table 5.1.1**), exhibited a higher discharge capacity than the PP/PE/PP separator over a wide range of discharge current densities (ranging from 0.2 to 5.0 C), which became more noticeable at higher discharge current densities (**Figure 5.1.10a**). To further highlight the advantageous effect of the c-mat separator, electrochemical performance of a full cell (comprising $LiCoO_2$ (LCO) cathode and natural graphite anode) was examined. The full cell was assembled by sandwiching a separator between LCO cathode (LCO/carbon black/PVdF binder = 95/2/3 (w/w/w)) and natural graphite anode (natural graphite/carbon black/PVdF binder = 90/2/8 (w/w/w)) and then activated by filling the liquid electrolyte. The cells were charged at a constant current density of 0.2 C and were discharged at various current densities (0.2 – 5.0 C) under a voltage range of 3.0 - 4.2 V. Similar to the result obtained with the half cells, the c-mat separator showed the better discharge C-rate capability than the PP/PE/PP separator (**Figure 5.1.10b**).

The cycling performance of cells was examined, and the cells were cycled between 3.0 and 4.3 V at a charge/discharge current density of 1.0C/1.0C. At room temperature, the c-mat separator exhibited a cycling performance superior to that of the PP/PE/PP separator (**Figure 5.1.10c**). This advantageous effect of the c-mat separator was more pronounced during the high-temperature (60 ºC) cycling test. The cell incorporating the c-mat separator delivered stable charge/discharge profiles for

100 cycles (**Figure 5.1.11a**). By comparison, the cell with the PP/PE/PP separator showed a sharp decay in the capacity and large cell polarization after 100 cycles (see the inset of **Figure 5.1.11a**), which were mainly attributed to undesirable Mn^{2+} dissolution from the LMO active materials at high temperatures, as previously reported.[18,30,31] The capacity retention after 100 cycles was estimated to be approximately 80% for the c-mat separator compared to 5% for the PP/PE/PP separator (**Figure 5.1.11b**). This superior capacity retention of the c-mat separator was confirmed through analysis of the variation in the AC impedance spectra of cells before/after 100 cycles (**Figure 5.1.11c** and **5.1.12**). The c-mat separator was better able to suppress the growth of cell impedance after 100 cycles (Z_{Re} (100^{th} cycle) − Z_{Re} (1^{st} cycle) = $\Delta Z_{Re} \approx 17\ \Omega$) compared with the PE separator ($\Delta Z_{Re} \approx 175\ \Omega$). A proper equivalent circuit model was also presented to further analyze the cell impedance spectra in terms of the bulk resistance (R_b), SEI resistance (R_{sf}) and charge transfer resistance (R_{ct}) (**Figure 5.1.12b**).[32] Notably, the c-mat separator exhibited a more substantial decrease in charge transfer resistance compared to that of the PP/PE/PP separator, verifying the Mn^{2+} chelation-enabled stabilization of the electrode/electrolyte interface. In addition, the long-term structural stability of the c-mat separator after the cycling test (100 cycles) was examined. Neither morphological disruptions nor structural defects were observed at the TPY-CNF top layer and also the PVP/PAN support layer of the c-mat separator (**Figure 5.1.13**).

Meanwhile, a supplementary experiment was conducted to investigate the effect of separator position on cell performance. In one cell (named as cell (I)), the TPY-CNF top layer was in contact with the LMO cathode. The other cell (cell (II)) had the opposite configuration (*i.e.*, the TPY-CNF top layer was positioned toward the Li metal anode). Intriguingly, the cell (I) showed the superior cycling performance compared to the cell (II) (**Figure 5.1.14**). This result demonstrates that the Mn^{2+} chelation enabled by the TPY-CNF top layer is more effective when the top layer is in close contact with the LMO cathode.

To highlight the unusual chemical functionalities (i.e., Mn^{2+} chelation by TPY-CNF and HF capture by PVP) of the c-mat separator, we fabricated a control separator comprising a TPY-CNF top layer and an electrospun PAN support layer (without PVP) and compared its cycling performance with that of the c-mat separator (**Figure 5.1.11b**). The control separator showed significant improvement in retaining the capacity during cycling compared to the PP/PE/PP separator, indicating that TPY is effective in chelating the Mn^{2+} ions dissolved from the LMO active materials. A notable finding is that the c-mat separator exhibited cycling performance superior to that of the control separator. This result indicates that the introduction of PVP into the support layer also contributed to the improvement in the high-temperature cycling performance, underlying the exceptional synergistic coupling of TPY and PVP as chemically active components.

The excellent high-temperature cycling performance of the c-mat separator was examined in detail, with particular attention to its Mn^{2+}-chelating and HF-scavenging capability. After the cycling test (100 cycles) at 60 °C, the cells were disassembled, and their major components, including the

lithium metal anodes and separators, were characterized. The amount of Mn^{2+} ions captured by the separators was quantitatively analyzed by ICP-MS technique. **Figure 5.1.11d** shows that the c-mat separator more effectively chelated Mn^{2+} ions than the PP/PE/PP separator (amount of captured Mn^{2+} ions = 1,915 ppm for the c-mat separator *vs*. 42 ppm for the PP/PE/PP separator). Furthermore, the deposition of metallic Mn on lithium metal anodes was remarkably alleviated by the c-mat separator (amount of deposited metallic Mn = 23 ppm for the c-mat separator *vs*. 160 ppm for the PP/PE/PP separator). In addition to the ICP-MS measurement, the chemical changes of the separator surface were investigated through analysis of the FT-IR spectra (**Figure 5.1.11e,f**). The characteristic peaks assigned to the Mn–N stretching vibrations[33,34] (553 cm^{-1} and 851 cm^{-1} for TPY-CNF side, **Figure 5.1.11e**) newly appeared in the spectrum of the c-mat separator. Moreover, the peaks corresponding to C=O/C–N groups[35] (1,661 cm^{-1}/1,285 cm^{-1}, respectively, for the PVP/PAN side, **Figure 5.1.11f**) decreased in intensity after the cycling test. The aforementioned ICP-MS and FT-IR results confirm that the TPY (for Mn^{2+} chelation) and the PVP (for HF capture) of the c-mat separator exhibit synergistically coupled chemical functionalities that improve its high-temperature cycling performance.

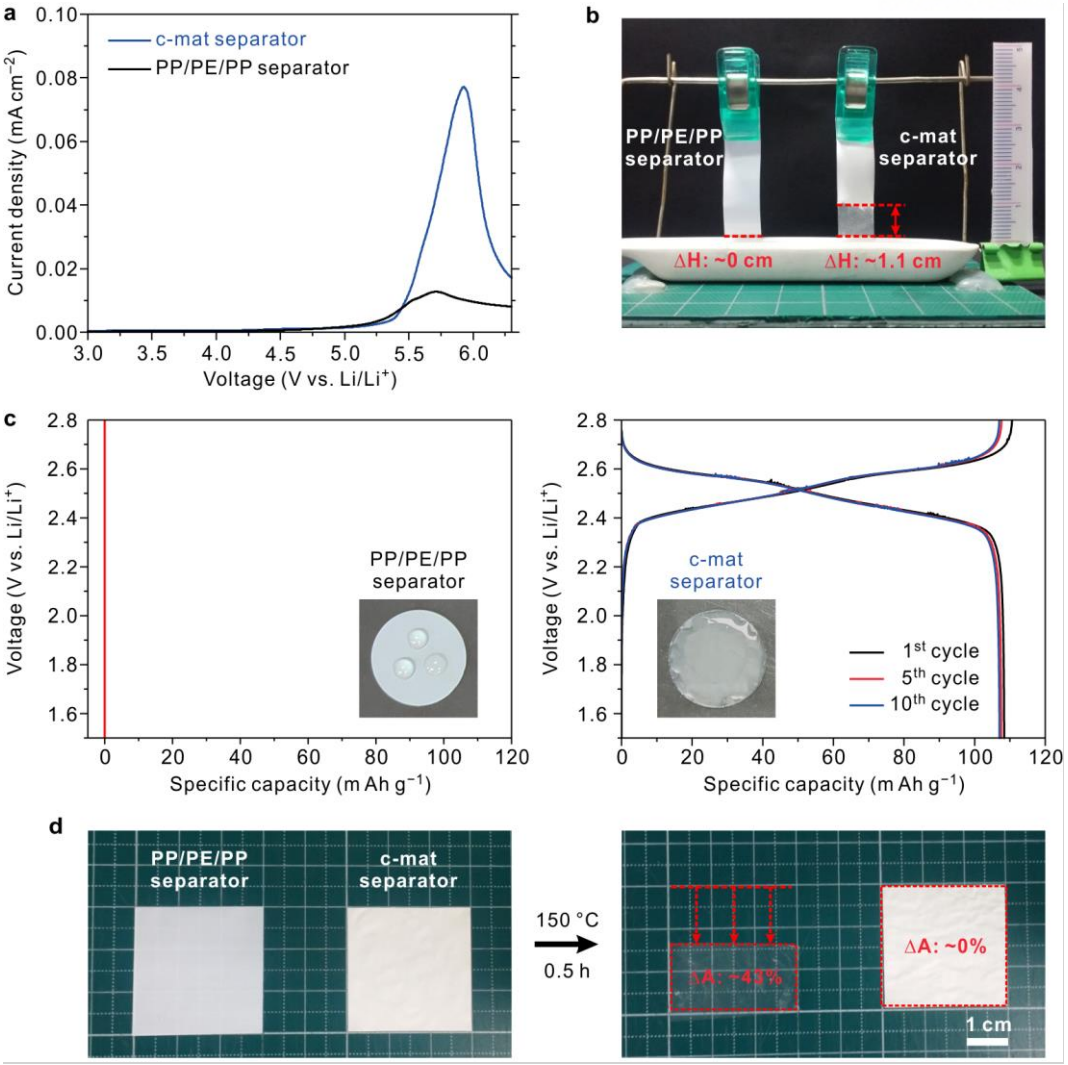

Figure 5.1.9. Characterization of the separator properties. (a) Linear sweep voltammograms. (b) Electrolyte wettability. (c) Effect of polar electrolyte (here, 1.0 M $LiPF_6$ in EC/PC = 1/1 (v/v)) on wettability of separators and charge/discharge profiles of cells incorporating PP/PE/PP separator and c-mat separator. (d) Thermal shrinkage after exposure to 150 ºC/0.5 h.

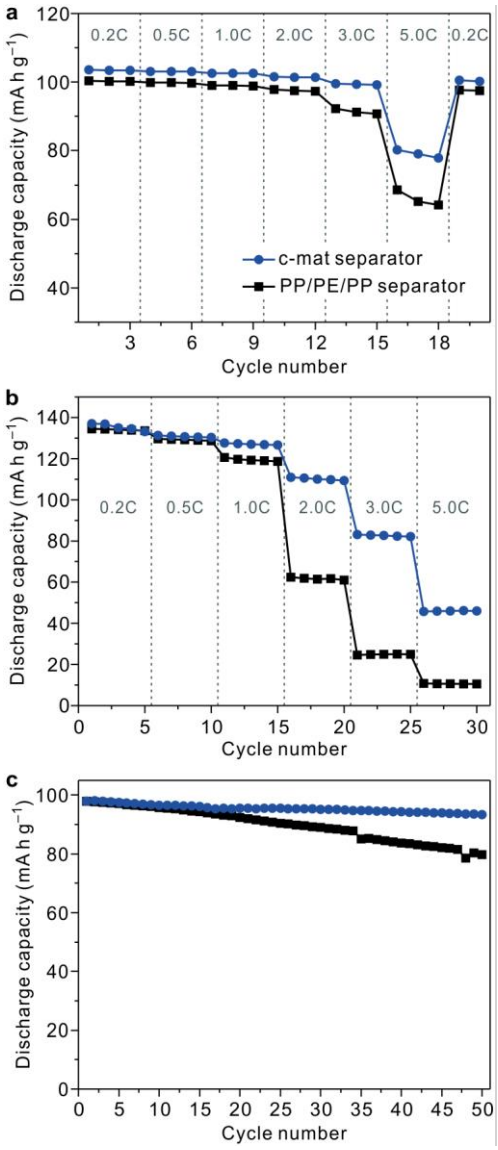

Figure 5.1.10. Comparison of the cell performance (at room temperature) of the c-mat and PP/PE/PP separators: (a) Discharge rate capability (LMO cathode/Li metal anode), (b) Discharge rate capability (LCO cathode/natural graphite anode), and (c) Cycling performance (LMO cathode/Li metal anode).

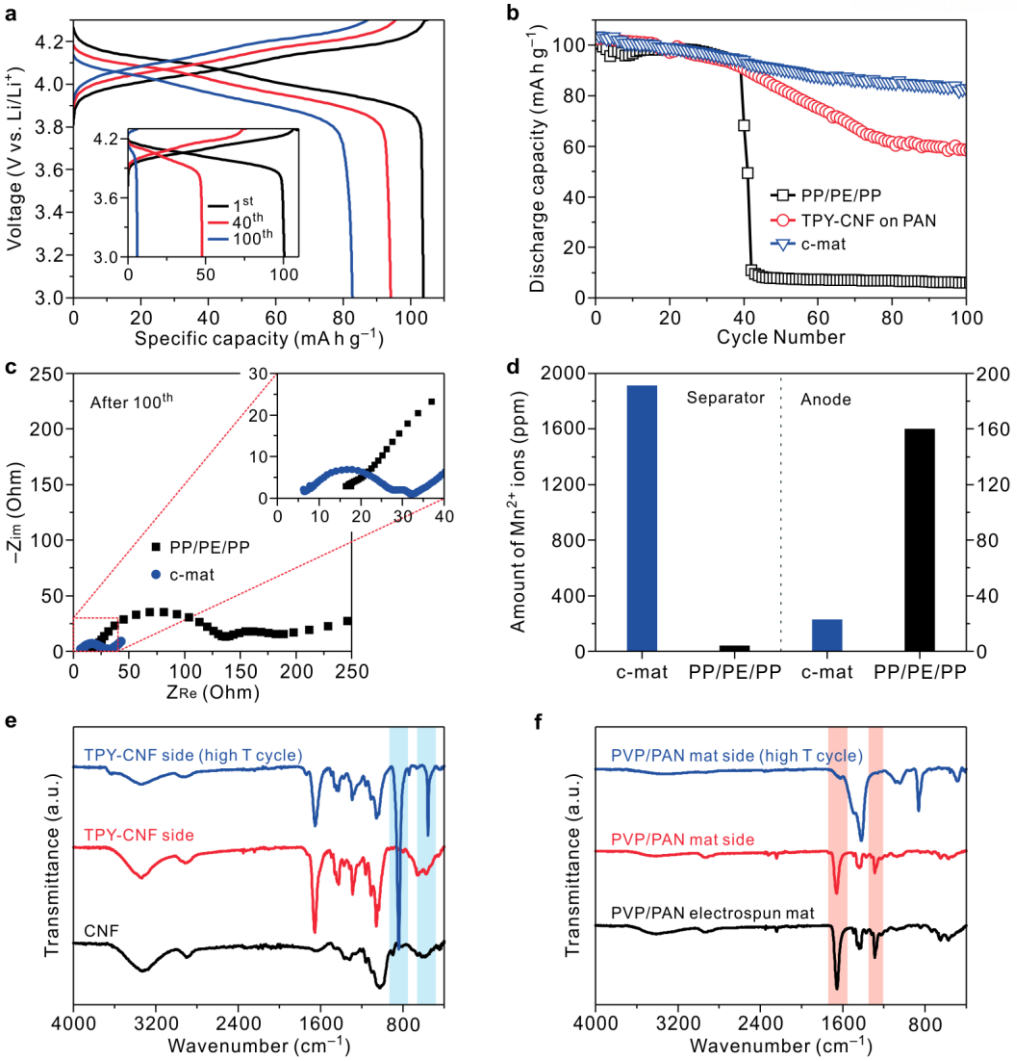

Figure 5.1.11. Cell performance of the c-mat and PP/PE/PP separators. (a) Charge/discharge profiles with cycling (100 cycles) at 60 °C. (b) High-temperature (60 °C) capacity retention as a function of cycle number. (c) AC impedance spectra after 100 cycles at 60 °C. (d) Amount of Mn^{2+} ions captured by separators and deposited on the Li metal anode (estimated from ICP-MS analysis). FT-IR spectra of the (e) TPY-CNF side and (f) PVP/PAN side of the c-mat separator after 100 cycles at 60 °C.

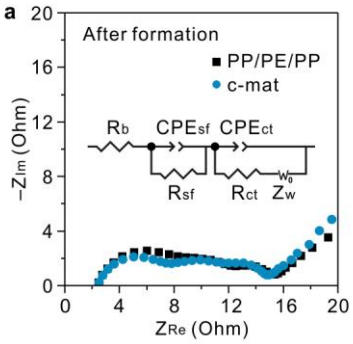

b

Sample	After 1st cycle			After 100th cycle		
	R_b	R_{sf}	R_{ct}	R_b	R_{sf}	R_{ct}
c-mat	1.9	4.1	11.1	4.9	12.9	27.1
PP/PE/PP	2.4	4.3	11.7	9.0	58.3	222.8

Figure 5.1.12. (a) Impedance spectra and (b) summary of the fitting results for the c-mat and PP/PE/PP separators after cycling (at 60 ºC). The inset in part (a) represents the equivalent circuit. Units of R_b, R_{sf} and R_{ct} are in ohms. R_b is the bulk resistance, R_{sf} is the surface resistance, and R_{ct} is the charge transfer resistance. CPE_{sf} and CPE_{ct} are the constant phase elements at high and low frequencies, respectively.

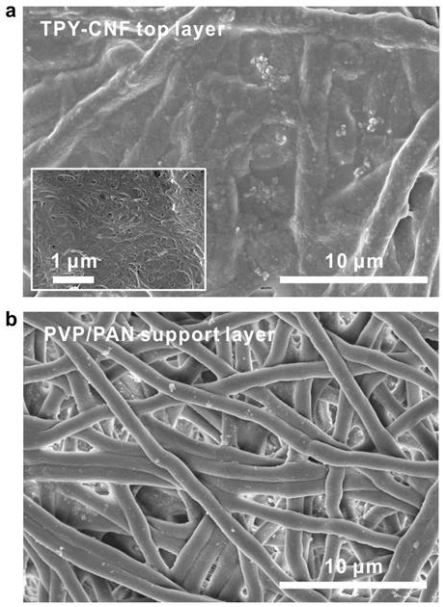

Figure 5.1.13. SEM images showing the long-term structural stability (after 100 charge/discharge cycles at 60 ˚C) of the c-mat separator: (a) TPY-CNF top layer and (b) PVP/PAN support layer.

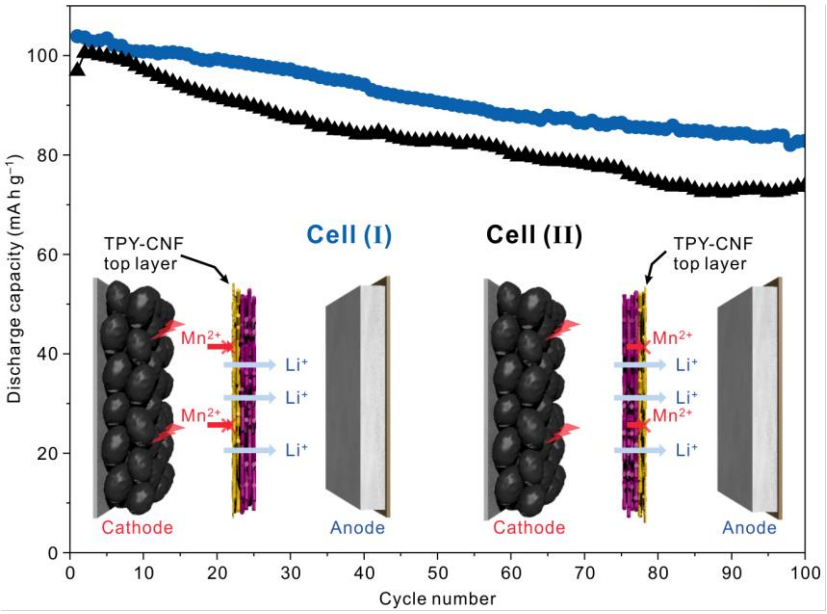

Figure 5.1.14. Comparison of high-temperature (60 ºC) cycling performance between the cell (I) and cell (II), in which the TPY-CNF top layer was in contact with the LMO cathode (for cell (I)) and positioned toward the Li metal anode (for cell (II)).

Table 5.1.1. Basic separator properties of the c-mat and PP/PE/PP separators.

	Thickness	Gurley value	Porosity	Ionic conductivity
	μm	s 100 cc air^{-1}	%	mS cm^{-1}
c-mat separator	~20	10	~65	0.75
PP/PE/PP separator	~20	500	~40	0.6

5.1.5 Conclusion

In summary, we demonstrated the heterolayered nanomatbased hierarchical/asymmetric porous membranes with synergistically coupled chemical functionalities (referred to as c-mat separators) as a nanocellulose-mediated green material approach to develop smart battery separators beyond the current state-of-the-art counterparts. The c-mat separator consisted of a thin nanoporous TPY-CNF mat as the top layer and a thick macroporous electrospun PVP/PAN mat as the support layer. The unusual porous structure of the c-mat separator was rationally designed considering the trade-off between leakage current and ion transport rate, eventually contributing to the higher discharge rate capability without suffering a drop in the OCV. The TPY molecules were conjugated with TEMPO-oxidized CNFs mediated by EDC chemistry. Notably, their Mn2+-chelating capability was also theoretically supported using DFT calculations/MD simulations; the results of these calculations/simulations were consistent with the experimental results. Meanwhile, the PVP in the PVP/PAN support layer served as an HF scavenger. The TPY and PVP, as the chemically active components of the c-mat separator, exhibited synergistic coupling in mitigating the Mn^{2+}-induced adverse effects, thereby enabling a remarkable improvement in the high-temperature (60 °C) cycling performance (capacity retention ~80% after 100 cycles) far beyond that attainable with conventional membrane technologies (5% for commercial PP/PE/PP separator). We envision that the c-mat separator, benefiting from its structural uniqueness and chemical functionalities, will open a new path for the development of high-performance smart separator membranes for potential use in next-generation power sources and in permselective membrane filtration systems for high mass flux/removal of heavy-metal ions.

5.1.6 References

(1) Armand, M.; Tarascon, J.-M. Building Better Batteries. *Nature* **2008,** *451,* 652–657.

(2) Tollefson, J. Charging Up the Future. *Nature* **2008,** *456,* 436–440.

(3) Dunn, B.; Kamath, H.; Tarascon, J.-M. Electrical Energy Storage for the Grid: A Battery of Choices. *Science* **2011,** *334,* 928–935.

(4) Habibi, Y.; Lucia, L. A.; Rojas, O. J. Cellulose Nanocrystals: Chemistry, Self-assembly, and Applications. *Chem. Rev.* **2010,** *110,* 3479–3500.

(5) Moon, R. J.; Martini, A.; Nairn, J.; Simonsen J.; Youngblood, J. Cellulose Nanomaterials Review: Structure, Properties and Nanocomposites. *Chem. Soc. Rev.* **2011,** *40,* 3941–3994.

(6) Leijonmarck, S.; Cornell, A.; Lindbergh G.; Wågberg, L. Flexible Nano-Paper-based Positive Electrodes for Li-Ion Batteries–Preparation Process and Properties. *Nano Energy* **2013,** *2,* 794–800.

(7) Zhu, H.; Jia, Z.; Chen, Y.; Weadock, N.; Wan, J.; Vaaland, O.; Han, X.; Li, T.; Hu, L. Tin Anode for Sodium-Ion Batteries using Natural Wood Fiber as a Mechanical Buffer and Electrolyte Reservoir. *Nano Lett.* **2013,** *13,* 3093–3100.

(8) Hu, L.; Pasta, M.; Mantia, F. L.; Cui, L.; Jeong, S.; Deshazer, H. D.; Choi, J. W.; Han, S. M.; Cui, Y. Stretchable, Porous, and Conductive Energy Textiles. *Nano Lett.* **2010,** *10,* 708–714.

(9) Chun, S.-J.; Choi, E.-S.; Lee, E.-H.; Kim, J. H.; Lee, S.-Y.; Lee, S.-Y. Eco-Friendly Cellulose Nanofiber Paper-Derived Separator Membranes Featuring Tunable Nanoporous Network Channels for Lithium-Ion Batteries. *J. Mater. Chem.* **2012,** *22,* 16618–16626.

(10) Arora, P.; Zhang, Z. Battery Separators. *Chem. Rev.* **2004,** *104,* 4419–4462.

(11) Zhang, S. S. A Review on the Separators of Liquid Electrolyte Li-Ion Batteries. *J. Power Sources* **2007,** *164,* 351–364.

(12) Lee, H.; Yanilmaz, M.; Toprakci, O.; Fu, K.; Zhang, X. A Review of Recent Developments in Membrane Separators for Rechargeable Lithium-Ion Batteries. *Energy Environ. Sci.* **2014,** *7,* 3857–3886.

(13) Whittingham, M. S. Lithium Batteries and Cathode Materials. *Chem. Rev.* **2004,** *104,* 4271–4301.

(14) Zhan, C.; Lu, J.; Kropf, A. J.; Wu, T.; Jansen, A. N.; Sun, Y.-K.; Qiu, X.; Amine, K. Mn(II) Deposition on Anodes and Its Effects on Capacity Fade in Spinel Lithium Manganate–Carbon Systems. *Nat. Commun.* **2013,** *4,* 2437.

(15) Xu, K. Nonaqueous Liquid Electrolytes for Lithium-based Rechargeable Batteries. *Chem. Rev.* **2004,** *104,* 4303–4417.

(16) Yim, T.; Ha, H.-J.; Park, M.-S.; Kim, K. J.; Yu, J.-S.; Kim, Y.-J. A Facile Method for Construction of a Functionalized Multi-Layered Separator to Enhance Cycle Performance of Lithium Manganese Oxide. *RSC Adv.* **2013,** *3,* 25657–25661.

(17) Woo, S. H.; Lim, H.-W.; Jeon, S.; Travis, J. J.; George, S. M.; Lee, S.-H.; Jo, Y. N.; Song, J. H.; Jung, Y. S.; Hong, S. Y.; Choi, N.-S.; Lee, K. T. Ion-Exchangeable Functional Binders and Separator

for High Temperature Performance of $Li_{1.1}Mn_{1.86}Mg_{0.04}O_4$ Spinel Electrodes in Lithium Ion Batteries. *J. Electrochem. Soc.* **2013,** *160,* A2234–A2243.

(18) Kim, J.-M.; Kim, C.; Yoo, S.; Kim, J.-H.; Kim, J.-H.; Lim, J.-M.; Park, S.; Lee, S.-Y. Agarose-Biofunctionalized, Dual-Electrospun Heteronanofiber Mats: Toward Metal-Ion Chelating Battery Separator Membranes. *J. Mater. Chem. A* **2015,** *3,* 10687–10692.

(19) Chen, H.; Tagore, R.; Das, S.; Incarvito, C.; Faller, J. W.; Crabtree, R. H.; Brudvig, G. W. General Synthesis of Di-μ-oxo dimanganese Complexes as Functional Models for the Oxygen Evolving Complex of Photosystem II. *Inorg. Chem.* **2005,** *44,* 7661–7670.

(20) Sakamoto, R.; Wu, K.-H.; Matsuoka, R.; Maeda, H.; Nishihara, H. π-Conjugated Bis(terpyridine) Metal Complex Molecular Wires. *Chem. Soc. Rev.* **2015,** *44,* 7698–7714.

(21) Chun S.-J.; Lee, S-Y.; Doh, G.-H.; Lee, S.; Kim, J. H. Preparation ofUultrastrength Nanopapers using Cellulose Nanofibrils. *J. Ind. Eng. Chem.* **2011,** *17,* 521–526.

(22) Nogi, M.; Iwamoto, S.; Nakagaito, A. N.; Yano, H. Optically Transparent Nanofiber Paper. *Adv. Mater.* **2009,** *21,* 1595–1598.

(23) Leijonmarck, S.; Cornell, A.; Lindbergh, G.; Wågberg, L. Single-Paper Flexible Li-Ion Battery Cells Through a Paper-Making Process based on Nano-Fibrillated Cellulose. *J. Mater. Chem. A* **2013,** *1,* 4671–4677.

(24) Choi, K.-H.; Cho, S.-J.; Chun, S.-J.; Yoo, J. T.; Lee, C. K.; Kim, W.; Wu, Q.; Park, S.-B.; Choi, D.-H.; Lee, S.-Y.; Lee, S.-Y. Heterolayered, One-Dimensional Nanobuilding Block Mat Batteries. *Nano Lett.* **2014,** *14,* 5677–5686.

(25) Cho, S.-J.; Choi, K.-H.; Yoo. J.-T.; Kim, J.-H.; Lee, Y.-H.; Chun, S.-J.; Park, S.-B.; Choi, D.-H.; Wu, Q.; Lee, S.-Y.; Lee, S.-Y. Hetero-Nanonet Rechargeable Paper Batteries: Toward Ultrahigh Energy Density and Origami Foldability. *Adv. Funct. Mater.* **2015,** *25*, 6029–6040.

(26) Kim, J.-H.; Kim, J.-H.; Choi, K.-H.; Yu, H. K.; Kim, J. H.; Lee, J. S.; Lee, S.-Y. Inverse Opal-Inspired, Nanoscaffold Battery Separators: A New Membrane Opportunity for High-Performance Energy Storage Systems. *Nano Lett.* **2014,** *14,* 4438–4448.

(27) Frisch, M. J.; Trucks, G. W.; Schlegel, H. B.; Cheeseman, J. R.; Scalmani, G.; Barone, V.; Mennucci, B.; Petersson, G. A. *Gaussian 09, revision C. 01.*; Gaussian Inc., 2010.

(28) Case, D. A.; Babin, V. Berryman, J. T.; Betz, R. M.; Cai, Q.; Cerutti, D. S.; Cheatham III, T. E.; Darden, T. A.; Duke, R. E.; Gohlke, H. *AMBER 14.*; University of California, 2014.

(29) Kim, J.-M.; Park, J.-H.; Lee C. K.; Lee, S.-Y. Multifunctional Semi-Interpenetrating Polymer Network-Nanoencapsulated Cathode Materials for High-Performance Lithium-Ion Batteries. *Sci. Rep.* **2014,** *4,* 4602.

(30) Cho, J.; Kim, T.-J.; Kim Y. J.; Park, B. Complete Blocking of Mn^{3+} Ion Dissolution from a $LiMn_2O_4$ Spinel Intercalation Compound by Co_3O_4 Coating. *Chem. Commun.* **2001,** 1074–1075.

(31) Lim, S.; Cho, J. PVP-Functionalized Nanometre Scale Metal Oxide Coatings for Cathode Materials:

Successful Application to $LiMn_2O_4$ Spinel Nanoparticles. *Chem. Commun.* **2008,** 4472–4474.

(32) Han, S. C.; Singh, S. P.; Hwang, Y.-H.; Bae, E. G.; Park, B. K.; Sohn, K.-S.; Pyo, M. Gadolinium-Doped $LiMn_2O_4$ Cathodes in Li Ion Batteries: Understanding the Stabilized Structure and Enhanced Electrochemical Kinetics. *J. Electrochem. Soc.* **2012,** *159,* A1867–A1873.

(33) Akyüz, S. The FT-IR Spectroscopic Investigation of Transition Metal(II) 4-Aminopyridine Tetracyanonickelate Complexes. *J. Mol. Struct.* **1999,** *482,* 171–174.

(34) Aghatabay, N. M.; Neshat, A.; Karabiyik, T.; Somer, M.; Haciu, D.; Dülger, B. *Eur.* Synthesis, Characterization and Antimicrobial Activity of Fe(II), Zn(II), Cd(II) and Hg(II) Complexes with 2,6-Bis(benzimidazol-2-yl) pyridine Ligand. *J. Med. Chem.* **2007,** *42,* 205–213.

(35) Borodko, Y.; Habas, S. E.; Koebel, M.; Yang, P.; Frei, H.; Somorjai, G. A. Probing the Interaction of Poly(vinylpyrrolidone) with Platinum Nanocrystals by UV-Raman and FTIR. *J. Phys. Chem. B* **2006,** *110,* 23052–23059.

5.2 Inhibiting the Shuttle Effect in Lithium–Sulfur Batteries using a Layer-by-Layer Assembled Ion-Permselective Separator

5.2.1 Abstract

A novel strategy for introducing ion-permselective properties in a conventional polyethylene (PE) separator to inhibit the shuttle effect of polysulfides in high-performance lithium–sulfur batteries is reported. This was accomplished by taking advantage of the pH-responsive multilayers of weak polyelectrolytes such as poly(allylamine hydrochloride) (PAH) and poly(acrylic acid) (PAA) assembled on the PE separator using layer-by-layer (LbL) assembly. It was found that the cationic permselectivity (permeability of cation/anion) of an ultrathin multilayer coated separator is highly tunable with respect to the number of bilayers and external pH, benefiting from fine tuning of the internal charge density of the multilayered films. The movement of polysulfide anions was significantly inhibited by five bilayers of PAH/PAA (ca. 98% with multilayers assembled at pH 3/3), while the movement of Li cations was preserved. As a result, the ion-permselective separator demonstrated a high initial reversible capacity of ca. 1418 mA h g1 with multilayers assembled at pH 3/3 because of the good permselectivity and the enhanced wetting properties of the LbL treated separator for electrolytes, leading to a significantly improved Coulombic efficiency as compared to a conventional PE separator, i.e., almost 100% over 50 cycles. We anticipate that the permselectivity controllable coating method will be applied for various other membrane technologies.

** Chapter 5.2 is reproduced in part with permission of "M. Gu, J. Lee, Y. Kim, J. S. Kim, B. Y. Jang,* K. T. Lee,* and B.-S. Kim* RSC Advances* **2014**, *4*, 46940–46946*". Copyright 2014 Royal Society of Chemistry*

5.2.2 Introduction

Increasing energy demands, coupled with the limited availability of fossil fuels and their associated environmental issues, have stimulated intense research on energy storage and conversion systems. Although lithium-ion batteries are the leading choice for energy storage today, they cannot sufficiently satisfy long-term storage requirements due to the inherent limitation of gravimetric energy density to meet various energy demands such as the transportation market and energy storage systems.[1] As one of the complements beyond lithium-ion batteries, lithium-sulfur (Li-S) batteries have recently received attention as promising power sources because of their remarkable theoretical specific capacity (1675 mAh g^{-1}) and energy density (2600 Wh kg^{-1}), which are three to five times higher than those of conventional lithium-ion batteries, together with the low cost of abundant sulfur.[2, 3]

Despite these promising features, there are still some issues that need to be resolved, including the poor electronic conductivity of sulfur, dissolution of intermediate polysulfides, and large volume expansion (~80%).[4-6] In particular, the dissolved intermediate of polysulfides (Li_2S_x, $2<x<8$) can diffuse from the cathode to the anode through the separator and this so-called "shuttle effect" can lead to rapid decay of the capacity and poor Coulombic efficiency during charging/discharging cycles. In that regard, there has been significant progress in improving these electrodes by using porous carbon,[7-9] hollow carbon spheres,[10-12] carbon nanotubes (CNT),[13-15] graphene oxide (GO),[16-22] conductive polymer coatings[23-25] and inorganic coatings[26-28] on sulfur particles. On the other hand, despite the separator also being critical to the performance of Li-S batteries, little research has been carried out on the separator. Some examples include, Manthiram and co-workers who reported that polysulfide can be trapped in a 3-dimensional carbon paper as an additional layer on the separator.[29, 30] Liu and co-workers showed that lithiated Nafion ionomer separator film, which is used in proton exchange membrane fuel cells, can be applied to Li-S batteries.[31] Cheng and co-workers introduced a flexible sulfur-carbon nanotube cathode membrane without any metal current collector and binder.[32] Wei and co-workers recently demonstrated a strategy of introducing an electrostatic shield using sulfonate (SO^{3-}) groups of Nafion coating on the Celgard membrane.[33] In addition, composite gel polymer electrolyte has been used as a membrane, instead of separator, in Li-S batteries.[34-36] However, it is still highly desirable to improve the performance of conventional separators.

Alternatively, our approach in this study was to inhibit the shuttle effect of polysulfides by coating the conventional polyethylene (PE) separator with ion-permselective ultrathin films of polyelectrolytes using the layer-by-layer (LbL) assembly method. LbL deposition is a versatile thin film fabrication technique that forms multilayer thin films by depositing alternating layers of oppositely charged materials.[37, 38] One of the advantages of using the LbL method is that it can easily control the composition and thickness of the nanoscale coating using a variety of materials of choice. Because of these unique features, LbL assembly has been applied to various membrane technologies such as proton exchange membrane fuel cells,[39] direct methanol fuel cells,[40-43] vanadium redox flow batteries,[44-46] Li-

air batteries,[47] desalination,[48] and nanofiltration membranes.[49] Furthermore, LbL assembly allows for fine tuning of the internal charge density of multilayer films with changes in the external pH when weak polyelectrolytes such as poly(allylamine hydrochloride) (PAH) and poly(acrylic acid) (PAA) are employed.[50-52] For example, it is known that the degree of ionization of PAH (pKa ~ 9) and PAA (pKa ~ 5) is highly sensitive to the pH of the dipping solution which influences the relative fraction charged to uncharged group such as NH^{3+}/NH_2 for PAH and COO^-/COOH for PAA as well as the population of ionic bonds.

Herein, we fabricated an ion-permselective membrane on a conventional PE separator using LbL assembly to alleviate the shuttle effect of polysulfides in Li-S batteries (**Figure 5.2.1**). This allows the positively charged Li-ion to freely diffuse through the separator, whereas the movement of the negatively charged polysulfide will be inhibited by due to the electrostatic repulsion of the ion-permselective multilayer films bearing large amounts of carboxylic acid groups.

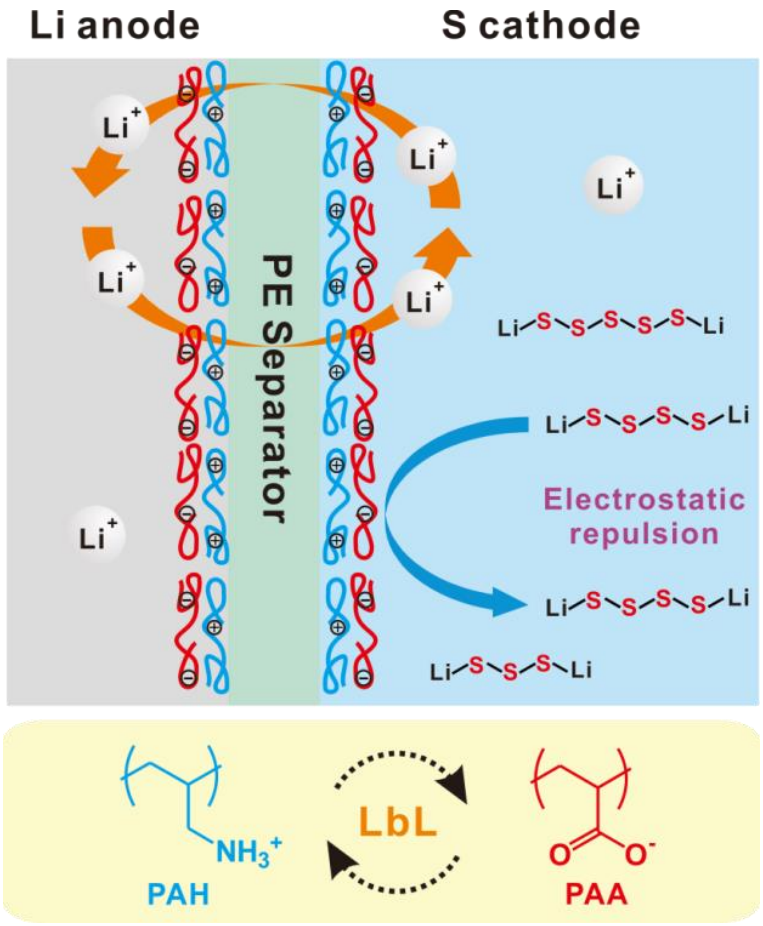

Figure 5.2.1. Schematic representation of layer-by-layer (LbL) assembled $(PAH/PAA)_n$ multilayer coated PE separator for inhibiting the shuttle effect of polysulfide across the separator in a Li-S battery.

5.2.3 Experimental

5.2.3.1 LbL assembly of $(PAH/PAA)_n$ multilayer coated separator

A PE separator (4.5 cm × 8.0 cm) was treated with oxygen plasma (Harrick plasma, PDC-32G) for 1 min to introduce a hydrophilic surface. The PE separator was dipped in a positively charged PAH solution (Sigma-Aldrich, Mw ~15,000, 5 mg/mL) at each pH condition for 10 min. It was then dipped into DI water at the same pH condition three times for 1 min each. Subsequently, the PE separator was dipped in a negatively charged PAA solution (Sigma-Aldrich, Mw ~250,000, 5 mg/mL) at each adjusted pH condition for 10 min, and washed with DI water at the same pH condition three times for 1 min, affording one-bilayer of $(PAH/PAA)_1$. The above procedures were repeated to achieve the desired number of bilayers (typically, n = 2 – 10). These as-assembled $(PAH/PAA)_n$ multilayer coated PE separators were dried at room temperature.

5.2.3.2 Cell assembly and electrochemical test

The active materials were composed of CMK-3 and sulfur at 50:50 weight ratios. Samples of electrochemically active materials were mixed with carbon black and polyvinylidene fluoride (PVdF) at 80:10:20 weight ratios. These as-prepared active materials were loaded on an Al foil current collector. The Li ion cells were assembled in an argon-filled glove box. The electrochemical performance of the Li ion batteries was evaluated using 2032 coin cells (Hohsen Co., Japan), with a Li metal anode and 1.3 M lithium bis(trifluoromethanesulfonyl)imide (LiTFSI) in tetraethylene glycol dimethyl ether (TEGDME) electrolyte solution. LbL coated PE film was used as a separator. Galvanostatic experiments were performed in the voltage range of 1.5 to 2.6 V at a 0.05 C-rate and a temperature of 30 °C.

5.2.3.3 Ion-permselective property test

A three-electrode cell was used at a scan rate of 100 mV s^{-1}. The PAH/PAA multilayer coated ITO glasses at each pH were used as the working electrodes. A platinum wire was used as a counter electrode, and Ag/AgCl (3.0 M NaCl) was used as a reference electrode. The electrolyte solution was prepared by adding 5 mM of either $Fe(CN)_6^{3-}$ or $Ru(NH3)_6^{3+}$ to 0.50 M Na_2SO_4 at pH 6. The measured current was divided by the area of the ITO electrode immersed in electrolyte solution (in our case 1.05 cm^2) to obtain the current density value.

5.2.3.4 Characterizations

Attenuated total reflectance-infrared (ATR-IR) spectra were analyzed with a FT-IR spectrophotometer (Varian, 670-IR). The surface morphology of the samples was investigated using a scanning electron microscope (FESEM, FEI, Nanonova 230). The contact angle was obtained using a contact angle analyzer (KRÜSS, DSA 100). The thickness of the as-prepared samples on the silicon substrates was measured by ellipsometry (J. A. Woollam Co. Inc., EC-400 and M-2000V).

5.2.4 Results and Discussion

Since both polymers employed in this study are weak polyelectrolytes, we investigated the assembly of PAH and PAA polyelectrolytes based on three different conditions in this study, namely pH 3/3, 6/3, and 8.5/8.5 for PAH/PAA. Initially, we monitored the stepwise fabrication of PAH/PAA multilayer films on a silicon wafer by using a spectroscopic ellipsometry. As shown in **Figure 5.2.2a**, the growth of the $(PAH/PAA)_n$ is linear with respect to the number of bilayers in both pH 3/3 and 8.5/8.5 conditions; however, it becomes exponential in the case of the pH 6/3 condition. It was found that the average thickness of one bilayer of (PAH/PAA) film corresponds to 3.6 nm (pH 3/3), 20.1 nm (pH 6/3), and 2.1 nm (pH 8.5/8.5), respectively. Similar to other reported systems, the assembly pH of each polymer is critical in determining the final thickness and composition of the resulting multilayers; for example, when both PAH and PAA are deposited at pH 3/3, the PAH is fully ionized while PAA is ionized less than 1% considering its pK_a value of ~5. Thus, the loopy PAA chains that contain a large amount of free carboxylic acid groups make complexes with example, PAA is now fully ionized (more than 60%) while the degree of ionization in the PAH chain is modestly diminished. Therefore, PAH adsorbs tightly onto the highly ionized PAA surface chains, forming a thinner layer. On the other hand, the pH 6/3 condition, moderately charged PAH alternated with partially charged PAA polymers, yields the thickest films. This is because the pH of the dipping solution not only affects the ionization of polyelectrolytes in solution, but it also changes the ionization of the polyelectrolytes multilayers on which adsorption occurs. Specifically, the pre-adsorbed PAA chains undergo a drastic charge density increase when the pH changed from 3 to 6, which in turn recruit more PAH chains to compensate for the increased charge density of the PAA chains, eventually leading to the formation of the thickest bilayers with an exponential growth behavior.

Once we confirmed the successful fabrication of multilayer films, we fabricated $(PAH/PAA)_n$ multilayers on the conventional PE separator at three different pH conditions. In order to enhance the wettability of the conventional hydrophobic PE membrane, the PE separator was initially subjected to oxygen plasma treatment for 1 min. The oxygen plasma treatment changed the contact angle of a water droplet on the surface of PE from 119° to 87°. In addition, it was observed that the oxygen plasma treatment did not significantly damage the surface structure of PE separator under scanning electron microscopy (SEM) (**Figure 5.2.3**). Attenuated total reflectance-infrared (ATR-IR) spectroscopy was employed to monitor the characteristic peaks of the multilayer coated PE corresponding to the functional groups present in the polyelectrolytes as in **Figure 5.2.4**. Five bilayer films of $(PAH/PAA)_5$ coated PE separator all showed the characteristic peaks of the PE separator with a scissoring band of the methylene ($-CH_2-$) backbone of PE at 1462 and 1473 cm^{-1}. the C=O stretching vibration peaks of carboxylic acid (-COOH) at 1712 cm^{-1} and carboxylate ($-COO^-$) peaks at 1541 cm^{-1} and 1400 cm^{-1}. As expected, the transition from carboxylic acid groups to the carboxylate of PAA is well observed with increasing pH of the dipping solution. For instance, according to the peak intensity in the IR spectra,

the relative fraction of carboxylate (COO^-) to carboxylic acid (COOH) at pH 3/3, 6/3, and 8.5/8.5 was determined to be 0.5, 1.31 and 3.33, respectively. This distinctly proved that the pH sensitive behavior of PAH/PAA multilayer films affect the LbL architecture, as shown in previous thickness growth curve (**Figure 5.2.2**).

On the basis of the stable coating of the polyelectrolytes on the PE separator, we studied the surface morphology of the PE separator with a different number of bilayers that are assembled at respective pH conditions using a scanning electron microscopy (SEM) in **Figure 5.2.5**. The first few layers of the polyelectrolyte coatings were hard to discern clearly due to the low contrast, yet we found that bare PE separators with a unique network of interconnected large pores were present. With increasing the number of bilayers, however, the pores of the bare PE separator were gradually blocked by the coated $(PAH/PAA)_n$ multilayer films. In particular, the pores of the PE separator were almost completely blocked by the thickest films of $(PAH/PAA)_5$ assembled at pH 6/3 in accord with the previous results of thickness measurements. Moreover, the surface property of the multilayer coated PE was also investigated with contact angle measurements, which revealed the internal composition of the polyelectrolytes within the multilayers. This is because the underlying layer of the LbL films is known to influence the surface property of films in concert with the previous literature of $(PAH/PAA)_n$ multilayer systems.[53] As a result, the PAH-rich multilayers displayed a more hydrophobic surface, as evidenced by the high pH assembly conditions of pH 8.5/8.5, whereas PAA-rich multilayers retained a more hydrophilic surface in the film assembled at pH 3/3 condition. On the other hand, because the segments of PAH and PAA are present in a similar amount in the case of pH 6/3, contact angle decreased at initial stage but increased gradually because of the exponential growth of the LbL films and enhanced surface roughness. These results are in good agreement with previous reports on which how different assembly conditions can lead to the internal structure of polyelectrolytes multilayers and their modified thin films.

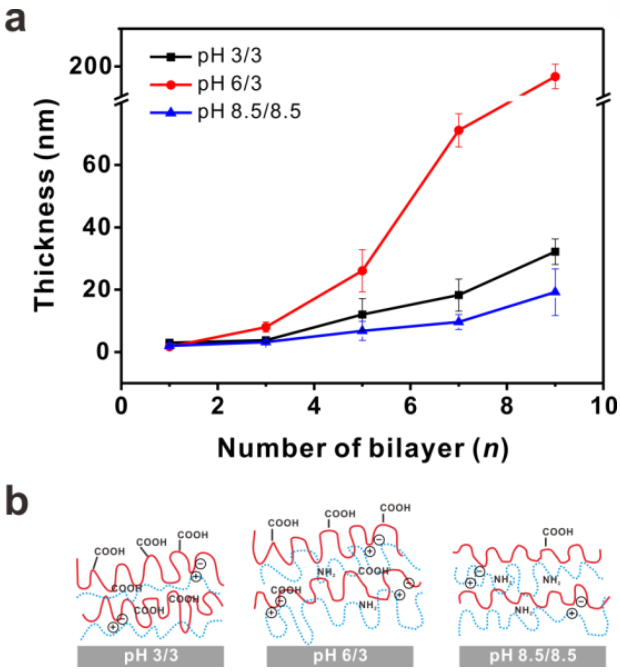

Figure 5.2.2. a) Thickness growth curve of the $(PAH/PAA)_n$ multilayer thin films on a silicon wafer with respect to the assembly pH conditions and b) schematic representation of the internal structure of $(PAH/PAA)_n$ multilayer thin films assembled at different pH conditions. Thickness was measured in five independent measurements with ellipsometry.

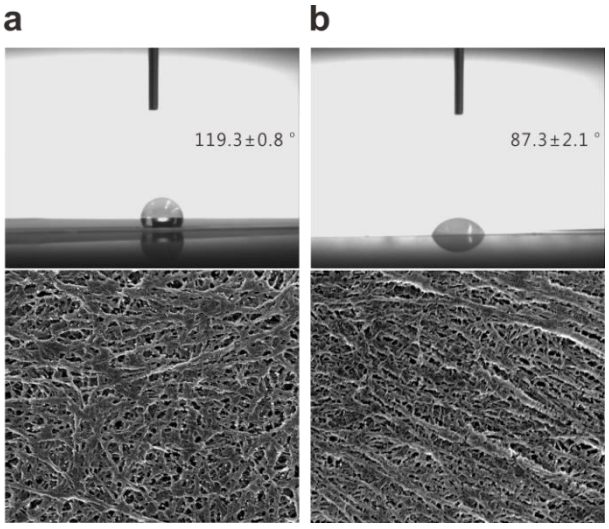

Figure 5.2.3. Contact angle and SEM images of a) bare PE and b) O_2-plasma treated PE separator.

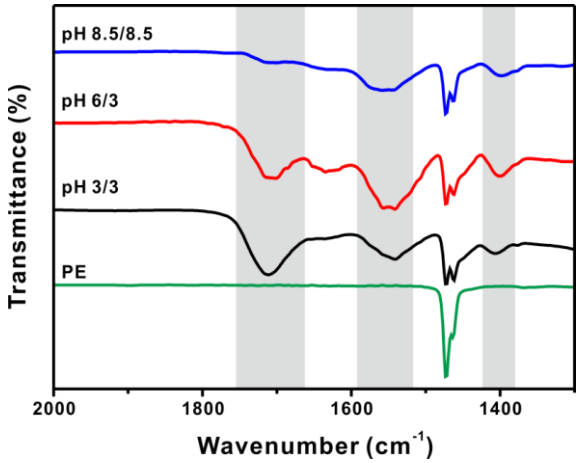

Figure 5.2.4. ATR-IR spectra of $(PAH/PAA)_5$ multilayer coated PE-separator at each assembly pH.

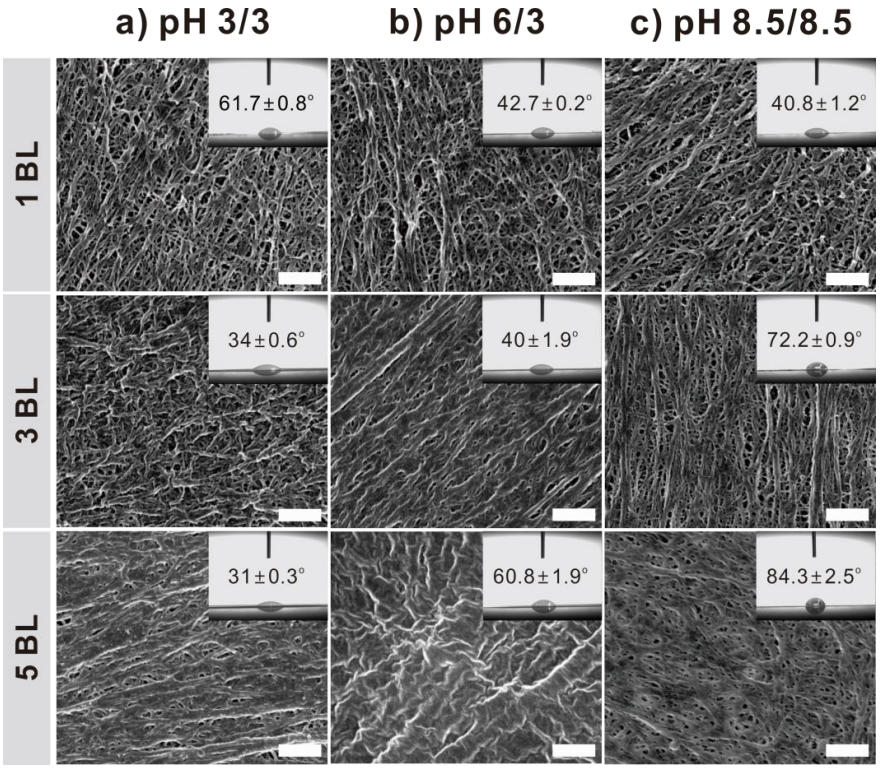

Figure 5.2.5. SEM images of PAH/PAA 1, 3, and 5 bilayer (BL) coated on separator by LbL assembly at a) pH 3/3, b) pH 6/3 and c) pH 8.5/8.5. The scale bar of each image is 1 μm.

To evaluate the ion-permselectivity of the multilayers that are assembled at different pH conditions, we used two different charged redox probe molecules, such as cationic $Ru(NH_3)_6^{3+}$ and anionic $Fe(CN)_6^{3-}$, respectively. Cyclic voltammogram (CV) analysis was carried out using $(PAH/PAA)_n$ multilayer coated ITO glass at pH 3/3. As shown in **Figure 5.2.6**, the cationic charge probe, $Ru(NH_3)_6^{3+}$, can penetrate through the PAH/PAA films, but the current density diminished marginally with the increase of film thickness because of the limited diffusion of the small molecule through the polyelectrolyte multilayers (*ca*. 15% with 5 BL film). In clear contrast, the movement of the anionic probe, $Fe(CN)_6^{3-}$, is significantly inhibited by the $(PAH/PAA)_n$ films, indicating a 72% decrease in current density even at 1 BL film and decreases further with growth of the $(PAH/PAA)_n$ films (*ca.* 98% with 5 BL). This observation can be explained by the following. At pH 3/3, PAA containing free carboxyl acid groups is adsorbed on fully ionized PAH. If this LbL film is dipped in a neutral solution above the pK_a of PAA, the many free carboxyl acid groups of PAA are deprotonated, forming carboxylate groups. As a result, the internal charge density of the $(PAH/PAA)_5$ films becomes considerably more negative, which repels anionic probe molecules like $Fe(CN)_6^{3-}$. This cation-exchangeable property was also seen at pH 6/3 and pH 8.5/8.5, but the amount of negative charges in the LbL films was different (**Figure 5.2.7**). Cationic retention (I^+/I_o^+ ,where I^+ is current density at each condition, and I_o^+ is current density on bare electrode of cation) of 5 BL at pH 3/3, 6/3, and 8.5/8.5 was maintained at 85%, 47%, and 59%, respectively, (**Figure 5.2.8a**), while anionic retention (I^-/I_o^- , where I^- is current density at each condition, and I_o^- is current density on bare electrode of anion) noticeably decreased to 2%, 1.4%, and 2.6%, respectively, with 5 BL (**Figure 5.2.8b**). In other words, LbL multilayer coating has an ion-permselective property similarly observed in other works,[52, 54] and our system is only cation-exchangeable. Furthermore, we calculated the cationic permselectivity (P^+) under different conditions using a simple equation (1).

$$P^+ = \frac{I^+/I_o^+}{I^-/I_o^-} \qquad (1)$$

As a result, cationic permselectivity increased at all of the pH conditions with respect to the number of bilayers. However, pH 3/3 showed the best ion-permselective property (pH 3/3 > pH 6/3 > pH 8.5/8.5), which corresponds to the amount of free carboxyl acid groups in PAA.

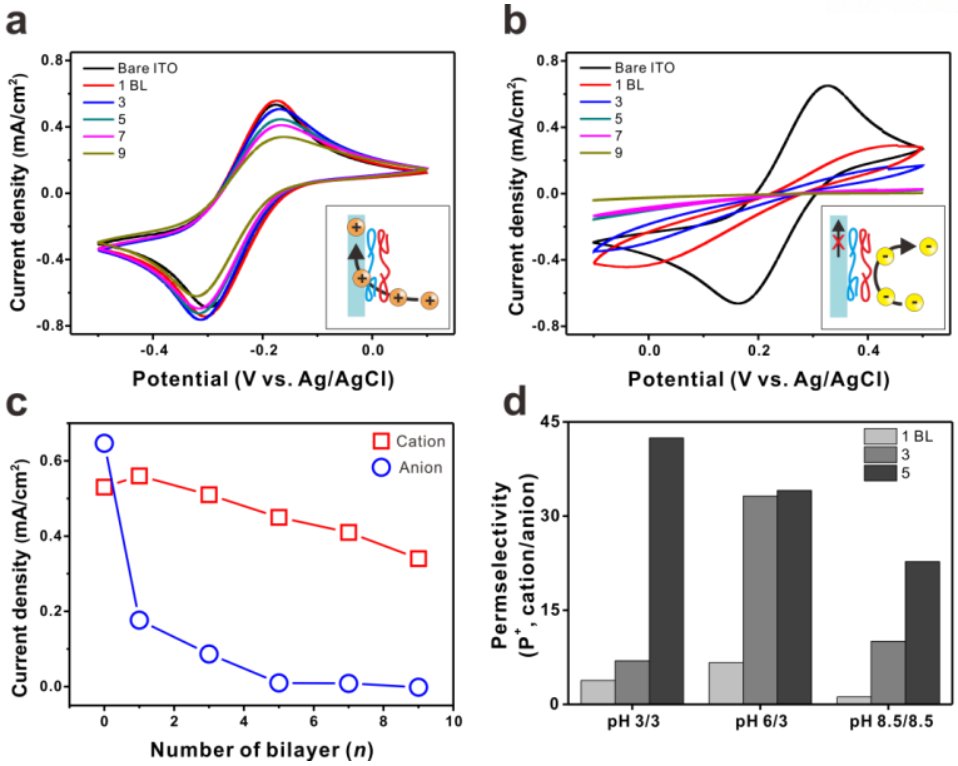

Figure 5.2.6. Cyclic voltammograms (CV) of $(PAH/PAA)_n$ multilayer of pH 3/3 coated on ITO glass by LbL assembly in an aqueous 0.50 M Na_2SO_4 electrolyte solution containing 5.0 mM of a) $Ru(NH_3)_6^{3+}$ as the cationic and b) $Fe(CN)_6^{3-}$ as the anionic probes, respectively. Inset image shows the schematic representation of the cation exchange property of LbL thin films. c) The comparison of anodic peak current density of each ion species. d) Calculated permselectivity, P^+, (selectivity ratio of cation to anion) with different numbers of bilayers and pH conditions.

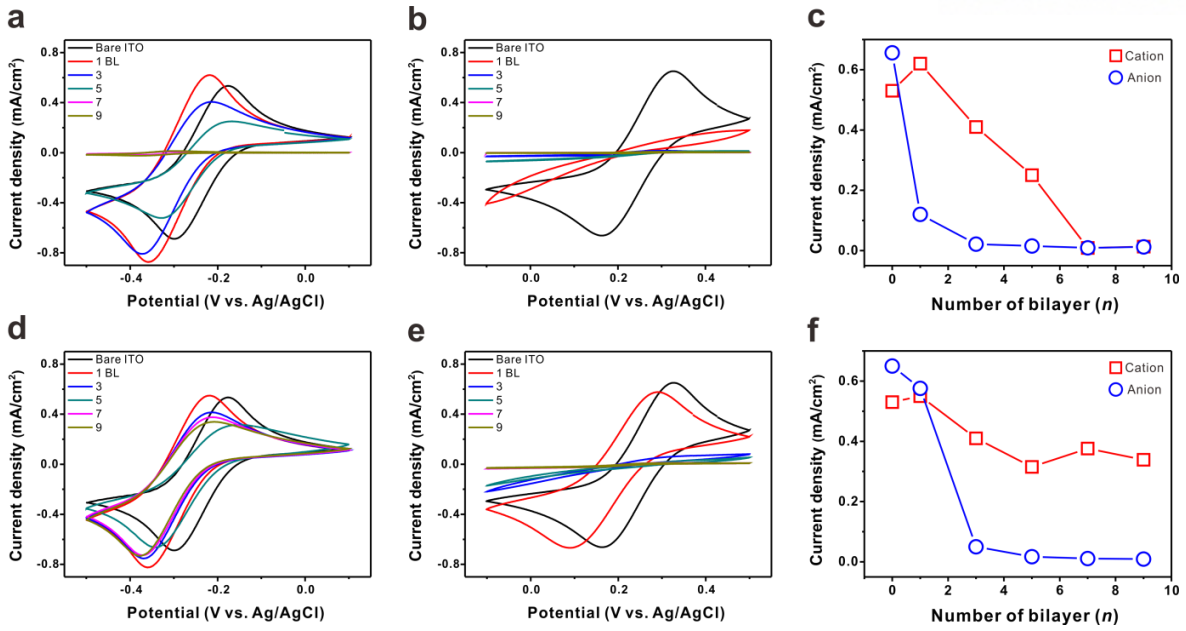

Figure 5.2.7. Cyclic voltammograms (CV) of $(PAH/PAA)_n$ multilayer of (a-b) pH 6/3 and (d-e) pH 8.5/8.5 coated on ITO glass by LbL assembly in aqueous 0.5 M Na_2SO_4 neutral electrolyte solution containing 5.0 mM of (a, d) $Ru(NH_3)_6^{3+}$ as the cationic and (b, e) $Fe(CN)_6^{3-}$ as the anionic probes, respectively. Comparison of the anodic peak current density of each ion species at c) pH 6/3 and f) pH 8.5/8.5.

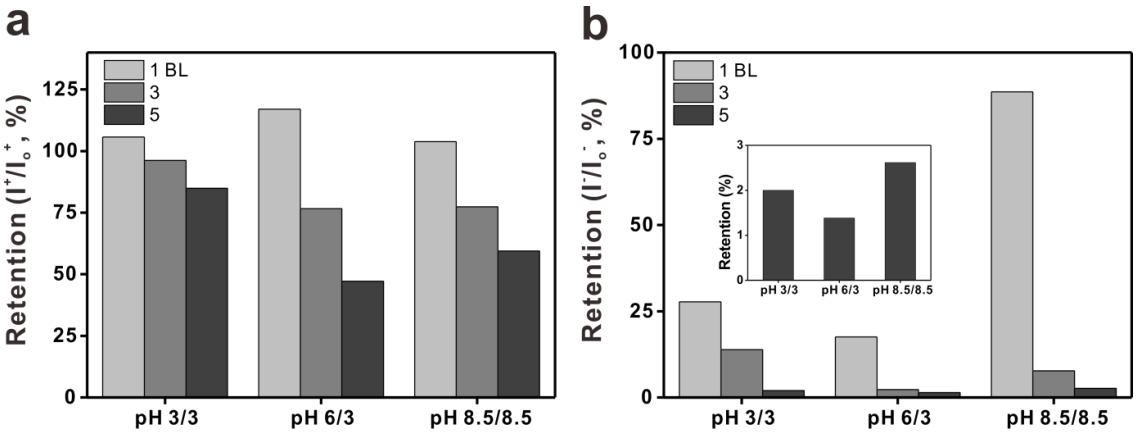

Figure 5.2.8. a) Cationic retention and b) anionic retention of 1, 3, 5 BL of $(PAH/PAA)_n$ assembled at pH 3/3, 6/3, and 8.5/8.5.

The electrochemical performance of CMK-3/S using bare PE and $(PAH/PAA)_5$ coated PE separators at each pH were compared (**Figure 5.2.9**). Note that any additive such as lithium nitrate forming stable passivation films on Li metal was not used to evaluate the inherent effect of separators on the shuttle phenomena of dissolved polysulfides, because it is well-known that stable passivation layers on Li itself inhibit the shuttle effect. The key parameter determining the appearance of the shuttle effect is Columbic efficiency which was defined as the ratio of discharge capacity to charge capacity, because charge capacity surpasses the discharge capacity when dissolved polysulfides cause self-discharges (shuttle effect). Remarkably, all of the LbL treated separators show highly improved Coulombic efficiencies with almost 100%, which means the shuttle effect of polysulfide is effectively inhibited, which is shown by comparing each pH to the bare PE separator in **Figure 5.2.9c**. The Coulombic efficiency of the bare PE separator was 59% at minimum and 69% after 50 cycles. However, pH 3/3, pH 6/3 and pH 8.5/8.5 maintain the Coulombic efficiency with 98%, 104%, and 99%, respectively. This clearly demonstrated that the ion-permselective LbL thin film coating on the PE separator effectively inhibited the movement of the dissolved polysulfides from the cathode to anode in Li-S batteries. The CMK-3/S electrodes with the bare PE separator and PAH/PAA coated separators at pH 3/3, and 8.5/8.5 delivered high reversible capacities of *ca*. 1302, 1418, and 1350 mA h g^{-1} at the first cycle, respectively (**Figure 5.2.9d** and **5.2.10**), indicating Li^+ ion conduction through both the bare and PAH/PAA coated separators is fast enough because of the good wetting property of both separators for electrolytes. However, the reversible capacity of pH 6/3 was significantly lower than that of any other cases, which is attributed to the fact that Li ions cannot diffuse into the separator because the pores of the separator were clogged by the densely packed coating layers as shown in **Figure 5.2.5b**. In addition, owing to the inhibited shuttle effect of the coated separators, the pH 3/3 and 8.5/8.5 conditions showed better cycle performance than the bare separator (**Figure 5.2.9d**). Moreover, the pH 3/3 exhibited slightly better capacity retention than the 8.5/8.5. This is attributed to that the amount of loaded PAA on the pH 3/3 LbL film is much higher than that of PAH, and the charge of LbL film is also highly negative. The negatively charged intensity of the pH 8.5/8.5 LbL film is relatively weaker because of the smaller amount of COOH of in the PAA chains than at pH 3/3 condition.

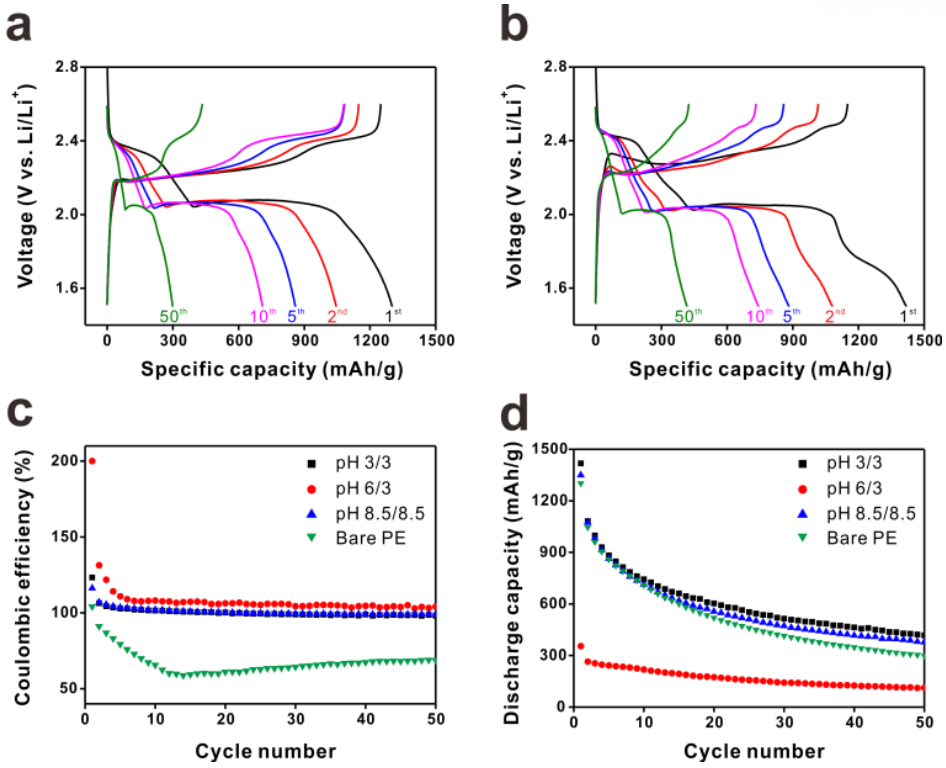

Figure 5.2.9. Voltage profiles of the a) bare PE separator and b) $(PAH/PAA)_5$ coated PE separator at pH 3/3. c) Cycle performance and d) Coulombic efficiency of the $(PAH/PAA)_5$ coated separator at each pH and comparison to bare PE separator.

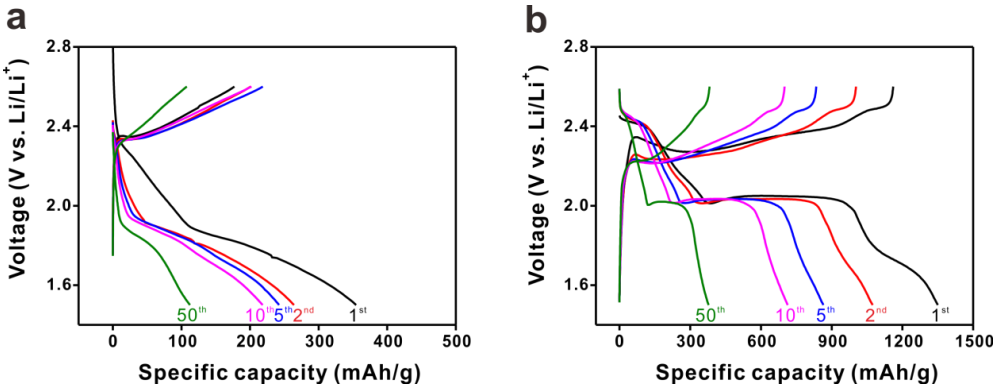

Figure 5.2.10. Voltage versus specific discharge capacity profiles of the $(PAH/PAA)_5$ at a) pH 6/3 and b) pH 8.5/8.5.

5.2.5 Conclusion

In conclusion, we have developed a simple method of constructing polymer coated separators by nanoscale thin film coating LbL assembly. The separator prepared by the LbL method offers precise control not only over the thickness of the coating films, but also the charge density of the whole films by changing the number of bilayers as well as external pH conditions (pH 3/3, 6/3, and 8.5/8.5) that can control the relative fraction of charged carboxylate group over noncharged carboxylic acid group. Especially, the case of pH 3/3, which has large amount of free carboxyl acid groups in PAA, showed the best cationic permselectivity, necessary for inhibiting the shuttle effect. As a result, ion-permselective separators showed the enhanced Coulombic efficiency reaching almost 100% and cycle performance of Li–S batteries. This study introduces a new strategy for creating the separator in Li–S batteries that can decrease the migration of soluble high-order Li–polysulfide (Li_2S_3 to Li_2S_6) from the cathode to the anode through the separator.

5.2.6 References

(1) Bruce, P. G.; Freunberger, S. A.; Hardwick, L. J.; Tarascon, J. M. Li-O_2 and Li-S batteries with high energy storage. *Nat. Mater.* **2012,** *11*, 19-29.

(2) Choi, N.-S.; Chen, Z.; Freunberger, S. A.; Ji, X.; Sun, Y.-K.; Amine, K.; Yushin, G.; Nazar, L. F.; Cho, J.; Bruce, P. G. Challenges Facing Lithium Batteries and Electrical Double-Layer Capacitors. *Angew. Chem. Int. Ed.* **2012,** *51*, 9994-10024.

(3) Song, M.-K.; Cairns, E. J.; Zhang, Y. Lithium/Sulfur Batteries with High Specific Energy: Old Challenges and New Opportunities. *Nanoscale* **2013,** *5*, 2186-2204.

(4) Yang, Y.; Zheng, G. Y.; Cui, Y. Nanostructured Sulfur Cathodes. *Chem. Soc. Rev.* **2013,** *42*, 3018-3032.

(5) Evers, S.; Nazar, L. F. New Approaches for High Energy Density Lithium-Sulfur Battery Cathodes. *Acc. Chem. Res.* **2013,** *46*, 1135-1143.

(6) Wang, D.-W.; Zeng, Q.; Zhou, G.; Yin, L.; Li, F.; Cheng, H.-M.; Gentle, I. R.; Lu, G. Q. M. Carbon-Sulfur Composites for Li-S Batteries: Status and Prospects. *J. Mater. Chem. A* **2013,** *1*, 9382-9394.

(7) Ji, X.; Lee, K. T.; Nazar, L. F. A Highly Ordered Nanostructured Carbon-Sulphur Cathode for Lithium-Sulphur Batteries. *Nat. Mater.* **2009,** *8*, 500-506.

(8) Zheng, G.; Zhang, Q.; Cha, J. J.; Yang, Y.; Li, W.; Seh, Z. W.; Cui, Y. Amphiphilic Surface Modification of Hollow Carbon Nanofibers for Improved Cycle Life of Lithium Sulfur Batteries. *Nano Lett.* **2013,** *13*, 1265-1270.

(9) Moon, S.; Jung, Y. H.; Jung, W. K.; Jung, D. S.; Choi, J. W.; Kim, D. K. Encapsulated Monoclinic Sulfur for Stable Cycling of Li-S Rechargeable Batteries. *Adv. Mater.* **2013,** *25*, 6547-6553.

(10) Schuster, J.; He, G.; Mandlmeier, B.; Yim, T.; Lee, K. T.; Bein, T.; Nazar, L. F. Spherical Ordered Mesoporous Carbon Nanoparticles with High Porosity for Lithium-Sulfur Batteries. *Angew. Chem. Int. Ed.* **2012,** *51*, 3591-3595.

(11) Zhang, C.; Wu, H. B.; Yuan, C.; Guo, Z.; Lou, X. W. Confining Sulfur in Double-Shelled Hollow Carbon Spheres for Lithium-Sulfur Batteries. *Angew. Chem. Int. Ed.* **2012,** *51*, 9592-9595.

(12) Xin, S.; Yin, Y.-X.; Wan, L.-J.; Guo, Y.-G. Encapsulation of Sulfur in a Hollow Porous Carbon Substrate for Superior Li-S Batteries with Long Lifespan. *Part. Part. Syst. Char.* **2013,** *30*, 321-325.

(13) Wang, L.; Dong, Z.; Wang, D.; Zhang, F.; Jin, J. Covalent Bond Glued Sulfur Nanosheet-Based Cathode Integration for Long-Cycle-Life Li-S Batteries. *Nano Lett.* **2013,** *13*, 6244-6250.

(14) Fu, Y.; Su, Y.-S.; Manthiram, A. Highly Reversible Lithium/Dissolved Polysulfide Batteries with Carbon Nanotube Electrodes. *Angew. Chem. Int. Ed.* **2013,** *52*, 6930-6935.

(15) Choi, J.-H.; Lee, C.-L.; Park, K.-S.; Jo, S.-M.; Lim, D.-S.; Kim, I.-D. Sulfur-Impregnated MWCNT Microball Cathode for Li-S Batteries. *RSC Adv.* **2014,** *4*, 16062-16066.

(16) Lu, S.; Chen, Y.; Wu, X.; Wang, Z.; Li, Y. Three-Dimensional Sulfur/Graphene Multifunctional Hybrid Sponges for Lithium-Sulfur Batteries with Large Areal Mass Loading. *Sci. Rep.* **2014,** *4*, 4629-

4632.

(17) Rong, J.; Ge, M.; Fang, X.; Zhou, C. Solution Ionic Strength Engineering As a Generic Strategy to Coat Graphene Oxide (GO) on Various Functional Particles and Its Application in High-Performance Lithium-Sulfur (Li-S) Batteries. *Nano Lett.* **2014,** *14*, 473-479.

(18) Lu, S.; Cheng, Y.; Wu, X.; Liu, J. Significantly Improved Long-Cycle Stability in High-Rate Li-S Batteries Enabled by Coaxial Graphene Wrapping over Sulfur-Coated Carbon Nanofibers. *Nano Lett.* **2013,** *13*, 2485-2489.

(19) Xiao, M.; Huang, M.; Zeng, S.; Han, D.; Wang, S.; Sun, L.; Meng, Y. Sulfur@Graphene Oxide Core-Shell Particles as a Rechargeable Lithium-Sulfur Battery Cathode Material with High Cycling Stability and Capacity. *RSC Adv.* **2013,** *3*, 4914-4916.

(20) Wang, H.; Yang, Y.; Liang, Y.; Robinson, J. T.; Li, Y.; Jackson, A.; Cui, Y.; Dai, H. Graphene-Wrapped Sulfur Particles as a Rechargeable Lithium-Sulfur Battery Cathode Material with High Capacity and Cycling Stability. *Nano Lett.* **2011,** *11*, 2644-2647.

(21) Ji, L. W.; Rao, M. M.; Zheng, H. M.; Zhang, L.; Li, Y. C.; Duan, W. H.; Guo, J. H.; Cairns, E. J.; Zhang, Y. G. Graphene Oxide as a Sulfur Immobilizer in High Performance Lithium/Sulfur Cells. *J. Am. Chem. Soc.* **2011,** *133*, 18522-18525.

(22) Li, W.; Zhang, Q.; Zheng, G.; Seh, Z. W.; Yao, H.; Cui, Y. Understanding the Role of Different Conductive Polymers in Improving the Nanostructured Sulfur Cathode Performance. *Nano Lett.* **2013,** *13*, 5534-5540.

(23) Yang, Y.; Yu, G. H.; Cha, J. J.; Wu, H.; Vosgueritchian, M.; Yao, Y.; Bao, Z. A.; Cui, Y. Improving the Performance of Lithium-Sulfur Batteries by Conductive Polymer Coating. *ACS Nano* **2011,** *5*, 9187-9193.

(24) Xiao, L.; Cao, Y.; Xiao, J.; Schwenzer, B.; Engelhard, M. H.; Saraf, L. V.; Nie, Z.; Exarhos, G. J.; Liu, J. A Soft Approach to Encapsulate Sulfur: Polyaniline Nanotubes for Lithium-Sulfur Batteries with Long Cycle Life. *Adv. Mater.* **2012,** *24*, 1176-1181.

(25) Wang, M.; Wang, W.; Wang, A.; Yuan, K.; Miao, L.; Zhang, X.; Huang, Y.; Yu, Z.; Qiu, J. A Multi-Core-Shell Structured Composite Cathode Material with a Conductive Polymer Network for Li-S batteries. *Chem. Comm.* **2013,** *49*, 10263-10265.

(26) Seh, Z. W.; Li, W.; Cha, J. J.; Zheng, G.; Yang, Y.; McDowell, M. T.; Hsu, P.-C.; Cui, Y. Sulphur-TiO_2 Yolk-Shell Nanoarchitecture with Internal Void Space for Long-Cycle Lithium-Sulphur Batteries. *Nat. Commun.* **2013,** *4*, 1331-1336.

(27) Lee, K. T.; Black, R.; Yim, T.; Ji, X.; Nazar, L. F. Surface-Initiated Growth of Thin Oxide Coatings for Li-Sulfur Battery Cathodes. *Adv. Energy Mater.* **2012,** *2*, 1490-1496.

(28) Li, J. Y.; Ding, B.; Xu, G. Y.; Hou, L. R.; Zhang, X. G.; Yuan, C. Z. Enhanced Cycling Performance and Electrochemical Reversibility of a Novel Sulfur-Impregnated Mesoporous Hollow TiO_2 Sphere Cathode for Advanced Li-S Batteries. *Nanoscale* **2013,** *5*, 5743-5746.

(29) Zu, C.; Su, Y.-S.; Fu, Y.; Manthiram, A. Improved Lithium-Sulfur Cells with a Treated Carbon Paper Interlayer. *Phys. Chem. Chem. Phys.* **2013,** *15*, 2291-2297.

(30) Chung, S.-H.; Manthiram, A. A Hierarchical Carbonized Paper with Controllable Thickness as a Modulable Interlayer System for High Performance Li-S Batteries. *Chem. Comm.* **2014,** *50*, 4184-4187.

(31) Jin, Z.; Xie, K.; Hong, X.; Hu, Z.; Liu, X. Application of Lithiated Nafion Ionomer Film as Functional Separator for Lithium Sulfur cells. *J. Power Sources* **2012,** *218*, 163-167.

(32) Zhou, G.; Wang, D.-W.; Li, F.; Hou, P.-X.; Yin, L.; Liu, C.; Lu, G. Q.; Gentle, I. R.; Cheng, H.-M. A Flexible Nanostructured Sulphur-Carbon Nanotube Cathode with High Rate Performance for Li-S Batteries. *Energy Environ. Sci.* **2012,** *5*, 8901-8906.

(33) Huang, J. Q.; Zhang, Q.; Peng, H. J.; Liu, X. Y.; Qian, W. Z.; Wei, F. Ionic Shield for Polysulfides Towards Highly-Stable Lithium-Sulfur Batteries. *Energy Environ. Sci.* **2014,** *7*, 347-353.

(34) Hassoun, J.; Scrosati, B. A High-Performance Polymer Tin Sulfur Lithium Ion Battery. *Angew. Chem. Int. Ed.* **2010,** *49*, 2371-2374.

(35) Jin, J.; Wen, Z. Y.; Hang, X.; Cui, Y. M.; Wu, X. W. Gel Polymer Electrolyte with Ionic Liquid for High Performance Lithium Sulfur Battery. *Solid State Ionics* **2012,** *225*, 604-607.

(36) Zhang, S. S. A Concept for Making Poly(ethylene oxide) Based Composite Gel Polymer Electrolyte Lithium/Sulfur Battery. *J. Electrochem. Soc.* **2013,** *160*, A1421-A1424.

(37) Decher, G. Fuzzy Nanoassemblies: Toward Layered Polymeric Multicomposites. *Science* **1997,** *277*, 1232-1237.

(38) Hong, J.; Han, J. Y.; Yoon, H.; Joo, P.; Lee, T.; Seo, E.; Char, K.; Kim, B.-S. Carbon-based Layer-by-Layer Nanostructures: From Films to Hollow Capsules. *Nanoscale* **2011,** *3*, 4515-4531.

(39) Tago, T.; Shibata, H.; Nishide, H. Proton Conductivity in the Dry Membrane of Poly(sulfonic acid) and Polyamine Layer-by-Layer Complex. *Chem. Comm.* **2007**, 2989-2991.

(40) Argun, A. A.; Ashcraft, J. N.; Hammond, P. T. Highly Conductive, Methanol Resistant Polyelectrolyte Multilayers. *Adv. Mater.* **2008,** *20*, 1539-1543.

(41) Ashcraft, J. N.; Argun, A. A.; Hammond, P. T. Structure-Property Studies of Highly Conductive Layer-by-Layer Assembled Membranes for Fuel Cell PEM Applications. *J. Mater. Chem.* **2010,** *20*, 6250-6257.

(42) Liu, D. S.; Ashcraft, J. N.; Mannarino, M. M.; Silberstein, M. N.; Argun, A. A.; Rutledge, G. C.; Boyce, M. C.; Hammond, P. T. Spray Layer-by-Layer Electrospun Composite Proton Exchange Membranes. *Adv. Funct. Mater.* **2013,** *23*, 3087-3095.

(43) Deligoz, H.; Yilmazturk, S.; Karaca, T.; Ozdemir, H.; Koc, S. N.; Oksuzomer, F.; Durmus, A.; Gurkaynak, M. A. Self-Assembled Polyelectrolyte Multilayered Films on Nafion with Lowered Methanol Cross-Over for DMFC Applications. *J. Membr. Sci.* **2009,** *326*, 643-649.

(44) Xi, J.; Wu, Z.; Teng, X.; Zhao, Y.; Chen, L.; Qiu, X. Self-Assembled Polyelectrolyte Multilayer Modified Nafion Membrane with Suppressed Vanadium Ion Crossover for Vanadium Redox Flow

Batteries. *J. Mater. Chem.* **2008,** *18*, 1232-1238.

(45) Jia, C.; Liu, J.; Yan, C. A Multilayered Membrane for Vanadium Redox Flow Battery. *J. Power Sources* **2012,** *203*, 190-194.

(46) Xu, W.; Li, X.; Cao, J.; Zhang, H.; Zhang, H. Membranes with Well-Defined Ions Transport Channels Fabricated via Solvent-Responsive Layer-by-Layer Assembly Method for Vanadium Flow Battery. *Sci. Rep.* **2014,** *4*, 4016-4024.

(47) Lee, S. H.; Harding, J. R.; Liu, D. S.; D'Arcy, J. M.; Shao-Horn, Y.; Hammond, P. T. Li-Anode Protective Layers for Li Rechargeable Batteries via Layer-by-Layer Approaches. *Chem. Mater.* **2014,** *26*, 2579-2585.

(48) Park, J.; Park, J.; Kim, S. H.; Cho, J.; Bang, J. Desalination Membranes from pH-Controlled and Thermally-Crosslinked Layer-by-Layer Assembled Multilayers. *J. Mater. Chem.* **2010,** *20*, 2085-2091.

(49) Cho, Y.; Lim, J.; Char, K. Layer-by-Layer Assembled Stimuli-Responsive Nanoporous Membranes. *Soft Matter* **2012,** *8*, 10271-10278.

(50) Shiratori, S. S.; Rubner, M. F. pH-Dependent Thickness Behavior of Sequentially Adsorbed Layers of Weak Polyelectrolytes. *Macromolecules* **2000,** *33*, 4213-4219.

(51) Mendelsohn, J. D.; Barrett, C. J.; Chan, V. V.; Pal, A. J.; Mayes, A. M.; Rubner, M. F. Fabrication of Microporous Thin Films from Polyelectrolyte Multilayers. *Langmuir* **2000,** *16*, 5017-5023.

(52) Park, M. K.; Deng, S. X.; Advincula, R. C. pH-Sensitive Bipolar Ion-Permselective Ultrathin Films. *J. Am. Chem. Soc.* **2004,** *126*, 13723-13731.

(53) Yoo, D.; Shiratori, S. S.; Rubner, M. F. Controlling Bilayer Composition and Surface Wettability of Sequentially Adsorbed Multilayers of Weak Polyelectrolytes. *Macromolecules* **1998,** *31*, 4309-4318.

(54) Li, Q.; Quinn, J. F.; Caruso, F. Nanoporous Polymer Thin Films via Polyelectrolyte Templating. *Adv. Mater.* **2005,** *17*, 2058-2062.

Chapter 6.
Gradient assembled polyurethane-based stretchable multilayer conductors

6.1 Abstract

As next-generation deformable and wearable applications in future, the development of highly desirable stretchable conductors has been required as an essential component that possesses high electrical conductivity under significant mechanical strain. However, there have been still some limitations to achieve the high electrical conductivity and stretchability, which generally displays the trade-off relationship in nanocomposites. In this study, we present a gradient assembled polyurethane (GAP)-based stretchable conductor with fine controlled internal architecture by using composite-by-composite (CbC) assembly as a universally applicable novel method. This CbC assembly integrates the advantages of the rapid and scale-up fabrication by conventional vacuum-assisted filtration as well as the fine nanoscale control over the thickness and composition of hybrid multi-components by layer-by-layer (LbL) assembly. By adjusting the gradient concentration of each gold nanoparticles (Au NPs) as conductive filler and water-dispersed polyurethane (PU) as elastic polymer, the GAP stretchable conductors accomplished not only metallic conductivity as below 1 Ω under over 300% strain, but also excellent electrical conductivity of vertical direction as entirely full conductor, which could not be obtained from conventional methods such as conductive surface onto elastomeric substrate and simple polymer nanocomposites. Furthermore, we also demonstrated the stretchable aqueous lithium ion battery which had the superior rate capability of even at 100 C rate with 77 mA h g^{-1} and also showed outstanding cycle retention of 96 % at a rate of 15 C after 1000 cycles.

6.2 Introduction

Stretchable electronics are forefront technologies with the growing demand toward future deformable and wearable applications, ranging from wearable healthcare devices to integrated artificial skins and muscles.[1-4] The rapidly evolving devices are strongly pushing to develop stretchable conductors as an essential component that possesses high electrical conductivity under significant mechanical strain.[5-7] Therefore, there have been intensive researches for the development of stretchable conductors based on carbon and metal nanomaterials.[8-13] However, highly desirable development of suitable stretchable conductors with comparable electrical conductivity during stretching is still required, because the required conductivity is different as degree of stretching in some case where one need to apply.

In general, two main strategies have been proposed to fabricate stretchable conductors such as geometrical structure-controlled design and ratio-controlled nanocomposite. In the first approach, coating or depositing conductive materials on the surface of an elastomeric substrate have been widely used to achieve stretchable conductors, including buckled,[14,15] wrinkled,[16] waved,[17] crumpled,[18] or island structures.[19] Although these methods afford stable electrical conductivity retention at high strain condition, there are still some limitations that are not only unscalable and complex manufacturing process, but also low volumetric packing density into the practically feasible devices.

Alternatively, polymer nanocomposites of in-plane structure possessed conductive pathway owing to conductive fillers homogeneously dispersed in elastomeric polymers.[6,10-13] They are considered as the most promising candidate because of their advantages of scalable and high-throughput fabrication process. Such elastic nanocomposites are an entirely full conductor from top to bottom surface, compared to only top-surface conductive structure assembled onto elastomeric substrate. However, the electrical conductivity of the nanocomposite is highly strain-sensitive, which displays the trade-off relationship between stretchability and conductivity in nanocomposites. For example, high content of elastomeric polymer shows superior strains albeit with its low intrinsic conductivity, limiting its practical applications. On the other hand, high loading of the stiff conductive component often demonstrates extremely low strains under 5% because the stress failure of rigid nanocomposites depends on the randomly distributed stress-concentrated hard segments, which can promote propagation of nano- and micro-cracks in nanocomposites.[20]

Therefore, it has been critical issues to balance this trade-off relationship by revealing a tensile behavior of interdependent components in nanocomposites. Accordingly, a strain-induced self-alignment restructuring property of the conductive filler such as metal nanoparticles was demonstrated within the elastic polymer matrix during deformation owing to the greater matrix mobility of nanoparticles. In addition, it is also important to develop new geometrical design achieving both stretchability and conductivity in the nanocomposites by utilizing such self-reorganization of conductive fillers under strain.[13]

In this regard, in order to develop a universally applicable method for fabricating the geometrically designed nanocomposite conductor, herein we report a gradient assembled polyurethane (GAP)-based stretchable conductor with fine controlled internal architecture assembled with gold nanoparticles (Au NPs) as a conductive filler (**Figure 6.1**). In this study, we propose a novel assembly protocol, composite-by-composite (CbC) assembly, which integrates the advantages of both conventional vacuum-assisted filtration and layer-by-layer assembly. Typically, vacuum-assisted filtration is advantageous to the rapid and scale-up fabrication of layered thin films and membranes.[21] Conversely, LbL assembly can manufacture the highly ordered architectures, allowing the fine nanoscale control over the thickness and composition of hybrid multi-components through the sequential assembly.[22-26]

Taken together the advantages of each assembly, the CbC assembled multilayer gradient conductor is constructed by the alternative physical trapping of the electrostatically complexed composite suspensions under vacuum using the positively charged water-dispersible polyurethane and the negatively charged Au NPs in varying ratio. Most uniquely, this GAP stretchable multilayer conductor demonstrates not only top-surface conductive structure with superior mechanical stretchability even above 300% strain in case of high gradient architecture, but also whole through-plane conductor from top to bottom surface of the conductor as increasing the number of interlayers in case of low gradient architecture. Using the GAP stretchable conductor, we demonstrate the highly stretchable energy storage device such as lithium-ion battery retaining stable electrochemical performance under strain. This novel approach for stretchable conductors developed in this study will offer new insights in the design of the stretchable conductors for future energy conversion and storage devices as well as advanced flexible and wearable electronics.

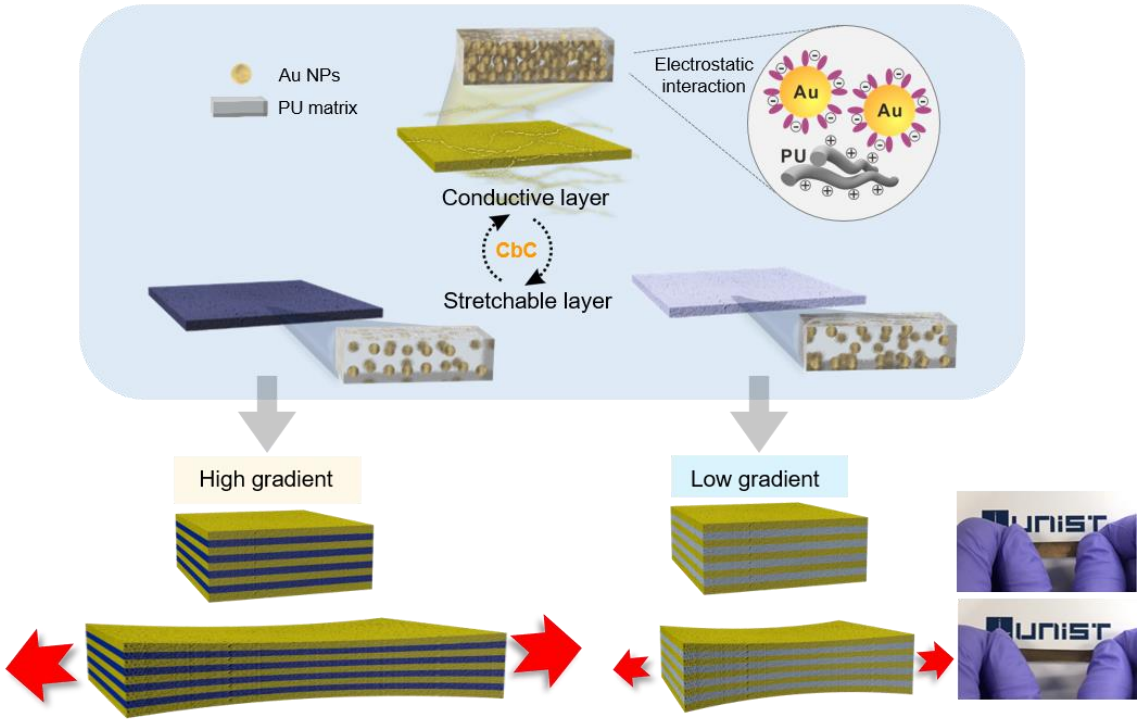

Figure 6.1. Schematic illustration of GAP multilayer conductors. Composite-by-composite (CbC) assembly of polyurethane (PU)-based stretchable multilayer of high and low gradient conductors with different concentration of Au NPs in stretchable layer. Photograph showing the resulting GAP multilayer conductor under 100% strain.

6.3 Experimental

6.3.1 Synthesis of Au nanoparticles

Gold(III)chloride trihydrate (360.0 mg) was added to deionized water (500 ml). This gold precursor solution was heated at 95 °C under vigorous stirring for 20 min. Subsequently, 34 mM sodium citrate solution (100 ml) was added to the mixture. The aqueous solution was heated for 20 min followed by cooling to room temperature.

6.3.2 Fabrication of single-layered AuPU nanocomposites

A 1.0 vol.% aqueous polyurethane of 0.50, 1.0, or 4.0 mL was slowly added to as-prepared Au NPs dispersion of 250 mL for the content of Au NPs of 90, 85, or 50 wt% in AuPU, respectively under stirring followed by additional stirring for 5 min. Each mixture was filtered with vacuum force by using filter papers of 0.8 μm pore size with 47 mm diameter. The resultant film was peeled off from the filter paper after drying the film completely for 1 day at room temperature.

6.3.3 Fabrication of CbC assembled GAP stretchable multilayer conductors

The CbC assembled multilayer architecture was constructed by the alternatively physical trapping single-layered AuPU nanocomposites under vacuum force. At first, the mixture of 90 wt% in AuPU nanocomposite as conductive layer was filtered, followed by each mixture of 50 wt% or 85 wt% in AuPU nanocomposite as stretchable layer. Finally, the 90 wt% AuPU nanocomposite as conductive layer was filtered again to afford high gradient (i.e., 95/50/95 wt%) and low gradient (i.e., 95/85/95 wt%) multilayer conductors of 3 L, respectively. To fabricate the more layered structure at the interlayer above 3 L, the mixture for stretchable layer was alternatively and evenly filtered with one-additional mixture of 90 wt% in AuPU while fixing the contents of conductive layer of 90 wt% at the outermost sides of both top and bottom.

6.3.4 Numerical simulation of GAP multilayer conductors

For finite element simulations to demonstrate mechanical and electrical properties of multilayer conductors, we used the commercial software ABAQUS/Standard 6.14 (Dassault System). Linear elastic analysis was conducted to describe stress distribution in layer under uniaxial tension. Also, electrical conduction analysis was implemented to identify the change of vertical conductivity of multilayer conductors. The contact layer between conductive layer and stretchable layer was considered with assumption of the contact ratio as one-to-one. Steady state analysis was concerned in both analysis. Elastic properties of each layer in conductor, dimensions of multilayer conductors, and strain-dependent electrical properties which had been measured by experiments were adopted in all simulations. In case of the low GAP conductor, thickness of whole conductor and each stretchable layer for 5 L and 9 L are 27.42 μm, 4.71 μm and 27.17 μm, 2.06 μm respectively.

6.3.5 Synthesis of active materials

In a typical experiment, 100 mg of CNT and a certain amount of $KMnO_4$ (Aldrich) were mixed together in an agate mortar. The mixed powder then was poured in 100 mL of water and stirring for 10 min. 0.5 mL of H_2SO_4 (95%, Samchun) was added to the above blend with an added 30 min of stirring. Then, the mixture was applied heat in an oil bath at 80 °C with stirring for 1 h. The precipitate was collected by filtration and washed repeatedly with deionized water and ethanol. The product then was dried in an oven at 60 °C for 12 h to obtain MnO_2/CNT. To make the LMO/CNT, 0.25 g of above as-obtained the MnO_2/CNT and 0.26 g of $LiOH·H_2O$ (Sigma Aldrich) were mixed with 60 mL of DI water. The mixture was transferred into 80 mL of an autoclave, and then heated at 160 °C for 12 h. After a hydrothermal treatment, the resulting precipitates were filtered and washed with distilled water. After the autoclave cooled to room temperature naturally, product was dried in an oven at 60 °C for 12 h. Finally, product was applied heat in a furnace at 200 °C for 3h under the air atmosphere.

1,4,5,8-naphthalenetetracarboxylic dianhydride (2.3 mmol) and CNT (0.50 g) were mixed with 4-chlorophenol (40 g) at 55 ºC under stirring until completely mixing. Ethylenediamine (0.15 mL) was added to the mixture, followed by heating and refluxing at 200 ºC for 6 h. The mixture was cooled to room temperature and the solid product was rinsed with ethanol, followed by vacuum filtration. The obtained product was dried at 300 ºC in N_2 atmosphe re for 8 h to remove residual solvent.

6.3.6 Electrochemical measurements

The electrode was fabricated by spray coating method onto hot plate at 60 ºC consisting of active materials (LMO/CNT or PI/CNT), conductive material (super P), and the binder (nafion) in a weight ratio of 8:1:1 onto the prepared electrode. The electrodes were cut in the form rectangular shape (30 x 10 mm). The electrochemical properties of half and full cell were measured using a (Biologic science instrument, VSP) with a 1M $LiSO_4$ aqueous electrolyte. The Pt electrode and saturated calomel electrode (SCE) were used as the counter and reference electrode, respectively. The active loading density was 0.5 mg cm^{-2}. The full cell was performed between 0.00 and 2.00V at room temperature and measured using two-electrode system, with an LMO/CNT and PI/CNT as working electrode and counter electrode, respectively.

To fabricate stretchable full batteries, we produce an aqueous Li_2SO_4 gel electrolyte. Firstly, 1g of sodium carboxymethylcellulose (CMC) was dissolved in 10 mL deionized water. In order to form a gel, the solution was heated at 75 ℃ for 2 h under vigorous stirring. And then, the 1M Li_2SO_4 solution was added to the CMC gel at 40 ℃ for 1 h under stirring. Packaging material (35 x 40 x 10 mm) and a spacer of stretchable full batteries was used as PDMS. The thin spacer (500 μm) accommodated sufficient space to fill the gel electrolyte. The stretchable cathode and anode were attached parallel to the bottom layer using un-cured PDMS solution. And then, a top layer, spacer, and the bottom layer was

assembled using O_2 plasma (CUTE, Femto Science, Korea) treatment. Finally, as-prepared gel electrolyte was prudently injected using syringe.

6.3.7 Characterization

The mechanical properties of the prepared electrode were measured by a tensile strength tester (DA-01, Petrol LAB, Korea). The specimen was cut in the form dog-bone shape and the test rate of tensile strength was conducted at 10 mm/min. The electrical conductivity was conducted using a four-point probe machine (FPP-RS8, Dasol Eng., Korea). The change in resistance during strain and release was measured using a multi-meter. The crystal structure of LMO/CNT was characterized by an X-ray diffractometer (XRD) on a Rigaku D/MAX at 2500 V. The morphology of electrode and active materials was measured by field-emission scanning electron microscopy (FE-SEM, Hitachi S-4800). Transmission electron microscopy (TEM) images were taken in the bright-field mode by using a JEM 2100 (JEOL). The FT-IR spectra of PI/CNT was measured by using a Varian 670 IR spectrometer. Thermogravimetric analysis (TGA, TA instruments, Q50) was used to calculate the mass content of LMO and PI.

6.4 Result and Discussion

To fabricate polymer nanocomposites-based stretchable conductor, a negatively charged Au NPs suspension stabilized by citrate was initially prepared as a conductive filler. The resulting citrate-stabilized Au NPs had an average diameter of 21.5 ± 5.3 nm (**Figure 6.2a**). Although one-dimensional (1D) nanomaterials are typically known to be a suitable candidate in a stretchable conductor due to its high aspect ratio, 0D NPs could potentially exhibit greater degree of freedom within the polymer matrix under strain besides their facile and scalable synthetic nature. As an elastomeric component, a highly stable and positively charged water-dispersible polyurethane (PU) suspension was used for fabricating stretchable conductors based on complementary electrostatic interactions with Au NPs (**Figure 6.2b**).

Initially, we prepared each Au NP-PU nanocomposite suspension (AuPU hereafter with a fraction of Au NPs) via simple mixing of Au NPs and PU suspension in a controlled ratio from 50 to 90 wt% of Au NP through electrostatic complexation (**Figure 6.3**). The pure PU film (without Au NPs) displayed a superior stretchability as high as 615%. However, as increasing the content of Au NPs within PU matrix from 50, 85, and 90 wt%, the stretchability of AuPU composite films decreased sharply to 380, 140, and 2%, respectively. In contrast, the resistance was decreased significantly; for example, the 90 wt% AuPU composite film demonstrated the resistance below 1 Ω, which was even comparable to the metal conductor (**Figure 6.4**). This film also indicated a successful durability over 100 cycles without any changes in resistance, highlighting the preservation of conductive pathway under deformation along with flexible PU backbone (**Figure 6.3**). However, one could not achieve high stretchability over 100% using a single polymer nanocomposite film with reasonable electrical conductivity.

Therefore, to augment the weakness of each single-layered AuPU nanocomposite film in either conductivity or stretchability, we suggest a novel geometric design of AuPU film through CbC assembled multilayers of respective single AuPU nanocomposite films to take advantages of both conventional vacuum-assisted filtration and layer-by-layer assembly. In specific, 90 wt% AuPU film was selected as a conductive layer at the outermost sides of both top and bottom, which is spaced by either with 50 wt% or 85 wt% AuPU film as a stretchable layer to afford a high gradient (i.e., combination of 95 and 50 wt% AuPU) or a low gradient (i.e., 95 and 85 wt% AuPU) multilayer structure of distributed Au NPs in whole conductor, respectively. This multilayered structure was referred to as a GAP conductor of 3-layer (3 L). Furthermore, to investigate the effect of the multilayers at a fixed content of Au NPs, the interlayer of multilayer conductor was further segmented evenly with different number of layers by adding additional conductive layer into stretchable layer, while fixing the contents of the multilayer conductor from 5 L to 9 L with total of three-conductive layers and one-stretchable layer.

The successful fabrication of these GAP multilayer conductors was confirmed by cross-sectional scanning electron microscopy (SEM) (**Figure 6.5**). The multilayered architectures were

clearly observed in the relative contrast between Au NPs and PU in each nanocomposite layer. Furthermore, the corresponding energy dispersive X-ray spectroscopy (EDS) images also revealed the gradient distribution of Au and carbon, respectively, indicating each Au NPs and PU was distributed in the entire conductor with the concentration gradient throughout the conductor.

Thermogravimetric analysis (TGA) was performed to classify the specific content of Au NPs of all conductors used in this study (**Figure 6.6**). High gradient multilayer conductors from 5 L to 9 L displayed nearly identical Au content of 75 wt%, which is in good agreement with the average amount of Au contents between 95 and 50 wt% single-layer AuPU conductors used to assemble the conductors. Similarly, the low gradient multilayer conductor showed the Au content of 88 wt% near to the average of 95 and 85 wt% of each AuPU composite suspension. These results clearly suggest the precise control over the number of layers and gradient distribution in internal structure without altering the compositional ratio of each conductive filler and elastic polymer, demonstrating the versatile nature of CbC assembly in building the architecture-controlled nanocomposite conductors.

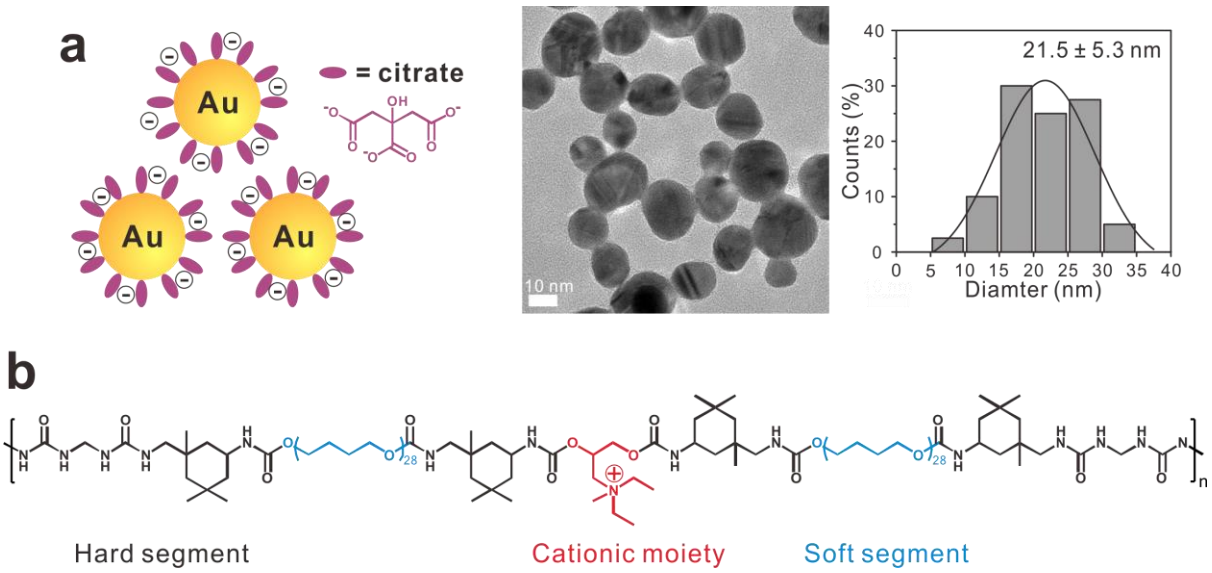

Figure 6.2. (a) Schematic illustration and TEM image with a corresponding size distribution histogram of citrate-stabilized Au NPs. (b) Polymer structure of water-dispersed PU.

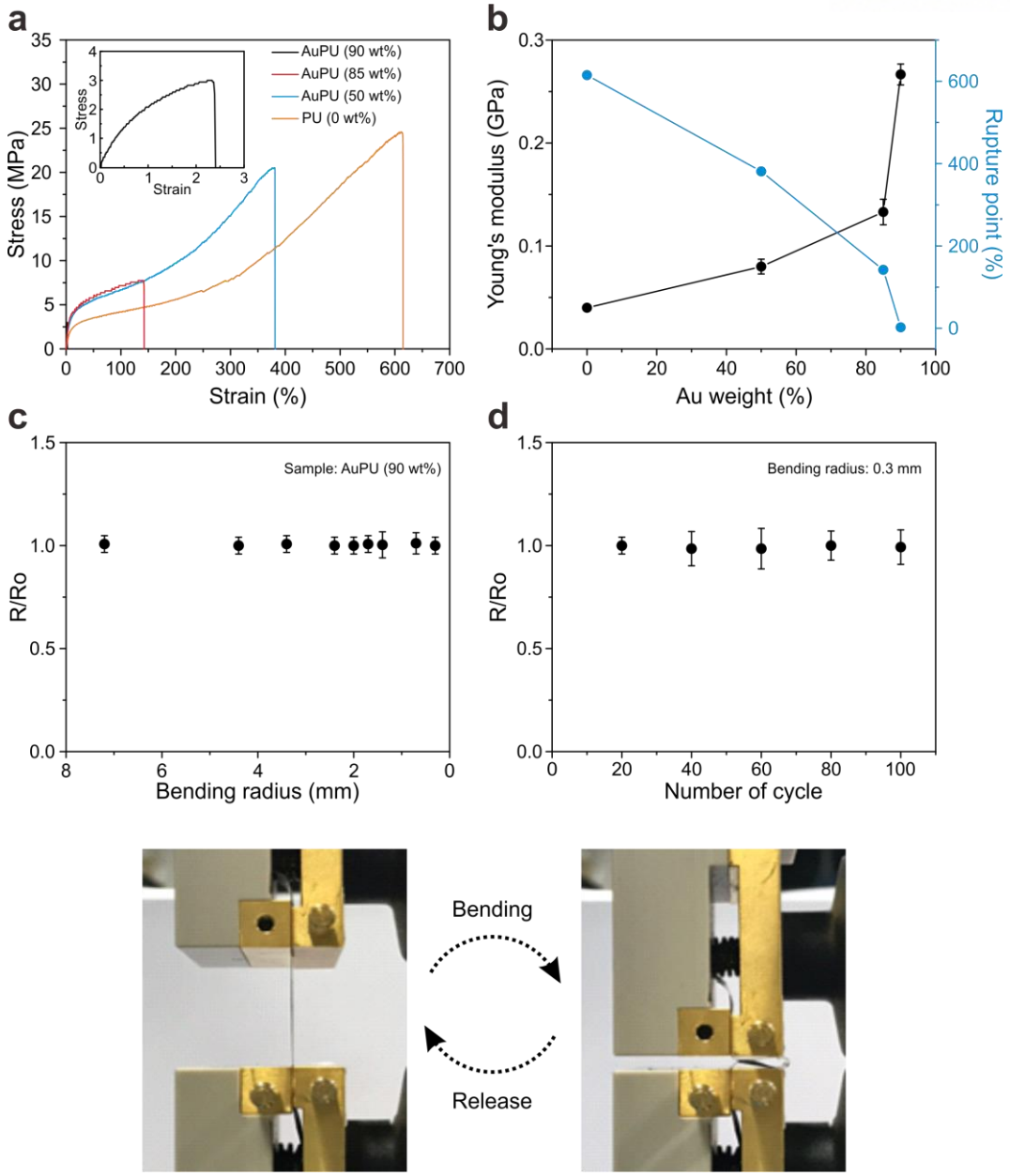

Figure 6.3. Characterization of single layer. (a) Stress-strain curves and (b) Young's modulus and rupture point for pure PU and single-layered AuPU nanocomposite films. (c) Normalized resistance of 90 wt% AuPU film as decreasing the bending radius and (d) bending durability test for 100 cycles at bending radius of 0.3 mm. Photograph showing the bending test of 90 wt% AuPU film.

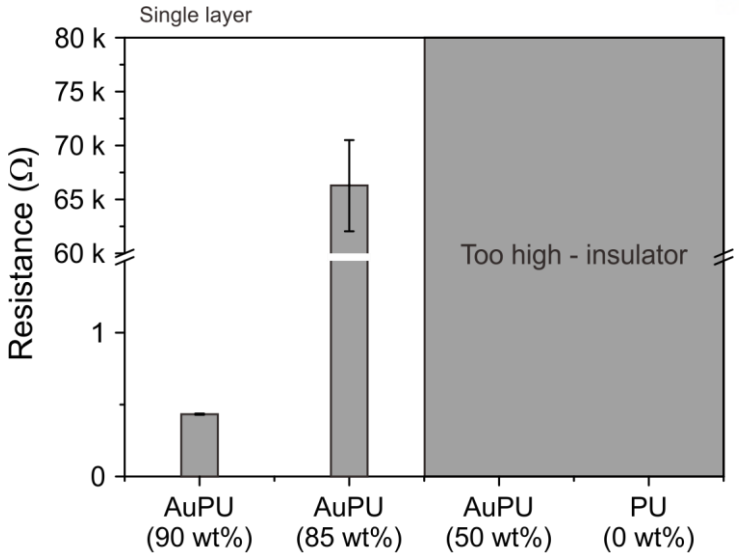

Figure 6.4. Resistance of single-layered AuPU and pure PU films.

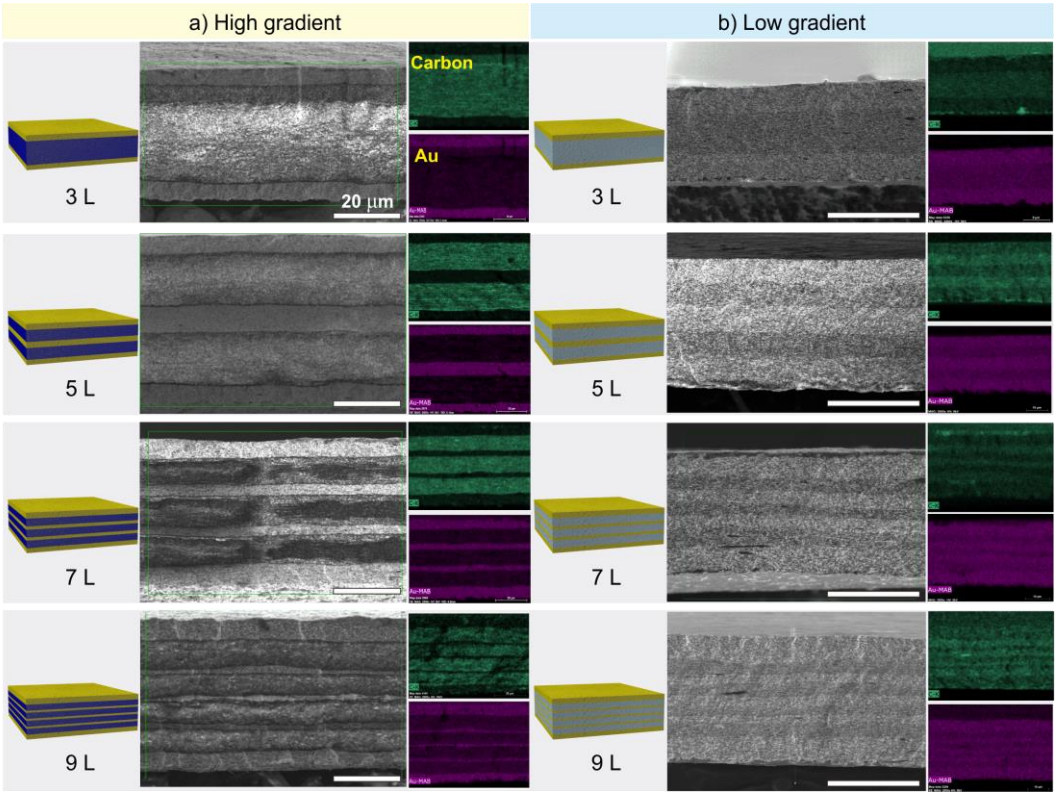

Figure 6.5. Architecture controlled GAP multilayer conductors. Schematic illustrations and representative cross-sectional SEM images with composed elemental mapping images of carbon and Au of (a) high and (b) low gradient multilayer conductors as increasing the number of layers. The scale bar in all SEM images is 20 μm.

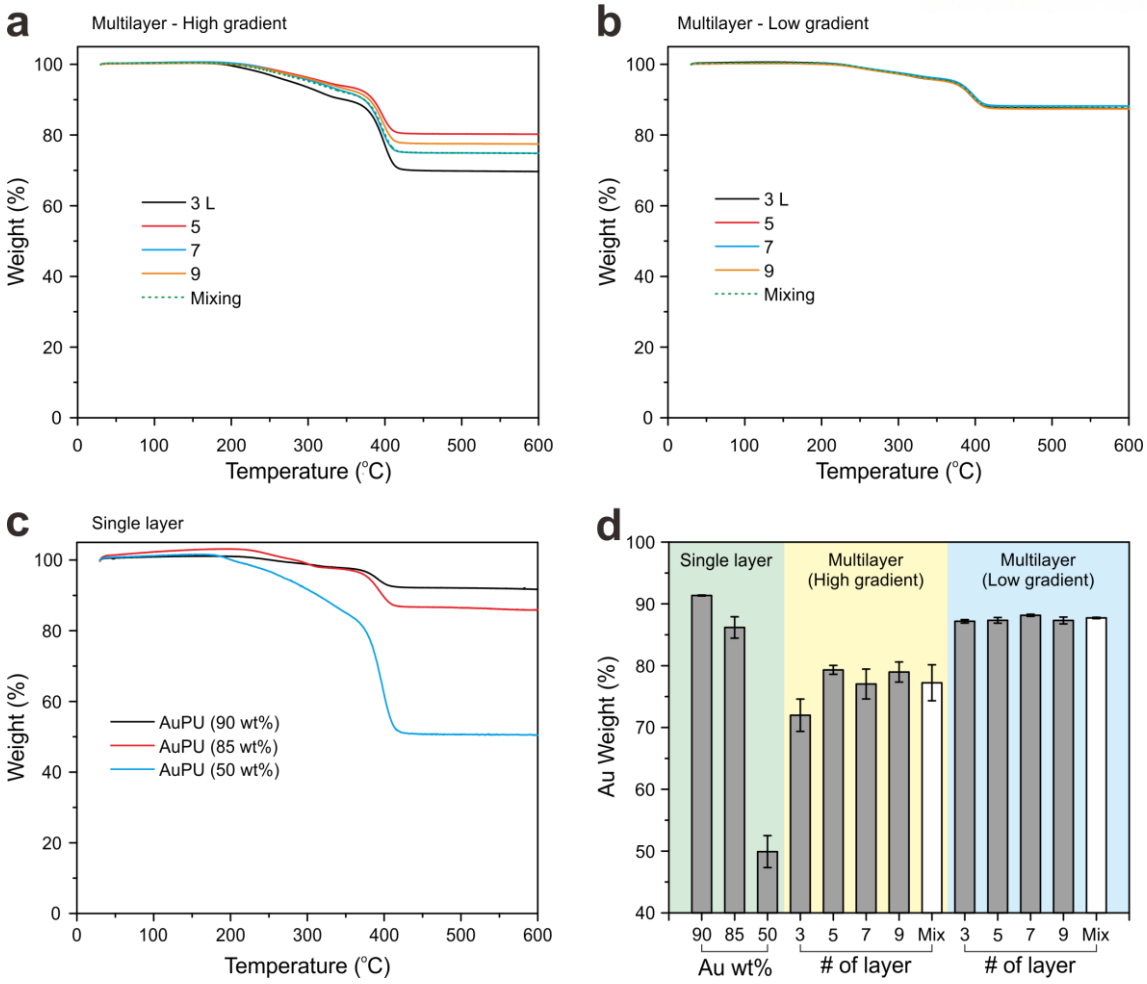

Figure 6.6. TGA of (a) high GAP, (b) low GAP conductors and (c) AuPU nanocomposite films. (d) The resulting content of Au in all electrode examined in this study.

We then examined the mechanical and electrical characterization of the stretchable GAP conductor (**Figure 6.7**). The high GAP conductors showed the superior stretchability as above 300%, comparing to that of the low GAP conductors as below 100% strain (Figure 3a). However, the rupture point of both high and low GAP conductors gradually decreased as increasing the number of interlayer, while the obtained Young's modulus increased as shown in Figure 3b and c. It is of note that the Young's modulus of high GAP conductors is lower than that of low gradient, indicating the high ratio of Au NPs to PU of low gradient conductor induced stiff and rigid nanocomposites, resulting in inferior stretchability.

We further investigated the change of internal structure under strain by surface morphology analysis using SEM. The top-surface view images showed 3D interconnected microporous networks of Au NPs-anchored PU chains (**Figure 6.8**). Although the porosity was increased with enlarged voids and cracks under strain, the robust PU backbone-induced good recovery was observed with reconstruction of AuPU nanocomposites. The stress failure of GAP multilayer conductors by nano- and micro-cracks in nanocomposites was also confirmed by cross-sectional SEM images of high-gradient multilayer conductor of 9 L under strain (**Figure 6.9**). Interestingly, the partially broken interlayer was observed at exactly middle layer among the whole interlayers. These results benefit from maintaining the electrical conductive surface as well as the outstanding recovery because of preventing the rupture of the conductive layer at the outermost sides of both top and bottom without severe cracks. In addition, there was no delamination of interlayers from the underneath layer due to the high affinity and compatibility of employing the identical components in each nanocomposite layer homogeneously. It should be again highlighted that the highly tunable CbC assembly can fabricate the mechanically powerful stretchable conductor with a simple and scalable solution process.

In order to verify this rupture point of GAP multilayer conductors by propagation of cracks starting at the middle layer as the number of interlayers, mechanical simulation for the stress distribution in horizontal and vertical direction in low GAP multilayer conductors of 5 L and 9 L was conducted by using the commercial software ABAQUS. The horizontal stress in line with stretching direction of 9 L conductor is the higher than that of 5 L conductor (Figure 3d), while the negative value of vertical stress (i.e. compression) is increased significantly (Figure 3e), indicating that the rupture point of GAP conductors was decreased as increasing the number of interlayer with corresponding results in Figure 3a-c. Another point to note is that the higher stress was concentrated on the middle and center layer rather than outer layers. As a result, the concentrated stress at the middle layer initiated the rupture of GAP conductor, instead of the rupture starting from the conductive layer at the outermost sides, which is well consistent with previous cross-sectional SEM images. Accordingly, this observation indicates that the multilayered architecture is advantageous in distributing the stress concentration under stretching.

The electrical conductivity of all GAP multilayer conductors showed a similar change in

resistance regardless of the number of interlayers and gradient assembly because the composed top-conductive layer is identical with 90 wt% in AuPU nanocomposite (**Figure 6.7d**). However, it is also important to consider the electrical connection of interlayers under strains toward entirely full conductor. We also performed the durability test of electrical conductivity of the GAP multilayer conductors under strain of 20%, 30%, and 40% (**Figure 6.7e**). It showed highly stable performance retention even after 1000 cycles. These outstanding mechanical and electrical properties demonstrate the uniqueness of high gradient architecture with in-plane structure to achieve both metallic top-surface conductivity as well as superior mechanical stretchability.

However, the high GAP multilayer conductor still has a limitation, which is only top-surface conductive like a conventional geometrically designed conductor. In contrast, the low GAP multilayer conductor is fully conductive from top to bottom surface with the low vertically directional resistance of ~50 Ω measured in low GAP conductor of 3 L, although its tensile strength is much lower than that of high GAP conductors. Therefore, the vertically directional conductivity in low GAP conductors was theoretically calculated to prove conductive pathway through stretchable layer as a function of the number of interlayers (**Figure 6.11**). We considered the contact layer between conductive layer and stretchable layer, resulting in the slightly decreased thickness of stretchable layer (i.e. resistance) with increasing the number of interlayers shown in SEM images (**Figure 6.5**), because the number of the mixed contact layers was increased. As a result, the vertical conductivity was increased with increasing the number of interlayers, enabling more facile through-plane electrical conduction from top to bottom surfaces.

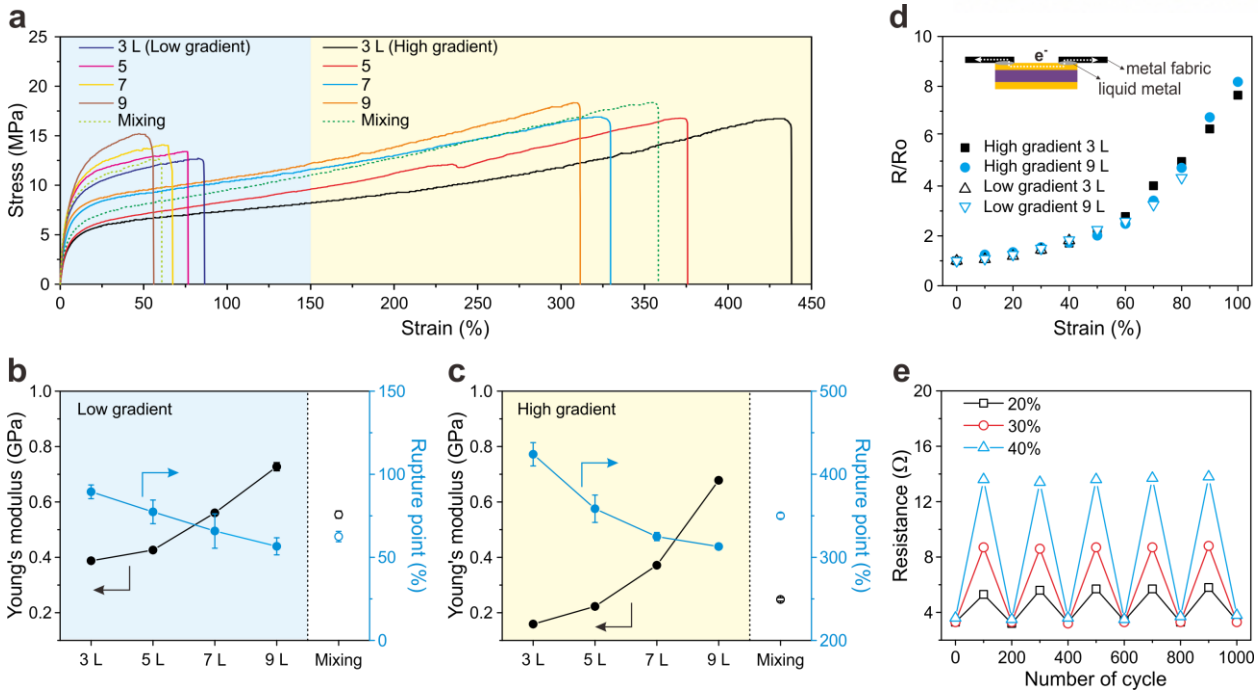

Figure 6.7. Mechanical and electrical properties of GAP multilayer conductors. (a) Stress-strain curves for all GAP multilayer conductors. (b, c) Young's modulus and rupture point of low and high GAP multilayer conductors. (d) Normalized resistance on top-surface of high and low GAP multilayer conductors of 3 L and 9 L under different strain conditions. (e) Change of resistance on top-surface of high GAP multilayer conductors of 9 L under different strains during 1000 cycles.

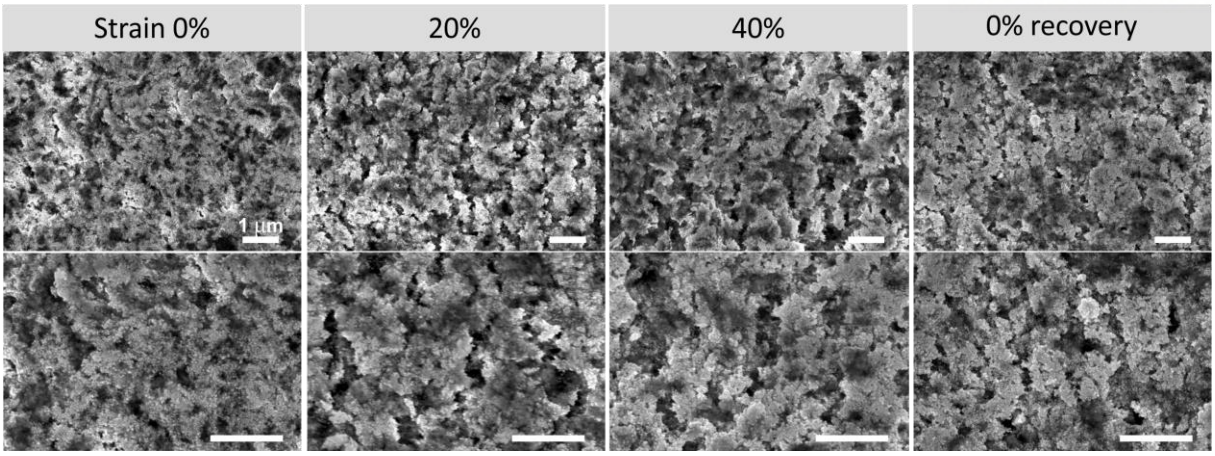

Figure 6.8. SEM of 9 L high GAP conductor under strain

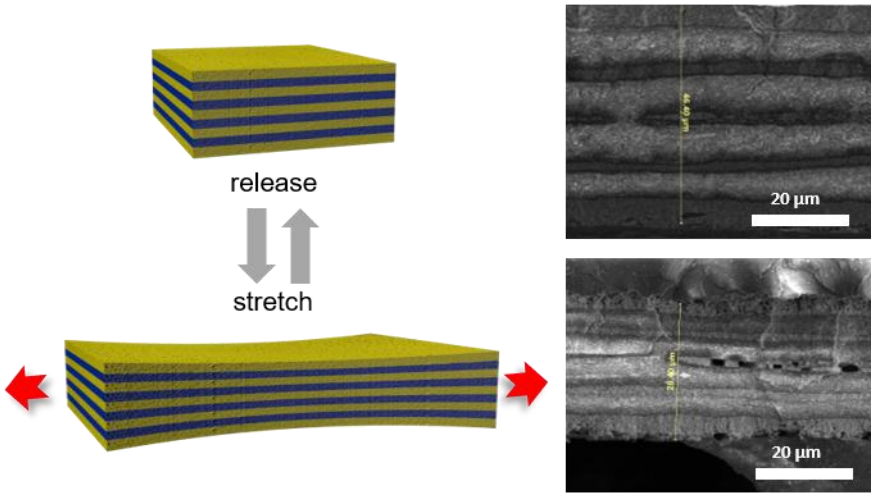

Figure 6.9. Cross-sectional SEM of 9 L high GAP conductor under strain.

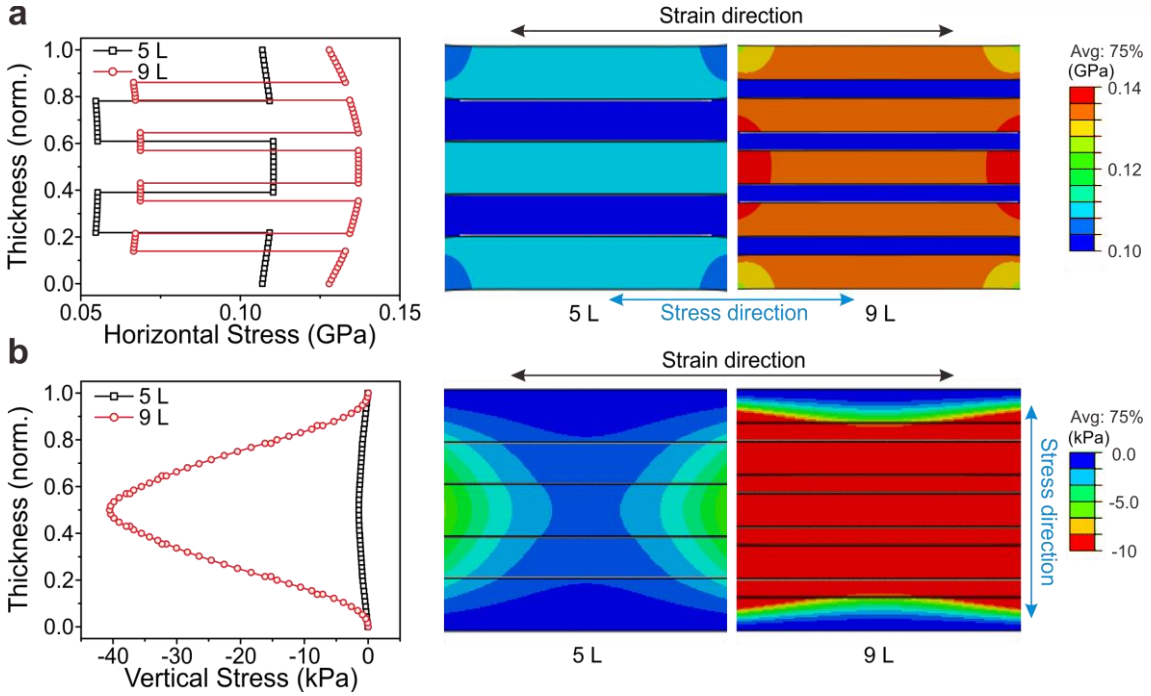

Figure 6.10. Finite element analysis (FEA) representing von Mises stress distribution of (a) horizontal and (b) vertical direction in 5 L and 9 L low GAP conductors under 50% strain.

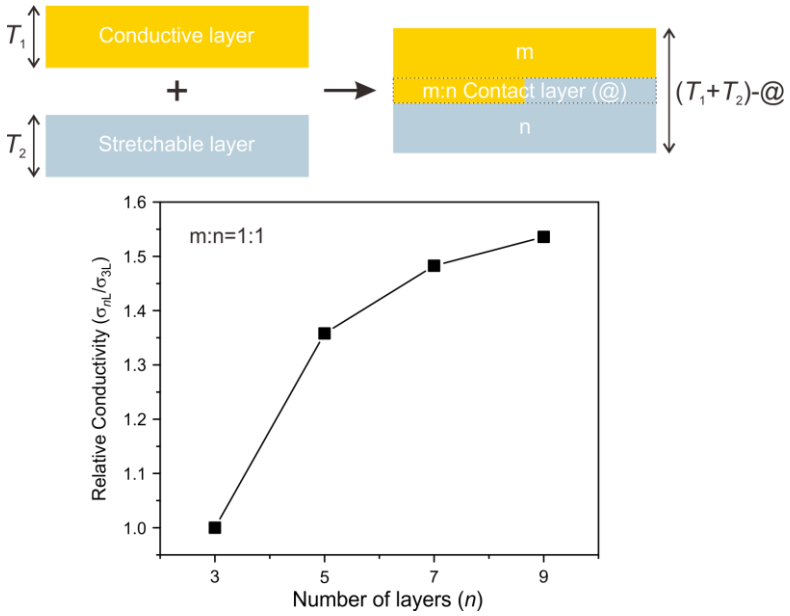

Figure 6.11. Calculation of Z-directional conductivity of low GAP conductors as increasing the number of layers.

Electrical conductivity is strongly related to connectivity between conductive fillers. Specially, to retain stable electrical conductivity of a stretchable conductor, the behavior of conductive filler is important under strain. In this regard, in situ small angle X-ray scattering (SAXS) is a fascinating method to better understand behavior of conductive filler in elastomer matrix (**Figure 6.12a**). The SAXS analysis of samples was conducted at a constant stretching rate of 80 μm sec^{-1} under strain range of 0 and 100 %. **Figure 6.12b** shows 2D SAXS patterns of pure PU and 50 wt% AuPU nanocomposite films at applied uniaxial strains of 0%, 50%, and 100%. In the initial unstrained state, 2D patterns of pure PU and AuPU nanocomposite films exhibited an isotropic scattering geometry, indicating random dispersion of hard segment of PU and Au NPs in the pure PU and AuPU nanocomposite films, respectively. However, the two samples began to develop different scattering patterns upon stretching. The patterns of pure PU evolved from circular to elliptical shape during strain, indicating that the hard segment of PU was aligned along stretching direction (**Figure 6.12b**). In contrast, AuPU nanocomposite film showed a butterfly-like pattern upon stretching, resulting from the non-affine relative displacements of the Au NPs in the polymer matrix under strain.[27] As the strain increased, the Au NPs was gradually forming clusters of raft-like structure in the direction perpendicular to the strain axis due to the Poisson contraction, leading to the banded Au NP clusters lying at the stretching direction. These phenomena may lead to a significant alignment and increased interconnection of Au NPs under uniaxial strain, resulting in effective maintenance of its electrical conductivity under strain.[28]

Moreover, in order to quantitatively investigate the alignment quality of AuPU nanocomposite films along a stretching direction, we calculated the Hermans orientation factor (*f*),

$$f = \frac{3(\cos^2 \varphi) - 1}{2}$$

where *f* is the orientation factor, varying from 0 to 1 for isotropic and perfectly perpendicular to strain direction, respectively and φ is the azimuthal angle. In **Figure 6.12c**, the orientation factor, *f*, indicated that percolation network in the stretching direction began to collapse at a strain of 80%; this result is consistent with the rapidly increasing point of resistance shown in Figure 3d.

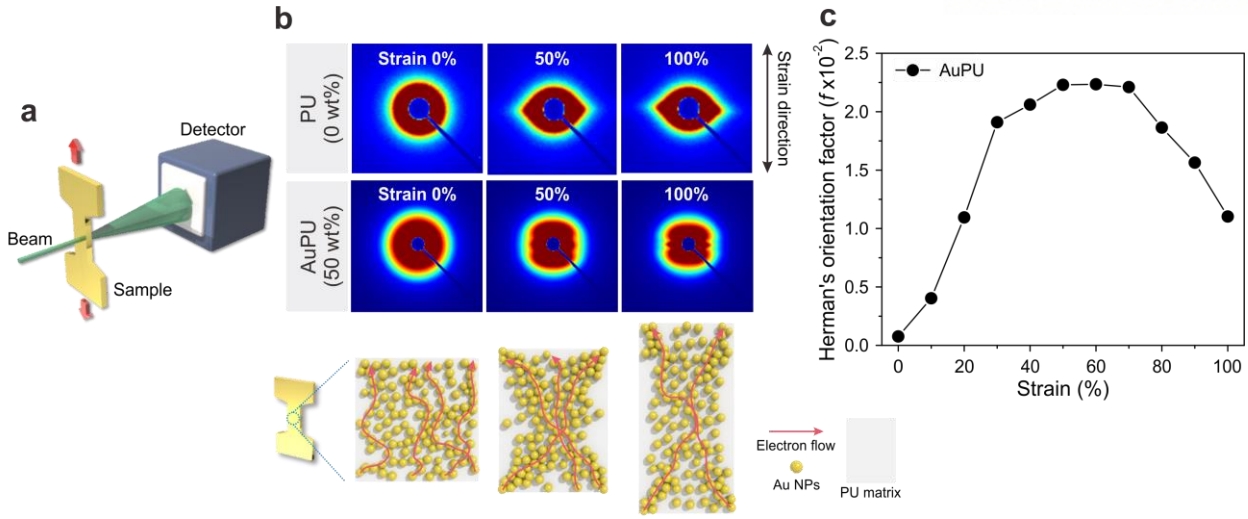

Figure 6.12. SAXS and simulation analysis for percolation network of Au NPs in PU matrix under strain. (a) Schematic illustration showing experimental setup of in situ SAXS measurement. (b) 2D SAXS patterns at selected uniaxial strains of 0%, 50%, and 100% for the pure PU and 50 wt% AuPU nanocomposite films. We summarized the behavior of the Au NPs in the matrix and change in electrical pathway under strain with corresponding schematic illustrations of the behaviour of Au NPs (yellow sphere) and electrical pathway (red line) under strain through SAXS analysis. (c) Calculated Hermans orientation factor, *f*, under strain.

To confirm the utilization of the stretchable GAP multilayer conductor as a current collector electrode for practical applications, the electrochemical performance of an aqueous rechargeable lithium-ion battery (ARLB) as a promising power source was examined. The ARLB has superior rate capability by fast transport of Li ions owing to the usage of aqueous electrolytes instead of conventional organic electrolytes, resulting in extremely safe from the risk of explosion.[29-30] Initially, we synthesized active materials on the surface of carbon nanotubes for the anode and cathode which are polyimides (PI/CNT)[31] and lithium manganese oxide, $LiMn_2O_4$ (LMO/CNT),[32] respectively (**Figure 6.13** and **6.14**). To fabricate stretchable electrode, as-prepared cathode and anode materials were deposited onto the GAP multilayer conductors by spray coating method (denoted as GAP cathode and GAP anode, respectively)

The electrochemical performance of the GAP electrode was conducted by cyclic voltammetry (CV) using a three-electrode system in 1 M Li_2SO_4 electrolyte with a Pt electrode and an Ag/AgCl electrode as the counter and the reference electrode, respectively. In **Figure 6.15a**, CV curves of the GAP anode and the GAP cathode with increasing scan rate from 2 to 20 mV s^{-1} showed typical redox peaks of PI and LMO; thus the GAP multilayer conductor clearly indicated the electrochemical stability in the range of working voltage, demonstrating that the GAP multilayer conductor can be used as a current collector for the ARLB system. **Figure 6.15b** displays voltage profiles of the GAP cathode between 0.0 V and 1.2 V at various C-rates. They delivered specific capacities of 132, 126, 115, and 102 mA h g^{-1} at 10, 15, 30, and 100 C, respectively. On the other hand, rate performance of the GAP anode at various current rate range from 20 C and 200 C under voltage window of 0 V and -1.0 V was presented in **Figure 6.15c**. Interestingly, the GAP anode can deliver 95 mA h g^{-1} even at a high rate of 200 C, corresponding to 78% of the capacity at 20 C. Moreover, both GAP anode and GAP cathode showed outstanding cycling performance at a rate of 100 C after 200 cycles (**Figure 6.16**)

The electrochemical performance of a full cell was evaluated between the voltage range of 0.0 V and 2.0 V without any strain applied. It should be noted that the full cell was tested in beaker cell containing 1 M Li_2SO_4 with continuous bubbling nitrogen to remove oxygen. The discharge capacities of the full cell were 100 and 77 mA h g^{-1} at 15 C and 100 C rates, respectively (**Figure 6.17)**. The long-term cycle performance of the full cell showed outstanding cycle retention of 96 % at a rate of 15 C after 1000 cycles, as shown in **Figure 6.15d**.

To further demonstrate the electrochemical performance under strain, we designed the stretchable ARLB to establish its practical feasibility for use in deformable electronic devices (**Figure 6.15e**). The recovery property of the proposed battery could be also introduced by packaging materials of polydimethylsiloxane (PDMS) (**Figure 6.18**). This stretchable ARLB was cycled at a rate of 15 C between 0% and 30% strain (**Figure 6.15f**). At 30% strain, the stretchable ARLB showed an outstanding capacity retention of 72 % for 10 cycles, compared to un-strained condition. After releasing the strain, the specific capacity of the stretchable ARLB was observed to completely recover to its initial values.

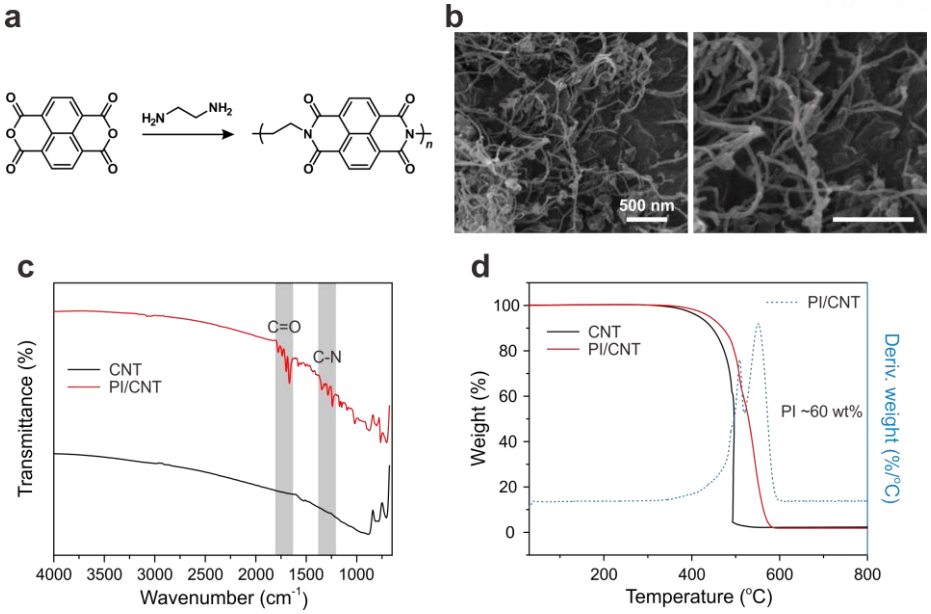

Figure 6.13. Characterization of anode materials. (a) Chemical reaction for synthesis of PI. (b) SEM images of synthesized PI on CNT. (c) FT-IR spectra and (d) TGA of CNT and PI/CNT.

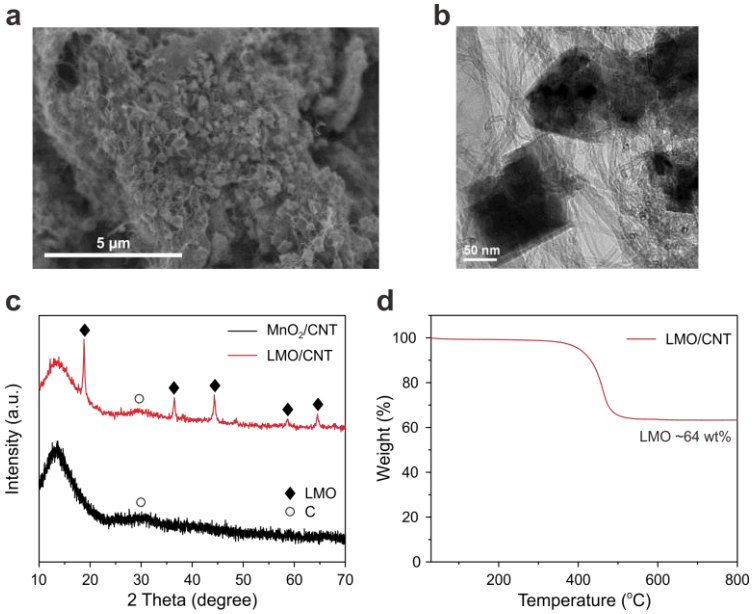

Figure 6.14. Characterization of cathode materials. (a) SEM image and (b) TEM image of synthesized LMO/CNT. (c) XRD of MnO_2/CNT and LMO/CNT. (d) TGA of LMO/CNT.

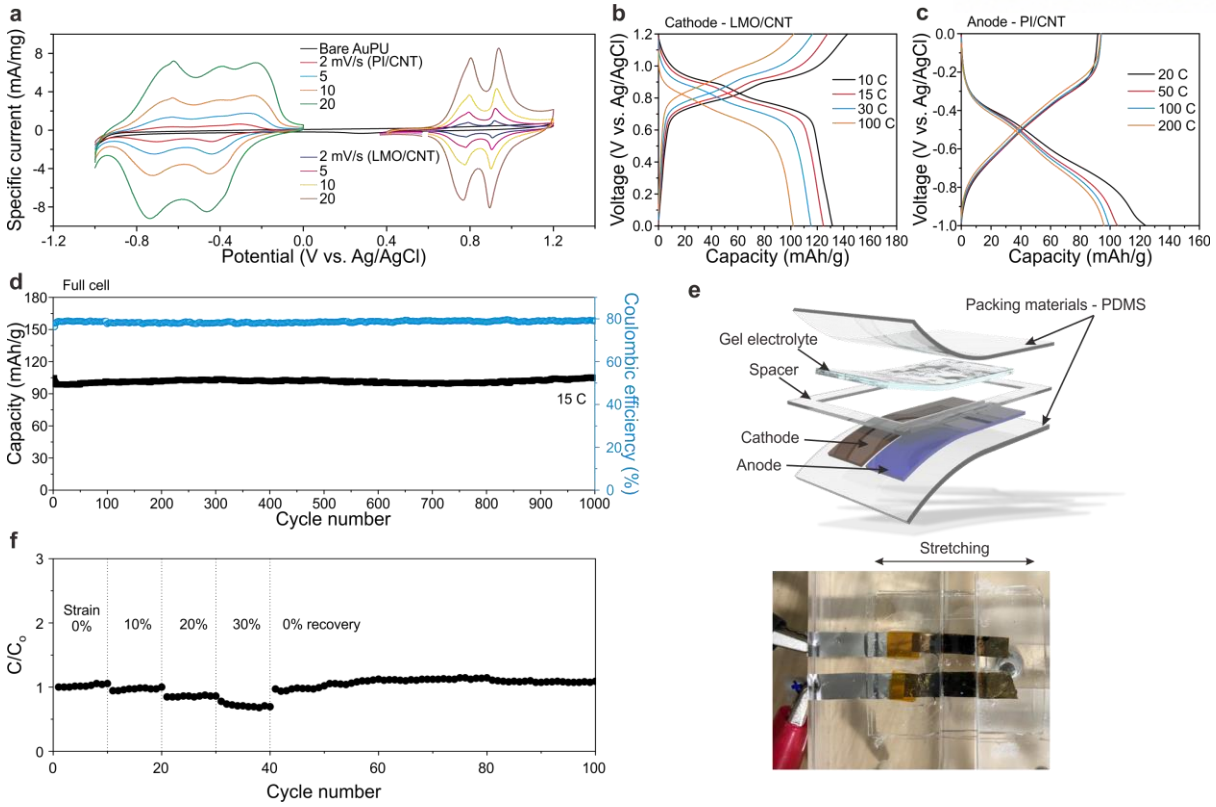

Figure 6.15. Electrochemical performance of stretchable aqueous rechargeable lithium-ion battery based on GAP multilayer conductor as a current collector. (a) Cyclic voltammetry profiles of GAP anode (PI/CNT) and GAP cathode (LMO/CNT) at various C-rates in three electrode systems with 1 M Li_2SO_4 electrolyte. (b,c) Galvanotactic charge-discharge curves of GAP cathode and GAP anode, respectively. (d) Cycling performance of full battery at a rate of 15 C between 0.0 and 2.0 V in 1 M Li_2SO_4 for 1000 cycles. (e) Schematic illustration of the stretchable aqueous rechargeable lithium-ion battery that was fabricated by using the GAP anode and cathode with coplanar layout. (f) Cycle performance of the stretchable full cell at a rate of 15 C under various strains from 0% to 30% for 100 cycles.

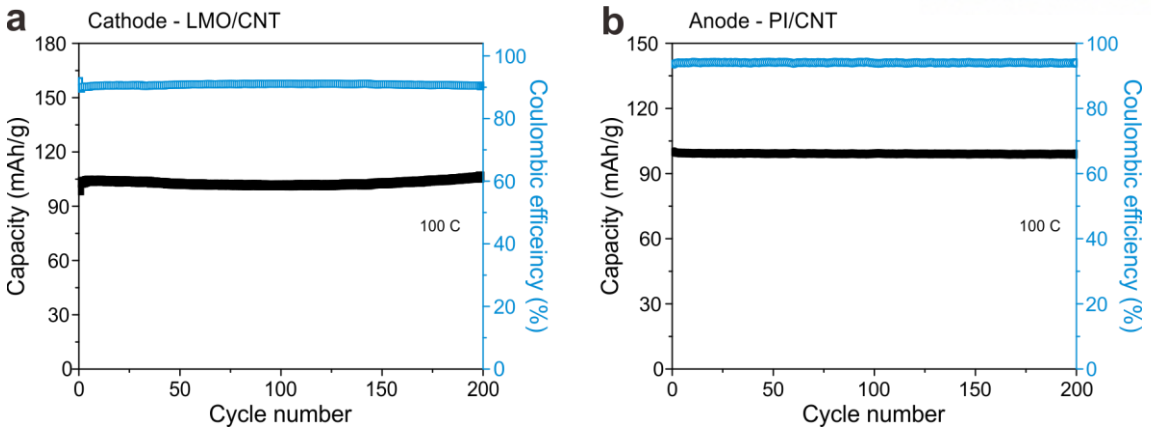

Figure 6.16. Cycling performance of (a) the cathode and (b) the anode of half cell at 100 C over 200 cycles.

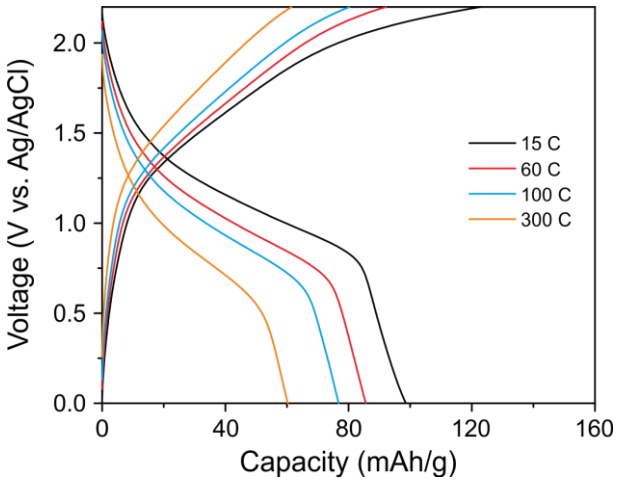

Figure 6.17. Galvanostatic charge-discharge curve of the full cell at various C-rate

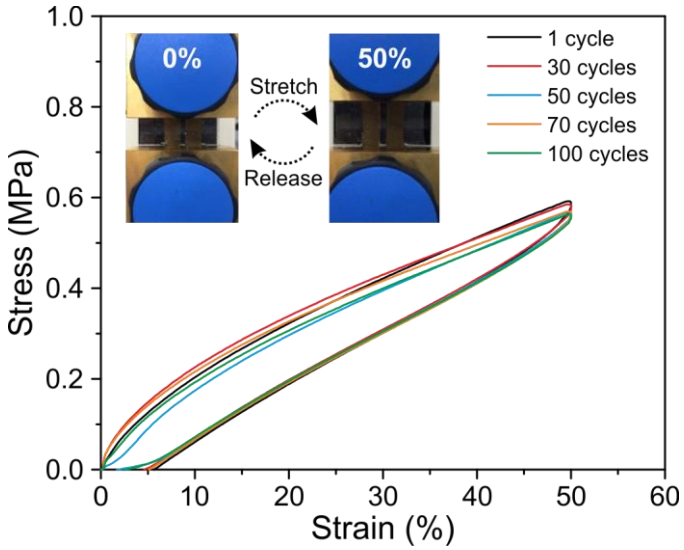

Figure 6.18. Fatigue test of the stretchable battery under 50 % strain for 100 cycles.

6.5 Conclusion

In summary, we developed the internal architecture-controlled GAP stretchable conductor by simple and scalable CbC assembly. This GAP stretchable multilayer conductor offers precise control not only over superior mechanical stretchability by adjusting the gradient concentration of each component, but also vertically directional conductivity by changing the number of interlayers. As a result, the high GAP conductors showed the in-plane structured stretchable metal conductor over 300% strain. The low GAP conductors exhibited an excellent electrical conductivity of vertical direction as well as parallel to surface over 50% strain. The in-depth study on the percolation network of Au NPs within PU matrix was further performed by in situ SAXS analysis and mechanical simulation to understand the stress-distributed behavior by propagation of cracks in multilayer architecture. We also demonstrated the stretchable ARLBs which delivered stable power with high rate capability under strain by using the GAP conductors. This novel approach for stretchable conductors is expected to encourage the design of the stretchable conductors showing high both mechanical and electrical performance for future energy conversion and storage devices as well as advanced flexible and wearable electronics.

6.6 References

(1) Rogers, J. A.; Someya, T.; Huang, Y. G. Materials and Mechanics for Stretchable Electronics. *Science* **2010,** *327*, 1603-1607.

(2) Kim, D. H.; Rogers, J. A. Stretchable Electronics: Materials Strategies and Devices. *Adv. Mater.* **2008,** *20*, 4887-4892.

(3) Matsuhisa, N.; Kaltenbrunner, M.; Yokota, T.; Jinno, H.; Kuribara, K.; Sekitani, T.; Someya, T. Printable Elastic Conductors with a High Conductivity for Electronic Textile Applications. *Nat. Commun.* **2015,** *6*, 7461.

(4) Lee, T.; Lee, W.; Kim, S. W.; Kim, J. J.; Kim, B. S. Flexible Textile Strain Wireless Sensor Functionalized with Hybrid Carbon Nanomaterials Supported ZnO Nanowires with Controlled Aspect Ratio. *Adv. Func. Mater.* **2016,** *26*, 6206-6214.

(5) Liu, W.; Song, M. S.; Kong, B.; Cui, Y. Flexible and Stretchable Energy Storage: Recent Advances and Future Perspectives. *Adv. Mater.* **2017,** *29*, 1603436.

(6) Song, W. J.; Park, J.; Kim, D. H.; Bae, S.; Kwak, M. J.; Shin, M.; Kim, S.; Choi, S.; Jang, J. H.; Shin, T. J.; Kim, S. Y.; Seo, K.; Park, S. Jabuticaba-Inspired Hybrid Carbon Filler/Polymer Electrode for Use in Highly Stretchable Aqueous Li-Ion Batteries. *Adv. Energy Mater.* **2018,** *8*, 1702478.

(7) Liu, N.; Chortos, A.; Lei, T.; Jin, L. H.; Kim, T. R.; Bae, W. G.; Zhu, C. X.; Wang, S. H.; Pfattner, R.; Chen, X. Y.; Sinclair, R.; Bao, Z. A. Ultratransparent and Stretchable Graphene Electrodes. *Sci. Adv.* **2017,** *3*, e1700159.

(8) Kim, K.; Kim, J.; Hyun, B. G.; Ji, S.; Kim, S. Y.; Kim, S.; An, B. W.; Park, J. U. Stretchable and Transparent Electrodes based on In-plane Structures. *Nanoscale* **2015,** *7*, 14577-14594.

(9) Hu, L. B.; Pasta, M.; La Mantia, F.; Cui, L. F.; Jeong, S.; Deshazer, H. D.; Choi, J. W.; Han, S. M.; Cui, Y. Stretchable, Porous, and Conductive Energy Textiles. *Nano Lett.* **2010,** *10*, 708-714.

(10) Chun, K. Y.; Oh, Y.; Rho, J.; Ahn, J. H.; Kim, Y. J.; Choi, H. R.; Baik, S. Highly Conductive, Printable and Stretchable Composite Films of Carbon Nanotubes and Silver. *Nat. Nanotechnol.* **2010,** *5*, 853-857.

(11) Matsuhisa, N.; Inoue, D.; Zalar, P.; Jin, H.; Matsuba, Y.; Itoh, A.; Yokota, T.; Hashizume, D.; Someya, T. Printable Elastic Conductors by in situ Formation of Silver Nanoparticles from Silver Flakes. *Nat. Mater.* **2017,** *16*, 834-840.

(12) Catenacci, M. J.; Reyes, C.; Cruz, M. A.; Wiley, B. J. Stretchable Conductive Composites from Cu-Ag Nanowire Felt. *ACS Nano* **2018,** *12*, 3689-3698.

(13) Kim, Y.; Zhu, J.; Yeom, B.; Di Prima, M.; Su, X. L.; Kim, J. G.; Yoo, S. J.; Uher, C.; Kotov, N. A. Stretchable Nanoparticle Conductors with Self-Organized Conductive Pathways. *Nature* **2013,** *500*, 59-63.

(14) Yu, C. J.; Masarapu, C.; Rong, J. P.; Wei, B. Q.; Jiang, H. Q. Stretchable Supercapacitors Based on Buckled Single-Walled Carbon Nanotube Macrofilms. *Adv. Mater.* **2009,** *21*, 4793-4797.

(15) Kim, D. H.; Song, J. Z.; Choi, W. M.; Kim, H. S.; Kim, R. H.; Liu, Z. J.; Huang, Y. Y.; Hwang, K. C.; Zhang, Y. W.; Rogers, J. A. Materials and Noncoplanar Mesh Designs for Integrated Circuits with Linear Elastic Responses to Extreme Mechanical Deformations. *Proc. Natl. Acad. Sci. U.S.A.* **2008,** *105*, 18675-18680.

(16) Mu, J. K.; Hou, C. Y.; Wang, G.; Wang, X. M.; Zhang, Q. H.; Li, Y. G.; Wang, H. Z.; Zhu, M. F. An Elastic Transparent Conductor Based on Hierarchically Wrinkled Reduced Graphene Oxide for Artificial Muscles and Sensors. *Adv. Mater.* **2016,** *28*, 9491-9497.

(17) Xu, F.; Wang, X.; Zhu, Y. T.; Zhu, Y. Wavy Ribbons of Carbon Nanotubes for Stretchable Conductors. *Adv. Func. Mater.* **2012,** *22*, 1279-1283.

(18) Zang, J. F.; Cao, C. Y.; Feng, Y. Y.; Liu, J.; Zhao, X. H. Stretchable and High-Performance Supercapacitors with Crumpled Graphene Papers. *Sci. Rep.* **2014,** *4*, 6492.

(19) Xu, S.; Zhang, Y. H.; Cho, J.; Lee, J.; Huang, X.; Jia, L.; Fan, J. A.; Su, Y. W.; Su, J.; Zhang, H. G.; Cheng, H. Y.; Lu, B. W.; Yu, C. J.; Chuang, C.; Kim, T. I.; Song, T.; Shigeta, K.; Kang, S.; Dagdeviren, C.; Petrov, I.; Braun, P. V.; Huang, Y. G.; Paik, U.; Rogers, J. A. Stretchable Batteries with Self-Similar Serpentine Interconnects and Integrated Wireless Recharging Systems. *Nat. Commun.* **2013,** *4*, 1543.

(20) Libanori, R.; Erb, R. M.; Reiser, A.; Le Ferrand, H.; Suess, M. J.; Spolenak, R.; Studart, A. R. Stretchable Heterogeneous Composites with Extreme Mechanical Gradients. *Nat. Commun.* **2012,** *3*, 1265.

(21) Zhu, J.; Zhang, H. N.; Kotov, N. A. Thermodynamic and Structural Insights into Nanocomposites Engineering by Comparing Two Materials Assembly Techniques for Graphene. *ACS Nano* **2013,** *7*, 4818-4829.

(22) Decher, G. Fuzzy Nanoassemblies: Toward Layered Polymeric Multicomposites. *Science* **1997,** *277*, 1232-1237.

(23) Richardson, J. J.; Bjornmalm, M.; Caruso, F. Technology-Driven Layer-by-Layer Assembly of Nanofilms. *Science* **2015,** *348*, aaa2491

(24) Lee, T.; Min, S. H.; Gu, M.; Jung, Y. K.; Lee, W.; Lee, J. U.; Seong, D. G.; Kim, B. S. Layer-by-Layer Assembly for Graphene-Based Multi layer Nanocomposites: Synthesis and Applications. *Chem. Mater.* **2015,** *27*, 3785-3796.

(25) Gu, M. S.; Kim, B. S. Unraveling the Importance of Controlled Architecture in Bimetallic Multilayer Electrode Toward Efficient Electrocatalyst. *Nano Energy* **2016,** *30*, 658-666.

(26) Rydzek, G.; Ji, Q. M.; Li, M.; Schaaf, P.; Hill, J. P.; Boulmedais, F.; Ariga, K. Electrochemical Nanoarchitectonics and Layer-by-Layer Assembly: From Basics to Future. *Nano Today* **2015,** *10*, 138-167.

(27) Zhang, H.; Scholz, A. K.; de Crevoisier, J.; Vion-Loisel, F.; Besnard, G.; Hexemer, A.; Brown, H. R.; Kramer, E. J.; Creton, C. Nanocavitation in Carbon Black Filled Styrene-Butadiene Rubber under

Tension Detected by Real Time Small Angle X-ray Scattering. *Macromolecules* **2012,** *45*, 1529-1543.

(28) Yamaguchi, K.; Busfield, J. J. C.; Thomas, A. G. Electrical and Mechanical Behavior of Filled Elastomers. I. The Effect of Strain. *J. Polym. Sci. B Polym. Phys.* **2003,** *41*, 2079-2089.

(29) Alias, N.; Mohamad, A. A. Advances of Aqueous Rechargeable Lithium-Ion Battery: A Review. *J. Power Sources* **2015,** *274*, 237-251.

(30) Zhao, Y.; Ding, Y.; Li, Y. T.; Peng, L. L.; Byon, H. R.; Goodenough, J. B.; Yu, G. H. A Chemistry and Material Perspective on Lithium Redox Flow Batteries Towards High-Density Electrical Energy Storage. *Chem. Soc. Rev.* **2015,** *44*, 7968-7996.

(31) Zhang, Y.; Wang, Y. H.; Wang, L.; Lo, C. M.; Zhao, Y.; Jiao, Y. D.; Zheng, G. F.; Peng, H. S. A Fiber-Shaped Aqueous Lithium Ion Battery with High Power Density. *J. Mater. Chem. A* **2016,** *4*, 9002-9008.

(32) Guo, Z. W.; Chen, L.; Wang, Y. G.; Wang, C. X.; Xia, Y. Y. Aqueous Lithium-Ion Batteries Using Polyimide-Activated Carbon Composites Anode and Spinel $LiMn_2O_4$ Cathode. *ACS Sustainable Chem. Eng.* **2017,** *5*, 1503-1508.

Chapter 7.
Summary and Outlook

We anticipate that unexplored fundamental studies and design strategies for LbL assembly composites remain to be discovered, and some of their future endeavors are proposed in the following. Chemically exfoliated graphene has been extensively utilized in various fields as a versatile platform due to its superior intrinsic properties together with a facile preparation method. It is well known that the physicochemical properties of graphene sheets are highly dependent on their chemical compositions such as sheet size, density of functional groups, heteroatom doping, and defect density. The electronic and mechanical properties of the nanocomposites will be benefited from the larger sized graphene sheets with less defect density. On the other hand, smaller sized graphene sheets show high dispersion stability in various media, providing improved processability for composite applications (**Chapter 3.2**). Thus, more controlled synthesis of graphene with well-defined structures and compositions not only expands the versatility of composite materials for diverse applications but also helps to provide the fundamental understanding of graphene-based LbL assembly.

Although most of LbL-assembled composites are based on the two-component assembly, multicomponent assembly beyond the conventional approach will be a subject of intensive research effort in LbL systems. Moreover, the internal architecture of composites is easily tunable by simply adjusting the layer sequence, resulting in various nanocomposites with controlled structures. For example, with a simple two component system composed of active species of A and B, one could produce the fully alternating structure (i.e., substrate/ABAB) or compartmented structure (i.e., substrate/ AABB or substrate/BBAA) (**Chapter 3.1**). This precise control of internal structure within the thin films can optimize the characteristics of the LbL-assembled graphene nanocomposites even under the identical composition, which is not attainable with a simple mixing method.

Diverse materials are widely used for LbL components in architecture control, regardless of the chemical compositions (e.g., organic, inorganic, carbon, and metal) and their dimensions (e.g., 0-, 1-, 2-, and 3D) (**Chapter 2, 4, 5, and 6**). Recent developments in materials science have continuously expanded the potential candidates for LbL components. Based on the discovery of novel nanomaterials and development of their surface modification techniques, numerous building blocks will be applied to the architecture-controlled LbL assembly and provide a new concept of nanocomposites and novel future applications.

List of Publications

(Currently, July 2018)

†These authors contributed equally to this work.

1) Dongseok Kim,† **Minsu Gu**,† Jungki Ryu, and Byeong-Su Kim* “Organic-based Artifical Photocatalytic Multilayer Anodes for Efficient Water Splitting” *Manuscript in preparation*

2) **Minsu Gu**,† Woo-Jin Song,† Jaehyung Hong, Jaewon Choi, Sungho Kim, Sung Youb Kim, Tae Joo Shin, Nicholas A. Kotov,* Soojin Park,* and Byeong-Su Kim* “Gradient assembled polyurethane-based stretchable multilayer conductors” *near to submit*

3) Yeongkyu Choi,† Dasom Jeon,† Yuri Choi, Taemin Lee, Nayeong Kim, **Minsu Gu**, Sanghyun Bae, Dongseok Kim, Hyun-Wook Lee, Byeong-Su Kim,* and Jungki Ryu* "Nacre-like Catalytic Multilayers of Graphene Oxide Nanosheets and Polyoxometalates on Hematite for Solar Water Oxidation" *submitted*

4) **Minsu Gu**,* Jaewon Choi, Taemin Lee, Minju Park, Ik-Soo Shin, Jinkee Hong, Hyun-Wook Lee and Byeong-Su Kim* "Diffusion-Controlled Multilayer Nanoelectrode via Sized Graphene Oxide Nanosheets" *under revision*

5) Dasom Jeon, Hyunwoo Kim, Cheolmin Lee, Yujin Han, **Minsu Gu**, Byeong-Su Kim, and Jungki Ryu* "Layer-by-Layer Assembly of Polyoxometalates for Photoelectrochemical (PEC) Water Splitting: Towards Modular PEC Devices" *ACS Applied Materials & Interfaces* **2017**, *9*, 40151–40161

6) Eungjin Ahn,† Taemin Lee,† **Minsu Gu**,† Minju Park,† Sa Hoon Min,† and Byeong-Su Kim* "Layer-by-Layer Assembly for Graphene-based Multilayer Nanocomposites: The Field Manual" *Chemistry of Materials* **2017**, *29*, 69–79

7) **Minsu Gu** and Byeong-Su Kim* "Unraveling the Importance of Controlled Architecture in Bimetallic Multilayer Electrode toward Efficient Electrocatalyst" *Nano Energy* **2016**, *30*, 658–666

8) Jung-Hwan Kim,† **Minsu Gu**,† Do Hyun Lee, Jeong-Hoon Kim, Yeon-Su Oh, Sa Hoon Min,* Byeong-Su Kim,* and Sang-Young Lee* "Functionalized Nanocellulose-Integrated Heterolayered Nanomats toward Smart Battery Separators" *Nano Letters* **2016**, *16*, 5533–5541

9) Kyeong Nam Kim,† Yun Kyung Jung,† Jinsung Chun, Byeong Uk Ye, **Minsu Gu**, Eunyong Seo, Seongsu Kim, Sang-Woo Kim, Byeong-Su Kim* and Jeong Min Baik* "Surface Dipole Enhanced Instantaneous Charge Pair Generation in Triboelectric Nanogenerator" *Nano Energy*

2016, *26*, 360–370

10) Kiyoung Jo,† **Minsu Gu**,† and Byeong-Su Kim* "Ultrathin Supercapacitor Electrode Based on Reduced Graphene Oxide Nanosheets Assembled with Photo-Cross-Linkable Polymer: Conversion of Electrochemical Kinetics in Ultrathin Films" *Chemistry of Materials* **2015**, *27*, 7982–7989.

11) **Minsu Gu**,† Seunghee Ko,† Seungmin Yoo,† Eunhee Lee, Sa Hoon Min, Soojin Park,* and Byeong-Su Kim* "Double Locked Silver-coated Silicon Nanoparticle/Graphene Core/Shell Fiber for High-Performance Lithium-Ion Battery Anodes" *Journal of Power Sources* **2015**, *300*, 351–357

12) Taemin Lee,† Sa Hoon Min,† **Minsu Gu**,† Yun Kyung Jung,† Wonoh Lee, Jea Uk Lee, Dong Gi Seong, and Byeong-Su Kim* "Layer-by-Layer Assembly for Graphene-based Multilayer Nanocomposites: Synthesis and Applications" *Chemistry of Materials* **2015**, *27*, 3785–3796 (Selected as the Top 20 most downloaded articles looking back over the past year from Chemistry of Materials)

13) **Minsu Gu**, Jukyoung Lee, Yongil Kim, Joon Soo Kim, Bo Yun Jang,* Kyu Tae Lee,* and Byeong-Su Kim* "Inhibiting the Shuttle Effect in Lithium–Sulfur Batteries Using a Layer-by-Layer Assembled Ion-Permselective Separator" *RSC Advances* **2014**, *4*, 46940–46946

14) Taemin Lee, **Minsu Gu**, and Byeong-Su Kim* "Versatile Graphene Nanocomposites by Layer-by-Layer Assembly for Electroactive Materials" *Polymer Science and Engineering (Korean)* **2013**, *24*, 512–516

15) Yuri Choi, **Minsu Gu**, Jongnam Park, Hyun-Kon Song and Byeong-Su Kim* "Graphene Multilayer Supported Gold Nanoparticles for Efficient Electrocatalysts toward Methanol Oxidation" *Advanced Energy Materials* **2012**, *2*, 1510–1518

Acknowledgements

First of all, I would like to express thanks to my advisor, Prof. Byeong-Su Kim for generous support and excellent advice to achieve successful Ph.D. thesis. He taught me what a Ph.D. as independent researcher was, and a perspective in chemistry.

I am also grateful to all committee members, Prof. Soojin Park (various battery application), Prof. Hyun-Kon Song (electrochemistry teacher), Prof. Jungki Ryu (photo-electrochemical application), and Prof. Ik-Soo Shin (advice on electrochemical analysis).

I also thank to Prof. Sang-Young Lee, Prof. Kyu Tae Lee, Prof. Jinkee Hong, Prof. Hyun-Wook Lee, Prof. Hu Young Jeong, Prof Sung Youb Kim, and Prof. Tae Joo Shin for assisting the analysis with collaboration. I would like to thank Prof. Nicholas Kotov for giving a great experience with his group students during visiting scholar at University of Michigan, Ann Arbor.

Many thanks to my co-workers (Woo-Jin Song, Jaehyung Hong, Woo-ram Lee, Jung-Hwan Kim, Seungmin Yoo, Seunghee Ko, and Yongil Kim). With their help and assistance, I could successfully complete my research projects.

It is a pleasure to express my gratitude to all KBS group members, including doctors (Sa Hoon Min, Yun Kyung Jung, Su Hee Song and Abu Bakkar Siddique), seniors (Taemin Lee, Yuri Choi, Eunyong Seo, Piljae Joo, Sueun Lee, Eun Kyung Jeon, and Eunhee Lee), colleagues (Kiyoung, Eungjin, Eeseul, Suhyun, Joonhee, Minju, Byeongho, Yeongkyu, Gyunhyeok, Songa, Haeree, Jaeeun, Taehyung, Minseong, Yungyeong, Eunbyul, Dongseok, and Youngjoo), and undergraduates (Jungil, Jaewon and Dongjun). Without them, I would have been hard during my graduate life.

I would like to thank UNIST soccer club, Earth Cops, members for enjoying in my UNIST life of 9-years, and my 17-best old friends in Guri (Sungmin, Woojin, Jaeseon, Eunkyu, Wonsik, Hoeseung, Ilsoo, Myungjun, Jangho, Jinwoo, Hyungjin, Gyubum, Minseok, Daeyoung, Seyoung, Hyoryung, and Jooha) for always being with me.

Finally, I would like to express the deepest appreciation to my family. I love you.

I acknowledge the financial support from the Global Ph.D. Fellowship (GPF) funded by the National Research Foundation of Korea (NRF) during my P.h.D. course of 5-years (Mar.2013~Feb.2018).